A single Rydberg Atom interacting with a Dense and Ultracold Gas

Von der Fakultät Mathematik und Physik der Universität Stuttgart
zur Erlangung der Würde eines Doktors der Naturwissenschaften
(Dr. rer. nat.) genehmigte Abhandlung.

vorgelegt von

Michael Thomas Schlagmüller

aus Stuttgart

Hauptberichter:	Prof. Dr. Tilman Pfau
Mitberichter:	Prof. Dr. Harald Giessen
Prüfungsvorsitzender:	Prof. Dr. Günter Wunner
Tag der mündlichen Prüfung:	01. April 2016

5. Physikalisches Institut
Universität Stuttgart
2016

D 93

List of publications

[S1] M. Schlagmüller, T. C. Liebisch, H. Nguyen, G. Lochead, F. Engel, F. Böttcher, K. M. Westphal, K. S. Kleinbach, R. Löw, S. Hofferberth, T. Pfau, J. Pérez-Ríos, and C. H. Greene. "Probing an Electron Scattering Resonance using Rydberg Molecules within a Dense and Ultracold Gas". Phys. Rev. Lett. **116** (2016), 053001 (cit. on pp. 7, 19, 22, 78, 85, 151).

[S2] T. C. Liebisch et al. "Controlling Rydberg atom excitations in dense background gases". J. Phys. B At. Mol. Opt. Phys. **49** (2016), 182001 (cit. on pp. 7, 96, 129, 152).

[S3] M. Schlagmüller, T. C. Liebisch, F. Engel, K. S. Kleinbach, F. Böttcher, U. Hermann, K. M. Westphal, A. Gaj, R. Löw, S. Hofferberth, T. Pfau, J. Pérez-Ríos, and C. H. Greene. "Ultracold Chemical Reactions of a Single Rydberg Atom in a Dense Gas". Phys. Rev. X **6** (2016), 031020 (cit. on pp. 7, 19, 22, 102, 112, 153, 155).

[S4] T. Karpiuk, M. Brewczyk, K. Rzażewski, A. Gaj, J. B. Balewski, A. T. Krupp, M. Schlagmüller, R. Löw, S. Hofferberth, and T. Pfau. "Imaging single Rydberg electrons in a Bose–Einstein condensate". New J. Phys. **17** (2015), 53046 (cit. on pp. 8, 19, 30, 101, 126, 150, 154).

[S5] F. Böttcher, A. Gaj, K. M. Westphal, M. Schlagmüller, K. S. Kleinbach, R. Löw, T. C. Liebisch, T. Pfau, and S. Hofferberth. "Observation of mixed singlet-triplet Rb_2 Rydberg molecules". Phys. Rev. A **93** (2016), 032512 (cit. on pp. 22, 74–76, 127, 134).

Zusammenfassung

Diese Dissertation beschreibt die Entwicklung und Realisierung einer neuen Experimentierapparatur zur Erforschung ultrakalter ($T < 1\,\mu\mathrm{K}$) Rubidium-Atome, sowie die Erforschung der elementaren Wechselwirkungen zwischen einem einzelnen Rydberg-Atom mit den umgebenden Atomen. Die Physik, als Teil der Naturwissenschaften, untersucht die grundlegenden Phänomene der Natur. Wir als Physiker versuchen zu erforschen und zu verstehen, wie unsere Welt aufgebaut ist. Die Nobelpreisträgerliste der letzten Jahre in der Physik spiegelt die große Bedeutung der Erforschung der elementaren Wechselwirkung wieder. 2011 wurde die Entdeckung der beschleunigten Expansion des Universums geehrt. 2013 wurde die Vorhersage des Higgs Teilchen [6–9] ausgezeichnet, nachdem es 2012 am Teilchenbeschleuniger des CERN experimentell bestätigt wurde [10], welches zu unserem Verständnis des Ursprungs der Masse subatomarer Teilchen beiträgt. 2015 wurden der Nachweis geehrt, dass Neutrinos eine Masse besitzen, welche für das Standardmodell der Elementarteilchenphysik von wichtiger Bedeutung ist. Ende 2015 [11] konnten zum ersten Mal Gravitationswellen [12, 13] gemessen werden, obwohl diese nur sehr schwach mit der Materie wechselwirken. Die Erforschung der elementaren Wechselwirkungen von Teilchen und Systemen bringt uns unserem Ziel näher, die Natur besser zu verstehen.

Auch im Kontext der Atomphysik spielen die Wechselwirkungen von Teilchen eine entscheidende Rolle für unser Verständnis. Im Rahmen dieser Dissertation wurden die elementaren Wechselwirkungen zwischen einem Rubidium Rydberg-Atom und einem Bose-Einstein Kondensat [14–17] untersucht und erklärt. Rydberg-Atome besitzen einige Eigenschaften, die sie besonders interessant für Forschungszwecke machen. Cäsium ist das größte stabilste Element mit einem Durchmesser von circa 500 pm. Die Größe der Rydberg-Atome wird durch das äußere Rydberg-Elektron bestimmt, das klassisch gesehen auf einer hohe Schale um das angeregte Atom kreist. Die Hauptquantenzahl der hier

untersuchten Atome reicht bis zu $n = 150$ und der Durchmesser des dazugehörigen Elektronenorbitals beträgt 4.0 µm. Die Größe hat zur Folge, dass das Rydberg-Elektron mit vielen umgebenden Teilchen elastisch kollidiert, da der mittlere Atomabstand an der dichtesten Stelle des erzeugten Bose-Einstein Kondensat nur 69 nm ist. Für den genannten Fall befinden sich circa 26000 Atome innerhalb des Rydberg-Orbitals welche alle mit dem Rydberg-Elektron wechselwirken, da sie durch die Ladung des Elektrons polarisiert werden. Der prinzipielle Mechanismus mit dem das Elektron mit den Teilchen wechselwirkt, ist derselbe, wie für gewöhnliche Atome. Nur die Stärke der Wechselwirkung und damit die Zeitskala auf der die Dynamik der Teilchen eine Rolle spielt, ist für ein einzelnes Rydberg-Atom in einem Bose-Einstein Kondensat im Mikrosekundenbereich, welches im Vergleich zu den Wechselwirkungszeiten der normalen Atome vergleichsweise einfach zu messen ist. Das Rydberg-Atom bietet die Möglichkeit, bestimmte elementare Wechselwirkungen an einem vergleichsweise einfach zugänglichen System zu messen, welche aber auf denselben Prinzipien der (Quanten-)Physik beruhen.

Die Erforschung von Rubidium Rydberg-Atomen hat eine erfolgreiche Vergangenheit am 5. Physikalischen Institut in Stuttgart. Verschiedene bahnbrechende Entdeckungen wurden mit der ersten Experimentierapparatur [18] (2004-2015) in diesem Forschungsfeld erreicht, wie beispielsweise der experimentelle Nachweis einer neuartigen Molekülbindung [19].

Das Nachfolger-Experiment wurde im Rahmen der Wissenschaftlichen Arbeit für dieses Dissertationsvorhaben von Grund auf neu entworfen und aufgebaut. Ein besonderer Schwerpunkt lag darauf, sehr effizient und präzise einzelne Rydberg-Atome anregen, manipulieren und detektieren zu können. Des Weiteren war es ein Ziel der Entwicklung, tagelange Messreihen am Experiment durchführen zu können, ohne dass ein Eingriff von außen nötig wird. Hierfür mussten alle eingesetzten Komponenten im Experiment auf ihre Langzeitstabilität geprüft und ausgewählt werden. Die konsequente Umsetzung ermöglicht es nun, das schwache Signal von einem einzelnen Rydberg-Atom als Messgröße der untersuchten Wechselwirkungen zu nutzen. Für den Aufbau wurden zahlreiche Elektronikgeräte neu entwickelt. Eine universelle Experimentsteuerungssoftware wurde programmiert und zudem Auswerteframework für die Analyse der Messdaten. Sowohl die entwickelte Hardware als auch Software wird mittlerweile an verschiedenen Experimenten im Institut eingesetzt.

Mit der neuen Apparatur können alle 25 s ein Bose-Einstein Kondensat mit 1.7 Millionen Atome erzeugt werden, die in einer magnetischen Falle gehalten werden, an denen mit einem einzigen Kondensat bis zu 5000 Versuche durchgeführt werden können. Die optische Auflösungsgenauigkeit des Abbildungssystems beträgt circa 1 µm und der fokussierte Laser für die Anregung hat eine Strahlbreite im Fokuspunkt von circa 2 µm. Die elektrischen Felder innerhalb der Experimentierkammer können auf $1\,\mathrm{mV\,cm^{-1}}$ genau kompensiert werden, wobei der Drift der elektrischen Felder $10\,\mathrm{mV\,cm^{-1}}$ pro Stunde beträgt. Die zeitliche Steuer- und Detektionsgenauigkeit der Apparatur liegt im 1 - 2 ns Bereich.

Mit Hilfe der neuen Apparatur wurden zum ersten Mal einzelne Rydberg-Atome in einem Bose-Einstein Kondensat spektroskopiert [S1]. Die Spektren wurden systematisch für verschiedene nS Rydberg-Zustände gemessen, mit einer Hauptquantenzahl von $n = 40$ bis 111. Die extrem hohen Dichten im Kondensat (bis zu 6×10^{14} Atome/cm^3) führen zu einer spektralen Verbreiterung und Frequenzverschiebung im Vergleich zur Anregung eines Rydberg-Atoms ohne zusätzliche Atome im Rydberg-Orbital, da das Rydberg-Elektron elastisch an den Atomen in seinem Orbital streut. Es wurde ein Modell entwickelt, mit dem die untersuchten Spektren erklärt werden können. Die Simulation der Spektren beruht auf der gemeinsamen Potentialkurve von einem Rydberg-Atom mit einem Grundzustand-Atom. Hierbei konnte nachgewiesen werden, dass die p-Wellen Streuresonanz in Rubidium für die Form des Spektrums von entscheidender Bedeutung ist. Die p-Wellen Resonanz führt dazu, dass besonders für niedrige Hauptquantenzahlen (z.B. $n = 40$) ein Signal bei über $-100\,\mathrm{MHz}$ Verstimmung von der Frequenz der atomaren Rydberg-Anregung gemessen wird.

Der Effekt der Frequenzverstimmung durch die Wechselwirkung zwischen dem Rydberg-Elektron und den Grundzustands-Atomen kann dazu genutzt werden, dass mit der Anregungs-Laserfrequenz eine bestimmte Dichteregion im Anregungsvolumen ausgewählt werden kann [S2]. Dieser Zusammenhang wurde experimentell für den 90S Rydberg-Zustand bestätigt. Die Empfindlichkeit dieser Auswahlmethode wurde Anhand des für die Spektren entwickelten Modells untersucht und der Zusammenhang zwischen der Anregungsfrequenz, der Hauptquantenzahl und der Dichte des Hintergrundgases erörtert.

Des Weiteren wurden die Dynamik eines einzelnen Rydberg-Atoms innerhalb des Bose-Einstein Kondensates erforscht [S3]. Wenige Mikrosekunden nach der Anregung das Rydberg-Atoms kollidiert dieses unelastisch mit einem Grundzustands-Atom. Durch diese Kollision gewinnt das Rydberg-Elektron einen Drehimpuls und wechselt das Orbital. In dieser Reaktion wird kinetische Energie freigesetzt, die sich beide Kollisionspartner teilen. Als zweites Reaktionsprodukt entsteht aus der Kollision ein tief gebundenes Rb_2^+ Molekül-Ion mit einem freien Elektron. Der Zusammenhang zwischen Dichte (1×10^{14} Atome/cm^3 bis 5×10^{14} Atome/cm^3) und Hauptquantenzahl ($n = 40$ bis 150) für die Reaktion wurde untersucht und die Lebenszeit der Rydberg-Atome für diese Parameter bestimmt. Die Lebenszeit der Rydberg-Atome und deren Obergrenze spielt eine wichtige Rolle für die Rydberg-Physik, da sie die maximale Experimentierdauer der sonst langlebigen Rydberg-Atome besonders bei hohen atomaren Dichten begrenzt.

Eine Analyse der neu gewonnenen Erkenntnisse über die Wechselwirkungsstärke und -dauer zeigt auf, dass die Wechselwirkung eines einzelnen Rydberg-Atoms so stark sein kann, dass die Dichte des Bose-Einstein Kondensates lokal durch das Rydberg-Elektron modifiziert wird. Die anziehende Wechselwirkung zwischen dem Elektron und dem Bose-Einstein Kondensat führt dazu, dass sich die Dichte der Atome genau an den Stellen erhöht, an denen das Rydberg-Elektron eine hohe Aufenthaltswahrscheinlichkeit besitzt. Für Rydberg-Atome mit einer Hauptquantenzahl von über $n = 100$ ist die Auflösung des Abbildungssystems (1 µm) genau genug, um zum aller ersten Mal das Elektronenorbital eines Rydberg-Atoms optisch auf eine Kamera abzubilden. Hierfür werden zwei verschiedene Experimente am Ende dieser Dissertation vorgeschlagen [S4].

Contents

All religions, arts and sciences are branches of the same tree. All these aspirations are directed toward ennobling man's life, lifting it from the sphere of mere physical existence and leading the individual towards freedom.

Out of My Later Years, Albert Einstein

1

Introduction

Natural science is a driving force of the knowledge we have of the world we live in. Fundamental research is continuously triggering advances in technology, which improve the way we live.

We all want to understand the world around us, how everything is related to each other. We want to know the building blocks of our world and how they interact. Our interest reaches from the end of the universe to the tiniest particles we know of and beyond. We have unanswered questions about dark matter [20] or dark energy [21], which play a crucial role for our universe, but which we do not understand. Maybe the very recent finding of a host galaxy of a fast radio burst [22] will solve the puzzle of dark matter. On the scale of tiny interactions beautiful discoveries were made in recent years. For example, the measurement of gravitational waves [11] ends a long journey, which began 1916 with Einstein predicting this phenomenon [12, 13]. The efforts of this research finally pay off and strengthens the hypothesis we have about the very elementary interactions of our universe, but also raises new questions we have to answer. Another astonishing example is the discovery of the Higgs particle in 2012 [10], which was only possible due to a worldwide collaboration of many physicists and engineers from 85 nations at CERN. The particle was predicted in 1964 [6–9], and after the experimental evidence of it, the Nobel prize was given in 2013 for the prediction. The last Nobel prize (2015) was given for the discovery of neutrino oscillations [23–25] between 1998 and 2002. This shows that neutrinos have mass, which again is related to very fundamental questions we have about our universe.

There are many more questions we have about the interactions of particles, especially in the quantum regime which still, after more than 100 years of research, is hard to access in experiments. This thesis is dedicated to rubidium Rydberg atoms and their fundamental interactions with rubidium ground-state atoms. The interaction is studied in a Bose-Einstein condensate [14–17], which gives a well-defined, and ultracold starting condition for the experiments. Rydberg atoms interact with their environment as normal atoms do, but with a different strength, and on a different length, and time scale. A single Rydberg atom can be excited with optical laser light. The relevant timescale for the dynamics in the ultracold environment is in the microsecond regime, which can be easily measured. The excitation, manipulation, and detection of the Rydberg atoms can be controlled with commercial products, which fulfill the timing requirements. Hence, Rydberg atoms can be examined in a direct way. Even though they have extreme properties, the interaction mechanisms of the atoms are the same for the large Rydberg atoms and the ordinary atoms. The latter is often hard to access in an experiment and the effort required to study physics at the very small scale is immense, which can be seen, for example, from a recent study tracking the nonlinear response of bound electrons with optical attosecond pulses [26]. The timescale for a Rydberg atom to undergo an inelastic collision in a Bose-Einstein condensate is four orders of magnitude slower and, therefore, more easily accessible.

Besides the interesting fundamental interactions, which can be studied with Rydberg atoms, there are many suggestions for future applications of Rydberg atoms. They can be used for quantum simulation [27] and quantum information processing [28]. Rydberg atoms have been already utilized for microwave electrometry even at room temperature in vapor cells [29]. The first steps to control many-body quantum systems with well controlled interactions are realized [30–32], which take us one step further towards a quantum simulator, which could, for example, simulate aspects of questions we have in the field of quantum biology [33]. With the advances of technology and research we find more and more quantum phenomena in nature. The research of these topics will give us a deeper understanding of our world and, in the long term, provide the basis for quantum technologies and quantum devices in our everyday life. Maybe, at some point, this will lead to a quantum era for mankind.

This thesis

In this context, the work described in this thesis contributes in two ways to the research field of Rydberg atoms. Part I describes the design considerations, the engineering and the realization of the experimental apparatus built-up to study Rydberg atoms in the ultracold environment. Technical details of the electronic devices built for the setup will be explained, as well as for the experiment control, data acquisition, and evaluation system. The components of the apparatus are characterized, which show that experiments using this apparatus can be performed over several days with an excellent long-term stability. This makes it possible to investigate a single Rydberg atom in Bose-Einstein condensate.

In part II, we study a Rydberg atom in a Bose-Einstein condensate to explore the interactions and limitations of Rydberg atoms in an ultracold and very dense gaseous environment. The elastic collisions of the Rydberg atom with ground-state atoms of the Bose-Einstein condensate lead to an energy shift of the Rydberg atom, for which a new model description is invented with which the measured spectra can be simulated successfully. The dynamics of the particles become important after a few microseconds. Inelastic collisions change the orbital angular momentum of the Rydberg state or create deeply bound Rb_2^+ molecules. Both of these ultracold chemical reactions will be studied in detail. With a deeper understanding of the interactions and the limitations of the lifetime of the Rydberg atoms, finally, two experiments are proposed to optically image the angular structure of a Rydberg electron orbital in real space in a single shot experiment.

Part I

Designing and building an experimental setup to investigate ultracold rubidium atoms

2

Experimental setup

The study of Rydberg physics with ultracold rubidium atoms has a long, successful history in our institute in Stuttgart. Several ground-breaking and astonishing results could be reported within this research field. With the experimental setup to investigate Rydberg atoms built up during 2004-2006 [18], evidence for coherent collective Rydberg excitations was provided in 2007 [34], along with the first Rydberg excitations in a Bose-Einstein condensate in 2008 [35]. The proposed novel binding mechanism of ultralong-range Rydberg molecules [36] was experimentally shown for the first time in 2009 [19]. Later in 2010, the importance of quantum reflections within the potential energy curve of the molecules was found [37]. Homonuclear molecules with a permanent dipole moment were shown in 2011 [38]. In 2013, the study of a single Rydberg atom within a Bose-Einstein condensate began [39]. Precision spectroscopy of Rydberg molecules were performed in 2014 [40]. Finally, in 2015, the experiments with this apparatus had come to an end.

To continue with the research in this interesting and broad field of Rydberg atoms in an ultracold environment, a second generation apparatus was built up between 2011-2014 by Sebastian Hofferberth, Huan Nguyen and myself and will be described in part I. The idea of the new setup, the design considerations and the realization including technical details will be explained. From 2014 on, new observations in the Rydberg physics field were made. Elastic [S1] and inelastic [S3] collisions of a Rydberg atom within a Bose-Einstein condensate will be discussed in part II of this thesis. As a result, the investigated interactions show the possibility that a Rydberg electron orbital can be imprinted onto the density profile of a Bose-Einstein condensate. This can be optically measured in real space with a direct imaging technique [S4], which is proposed in chapter 8 of this thesis.

2.1 Design considerations

As in the first generation apparatus, the rubidium atoms inside the science chamber are trapped magnetically. This technique has proven itself an advantage for the Rydberg experiments performed. The magnetic trap does not have to be turned off during the excitation and detection of the Rydberg atoms and therefore thousands of experiments can be performed with only a single Bose-Einstein condensate. The magnetic field interacts with the atoms only via the weak magnetic properties of the atom, which is an independent degree of freedom of the atoms and is only used for the purpose of trapping them. All other coupling mechanisms are unperturbed and can be controlled independently. Another positive side effect of magnetically trapping the atoms is that the atoms investigated are perfectly spin polarized. No admixture of different states has to be taken into account in the analysis, which reduces the complexity of the system studied. Rydberg atoms have exceptional properties [41], which have to be thought of in the design of a new experimental apparatus. Especially the high polarizability due to the large orbit size of the Rydberg electron demands a very precise electric field control. One key design goal was the ability to excite and measure a single Rydberg atom inside a Bose-Einstein condensate. This is technically possible, because the excitation probability can be set low enough with the excitation lasers that two Rydberg excitations are unlikely and the Rydberg atom can be detected with high efficiency by ionizing and accelerating it onto a microchannel plate detector (MCP), which is a prerequisite of studying single Rydberg excitations. The fundamental physics responsible for the interaction of a Rydberg atom and the surrounding ground-state atoms can be studied in a direct way with a single impurity only.

The new apparatus was designed to overcome several limitations of the first generation apparatus [18] and to study new interesting research topics the former setup could not reach. In particular, the following design goals were considered:

Long-term stability The apparatus should be able to measure day and night without any surveillance of a person on site. The safety concept must be redundant to avoid any serious damage in case of an error. All components of the setup should be capable to run a measurement series for several days without interruption.

Field inhomogeneities The absolute electric field and the field gradient over the cold atom cloud should be as low as possible to be able to excite high Rydberg states and to limit the inhomogeneous dephasing rate. The ultracold atoms inside the science chamber should be shielded with a Faraday cage of electric field plates.

Rydberg state selective detection The timing and the electric field control should be precise so that state selective ionization is applicable for the Rydberg atoms and different Rydberg states can be distinguished on the detector.

Detection efficiency and noise level The detection efficiency should exceed 60 % with a microchannel plate detector. Therefore, the detector can run in a single counting mode to be able to investigate the regime of single or few Rydberg atoms in the experiment.

Optical spatial resolution The optical resolution for the excitation and the imaging should be in the 1-2 µm range to excite the Rydberg atom at a defined spatial position and to image the atom cloud with a resolution better than the Rydberg orbit size at high principal quantum numbers.

Repetition rate The time to create a cold atom cloud should be on the order of 20 s, which is fast for magnetically trapped atoms, to have a high repetition rate of the experiments. This increases the signal-to-noise ratio because more data averaging can be done.

2.2 Realization of the new experimental apparatus

The realization of the design goals is described or referenced within this part of the thesis. Except for the field inhomogeneities, all design goals are reached in the new apparatus. Out of the building up phase of the experiment, several bachelor and master theses were written describing different aspects of the experimental setup in detail: Stephan Jennewein [42] wrote the first version of the computer control software, whereas Christoph Tresp [43] planned the in-vacuum science chamber and started to build up the laser locking system with a high finesse cavity. Felix Engel developed a breakout board for a nanosecond pulse generator [44]. Thomas Schmid [45] built and installed the in-vacuum science chamber, continued to set up the laser system and did a theoretical analysis of how phase contrast imaging can be applied in the new system. Udo Hermann worked on the computer control software and especially the program for generating fast pulses [46]. He designed a new version of the in-vacuum science chamber [47] to meet the last remaining design goal concerning the field inhomogeneities of the chamber. In the master thesis of Fabian Böttcher [48], the mixed singlet and triplet Rydberg molecules are discussed and the results are published in [S5]. Felix Engel will soon present detailed simulations of spectra in a Bose-Einstein condensate [S1] and of the collision dynamics of a Rydberg atom within the system [S3] in his master thesis [49].

The majority of the experiment (figure 2.1) was built up by the two PhD students, Huan Nguyen and myself, who also supervised the bachelor and master students working on the experiment. Huan Nguyen was focusing on the mechanical elements of the vacuum system, the optical setup, the magnetic transport and the trap design, which will be described in detail in his PhD thesis. Only the very essential information about the apparatus is provided here. My focus was on the electronic hardware (chapter 3), the computer control system (chapter 4) including the data handling and evaluation, as well as the aspects required to perform long-term stable experiments with the new experimental setup (chapter 5).

For reasons of brevity it is not possible to describe the electronic devices developed and the computer control software in all details. However, there is extensive documentation available upon request.

The following sections of chapter 2, describing the experimental setup, are based on [45] and [47], from which also some of the figures shown were taken and modified.

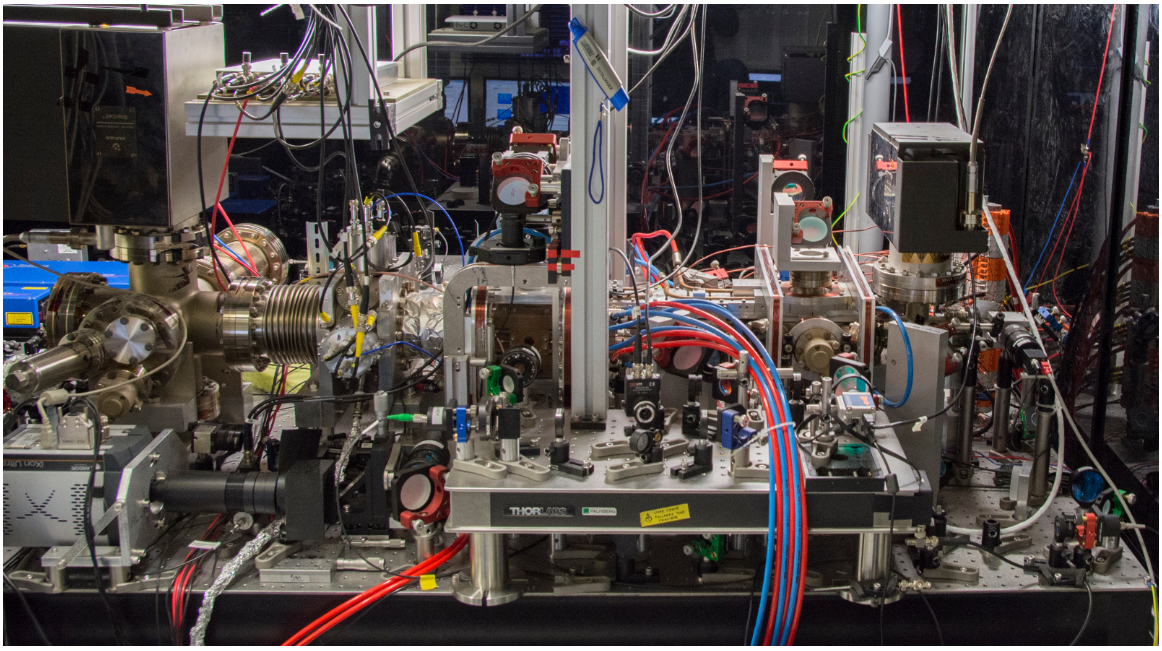

Fig. 2.1: Picture of the experimental apparatus taken on February 19, 2015.

2.3 Two-chamber setup

To reach a macroscopic occupation of the ground-state for ^{87}Rb atoms in the trapping potential, a so-called Bose-Einstein condensate [14–17], the atoms have to be cooled down from room temperature to below 1 µK during an experiment cycle. All heating and loss mechanisms must be suppressed to finally reach a stable and reproducible Bose-Einstein condensate. Therefore, a two chamber setup, as shown in figure 2.2, is well suited to reach the degeneracy of the rubidium atoms. In the first chamber (figure 2.3), the atoms are loaded into a magneto optical trap (MOT) from the background gas with a pressure on the order of 10^{-8} mbar. The rubidium pressure can be controlled by a valve separating an outgassing droplet of rubidium from the MOT chamber. After loading the MOT for 6 s, a few billion atoms at a temperature of typically 200 µK are accumulated, compressed, in a molasses stage cooled to 50 µK, and optically pumped into the low field seeking $5\mathrm{S}_{1/2}$, $F = 2, m_f = +2$ state. A magnetic transport [50] (figure 2.4) transfers the atoms within 1.4 s, without a significant loss, into the science chamber 45 cm away, in which the background pressure is on the order of 10^{-11} mbar only. The atoms are heated to about 400 µK during the transport. The two chambers are separated by a small tube with an inner diameter of 1.3 cm. Due to the differential pumping with ion pumps on both

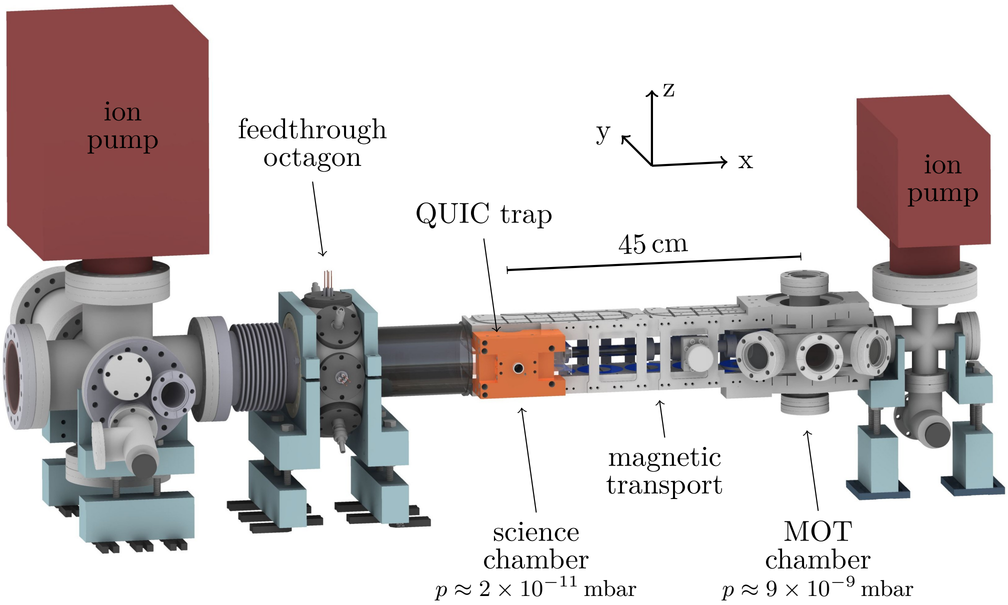

Fig. 2.2: Engineering drawing of the two-chamber vacuum setup.

sides of the experiment, the pressure inside the science chamber is more than two orders of magnitude lower than in the MOT chamber, which reduces to atom loss due to collisions with the background gas significantly. After the transport the atoms are loaded into a quadrupole Ioffe configuration (QUIC) trap [51]. Evaporative cooling is applied by ramping down the frequency of an electromagnetic alternating field from 45 MHz to approximately 1 MHz in three linear ramps, during the course of 15 s. After the cooling a pure Bose-Einstein condensate of up to $1.7(3) \times 10^6$ atoms is created. The schematic sequence of this process is illustrated in figure 2.5.

The trap frequencies in the final trap have been measured and are $\omega_{\mathrm{ax}} = 2\pi \times 200\,\mathrm{Hz}$ in the axial and $\omega_{\mathrm{r}} = 2\pi \times 15\,\mathrm{Hz}$ in the radial direction. This results in a Thomas-Fermi radius [52] of 5.1 µm and 68 µm for 1.7×10^6 atoms, a BEC peak density of 5.7×10^{14} atoms/cm^3, and a chemical potential of $h \times 4.5\,\mathrm{kHz}$. The critical temperature for the condensation is 480 nK at these parameters.

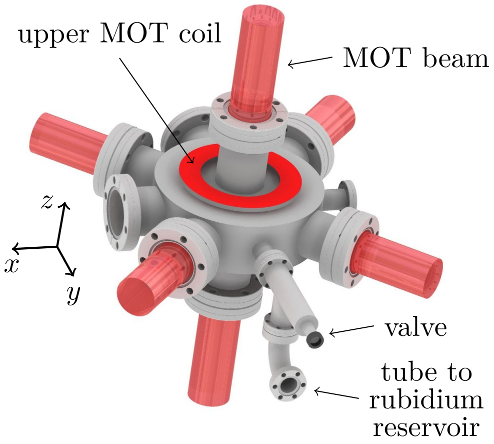

Fig. 2.3: Engineering drawing of the MOT chamber.

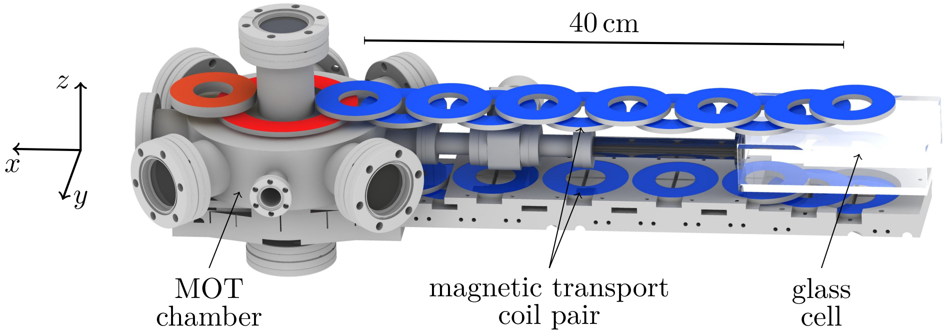

Fig. 2.4: Engineering drawing showing the magnetic transport from the MOT chamber (left) to the glass cell (right). The magnetic transport coils are mounted in an aluminum rack (displayed only for the coils below the connection tube), which is water cooled.

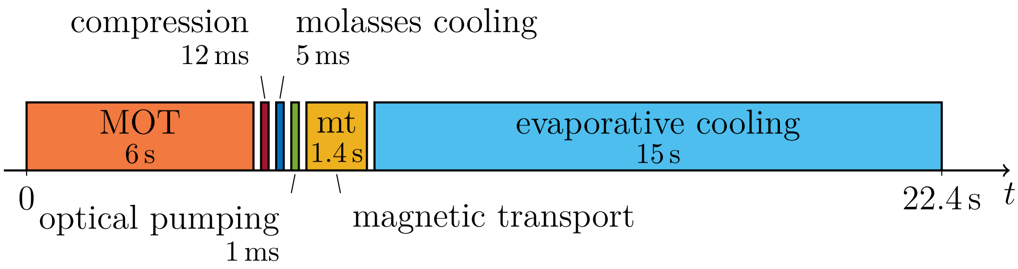

Fig. 2.5: Schematic sequence for cooling down the ^{87}Rb atoms from room temperature to degeneracy, a Bose-Einstein condensate.

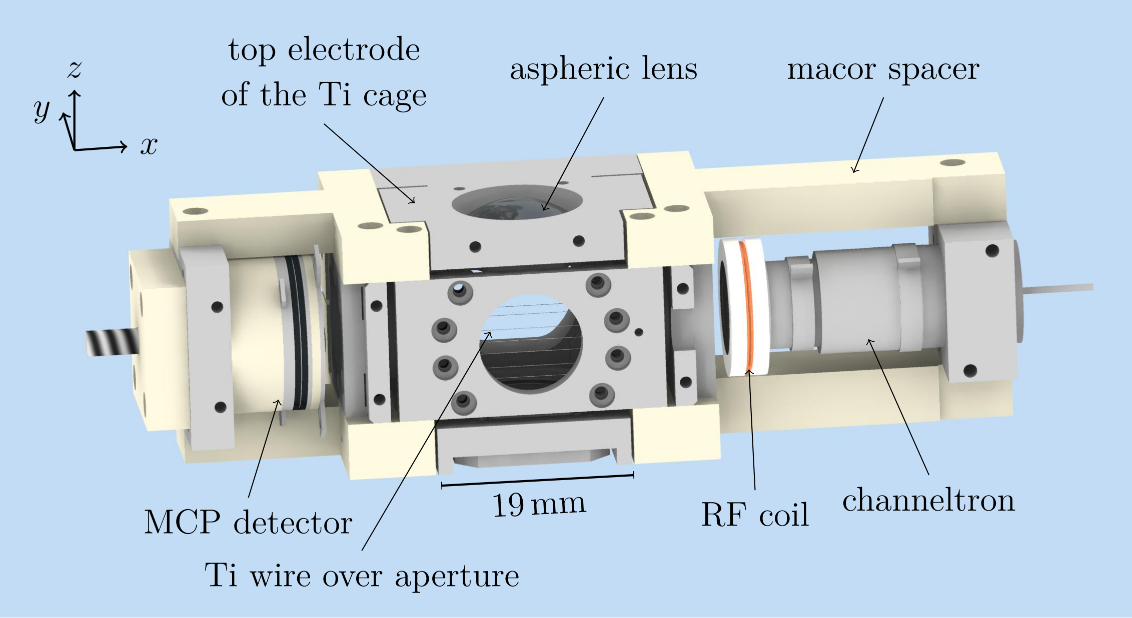

Fig. 2.6: Complete engineering drawing of the science chamber excluding the screws.

2.4 Science chamber

The in-vacuum science chamber (figure 2.6) is designed to shield electric fields from the outside and to apply and switch electric fields inside at the position of the ultracold atoms. Titanium was used as a bulk material for the electric field plates because it is non-magnetic [53]. All holes of the field plates for optical access or to transport the atoms in and out are covered by 50 µm thin titanium wires. Macor parts are used to isolate and hold the field plates. Two ion detectors, a channeltron and a microchannel plate detector, are installed on opposing sides to be able to detect single and multiple ions with a high efficiency. In addition, two high numerical aperture lenses are mounted on the chamber with which a micrometer resolution for the excitation of the Rydberg atoms and the imaging of the ultracold cloud or BEC is reached. The lenses have a four color anti-reflection coating to minimize reflections. A single winding of a copper wire outside the plates is used as a RF coil for evaporative cooling.

Unfortunately, the use of titanium instead of stainless steel, which is most often used, turned out to cause inhomogeneous and drifting electric fields inside the chamber, limiting the Rydberg excitation to a principal quantum number of approximately $n = 160$. For the experiments described in this thesis, this restriction did not play a role, but for the future experiments, the in-vacuum science chamber will be replaced by an improved design [47].

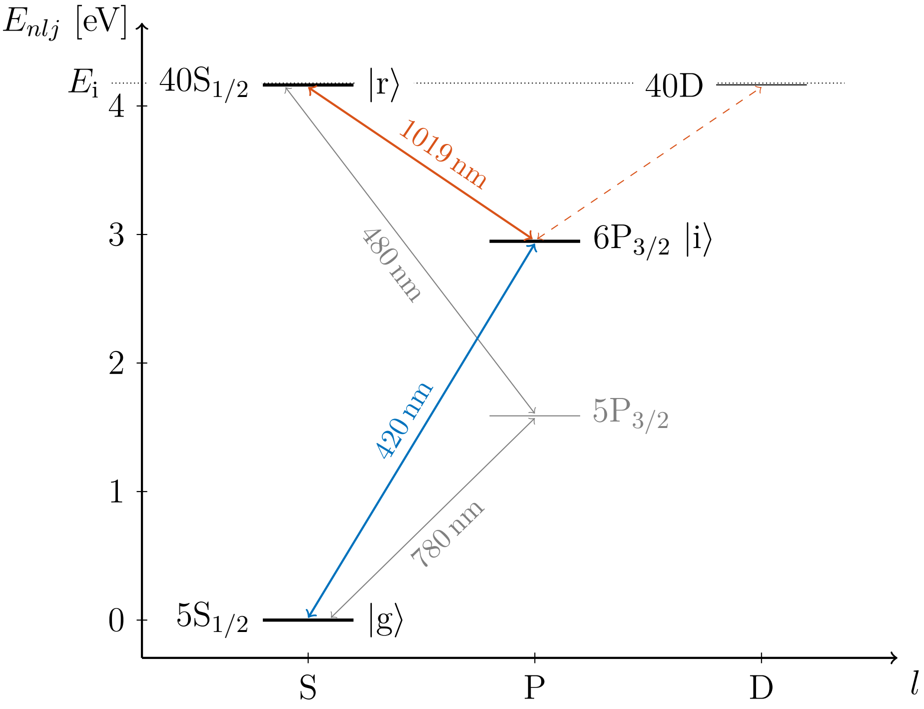

Fig. 2.7: Simplified level schema for the excitation of a rubidium ground-state atom $|\mathrm{g}\rangle$ to a $40\mathrm{S}_{1/2}$ Rydberg state $|\mathrm{r}\rangle$. The excitation is off resonant in the intermediate state $|\mathrm{i}\rangle$ with $\Delta = 80\,\mathrm{MHz}$, which is about 56 times the linewidth of the $5\mathrm{P}_{3/2}$ - $6\mathrm{P}_{3/2}$ transition, so that the otherwise fast decay of the intermediate state is negligible. The dotted line shows the ionization energy E_i [54]. The energies of the intermediate states $5\mathrm{P}_{3/2}$ and $6\mathrm{P}_{3/2}$ are taken from [55] and [56]. The energy of the Rydberg states can be calculated with equation (2.1).

2.5 Rydberg excitation

The physics investigated in this thesis is based on Rydberg S states, which have no orbital angular momentum. Due to the selection rules of electric dipole transitions [57], the 5S ground-state electron of a rubidium atom has to be excited with two photons to a Rydberg S state. The energy of a rubidium Rydberg atom can be calculated using quantum defect theory [41]. An alkali atom with only one valence electron is comparable to a hydrogen atom, which exactly has one electron. The quantum defect δ_{nlj} takes into account that for alkali atoms the inner electrons do not entirely shield the nucleus. The energy of the state above the absolute ground state, with the principal quantum number n, the orbital angular momentum l and the total angular momentum j is given by

$$E_{nlj} = E_i - \frac{\mathcal{R}_{\mathrm{Rb87}}}{(n-\delta_{nlj})^2}, \tag{2.1}$$

with the ionization energy $E_i = h \times 1010.029\,164\,6(3)$ THz [54] of the ^{87}Rb $F=1$ ground-state, the Planck constant h, and the modified Rydberg constant [54]

$$\mathcal{R}_{\mathrm{Rb87}} = \frac{\mathcal{R}_\infty}{1+\frac{m_e}{m_{\mathrm{Rb87}}}} = h \times 328\,982\,119\,466(2)\,\mathrm{THz}, \tag{2.2}$$

which takes into account the effective mass of the system. The quantum defect δ_{nlj} can be approximated by the modified Rydberg-Ritz parameters

$$\delta_{nlj} = \delta_0 + \frac{\delta_2}{(n-\delta_0)^2} \tag{2.3}$$

with $\delta_0 = 3.131\,180\,7(8)$ and $\delta_2 = 0.1787(2)$ for ^{87}Rb $n\mathrm{S}_{1/2}$ Rydberg states [54]. The principal quantum number n corrected for the quantum defect δ_{nlj} is called the effective principal quantum number $n^* = n - \delta_{nlj}$. The investigated nS Rydberg atoms can be excited with a two photon $5\mathrm{S}_{1/2}{\rightarrow}5\mathrm{P}_{3/2}{\rightarrow}n\mathrm{S}_{1/2}$ transition applying a 780 nm and 480 nm laser pulse. The experiments in this thesis use instead the $5\mathrm{S}_{1/2}{\rightarrow}6\mathrm{P}_{3/2}{\rightarrow}n\mathrm{S}_{1/2}$ transition with a 420 nm and 1020 nm laser, as shown in figure 2.7. The matrix element of the upper transition is much weaker than the lower transition, so that the power of the upper transition limits the coupling to the Rydberg state. Commercial narrow-band high power lasers at 1020 nm give out higher powers than 480 nm lasers and the dipole matrix element coupling the $6\mathrm{P}_{3/2}{\rightarrow}n\mathrm{S}_{1/2}$ state is much stronger compared to the $5\mathrm{P}_{3/2}{\rightarrow}n\mathrm{S}_{1/2}$ transition. That is why the Rydberg excitation with the infrared upper transition is preferred. All Rydberg lasers are stabilized to a high finesse cavity with mirrors mounted on a temperature stabilized spacer made from ultra-low expansion glass. With a free spectral range of 1.5 GHz and a finesse of 1600, the locked laser bandwidth is less than 40 kHz [43]. The laser beam going to the cavity is phase modulated using a fiber EOM to generate movable frequency sidebands used for locking. The frequencies for static operation are generated with commercial RF modules[1], whereas the lasers which change their frequency during an experiment cycle are controlled by a digital direct synthesizer (DDS) connected to a self-built controller which will be described

---

[1] Windfreak Technologies SynthUSBII

in section 3.2. The mode hop free scan range of the Rydberg lasers covers several GHz. To be able to address Rydberg states from $n = 40$ to 200, the upper laser frequency must be changed several THz from 1011 nm to 1019 nm which is possible by adjusting the grating within the laser.

The electric field inside the chamber must be on the order of a few $\mathrm{mV\,cm^{-1}}$ with a low field gradient, so that the Rydberg line is not broadened significantly especially for high Rydberg states (e.g. 150S). Due to the symmetry of the three field plate pairs of the in-vacuum science chamber, the offset electric field can be adjusted individually in each direction in space by applying a difference voltage to the plate pairs [43, 47]. The field gradient can be modified by changing the applied offset voltages of each plate pair with respect to the other pairs of field plates. By repeating the gradient and offset compensation, the remaining electric field can be suppressed down to $1\,\mathrm{mV\,cm^{-1}}$. However, the electric field drifts up to $10\,\mathrm{mV\,cm^{-1}}$ per hour so that the measurement time for high Rydberg states is limited. The electric field drift is probably caused by stray charges on the inside of the field plates and wires. The plates built out of titanium will have oxidized during construction of the science chamber and therefore the conducting field plate is isolated from charges on the surface. These charges accumulate and therefore the electric field inside the chamber is not stable on the $\mathrm{mV\,cm^{-1}}$ level over time.

2.6 Ionization and detection

After the ground-state atoms have been excited to Rydberg states they need to be detected. To do this they are field ionized and accelerated towards one of the ion detectors by applying a high voltage on one or two of the field plates. The ionization voltage is applied in three different ways: For low voltages and high principal quantum numbers, an arbitrary function generator (Keysight 33522B) directly attached to the field plate provides the compensation voltage until an external trigger switches the output of the arbitrary function generator to the ionization voltage. The maximum output of the arbitrary function generator into a high Z load is limited to ±10 V. For intermediate voltages of up to 500 V, the ionization voltage[2] is switched via a CGC high voltage switch[3] and for voltages above, a Behlke switch[4] is used.

---

[2] TDK-Lamda Z650-0.32

[3] CGC Instruments NIM-AMX500-3

[4] Behlke HTS 11-07-HB-C, AB2013-0091.03.13

For the measurements presented in this thesis, all ions were detected with the microchannel plate detector[5] and the data was acquired with a Lecroy WaveRunner 610Zi with sampling rates between 0.5 and 5 GS/s and up to 5000 time traces within one experiment cycle. Each ion arriving at the detector creates a short voltage pulse which falls off ($1/e$) in 2 ns but is followed by 20 ns of ringing. The ringing signal is probably caused by a custom made modification to the housing of the MCP, which was required to fit the detector into the glass cell. Only the properties of the original backplate [58] ensure a clean ion signal. Nevertheless, single or few ions are counted precisely by post-processing the time traces of the oscilloscope, which will be described in section 4.2.

The efficiency of the detector was determined by measuring the ion count rate of a blockaded Rydberg system [28], which means that only one Rydberg atom can be excited in the system. The Mandel Q parameter [59, 60] gives a quantitative parameter characterizing the distribution of the number of excitations N in the system:

$$Q = \frac{\langle N^2 \rangle - \langle N \rangle^2}{\langle N \rangle} - 1 \tag{2.4}$$

The absolute value of the Q parameter of a fully blockaded system is $Q = -1$. The measured Q^* parameter is modified by the detector efficiency $Q^* = Q \times \eta$ [61] from which the detector efficiency η can be calculated. A measurement of the Q^* parameter at $n = 90$ with a BEC and the excitation laser detuned -30 MHz from the atomic resonance, to only address the dense part in the center of the BEC (see section 6.4.5), is shown in figure 2.8. The excitation duration is varied, while keeping the excitation power the same, so that after approximately 3 µs the excitation is saturated. The measured $Q^* \approx -0.7$ parameter corresponds to a detector efficiency of the MCP of 70 %, which agrees with the specifications of the detector.

Besides the ion signal as a measurable property, images of the atom cloud can be taken with a PCO Pixelfly USB camera to determine the position and atom number of the cold gas. An Andor iXon Ultra camera provides the capability to apply high resolution in situ phase contrast imaging as described in [45]. The imaging resolution of approximately 1 µm allows one to image the structure of a Rydberg orbit, which exceeds a radial size of 1 µm above a principal quantum number of $n = 100$. An experimental proposal [S4] to capture the imprint of the Rydberg wave function will be described in the chapter 8 of this thesis.

---

[5] Hamamatsu F4655-10

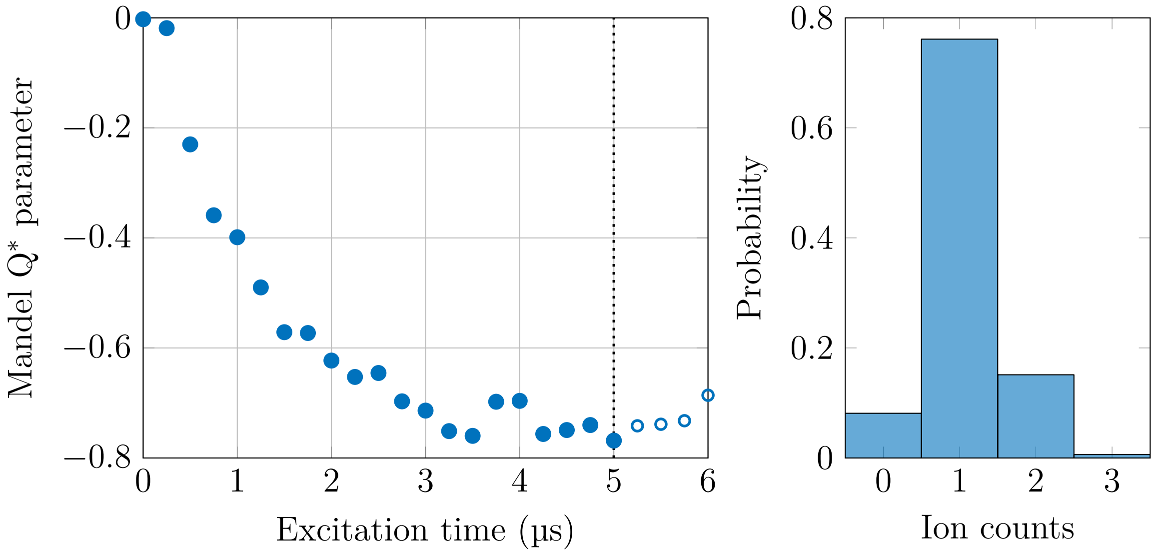

Fig. 2.8: Mandel Q parameter analysis for a blockaded 90S Rydberg excitation in a BEC. On the left, the measured $Q^* = Q \times \eta$ parameter including the detector efficiency η is plotted as a function of excitation duration with each data point averaged 200 times. The maximum excitation duration is 5 µs, for which the ion count histogram is plotted on the right showing a sub-Poissonian statistic of $\mathrm{Q}^* = -0.77$. The open circles show the time evolution of the Q* parameter after the excitation pulse has ended.

3

Electronic control

The experimental apparatus consists of hundreds of mechanical, optical and electronic components. The specifications for electronic devices in an atomic physics experimental setup can be very constrained, so that no commercial devices fit the requirements, or are too expensive. Therefore, self-built electronics are necessary to control the experiment in a convenient way. Self-built electronics should be considered only when necessary. Commercial devices which break can be replaced easily and support is available from a company, whereas self-built electronics are prone to error and difficult repairs.

Nevertheless, several custom electronic devices were designed and built to meet the unique requirements of the new experimental setup. A special focus was put on reliability and robustness in the design of the devices.

3.1 PID controller

A proportional integral derivative (PID) controller [62] is a versatile device to create a feedback loop controlling other devices. A PID will be explained by the means of figure 3.1 and the example of controlling the temperature of a room: In a setting with a room temperature of $T(t) = 18\,°\mathrm{C}$ and a set temperature of $s = 20\,°\mathrm{C}$, the error signal is $e(t) = s - T(t) = 2\,\mathrm{K}$, which is the input signal for the PID controller. Now each component of the PID (figure 3.2) generates an output signal which is summed up and used to set an actuator, in this case the valve controller of the heater. The P component gives out a signal proportional to the error:

$$P(t) = a_P \times e(t). \tag{3.1}$$

For most systems the proportional gain is not enough to reach a steady state with no remaining error. To zero the error, the input signal must be integrated over time:

$$I(t) = a_I \times \int e(t)dt. \tag{3.2}$$

The settling time can be reduced with a derivative term

$$D(t) = a_D \times \frac{de(t)}{dt}, \tag{3.3}$$

but is used seldom, because it can lead to additional instabilities of the system.

The main purpose of the PID controller developed here is to stabilize the laser frequency. It is also used to stabilize laser power or to control and drive piezo elements. The heart of the PID controller is the operational amplifier OP467, which is a quad precision, high speed operational amplifier with a bandwidth of 28 MHz, which is unity gain stable. The PID controller reaches an open-loop bandwidth of 3 MHz (-3 dB). A frequency laser lock using this PID narrowed down the beat note linewidth between the master and slave laser to below 1 kHz, as shown in figure 3.3, when the locking parameters are optimized. Additional information and the schematic can be found in appendix A.1.

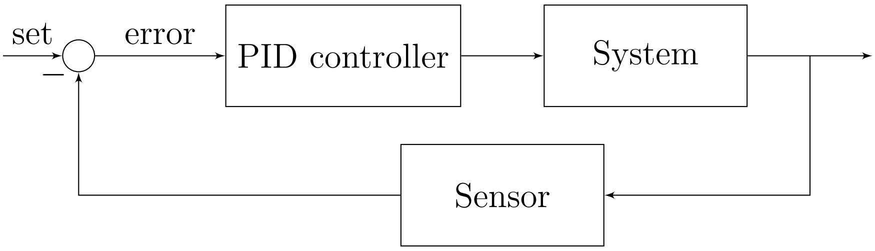

Fig. 3.1: Schematic illustration of a closed feedback loop with a PID controller.

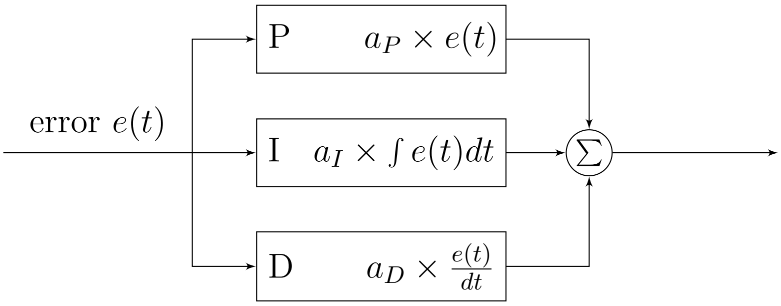

Fig. 3.2: Schematic illustration of the different terms of a PID controller.

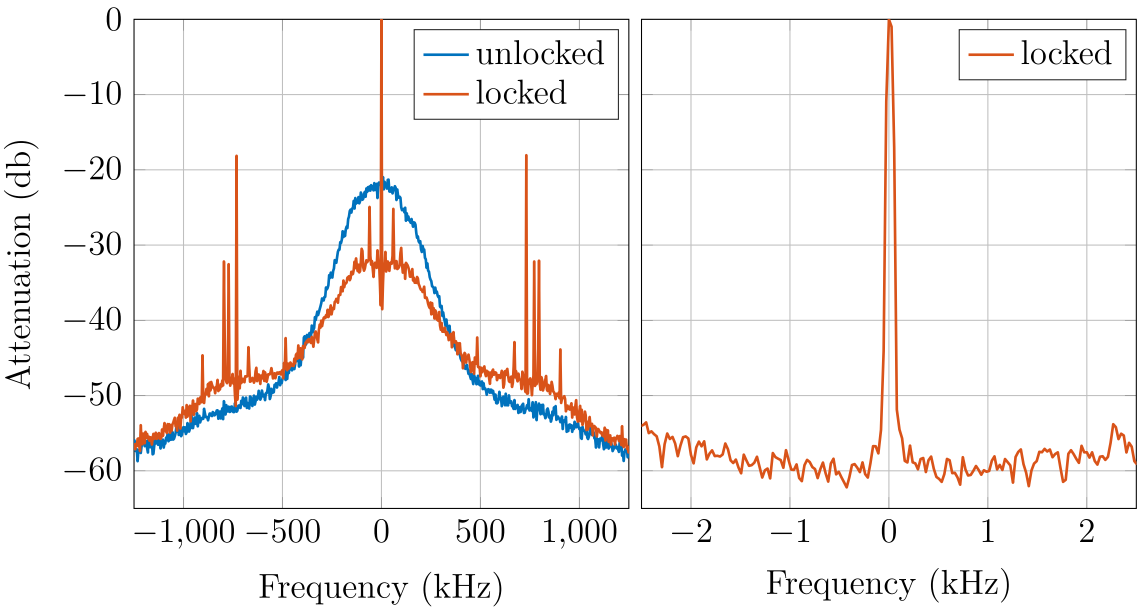

Fig. 3.3: Frequency analysis of a free running laser (blue) and a laser locked with the PID (red) to a laser, which is locked to a cavity. The left graph shows the comparison of the unlocked and locked signal. The beat note linewidth is well below 1 kHz as shown in the right. The signal is not going down to −60 db on the left graph in the very center because of the different frequency step width and the bandwidth settings of the measurement compared to the measurement on the right.

3.2 Frequency generation via direct digital synthesis

Radio frequency (RF) signals up to 500 MHz are used in a variety of places in the experimental setup. For example, the atoms are evaporatively cooled by applying a radio frequency source ramping down the frequency from 45 MHz to about 1 MHz to form a Bose-Einstein condensate. The acousto-optic modulators (AOMs), used for setting the power of the lasers beams, have a crystal inside which oscillates typically with frequencies between 50 MHz and 200 MHz. The electro-optic modulators (EOMs), used for shifting the laser frequency, can be modulated faster with frequencies of up to several GHz. In addition, RF frequencies of up to 200 MHz serve as a reference for beat note locks [45] of a master laser and several slave lasers.

There are two common methods available to generate RF signals in the required frequency range. A voltage controlled oscillator is locked to a 10 MHz quartz crystal reference oscillator with a fractional frequency divider and a phase-locked loop (PLL), e.g. the integrated circuit ADF4351 from Analog Devices. An output frequency of several GHz can be reached with a linewidth on the Hz scale. The disadvantage of these kind of devices is the limited scan range. The total output frequency range is split in fixed frequency sections and the section borders cannot be crossed in a frequency scan. The second way of generating RF, the direct digital synthesis (DDS), is capable of scanning and jumping over the full output frequency range instantaneously. In addition, defined triggered phase jumps and modulations can be generated with DDS devices. The only disadvantage of these devices is the limited output frequency of typically up to 500 MHz. The frequency in a DDS device is generated by an internal clock, e.g. with $f_{clk} = 1\,\text{GHz}$, which has a phase accumulation register which adds up the phase φ for the current output frequency f (see figure 3.4). The new value at the next clock cycle for the phase register can be calculated with $\varphi_{N+1} = \varphi_N + 2\pi(f/f_{clk})$. The output voltage is extracted from a look up table inside the chip giving out the voltage according to the current phase in the phase accumulator. Several of the experiments performed for the work in this thesis required to change the frequency 5000 times within 2 seconds. Therefore, a DDS RF frequency generator is well suited to set precisely the required offset frequencies for the laser locks. To be able to control the DDS board from the experiment control and to change the frequency in a synchronous triggered mode, a control interface was built for the AD9858 and AD9959 DDS evaluation board. The AD9858 integrated circuit has one output channel with a frequency

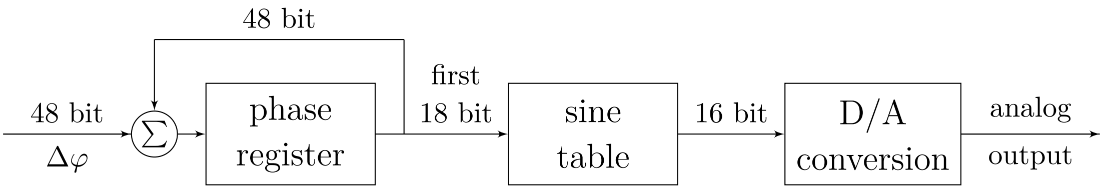

Fig. 3.4: Simplified diagram of a DDS device. The phase register accumulates the phase $\Delta\varphi(f)$ according to the selected output frequency f. The highest 18 bit of the phase register are converted with a sine lookup table into an amplitude, which is afterwards converted into an analog voltage.

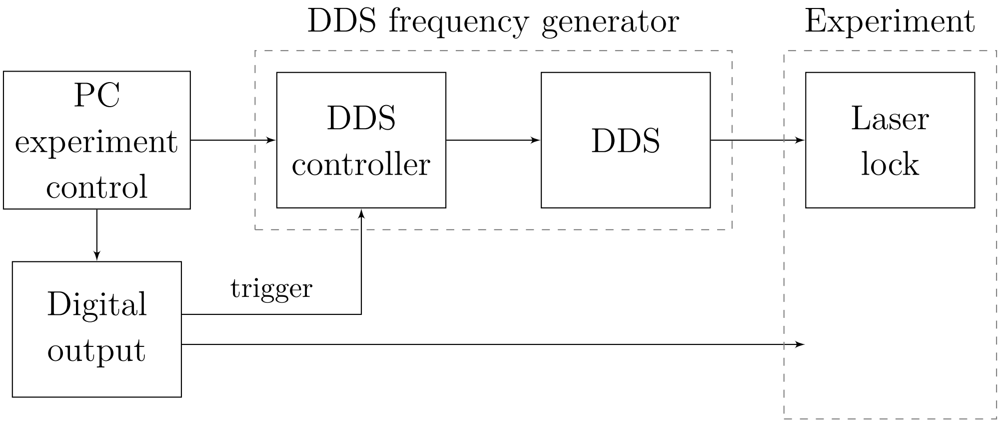

Fig. 3.5: RF frequency generation with a DDS device. The experimental control software on the PC sets the operation mode in the DDS controller, e.g. 5000 different output frequencies are sent to the DDS controller. The digital output hardware synchronously controls the experiment and the frequency switching by applying trigger pulses to the DDS controller which sets a new frequency within 4.5 µs.

limit of 500 MHz, whereas the AD9959 integrated circuit has four channels with limits of 250 MHz. An Arduino Due microcontroller with a core clock of 84 MHz has a hardware serial peripheral interface (SPI), with which the DDS board can be programmed in a simple and fast way due to the high level application programming interface (API) provided with the Arduino microcontroller. With several optimizations of the communication library, the time required to change the output frequency of the DDS chip is between 3.5 µs and 4.5 µs for a single channel. Different ramping modes for the frequencies are implemented, as well as the option to control the output frequency with an analog input. How the DDS device is connected to the experimental control and the experiment is illustrated in figure 3.5. Further details and the schematic can be found in the appendix A.5. The self-built DDS system is a four channel, computer controlled function generator, optimized for synchronous triggered frequency switching. All components required are cost-effective compared to commercial solutions for this purpose.

3.3 Isolated analog and digital outputs

The new experimental apparatus currently requires 56 digital and 23 analog channels. The channels are used, for example, to control the laser frequencies over the DDS boards, the laser powers with the AOMs and the shutters, the current of the power supplies for the offset magnetic fields and the trap coils, the switching of the coils for the magnetic transport, setting the ionization voltage and the compensation electric fields, triggering the oscilloscope and the ionization pulses, and so forth. With that many devices connected, it is very likely to create ground loops within the experimental setup which can be a noise source in the system or cause instabilities. There are only two ways to avoid ground loops. One possibility is to have a single ground from which all devices are star-shaped connected to and no interconnection of the devices should be made. This is simply impossible in an experimental setup. The second option is to split the ground connection within the signal line, which can be done with integrated circuits based on inductive, capacitive or light coupling of the signal, which needs no physical connection of the input and output side. Digital signals can be transmitted in a fast and reliable way with these methods. It is more complicated to split the ground connection for analog signals. Therefore, the transmission bandwidth is limited and the circuit required can lead to additional offset drifts or noise in the analog case.

In the experimental setup, all digital channels from the computer control which do not require nanosecond timing are isolated with the developed isolator cards explained in the following, as well as the analog outputs to devices which only work with ground free signals (e.g. EA PS power supplies).

The ground plane of the digital signals is split with an ADuM6200 integrated circuit and a 74ACT244 serves as a 50 Ω line driver. Inside the isolation amplifier a state change of the input signal is transmitted as a pulse over a transformer to the ground-free output side, which adjusts the output signal according to the pulses received. The output signal of the isolation board, usually set by the computer control, can be manually overwritten with two switches on the front panel for test purposes and the current status is indicated with LEDs. The total propagation delay of the isolation board is 70 ns. Further details and the schematic is shown in appendix A.2.

The analog signal is isolated with a ISO124 isolation amplifier, which uses a differential capacitive barrier to break the ground loop. A duty cycle modulation-demodulation technique is applied to transmit the amplitude over the capacitance. The isolation amplifier is followed by a BUF634 line driver, capable of driving ±10 V into 50 Ω. The system reaches a bandwidth of 40 kHz as shown in figure 3.6 and has a noise level of 4 $\mathrm{mV_{rms}}$ at unity gain. Further details and the schematic is shown in appendix A.3.

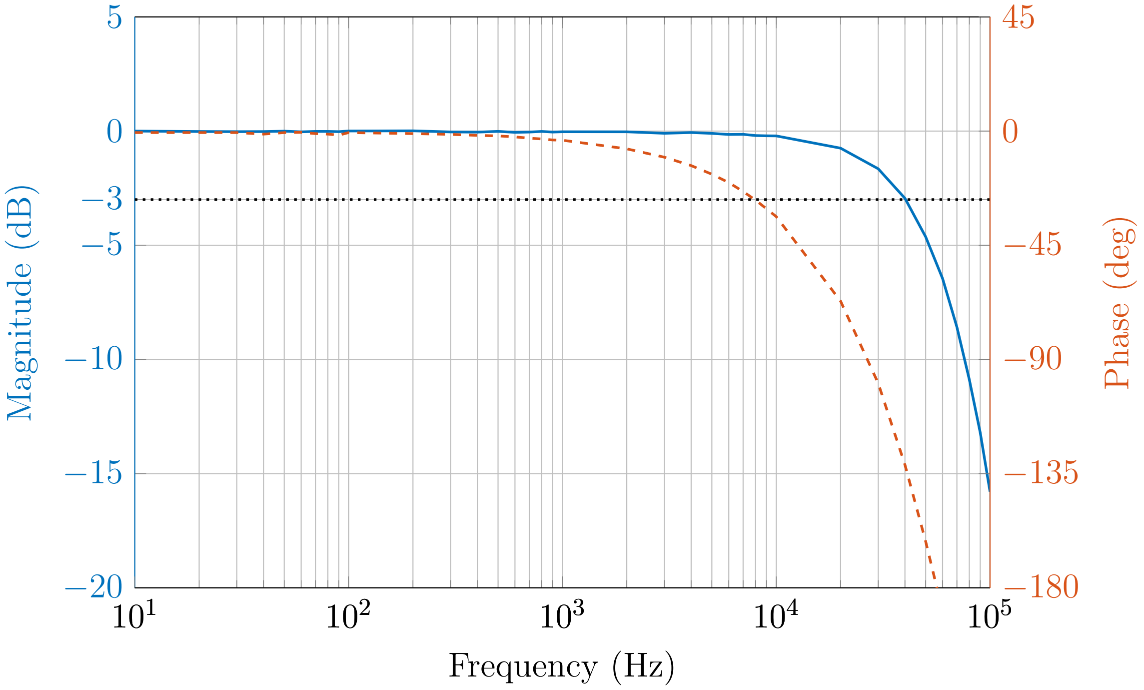

Fig. 3.6: Bode diagram of the analog isolation board. The measured bandwidth of isolation amplifier is 40 kHz at −3 dB.

3.4 Analog control and digital switching of magnetic coils

The experimental setup contains 21 coil pairs and an additional single coil to manipulate the atoms. The offset magnetic field at the MOT and the QUIC trap are set with 3 Helmholtz coil pairs each. 15 coil pairs are integrated to trap the atoms in the initial phase in the high pressure chamber, to transport them to the low pressure chamber and to trap them within the QUIC configuration. An additional Ioffe coil is required for the QUIC trap. All non-offset coils are supplied by four Delta-Elektronika ESM 30-100-D power supplies, driving up to 100 A at a maximum voltage of 30 V. The current for the coils must be switchable well below 1 ms and therefore custom electronics had to be designed, including a method of shutting off the power supplies in the case of a system failure, as the maximum power consumption of the coils is limited before breakdown.

The coil switching is based on the insulated-gate bipolar transistor (IGBT)

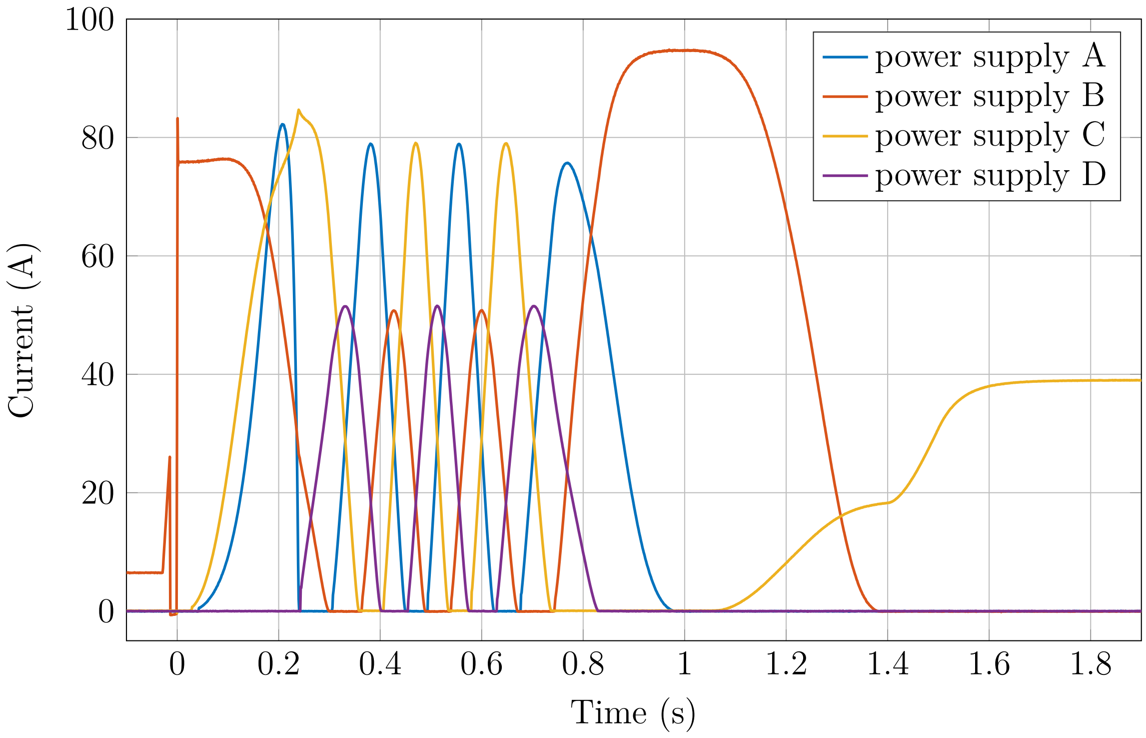

Fig. 3.7: Output current for all four power supplies from the MOT loading phase over the transport to the QUIC trap. The magnetic transport starts at $t = 0$. The power supplies switch between the connected coils in the time they are idle.

STGE200NB60S, which is capable of driving 150 A with a low on-voltage drop of 1.3 V. A digital switching system and driver board for the IGBT was developed, including the monitoring and emergency shut down circuit, which will be described in section 3.5. At any time during the magnetic transport three power supplies drive three coil pairs (see figure 3.7) and the forth power supply is idle and can switch the coil pair addressed. Each power supply must switch between four coil pairs except the last one which is connected to three, to supply the 15 coil pairs in total. The IGBTs of the coil pairs connected to a power supply are selected over a 2-bit demultiplexer. A simplified schematic of the system is shown in figure 3.8. After the magnetic transport, a large capacitor of 1 F is added in parallel to the power supply to reduce the current noise, which otherwise leads to heating of the atoms in the QUIC trap. After the atoms are loaded into the quadrupole coils of the QUIC trap, the Ioffe coil is slowly turned on. The Ioffe coil and the quadrupole coils are powered from the same power supply, so that current noise affects all trap coils simultaneously. This reduces the heating of the atoms compared to a configuration in which both coils have separate supplies. The position of the trapped atoms can be controlled in two

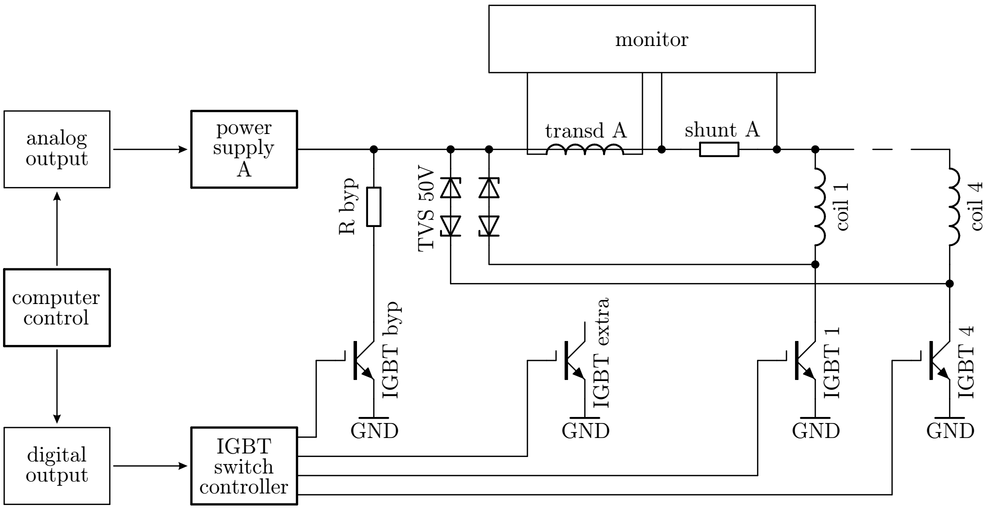

Fig. 3.8: Simplified schematic of the current switch of a single power supply. The output current of the power supply is set by the analog input of the power supply. The circuit can be opened or closed by the IGBT controller, which serves a digital switch for the current. The current through the coils can be measured with a built-in transducer and shunt. All four coils connected to a power supply have a separate IGBT and a 50 V TVS diode, which consumes the energy stored in the coils when switched off digitally. In addition, a bypass resistor can be enabled and a spare IGBT channel is available.

directions with two offset magnetic offset fields and in the third direction with a low noise power supply adding a small current to the Ioffe coil only. The required electronic circuit is shown in figure 3.9.

The switching electronics must be protected from the high induction voltage caused by the IGBTs breaking the circuit of the coils. Transient voltage suppression (TVS) diodes are installed in parallel with the coils, which reliably consume the stored energy inside the coils, when the coils are switched off fast as shown in figure 3.10. The current through the coils is monitored with a

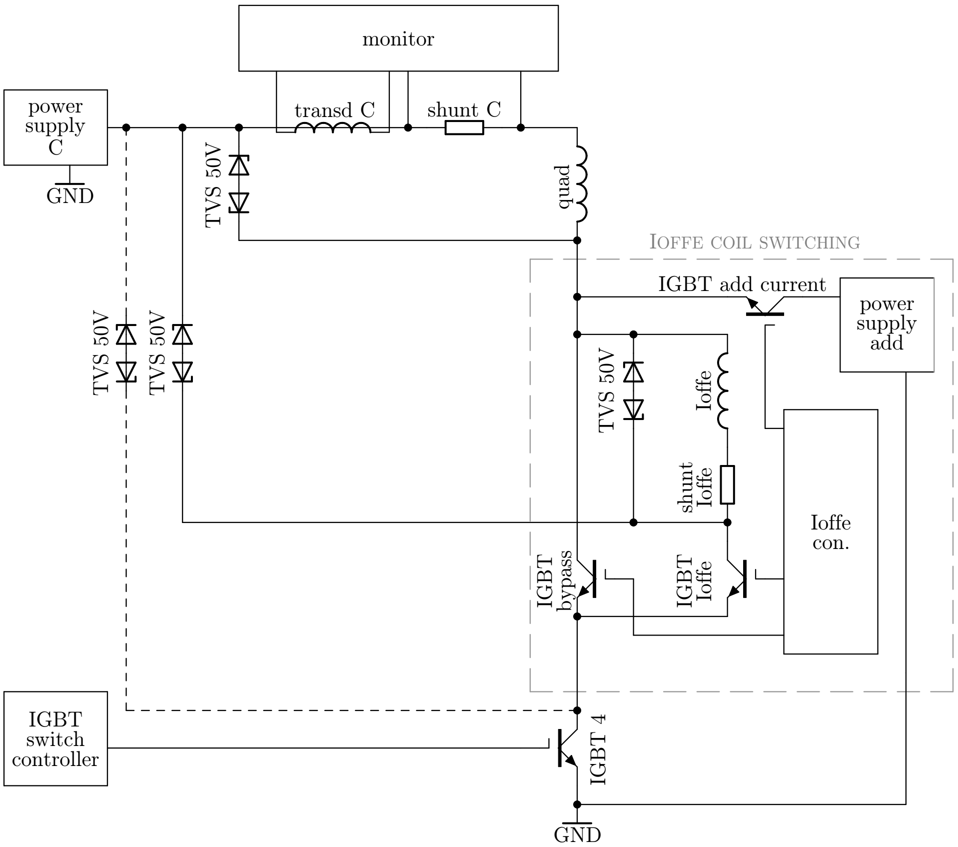

Fig. 3.9: Schematic of the circuit to include the Ioffe coil into the circuit of the quadrupole coils with the capability of adding an additional current to Ioffe coil only. As long as the 'bypass' IGBT is turned on and 'Ioffe' IGBT is off, no current flows through the Ioffe coil. By slowly turning on the 'Ioffe' IGBT and afterwards releasing the 'bypass' IGBT, the Ioffe coil can be added into the circuit smoothly. The additional current for the Ioffe coil is provided from a low noise power supply over the 'add current' IGBT, which can isolate the power supply from the system when switched off. The IGBTs are controlled over analog channels from the computer control to cross the switching threshold slowly without disturbing the trapped atoms.

transducer and a shunt resistor in series with the coils. It is possible to activate a bypass resistor parallel to the coils, which is not in use in the experiment. Further details can be found in appendix A.4.

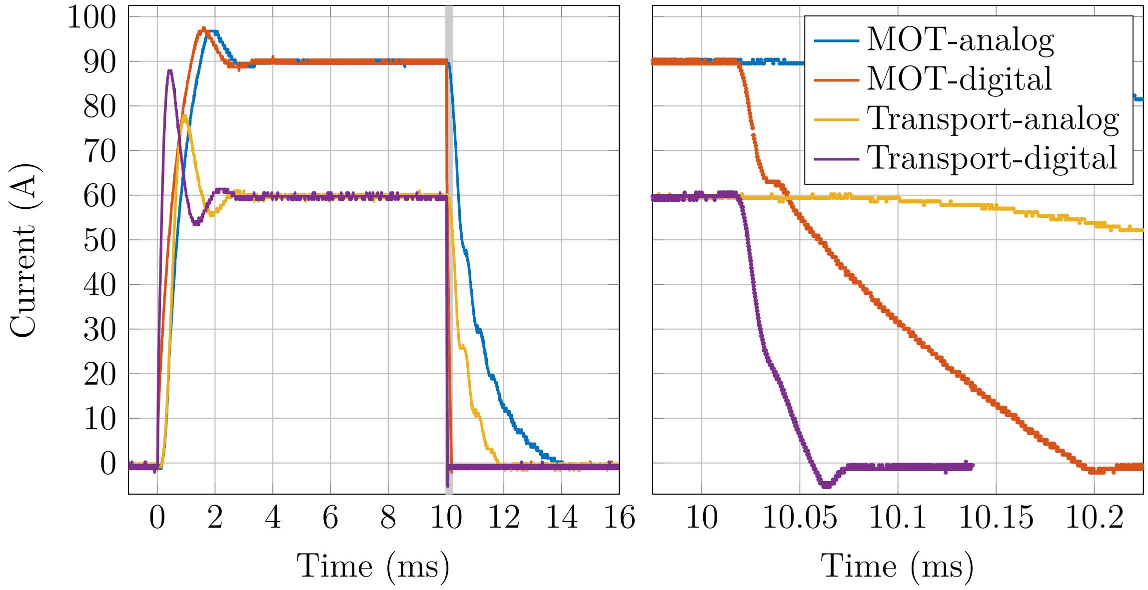

Fig. 3.10: Switching performance of the magnetic coils. The rise and decay times are plotted for a MOT coil pair and a transport coil pail. They are either switched in a digital way, controlling the IGBT, or by changing the control of the power supplies, depicted as analog. The settling time is about 20 % faster with the digital switching as compared to the analog. When the current is turned off, the digital switching time is at least a factor of 20 faster because the energy stored in the coils can be consumed by the TVS diode in parallel to the coils. A zoom in of the gray shaded region is shown on the right to see the digital turn off behavior. Even the MOT coils, which have a large inductance, can be switched off within 200 ns from a current of 90 A.

3.5 Monitoring system of the experiment

One key aspect in the design considerations was the long-term stability of the experiment and the ability to perform uninterrupted measurements over the course of several days. A surveillance system was developed which shuts down the high current power supplies as soon as an anomaly is detected during an experiment cycle. Of special concern is the temporary high current during the transport phase and afterwards in the QUIC trap which would damage the coils and the experiment if the current is applied too long or without water cooling. A microcontroller (detailed circuit is shown in appendix A.6) measures the current of all channels every 0.5 s, and determines the mean power consumption with the known resistance of each coil over 1.5 s and 120 s. A current limit and a short-term and long-term power limit is set for all coil pairs individually within the software. This protects the coils from an incorrect user input applying too high of a current for too long. In a rare, but typical, error case, the computer control system does not respond anymore and therefore the digital and analog controls can freeze at a certain output level. The power consumption measurement detects this error case. In addition, several temperature sensors are attached to the microcontroller for an additional redundant error detection mechanism. The individual temperature limit protects, for example, from overheating of the coils due to too high of a current or from a fault of the water cooling system. The water cooling is monitored in addition by a flow guard within the water cooling system. Input errors in the computer control system can be prevented by setting the output limits for the analog outputs of each channel individually. An overview of the protection mechanisms is shown in figure 3.11.

With this surveillance and protection system all harmful error cases are monitored twice with independent sensors. The microcontroller itself has a built-in hardware watchdog to detect and recover from malfunctions. Therefore, the system can run safely and can be controlled from a remote place without any person at the experiment itself. This has the advantage that experiments can be prepared during the day and can run during the night or on the weekend, and therefore big parameter spaces can be scanned in a measurement, gathering a lot of averages to achieve good signal-to-noise ratios.

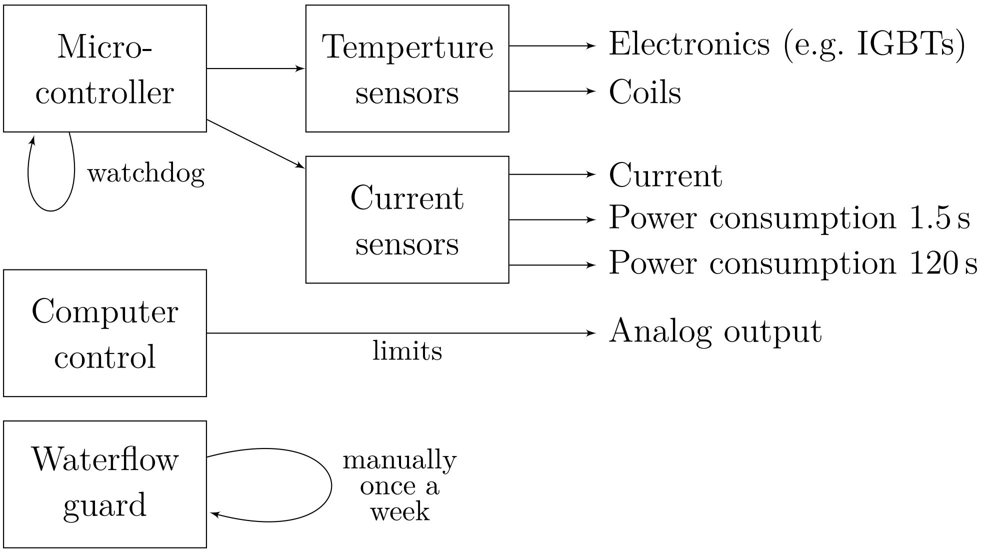

Fig. 3.11: Overview over the surveillance system of the experiment. On the left, the surveillance device is listed whereas on the right the device which is protected or limited, is shown.

4

Computer control and data acquisition, handling and storage

Almost all parameters of the experiment are controlled by the main experiment control program. There are static parameters like the electric field compensation voltages, which do not change during an experiment cycle and can be set before the experiment cycle starts. However, most of the parameters have to change synchronously in respect to all other devices during the experiment, this is realized over digital triggers and analog voltages controlling them. The sequence for the analog and digital channels is generated by the experiment control program with output cards from National Instruments, which is described in more detail in [42]. Each of the 64 digital and 24 analog channels can be programmed in 20 µs steps, and for the very fast digital outputs a 12 channel pulse generator from Swabian Instruments[1] is used with a time resolution down to 1.5 ns. With the digital and analog signals, all laser frequencies are switched, the MOT parameters are set, the magnetic transport is controlled, the experiment performed is programmed, and so on.

Not only the data output but also the data acquisition is controlled via the experiment control system. For each experiment cycle, up to 50 MB of data is produced within 25 s, which results in a data rate of 173 GB per day in a non-stop measurement. The biggest portion of the data are the oscilloscope

---

[1] Swabian Instruments is a company, which is founded by a postdoctoral researcher, a PhD student, and myself from the University of Stuttgart.

traces from the ion detector and the images taken of the atom cloud at the end of each experiment cycle. The design considerations for the implementation of the new experiment control system are described in section 4.1 and [42]. The data handling and evaluation will be discussed in section 4.2, whereas the image acquisition and evaluation system is explained in section 4.3.

4.1 Experiment control system

The central program coordinating the experiment cycle and programming the devices attached to the experiment is the main experiment control program. There are no general purpose experiment control software packages available which fulfill the sophisticated and special requirements of the newly designed experimental apparatus described here. Therefore, a new experiment control software was written in C#, which was chosen as the programming language preferred over LabVIEW, Matlab and python for the following reasons:

LabVIEW Most companies of input or output hardware provide a LabVIEW driver for their devices. Hence, LabVIEW is an option for programming an experiment control system. But due to the graphical way of programming in this language and the old age of 30 years from the first release, the architecture and the tools supporting the developer are very limited compared to modern programming languages. Large and complex programs often become confusing and are hard to maintain and modify. LabVIEW is therefore inferior to more recent programming languages.

Matlab The programming language Matlab is a very common language for physicists and needs to be considered. Unfortunately, Matlab does not support multi-threading in a convenient way, which is absolutely necessary for an experiment control program. In addition, there is no way to capture asynchronous external events or to communicate with other external programs efficiently. Also, external hardware is not supported well by the hardware companies. As a last disadvantage, the bad performance of complex graphical user interfaces has to be mentioned, which as a consequence provides a bad user experience.

Python More recently, python is becoming very popular as a programming language in the physics environment. It is possible to program and maintain very complex software programs and a lot of well suited libraries exist for the purpose of an experiment control. But to create robust, scalable and sustainable applications, more experienced programmers are required in python as a dynamically typed language compared to a statically typed language. This is why for the heart of the experiment control C# was chosen.

C# Microsoft C# provides everything required to develop an experiment control software. It is well supported from the companies of the input and output hardware and is a modern, statically typed language with excellent support for the developer due to the Visual Studio programming environment. The modern features of the programming language, such as built-in serializers and data bindings, reduce the lines of code which have to be written to provide the functionality required. The debugging and profiling tools are unique and the community support is outstanding.

The main experiment software is therefore written in C#, which includes the database handling, the control of the analog and digital output cards and the graphical user interface for the physicist setting the parameters of the experiment cycle. The data amount which has to be created for each cycle is enormous. Each of the 64 digital channels requires 1 bit of data per time step and each of the 24 analog channels 16 bit of data. With a total duration of 25 s per cycle and a time stepping of 20 µs, this results in 448 bit per time step and therefore 560 MB per cycle, which has to be created and sent to the output cards. Screenshots for controlling the status of the experiment and of an analog card are shown in figure 4.1.

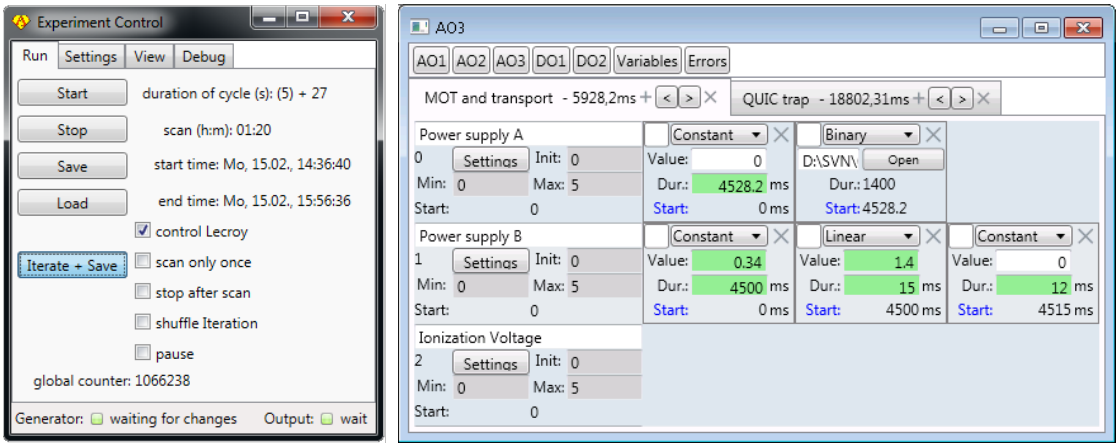

duration of cycle (s): (5) + 27
scan (h:m): 01:20
start time: Mo, 15.02., 14:36:40
end time: Mo, 15.02., 15:56:36
☑ control Lecroy
☐ scan only once
☐ stop after scan
☐ shuffle Iteration
☐ pause
global counter: 1066238
Generator: 🟩 waiting for changes Output: 🟩 wait

MOT and transport - 5928,2ms
QUIC trap - 18802,31ms

Power supply A
0 Init: 0
Min: 0 Max: 5
Start: 0
Constant
Value: 0
Dur.: 4528.2 ms
Start: 0 ms
Binary
D:\SVN\
Dur.: 1400
Start: 4528.2

Power supply B
1 Init: 0
Min: 0 Max: 5
Start: 0
Constant
Value: 0.34
Dur.: 4500 ms
Start: 0 ms
Linear
Value: 1.4
Dur.: 15 ms
Start: 4500 ms
Constant
Value: 0
Dur.: 12 ms
Start: 4515 ms

Ionization Voltage
2 Init: 0
Min: 0 Max: 5
Start: 0

Fig. 4.1: Screenshot of the main experiment control program (left) and the control of three analog channels (right).

One key aspect considered to create stable and reproducible results is running the experiment cycle continuously, even though no experiment is performed. This keeps every component of the system in thermal equilibrium with respect to the previous and the next experiment cycle. Hence, the experiment control software must take care that the generation of the data and the upload to the output cards does not affect the start time of an experiment cycle. This is solved in the following way (figure 4.2):

The MOT loading phase of the experiment is a static section in which none of the digital or analog output cards have to change. At the very last time step of each experiment cycle, the MOT parameters are set and the output channels stay at these values until a new cycle is started. The time in between can be used to upload a new cycle and to update other external devices. The latter is done from a python script with which non-time critical hardware can be added to the experiment in a simple way without changing the source code of the main experiment control software. A new experiment cycle is started after a defined MOT loading duration with a precise timer within the C# experiment control program, so that every cycle time including the MOT loading duration is constant. The jitter can be analyzed by measuring the time difference of the last time step of a sequence and the first time step of the subsequent sequence. The total output duration of the hardware has not to be taken into account, since it is clocked by a 10 MHz oscillator with very low jitter and temperature

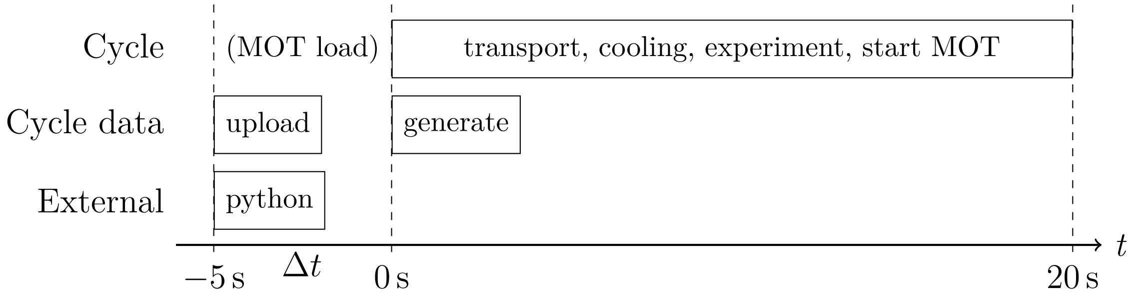

Fig. 4.2: Schematic sequence of the experiment cycle. During the static MOT loading phase, the new sequence is uploaded and external devices are programmed asynchronously with a python script. After the new sequence has started, the scan parameters are automatically incremented and the new output sequence is generated. The MOT loading time Δt, which is the delay time between two cycles, can be set by the experiment control. This time buffer ensures that every cycle has the very same length.

drift. The standard deviation measured for 1500 cycles with a cycle duration of 25 s each is 3.8 µs as shown in figure 4.3. Therefore, the cycles have a very well defined duration with a relative uncertainty below 10^{-6} and the controlled apparatus stays in thermal equilibrium.

All controlled devices can have several variable parameters, which are set from the computer control. For example, the pulse duration of the excitation light is set by a variable, and the intensity of the pulse by another one. The computer control software can systematically perform multi-dimensional parameter scans by incrementing the scan variables accordingly from one experiment cycle to the next. The new binary output sequence is generated in a background thread to not block the user interface. This happens also if manual changes are made in the experiment control program. A typical sequence of 25 s is generated on an Intel i7-6700 processor within one second. A double buffering system [42] keeps the last generated output sequence which passed all consistency checks in a buffer and as soon as the cycle has ended, this sequence is uploaded even though it could be that there is another sequence generated in the background. This ensures a constant cycle time and therefore the stability of the system.

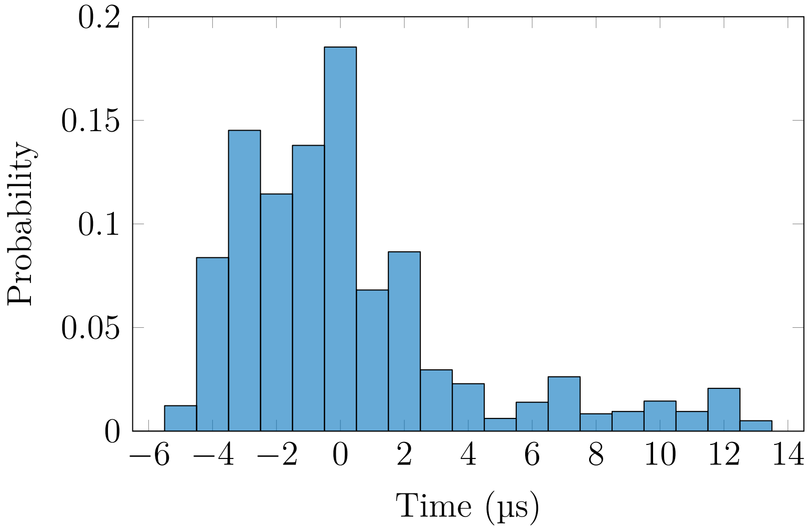

Fig. 4.3: Jitter of the start time measured for 1500 experiment cycles. The standard deviation for a cycle duration of 25 s is 3.8 µs. Hence, the relative cycle time stability exceeds six orders of magnitude. The experimental apparatus stays in thermal equilibrium due to negligible time jitter.

4.2 Data handling and evaluation

Every single experiment cycle performed and the respective data taken is identified by a unique count number. All control parameters and the time sequence from the experiment control are automatically stored in a file storage and the main parameters such as the unique count number, scan variables, time stamp, etc. are stored in addition in a database so that they can be accessed very fast from other devices and the evaluation software. Every single experiment cycle can be loaded again within the experiment control to rerun a sequence or to compare the parameters with more recent sequences. Only the unique count number has to be known to be able to access the data for the evaluation and documentation of the measurements. All captured incoming data, such as the oscilloscope traces or the images from the camera, are stored with a filename containing the unique count number of the specific experiment cycle with which it was taken. The write and read process of the data is shown in figure 4.4.

The data evaluation system is written in Matlab because of the convenient way Matlab can load, analyze and plot data. The disadvantages of Matlab described in section 4.1 do not play a role for the data analysis. Since 2008, the object-oriented programming capabilities of Matlab have improved, so that modern programming concepts can be implemented for a better ease of use.

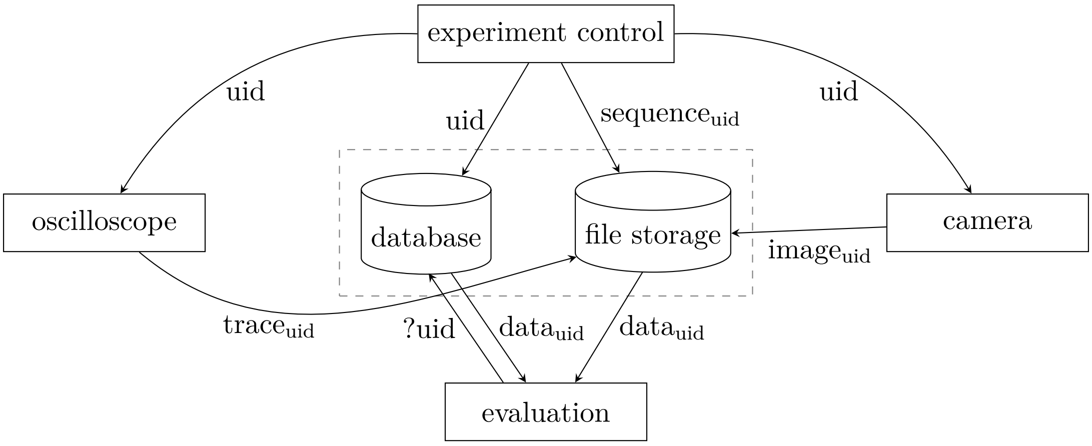

Fig. 4.4: Data flow of the data storage and the data evaluation. Every single experiment cycle has a unique count number (uid) which is broadcasted by the experiment control. All external data acquisition devices store the data according the unique id. Datasets can be evaluated by querying the database with the unique id (?uid) which returns the settings of an experiment cycle and, in addition, the corresponding data path of the evaluated data.

The key class of the evaluation system is called `ExperimentCycle`. With only one line of code and the unique count number of the experiment cycle (uid), `ExperimentCycle.load(uid)`, an object is created containing all settings, images, already evaluated results, the time stamp and the data path. This object is used within the evaluation scripts to access, for example, the laser detuning with `experimentCycle.variables.laserDetuning`. This reduces the error probability and ensures the consistency within the evaluation scripts, because no data has to be entered manually.

The main data source of the experiment is the oscilloscope trace, containing the ion data. Unfortunately, our custom made modification of the MCP, as mentioned in section 2.6, causes ringing after an ion event. In addition, the signal height of ions can vary by a factor of 10, so that the ion counts cannot be analyzed by setting a static trigger level only. Hence, a dynamic software trigger is applied to extract the ion counts and arrival times, as shown in figure 4.5.

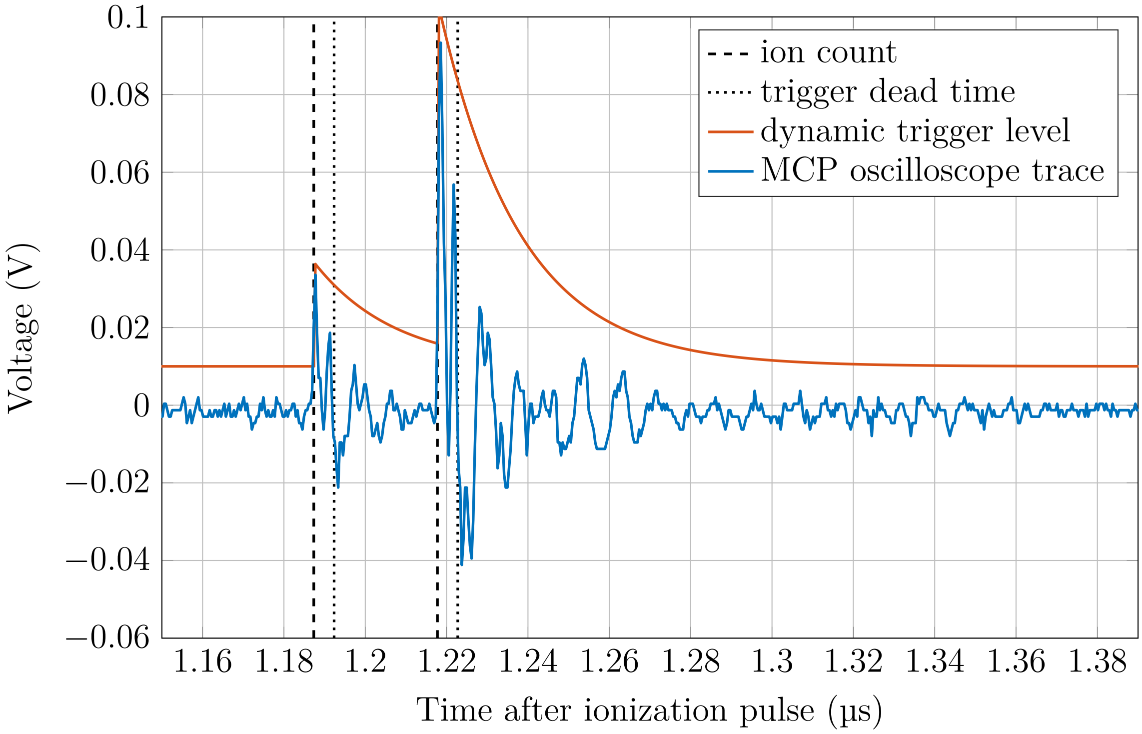

Fig. 4.5: Oscilloscope signal of two ion events sampled with 2.5 GS/s. The dashed lines indicate ion events. The dynamic trigger level is increased to the maximum voltage of each event with a headroom of 5 %. A small dead time of 5 ns prevents double counts from single ions. Afterwards, the dynamical trigger is lowered with an exponential decay time $\tau_{\text{ring}} = 20\,\text{ns}$ according to the decay of the ringing signal (equation 4.1).

The analysis starts at t_{start} after the signal from switching the high voltage for the ionization has decayed. The initial trigger voltage is set to U_{min}, which has to be above the noise level from the detector and amplifier. As soon as the oscilloscope signal exceeds the trigger level, which means that an ion has arrived at t_0, the dynamical new trigger level is calculated with

$$U(t) = U_{\mathrm{min}} + (1 + a) \times (U(t_0) - U_{\mathrm{min}}) \times \exp\left(\frac{t_0 - t}{\tau_{\mathrm{ring}}}\right). \qquad (4.1)$$

The factor a depicts a safety margin for the amplitude and τ_{ring} must be set according to the decay time of the ringing ion signal, which is in our case 20 ns. With this dynamical software trigger, ion events are detected with a high probability even within the ringing signal of a previously detected ion.

The evaluation process of the ions is highly automated. The ion evaluation settings t_{start}, t_{end}, U_{min}, a and τ_{ring} have to be set in an `IonSettings` object. Together with the unique count number of the experiment cycle, an `Ions` object can be created by calling `Ions.load(uid, ionSettings)`. The oscilloscope trace is evaluated with this single command only, and the analyzed data is stored within the object and cached on the file storage for subsequent evaluations. There are several more single line of code analysis programs available, e.g. for evaluating spectra which are taken over many experiment cycles. Only the range of the unique count numbers must be provided to visualize a spectrum by running `SpectrumBEC(uidFrom:uidTo, ionSettings)`. Also for these evaluation types, an efficient caching system is running in the background so that an evaluation carried out with the same parameters takes only a few milliseconds instead of hours if thousands of experiment cycles have to be evaluated.

4.3 Image acquisition and evaluation

Besides the ion signal, an image is taken of the atom cloud containing information about the experiment performed. The shape and size of the cold atoms show immediately whether the correct parameters are set for cooling the atoms and when compared for subsequent experiment cycles whether the system is stable. The image acquisition program is written in Matlab, because it must be changed from time to time for the special purpose of the experiments performed and most physicists are familiar with Matlab, which is often taken to process and

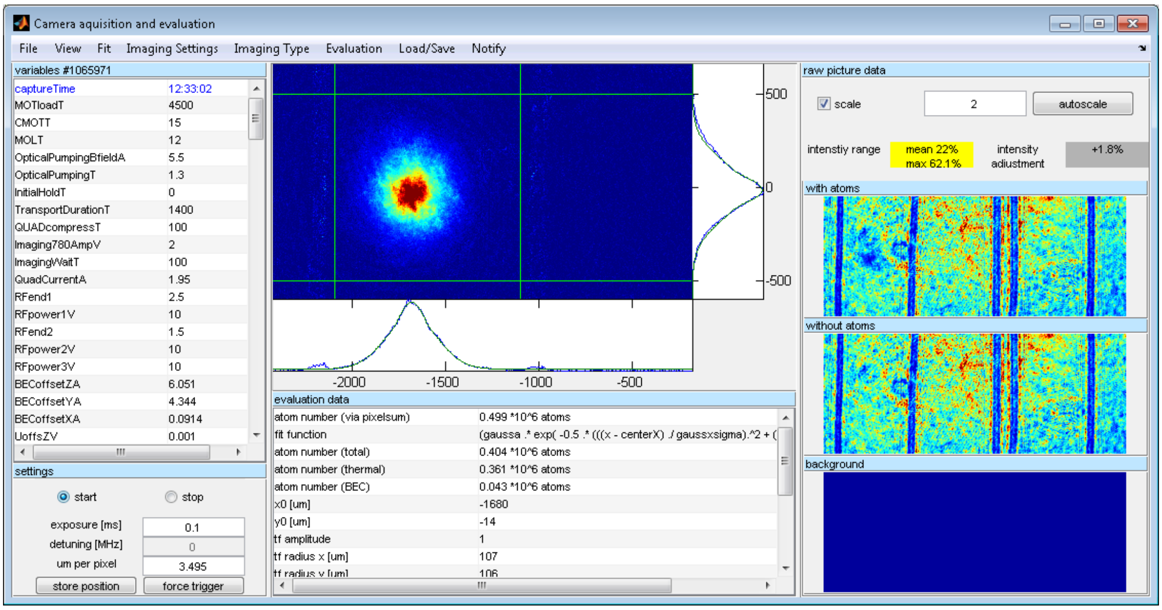

variables #1065971

captureTime	12:33:02
MOTloadT	4500
CMOTT	15
MOLT	12
OpticalPumpingBfieldA	5.5
OpticalPumpingT	1.3
InitialHoldT	0
TransportDurationT	1400
QUADcompressT	100
Imaging780AmpV	2
ImagingWaitT	100
QuadCurrentA	1.95
RFend1	2.5
RFpower1V	10
RFend2	1.5
RFpower2V	10
RFpower3V	10
BECoffsetZA	6.051
BECoffsetYA	4.344
BECoffsetXA	0.0914
UoffsZV	0.001

settings

● start ○ stop

exposure [ms] 0.1

detuning [MHz] 0

um per pixel 3.495

evaluation data

atom number (via pixelsum)	0.499 *10^6 atoms
fit function	(gaussa .* exp(-0.5 .* (((x - centerX) ./ gaussxsigma).^2 + (
atom number (total)	0.404 *10^6 atoms
atom number (thermal)	0.361 *10^6 atoms
atom number (BEC)	0.043 *10^6 atoms
x0 [um]	-1680
y0 [um]	-14
tf amplitude	1
tf radius x [um]	107
tf radius y [um]	106

☑ scale 2

intenstiy range: mean 22% max 62.1%

intensity adjustment: +1.8%

Fig. 4.6: Screenshot of the image acquisition program, showing a bimodal atom distribution.

visualize data. A screenshot of the image acquisition program is shown in figure 4.6.

The object oriented programming style, which Matlab supports, allowed the development of a flexible, clean and maintainable application. This is explained by the means of the different cameras attached to the experiment. It is very convenient to create a parent class called `Camera`, which has all functions required to handle a camera such as `open()`, `hasData()`, `getData()`, `setExposure()` and so forth. The specific implementation for the different cameras attached (pco Pixelfly, Andor iXon, USB cameras), e.g. `CameraPixelfly:Camera`, is very different, but inheriting from the parent class `Camera` provides a common interface for all cameras attached. Regardless of which camera is in use, there is no need to distinguish in the code between them if the superclass `Camera` is used. For example, the exposure can be set by

```
camera = CameraPixelfly();
camera.setExposure(time);
```

for a pixelfly camera and

```
camera = CameraAndor();
camera.setExposure(time);
```

for an Andor camera. The object oriented programming style supports a common interface and otherwise redundant code can be implemented in the parent class.

An absorption or phase contrast image is created out of a series of three images. The atoms are present in the first image and absorb light. A reference image is taken without the atoms. The third image has no light going to the camera which leads to the dark-ground image.

The optical density for absorption imaging is calculated by

```
withAtoms_corr    = max(0.01,withAtoms-darkground);
withoutAtoms_corr = max(0.01,withoutAtoms-darkground);
transmission      = min(1,withAtoms_corr./withoutAtoms_corr);
opticalDensity    = -log(transmission);
```

according to the definition of the optical density (OD):

$$\frac{I_{\text{withAtoms}}}{I_{\text{withoutAtoms}}} = e^{-OD}. \tag{4.2}$$

The `max` commands take care that the valid domain is not left due to the correction of the dark-ground image. The `min` statement restricts the value range for the logarithm.

Phase contrast images are taken with a phase plate shifting the phase of the light which is not scattered by the atoms by $\pi/2$. The phase shift of the atoms under investigation is evaluated with

```
withAtoms_corr    = max(0.01,withAtoms-darkground);
withoutAtoms_corr = max(0.01,withoutAtoms-darkground);
transmission      = withAtoms_corr./withoutAtoms_corr;
phaseContrast     = (transmission - 1.0) / 2;
```

because the intensity for large detuning from resonance depends on the phase shift ϕ caused by the atoms as [45]

$$\frac{I_{\text{withAtoms}}}{I_{\text{withoutAtoms}}} \approx 1 + 2\phi. \tag{4.3}$$

It is crucial for both evaluation methods that the integrated light intensity during the exposure time is constant for the images with and without the atoms. Intensity fluctuations between these two images will lead to noise in the evaluated data. Hence, a region of interest can be set by the user to set the area in the image in which the atom cloud is positioned (green lines in figure 4.6). The outside region in both images is therefore, by definition, without atoms and should have the same intensity. The intensity fluctuation of the image pair can be calculated from this outside region. Hence, for example, the intensity of the reference image can be rescaled according to the extracted intensity change. This cancels intensity fluctuations and increases the precision.

The atom cloud can be fitted within the program with several different distributions, such as a Gaussian profile for the thermal cloud or a Thomas-Fermi profile for a pure BEC. The intermediate regime between these two is difficult to address, especially if one portion is very small. There are sophisticated guides [63] of how a bimodal distribution of such an atom cloud can be analyzed. However, it was found that these methods may be more accurate but are not robust in respect to changing atom cloud sizes and shapes. Therefore, a more direct analysis was found to give reliable results: At first, a 1D Gaussian fit is applied on the horizontal and vertical axis to get a fast estimate of the center and the width of the atom distribution. Afterwards, a 2D bimodal fit $f(x, y)$ is applied according to

$$\begin{aligned} f(x,y) &= G(x,y) + TF(x,y) + o \\ G(x,y) &= a_G \times \exp\left[-\left(\frac{x-x_0}{\sqrt{2}\sigma_x}\right)^2 - \left(\frac{y-y_0}{\sqrt{2}\sigma_y}\right)^2\right] \\ TF(x,y) &= a_{TF} \times \left[1-\left(\frac{x-x_0}{r_x}\right)^2 - \left(\frac{y-y_0}{r_y}\right)^2\right]. \end{aligned} \tag{4.4}$$

The evaluation range for the Thomas-Fermi profile TF is limited to positive values, and the offset o provides an overall offset to the signal.

The results extracted out of the images and the raw images are stored according to the unique count number of the experiment cycle, as already shown in figure 4.4. The program displays beside the images all parameters set in the experiment control interface. A history mode for the experiment cycles is implemented. Only the unique count number range of a measurement has to be entered and all images and input parameters can be stepped through as if it would be a live analysis. This helps to review old experiments in a fast and convenient way.

5

Long-term stability

The long-term stability of the experiment is a prerequisite to acquire data with an excellent signal-to-noise ratio. Especially in the case of a Bose-Einstein condensate in a magnetic trap, very small drifts in the offset magnetic field change the atom number by a large amount and noise in the trap coils heats the cold atoms very fast. The repeatability and the suppression of noise sources were a key aspect during the design and building up phase for the experiment. A lot of long-term measurements had to be performed to be able to study only a single Rydberg atom inside the Bose-Einstein condensate, which is the topic of this thesis. After several optimization steps, especially by improving the noise-level of the QUIC trap as described in section 3.4, the process to create a Bose-Einstein condensate was reliable and lead to stable and large atom numbers over several consecutive days with a long-term atom number fluctuation of less than $\pm 10\,\%$. The experiment has to be in thermal equilibrium to achieve this stability. As already shown in figure 4.3, the relative uncertainty of the total duration of the experiment cycle is below 10^{-6}, which was reached by implementing the appropriate design concepts as described in section 4.1. For stable operation, also the Rydberg excitation and ion detection needs to be very reliable. The long-term ion count rate stays within $\pm 10\,\%$ during long scans as well. In the following, two long-term measurements are presented showing an astonishing signal-to-noise ratio even though the mean number of Rydberg atoms per shot is well below one. The mean ion count rate had to be low because a single Rydberg atom was investigated.

5.1 Inelastic collision of a Rydberg atom with a ground-state atom

The first measurement presented (figure 5.1) shows the number of Rydberg atoms which went through an orbital angular momentum state changing collision for a 100S state. The detailed physics describing this phenomenon will be explained in section 7.1 and is just summarized in the following.

The laser pulse of the Rydberg excitation ends at $t = 0\,\mu\text{s}$. After the ionization delay time t, two ionization pulses are applied: The first ionizes all Rydberg atoms which stayed in the initially excited state (not shown in the figure), and the subsequent higher field pulse ionizes the remaining Rydberg atoms which went through an angular state changing collision. The measurement was taken for four different excitation laser detunings, which are related to the density in which the Rydberg atom is excited in. The signal at a detuning of $-48\,\text{MHz}$ is lower compared to the other laser detuning, because it comes from the peak density of the Bose-Einstein condensate with approximately $5\times10^{14}\,\text{atoms/cm}^3$. This signal is depleted during the 400 experiments performed in each Bose-Einstein condensate. It was found, however, that the fitted collision time τ is not affected by the change in amplitude.

This was measured for 16 hours, which corresponds to a total number of 2048 Bose-Einstein condensates that were measured in series. The magnetic trap can be kept on during the experiments and with the low mean number of Rydberg atoms excited, the Bose-Einstein condensate is not destroyed so that the experiments could be performed multiple times in a single Bose-Einstein condensate. Hence, the Rydberg excitation, ionization and detection sequence was applied 400 times for each Bose-Einstein condensate. This results in 8.2 million data traces taken and, therefore, every data is the average of 12 800 measurements. A very good signal-no-noise ratio was achieved even though a two dimensional parameter scan was performed with 4 different excitation frequencies and 16 different delay times. The long-term mean atom number drift was within $\pm 2\,\%$, while the ion count rate was changing below $\pm 7\,\%$. This results in a very small error of the mean of the data points.

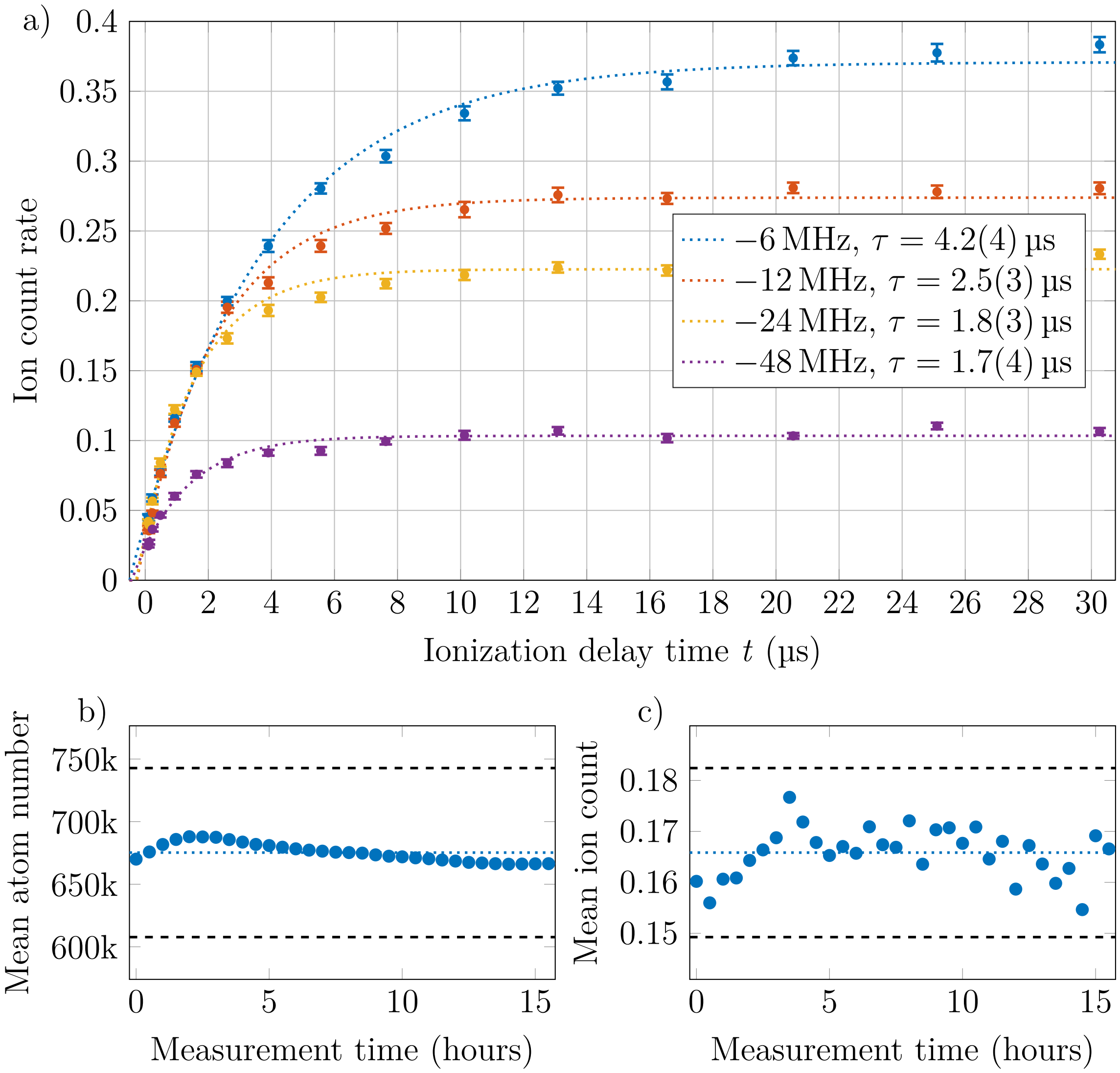

Fig. 5.1: Long-term stability of a 16 hours long measurement. (a) Ion count rate of an l-changing collision measurement for a 100S state. The collision time τ shown in the legend is extracted out of the dotted fit curve $f(t) \propto 1 - \exp(t/\tau)$ and the error given shows the confidence bounds of the fit. Each data point consists of 12 800 measurements. The small error bars indicate the standard error of the mean. (b) Average remaining atom number measured at the end of each experiment cycle and averaged for a complete scan through all parameters. The dashed lines indicate the ±10 % thresholds. The mean atom number over time does not change more than ±2 %. (c) Mean ion count rate averaged the same way as in (b). The count rate stays within ±7 % of the mean value.

5.2 High resolution spectrum for single 40S Rydberg atoms in a BEC

The second measurement (figure 5.2) shows a high resolution spectrum for single 40S Rydberg atoms in a Bose-Einstein condensate, which will be briefly discussed in the following and in detail in section 6.4. The Rydberg atoms are excited for 2 µs and are ionized 200 ns later. The spectrum shows for small negative detuning ($-40\,\mathrm{MHz} > \delta \geq 0\,\mathrm{MHz}$) several lines caused by the ultralong-range Rydberg molecules [19], which have a binding energy of $N \times 8.7\,\mathrm{MHz}$ with N atoms bound to the outermost potential well of the Rydberg orbit. The lines are distinguishable from the broad signal until $N = 6$, the hexamer molecule. The broad signal, especially to far red detuning, is caused from the high density regions of the Bose-Einstein condensate. The signal was split into Rb^+ and Rb_2^+ ions according to their different arrival time on the detector. The pronounced peaks for the ultralong-range molecules is not reflected in the Rb_2^+ signal. That means that Rb_2^+ molecules are not created, or not so fast created from the ultralong-range Rydberg molecules.

The spectrum was measured for 40 hours long and the data was taken with 5140 Bose-Einstein condensates. Each Bose-Einstein condensate was probed 1200 times but only the first 50 excitation pulses were evaluated because too many pulses deplete the dense part of the Bose-Einstein condensate. In total 257 000 data traces were evaluated. 257 different frequencies were scanned from $-120\,\mathrm{MHz}$ to $8\,\mathrm{MHz}$ in steps of $500\,\mathrm{kHz}$ with every single data point averaged 1000 times. Due to the very good signal-to-noise level, even the signal at very high red detuning has meaning even though the mean count rate is below 0.05 ions per shot. The long-term mean atom number and ion count rate stayed within $\pm 10\,\%$ over the whole measurement time, which shows the excellent stability and capability of the experimental setup.

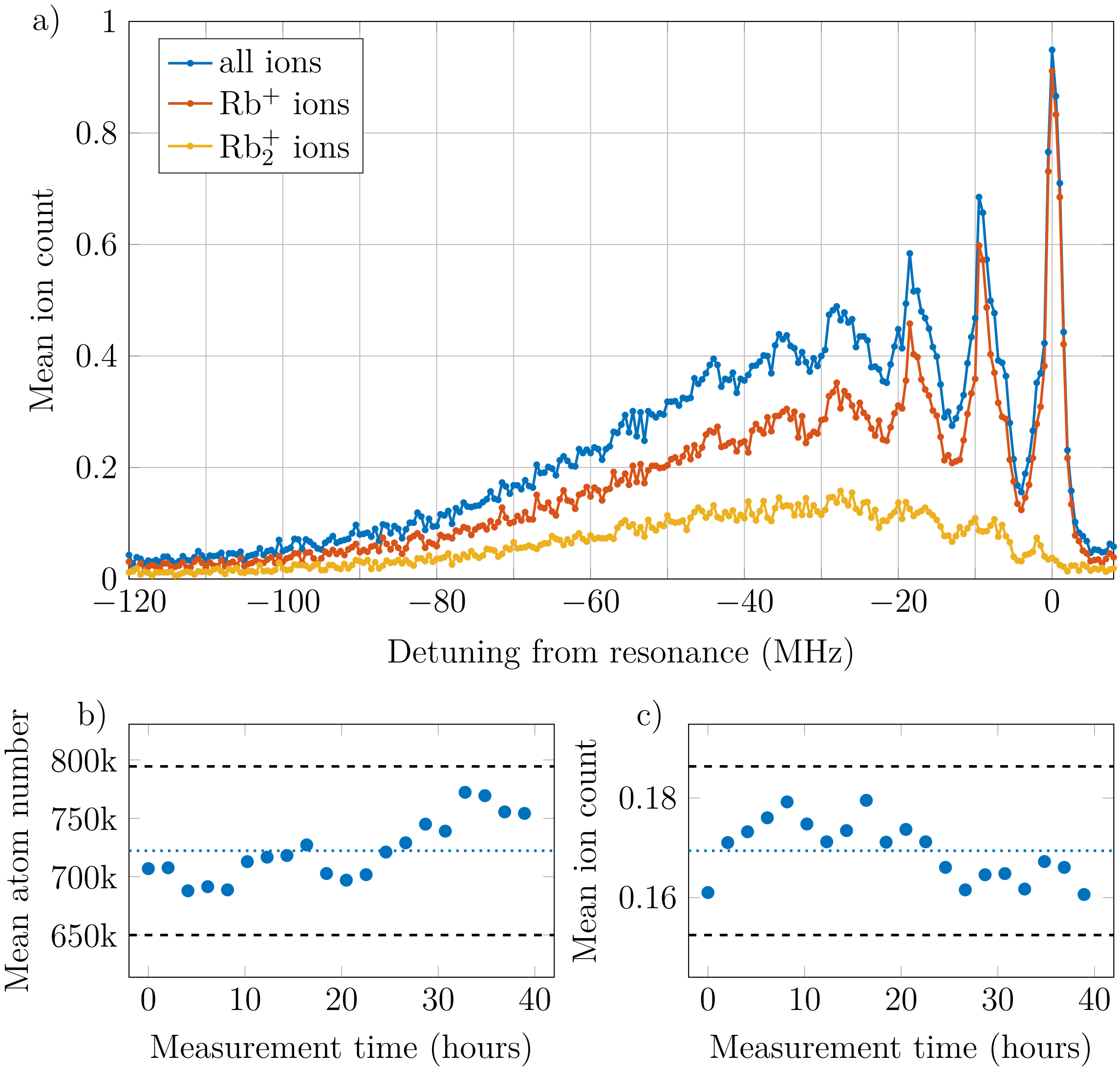

Fig. 5.2: Long-term stability of a 40 hours long measurement. (a) 40S Rydberg spectrum measured in a Bose-Einstein condensate. The spectrum is broadened due to the high density of a BEC so that even at a detuning of −120 MHz from the atomic resonance a signal could be measured. Each of the 257 data points consists of 1000 averages. (b) Remaining atom number measured at the end of each experiment cycle and averaged for a complete scan through all parameters. The dashed lines indicate a change of ±10 % which is not exceeded. (c) Mean ion count rate, which is stable to ±8 % with respect to the total mean value.

Conclusion

We have built a new experimental apparatus which is capable of cooling rubidium atoms from room temperature to below 1 µK to create large Bose-Einstein condensates of up to 1.7 million atoms. A single Rydberg atom can be excited inside the Bose-Einstein condensate, which has a well-defined spatial position due to the focused excitation laser with a beam waist of 2.1 µm. The precise field control ($\sim$ 1 meV) inside the science chamber allows the excitation of Rydberg atoms up to a principal quantum number of $n = 160$. Single Rydberg excitations can be measured because the ion detector efficiency is very high (70 %). The fast digital channels (1.5 ns) and the oscilloscope (1 GHz bandwidth) provide a very accurate timing resolution for the experiments. The kinetic energy of the Rydberg atoms can be examined by ion trajectory simulations, and state selective ionization can be applied to distinguish between the angular momentum states of the Rydberg atom. A high resolution (1 µm) imaging system can be used to take in situ images of the Bose-Einstein condensate. Special care was taken that all components of the apparatus are long-term stable so that an experiment sequence can run day and night without interruption, so that a very good signal-to-noise can be achieved even if the ion count rate is well below 1. In the next section we will use these properties to investigate the interaction between a single Rydberg atom and a Bose-Einstein condensate.

Part II

A single Rydberg atom within a Bose-Einstein condensate

Curiosity demands that we ask questions, that we try to put things together and try to understand this multitude of aspects as perhaps resulting from the action of a relatively small number of elemental things and forces acting in an infinite variety of combinations.

Richard Feynman
The Feynman Lectures on Physics Vol. 1 Ch. 2

A single Rydberg atom in a Bose-Einstein condensate is an exceptional system to investigate *elementary things and forces*, as Richard Feynman called it in the quote above. The experiments and results presented in this part of the thesis show elementary processes of atomic physics on the micrometer and microsecond scales, which can be investigated due to the unique properties of Rydberg atoms. By exciting exactly one Rydberg atom in the Bose-Einstein condensate, the elastic and inelastic collisions on the ground-state atoms are the dominant interactions and can thus be investigated.

To study the collisions, the atoms are first prepared in their ground-state as explained in section 2.3, so neither excited states play a role in the system, nor the motion of the atoms. A typical ultracold temperature of the system under investigation is only 300 nK, which corresponds to an energy of $h \times 6\,\mathrm{kHz}$ where h is the Plank constant. For better readability the energies are given without the Planck constant in the following. The atoms are trapped magnetically and the resulting chemical potential of the system is below 5 kHz. Therefore, the degenerate atom gas, described by a single wave function, is sensitive to small interactions as soon as they exceed a few kHz, which is the case for a rubidium Rydberg electron interacting with rubidium ground-state atoms in a spin-polarized sample.

Then, a single Rydberg atom is excited within this system. With focused and crossed laser beams, this impurity can be located at the very center of the Bose-Einstein condensate. The laser power can be chosen such that with a high probability not more than a single Rydberg atom is created within the sample. In addition, the Rydberg blockade effect [28] also suppresses multiple Rydberg excitations (further details can be found in section 2.5). The properties of the single impurity can be probed, after ionizing it, with a microchannel plate detector, which has a high detection efficiency of 70 %, as shown in section 2.6. A main property of a Rydberg atom is its enormous size, with a radius of more than 1 µm for principal quantum numbers above 100. The different Rydberg states are energetically well separated and can be excited reliably and therefore provide an ideal testbed for the interaction of a Rydberg atom with the surrounding ground-state atoms. The Rydberg electron, which explores the area around the ionic Rydberg core, plays the dominant role in this system.

6

Elastic collisions of a Rydberg electron

The Rydberg atom interacts in two different ways with the surrounding ground-state atoms. On the one hand, the positive Rydberg core polarizes the ground-state atoms and therefore attracts them, which is the predominant interaction for Rydberg ground-state distances of up to approximately $500\,a_0$, with an interaction potential of $V_{C_4} > 17\,\mathrm{MHz}$ at that distance. For typical densities of a Bose-Einstein condensate, however, the mean interparticle distance is at least twice as large and therefore the ion-atom interaction plays a minor role. On the other hand, the loosely bound negatively charged electron also polarizes the ground-state atoms. Due to the wave character of the Rydberg electron, the electron comes very close to the neutral particles within the Rydberg orbit. The resulting electron ground-state potential at the outer node of a rubidium Rydberg S-orbit ranges from almost $13\,\mathrm{MHz}$ to $1\,\mathrm{kHz}$ over the principal quantum numbers $40 \geq n \geq 200$.

6.1 Ion-atom interaction

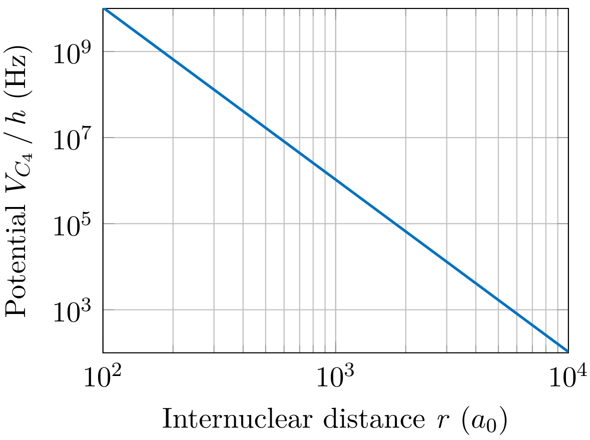

Fig. 6.1: Polarization potential $V_{C_4} \propto r^{-4}$ for an ion with a rubidium ground-state atom for a ground-state polarizability of $\alpha = 318.8(14)$ a.u. [64].

The positively charged Rydberg nucleus is not shielded perfectly any more by the Rydberg electron for an atom inside the Rydberg orbit, which leads to an attractive polarization potential between the Rydberg core and the polarizable ground-state atoms. The polarization potential is the most dominant interaction for neutral atoms inside the Rydberg orbit for internuclear distances below $500\,a_0$. The ion-atom interaction [65, 66] leads to the so-called C_4 polarization potential

$$V_{C_4}(r) = -\frac{\alpha/2}{r^4} = -\frac{C_4}{r^4}, \tag{6.1}$$

with the polarizability $\alpha = 318.8(14)$ a.u. [64] for rubidium ground-state atoms. The interaction strength is shown in figure 6.1. This potential describes the long range part of the Rb^+- Rb $^2\Sigma_g^+$ molecular potential. As a comparison the C_4 potential is plotted together with the lowest Rb^+ - Rb $^2\Sigma_g^+$ potential in figure 6.2 from high level ab initio electronic structure calculations [67].

A characteristic length scale for the ion-atom interaction can be defined [68] by equating the interaction energy (equation 6.1) and the relative kinetic energy E_{kin} of the two particles

$$E_{\mathrm{kin}} = \frac{p^2}{2\mu} = \frac{k^2}{2\mu} = \frac{1}{2\mu r^2}, \tag{6.2}$$

which leads to the characteristic radius

$$r^* = \sqrt{\mu\alpha}. \tag{6.3}$$

The reduced mass, $\mu = 0.5\,m$, must be taken into account in the case of same species atoms with the mass m. Therefore, the characteristic interaction radius for a rubidium ion and a rubidium ground-state atom is approximately $5000\,a_0$.

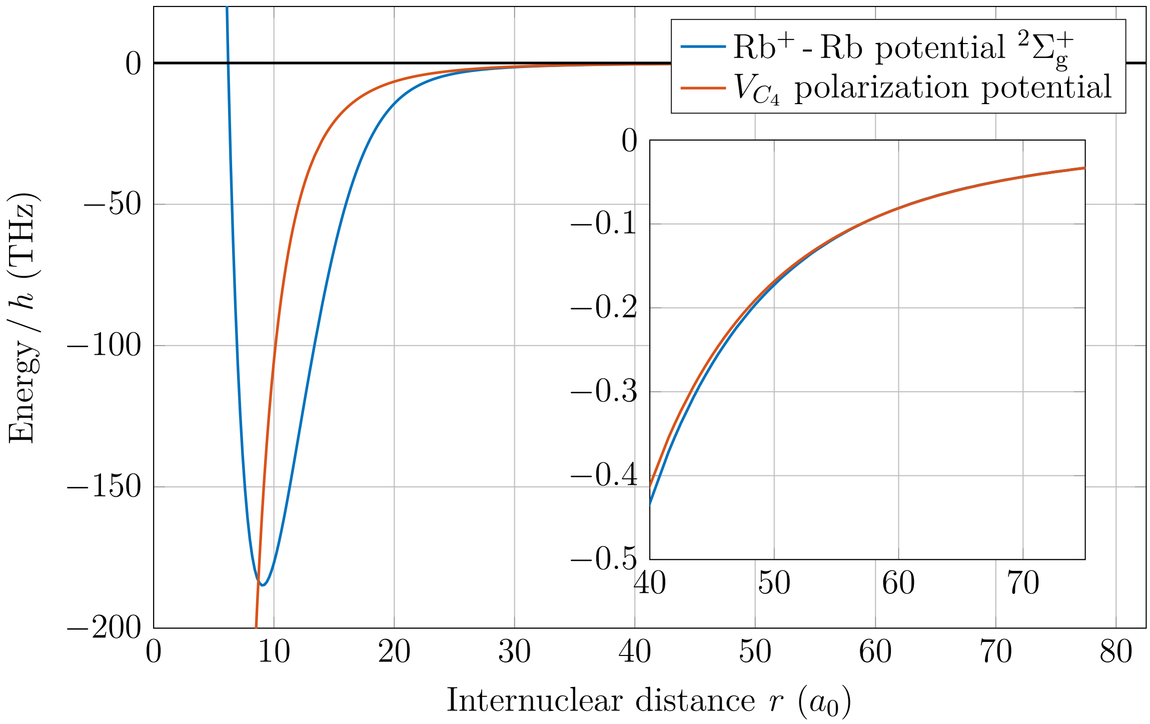

Fig. 6.2: Comparison of the lowest Rb$^+$ - Rb molecular potential ($^2\Sigma_g^+$) [67] with the C_4 polarization potential only. The interaction of the rubidium molecule with internuclear distances above $100\,a_0$ is very well described by the polarization potential. At internuclear distances $r \ll 100\,a_0$ short range physics become relevant and the potential of an ion with a neutral atom cannot be described by the polarization potential only.

6.2 Electron-atom scattering

Compared to the weak long range interaction of the ion with the ground-state atom, the electron scattering on a neutral atom interaction is a short range interaction. Both interactions are based on the polarizability of the ground-state atoms, but mainly due to the mass difference of the Rydberg atom and the electron, the characteristic interaction radius of equation (6.3) drops to $r^* = 18\,a_0$. Even at very high densities like $\rho = 1\times10^{15}$ atoms/cm^3 the mean interparticle distance [69] calculated with the gamma function Γ

$$\langle r\rangle = \left(\frac{3}{4\pi\rho}\right)^{1/3}\Gamma\left(\frac{4}{3}\right) \tag{6.4}$$

exceeds $1000\,a_0$ (figure 6.3), which is much larger than the interaction radius of an electron with a ground-state atom. In addition, the de Broglie wavelength λ_{db} of the slow Rydberg electron is larger than the interaction radius, and therefore s-wave scattering dominates.

Already in 1934, Enrico Fermi could explain [70] the line shifts observed by Edoardo Amaldi and Emilio Segrè [71, 72] in alkali spectra at very high densities with a quasi-free electron model and s-wave scattering. The model was based on the, nowadays called, Fermi pseudopotential

$$V_{\mathrm{pseudo}}(\mathbf{r}) = 2\pi a_s\delta(\mathbf{r}), \tag{6.5}$$

which treats the electron-neutral scattering, to a good approximation, as a point-like interaction with the s-wave scattering length a_s describing the interaction strength. Compared to the ion-neutral interaction, the electron-neutral interaction can be attractive or repulsive, depending on the scattering partners.

When considering the interaction of two atoms with respect to each other, the positions of the nuclei can be treated as static, due to their heavy mass, as compared to the electrons, which are light and explore their environment on a very different time scale. This leads to the idea of the Born-Oppenheimer approximation [73], which treats the movement of atom nuclei and electrons separately. Within the approximation, the s-wave scattering potential can be calculated by integrating equation (6.5) over the Rydberg orbit for a ground-state atom at the position $\mathbf{R}$ with respect to the Rydberg core, and is therefore

$$V_{\mathrm{s}}(\mathbf{R}) = \int V_{\mathrm{pseudo}}(\mathbf{r}-\mathbf{R})|\psi(\mathbf{r})|^2 d\mathbf{r} = 2\pi a_s|\psi(\mathbf{R})|^2. \tag{6.6}$$

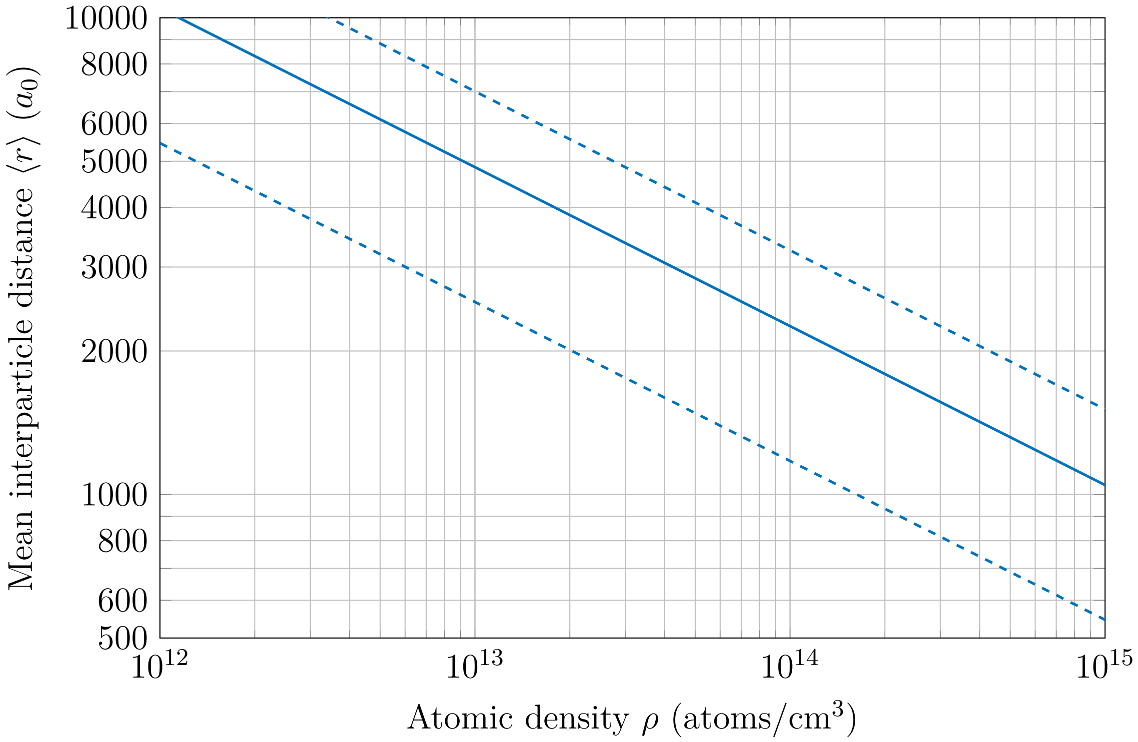

Fig. 6.3: Mean interparticle distance (solid line) for different densities and the respective full width at half maximum (dashed lines) of the distribution. In the high density region of a Bose-Einstein condensate with densities of 10^{14} to 10^{15} atoms/cm^3, the mean interparticle spacing is between 2000 and 1000 a_0 and therefore on the order of the interatomic distance where the butterfly state crosses the excited nS Rydberg state as shown in section 6.3.1. For thermal clouds with densities of 10^{12} and 10^{13} atoms/cm^3 with mean interparticle distances of 10000 and 5000 a_0 respectively, this regime cannot be entered.

For this two body potential, Chris Greene et al. predicted in 2000 [36] ultralong-range Rydberg molecules , which were first experimentally realized in 2009 by the predecessor of this experiment [19, 37, 38].

The bound states calculated from the potential energy curve describe the spectral lines of the system very well, as long as only one or few particles are inside the Rydberg orbit. In the case where there are many atoms inside the Rydberg orbit the total energy shift of a Rydberg atom can be calculated from the mean shift per particle by integrating the s-wave scattering potential V_s

over the volume of the Rydberg atom $\mathcal{V}_{\mathrm{Ryd}}$

$$\Delta\bar{E}_{\mathrm{single}} = \frac{\int_{\mathrm{Ryd}} V_s(\mathbf{r})d\mathbf{r}}{\int_{\mathrm{Ryd}} d\mathbf{r}} = \frac{2\pi a_s}{\mathcal{V}_{\mathrm{Ryd}}}. \tag{6.7}$$

The Rydberg volume of an nS state can be calculated from

$$\mathcal{V}_{\mathrm{Ryd}} = 4/3\,\pi r^3 = 4/3\,\pi(2(n^*)^2)^3 \propto (n^*)^6. \tag{6.8}$$

with the effective principal quantum number n^*, which includes the quantum defect (see section 2.5). To improve the readability, the scaling of the various properties will be shown only as a function of n. It should be noted that in all calculations n^* is actually used.

The mean shift per particle $\Delta\bar{E}_{\mathrm{single}}$ is plotted together with the binding energy of the ultralong-range dimer and the depth of the outermost potential well in figure 6.4 for the triplet scattering length $a_{s,\uparrow\uparrow} = -15.7\,a_0$ [S5] of rubidium. All listed energies scale approximately with n^{-6}. To obtain the total energy shift ΔE from the mean shift per particle $\Delta\bar{E}_{\mathrm{single}}$ of equation (6.7), the number of atoms inside the Rydberg orbit $N_{\mathrm{Ryd}} = \rho\,\mathcal{V}_{\mathrm{Ryd}}$ has to be multiplied by the shift per particle:

$$\Delta E(\rho) = N_{\mathrm{Ryd}}\;\Delta\bar{E}_{\mathrm{single}} = N_{\mathrm{Ryd}}\frac{2\pi a_s}{\mathcal{V}_{\mathrm{Ryd}}} = 2\pi a_s\rho \tag{6.9}$$

The total energy shift from Fermi's pseudopotential is directly proportional to the s-wave scattering length a_s and the background atom density ρ. The shift is independent of the principal quantum number of the Rydberg atom.

The energy shift ΔE of equation (6.9) explained the line shift seen experimentally in 1934 [71, 72]. Later, the model had to be refined to explain the results observed for different species atoms measured at higher spectral resolution. Instead of assuming a constant scattering length a, the velocity of the electron and therefore the momentum k was taken into account for the interaction. For higher momentum, the de Broglie wavelength shrinks and p-wave scattering components can play a significant role for the electron-neutral scattering interaction as described in detail by Alain Omont [77], giving rise to the so-called butterfly state (figure 6.5) as predicted by Hamilton et al. [76]. A good overview of the interaction of a Rydberg atom with a neutral atom can be found in the publication of Khushkivadze et al. [78]. Hyperfine coupling was added by Anderson et al. [79], which allows one to calculate mixed singlet/triplet spectra,

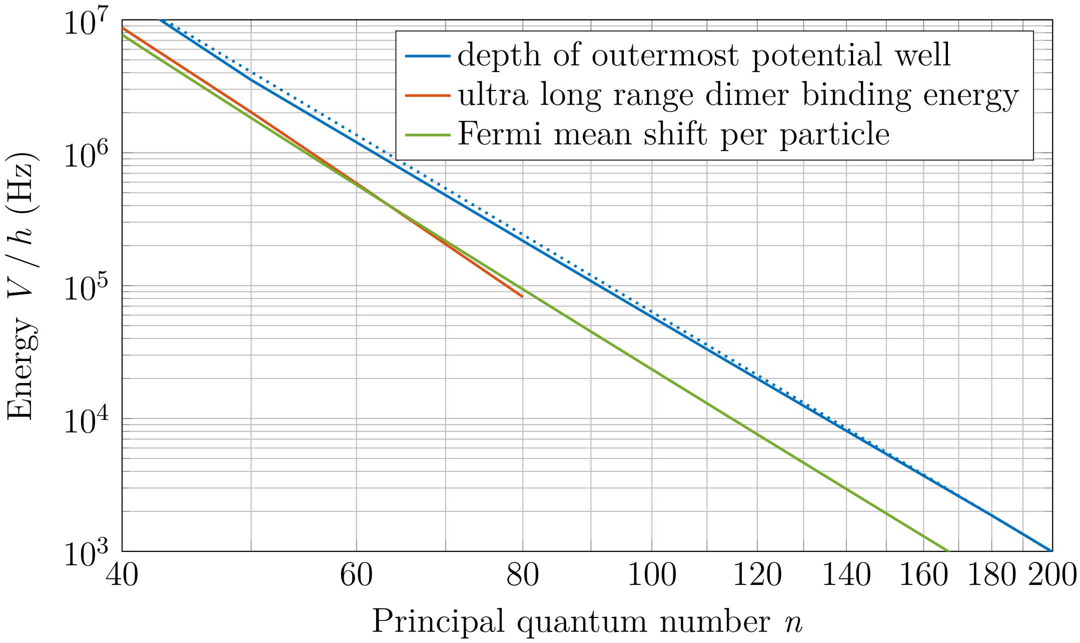

Fig. 6.4: Energy analysis of the outer most potential well of a nS Rydberg atom together with the Fermi mean shift per particle from equation (6.9) with the triplet scattering length $a_{s,\uparrow\uparrow} = -15.7\,a_0$ [S5] for rubidium. The binding energies of the ultralong-range dimer are extracted with an Numerov [74] algorithm from the potential energy curves. The dotted blue line shows a n^{-6} scaling as a reference.

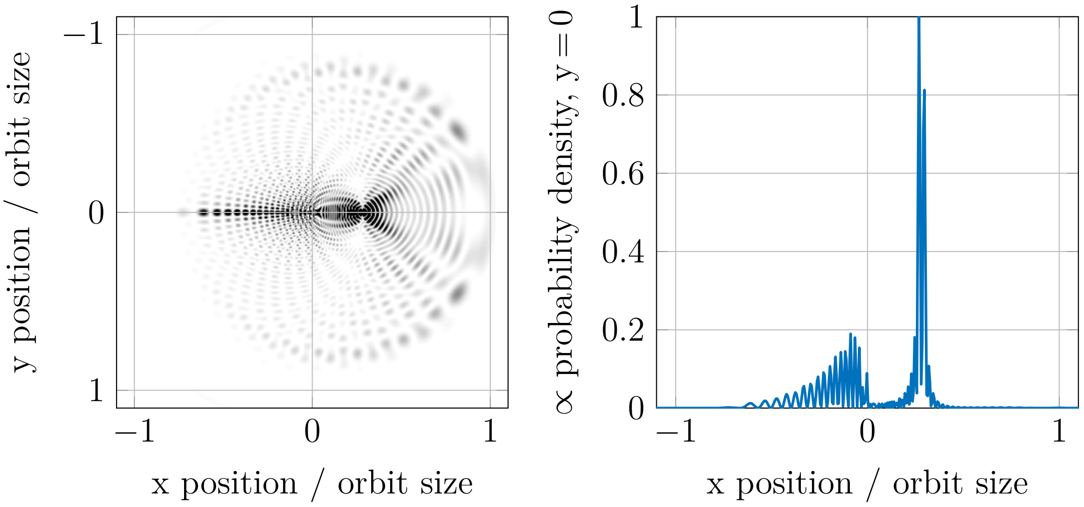

Fig. 6.5: 2D-cut (left graph) through the electron density distribution of a 53S + 5S atom pair [75] at an internuclear separation of $1400\,a_0$ in the butterfly [76] state plotted in Cartesian coordinates. The electron density is highly enhanced at the position of the 5S ground-state atom. The orbit size of the 53S state, which is defined as the classical Rydberg electron radius, is $4970\,a_0$. A 1D-cut of the electron probability density along the axis of the Rydberg atom and the ground-state atom is shown on the right.

which were experimentally measured for cesium by Saßmannshausen et al. [80] and for rubidium by Böttcher et al. [S5].

For the work presented here, only bare electron ground-state atom interaction for the triplet case is taken into account, not including fine structure, hyperfine interaction, or relativistic effects. Test calculations were performed showing that these effects lead only to minor modifications to the theory presented here.

The s-wave scattering potential can be rewritten to include the k-dependence of the electron as

$$\hat{V}_s(\mathbf{r},\mathbf{R}) = 2\pi a_s(k(R))\delta(\mathbf{r}-\mathbf{R}), \tag{6.10}$$

where $\mathbf{r}$ is the position of the electron and $\mathbf{R}$ the position of the scattering atom, both with respect to the Rydberg core. The s-wave scattering length $a_s(k(R))$ can be identified with

$$a_s(k(R)) = -\tan\frac{\delta_s(k(R))}{k(R)}. \tag{6.11}$$

The valence electron wavenumber $k(R)$ can be calculated from the semi-classical kinetic energy

$$E_{\text{kin}} = \frac{k(R)^2}{2} = -\frac{1}{2n^2} + \frac{1}{R} \tag{6.12}$$

for a Rydberg electron with effective principal quantum number n, which takes into account the quantum defect δ_l [54] of the respective angular momentum l:

$$n = n_0 - \delta_l. \tag{6.13}$$

The p-wave scattering potential, compared to the s-wave potential, depends on the derivative of the wave function as

$$\hat{V}_p(\mathbf{r},\mathbf{R}) = 6\pi a_p(k(R))\overleftarrow{\nabla}\delta(\mathbf{r}-\mathbf{R})\overrightarrow{\nabla} \tag{6.14}$$

with the corresponding p-wave scattering length

$$a_p(k(R)) = -\frac{\tan\delta_p(k(R))}{k(R)^3}, \tag{6.15}$$

and the p-wave scattering phase shift δ_p. The relevant non-relativistic triplet phase shifts for rubidium are shown in figure 6.6 from calculations of Ilya Fabrikant [81]. The fast and profound change of the p-wave scattering phase for rubidium has a strong impact on the potential energy curves as described in the following section.

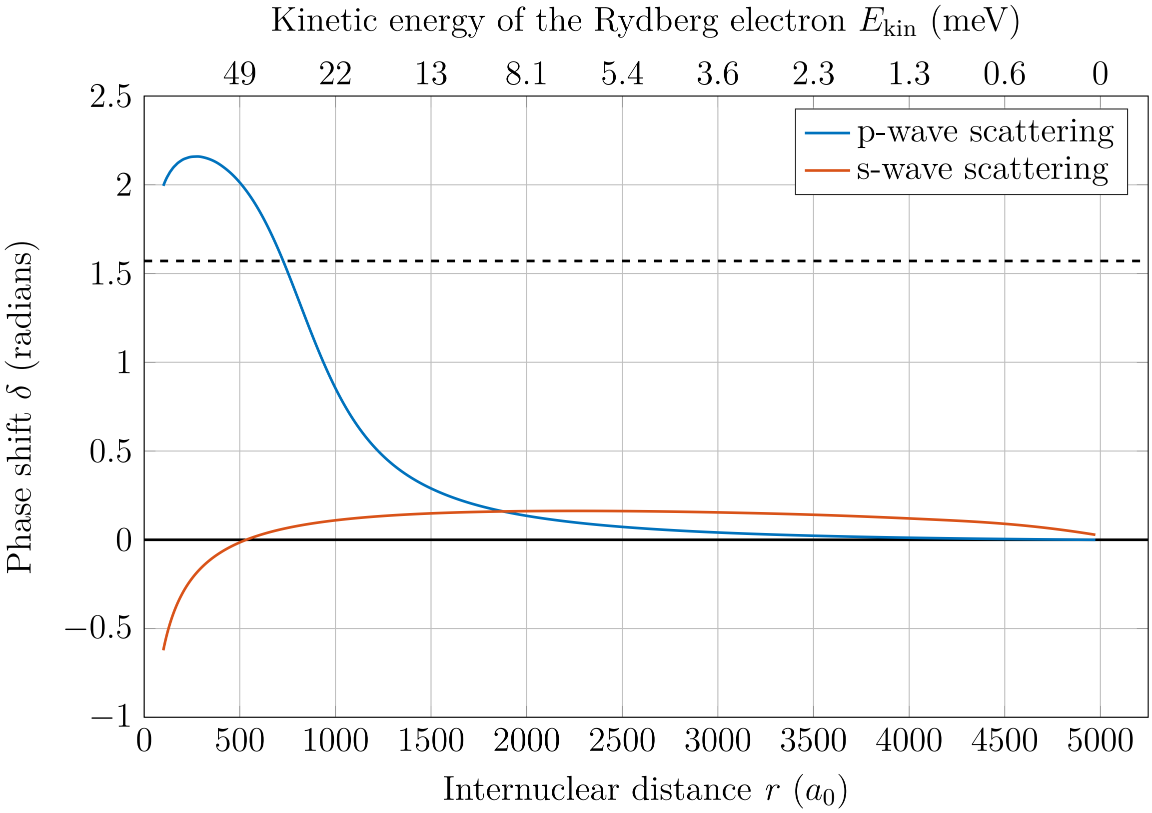

Fig. 6.6: The s- and p-wave triplet scattering phase shifts are plotted for rubidium versus the kinetic energy of the electron (nonlinear top axis) and for the internuclear distance of a 53S state (bottom axis) from calculations of I. Fabrikant [81]. The s-wave scattering phase (red) changes slowly over the relevant internuclear distances ($r > 500\,a_0$) in contrast to the p-wave scattering phase (blue), which has a steep slope for $500\,a_0 < r < 1500\,a_0$ and crosses $\pi/2$ (dashed line). Therefore, the tangent of the scattering length calculation from equation (6.15) diverges, leading to the p-wave scattering resonance at $E_{\mathrm{kin}} = 23\,\mathrm{meV}$ [82] and the deep butterfly potential shown in figure 6.8.

6.3 Potential energy curves

Within the Born-Oppenheimer approximation [73], the potential energy of a nS Rydberg atom and a ground-state atom can be calculated as a parameter of the distance of the two nuclei. In the case of many atoms inside the Rydberg orbit, the pairwise treatment is still valid because the backaction on the Rydberg electron wave function from the ground-state atoms is almost always negligible in this system.

There are different approaches and approximations available to calculate the potential energy surfaces of a Rydberg atom with a neutral ground-state atom. A very simple approach is to take Fermi's pseudopotential of equation (6.5), which depends only on the Rydberg wave function and a constant s-wave scattering length a_s. The most accurate, but computationally demanding method, is to fully diagonalize the interaction Hamiltonian, e.g. equations (6.10) and (6.14), including momentum dependent scattering phase shifts, and taking into account many states above and below the target principal quantum number. Instead of diagonalizing the Hamiltonian, the influence from p-wave scattering can be added in a perturbative approach, which is of course a poor approximation, especially close to the p-wave shape resonance described in section 6.3.1. Another way to calculate the potential energy curves is the Green's function method [83], treating the neutral atom as an additional boundary condition for the atomic solution. Potentials for each of these different methods are compared for a 53S Rydberg state in figure 6.7. To verify the accuracy of the Green's function and the full diagonalization method, the binding energy of the outermost dimer is compared to high resolution spectroscopy [S1]. With the Green's function potential energy curve, the ultralong-range dimer has a binding energy of 1.47 MHz and the full diagonalization leads to 1.37 MHz when including six n-manifolds below and two above the target state with respect to the fractional quantum defect. Both binding energies deviate less than 5 % from the measured binding energy, which is 1.41(3) MHz. For the following discussion all potential energy curves were calculated with the full diagonalization method in collaboration with Jesús Pérez-Ríos and Chris H. Greene. The S-character of the eigenstates i

$$s_i(R) = |\langle\psi_{n\mathrm{S}}(\infty)|\psi_i(R)\rangle|^2 \tag{6.16}$$

is also extracted out of the eigensystem of the potential energy curve calculation with a ground-state atom at an internuclear distance R and the unperturbed nS wave function $\psi_{n\mathrm{S}}(\infty)$. The quantization axis between the two atoms is chosen

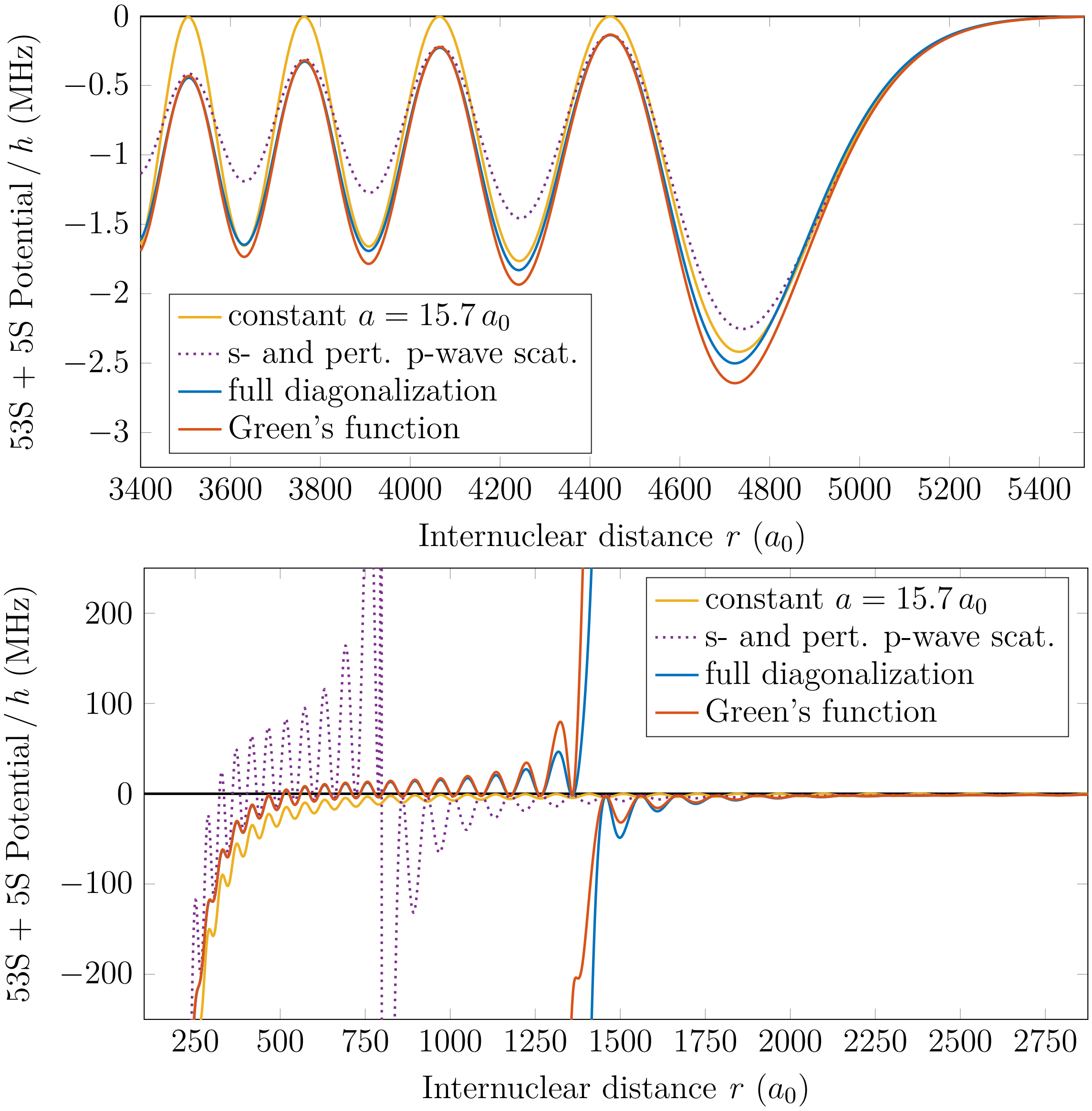

Fig. 6.7: Comparison of different $53\mathrm{S}+5\mathrm{S}$ potential energy curves from different calculation methods. The potential energy curves are slightly different for the outer region of the Rydberg orbit shown in the top graph. The experimentally measured dimer in the outermost node has a binding energy of 1.41(3) MHz. For the potential of the constant scattering length (yellow) the scattering length is chosen as $a = -15.7\,a_0$ to match the binding energy. The Green's function approach (red) results in a binding energy of 1.47 MHz, whereas the full diagonalization approach (blue) gives 1.37 MHz. The bottom graph reveals that only the full diagonalization and the Green's function method include the anti-crossing of the nS state with the butterfly potential at approximately $1400\,a_0$ and both agree with each other. The difference of both methods in this region is negligible compared to the uncertainty of each potential resulting from the uncertainty of the scattering phase shift used. The approach to add the p-wave interaction in a perturbative approach (violet) leads to large deviations.

to be along the internuclear axis, so that for s-wave scattering only $m_l = 0$, contributes to the solution [79]. For p-wave scattering also $m_l = \pm 1$ plays a role, giving rise to an additional smooth butterfly potential [76] which can be neglected in the following because the probability to excite into these states is very low for the principal quantum numbers $40 \geq n \geq 160$ investigated.

6.3.1 p-wave shape resonance

The p-wave scattering phase of rubidium has a big influence on the potential energy curves and therefore on the interaction of a Rydberg atom with its surrounding ground-state atoms. The shape resonance leads to interesting effects for the system investigated, because the mean internuclear distance

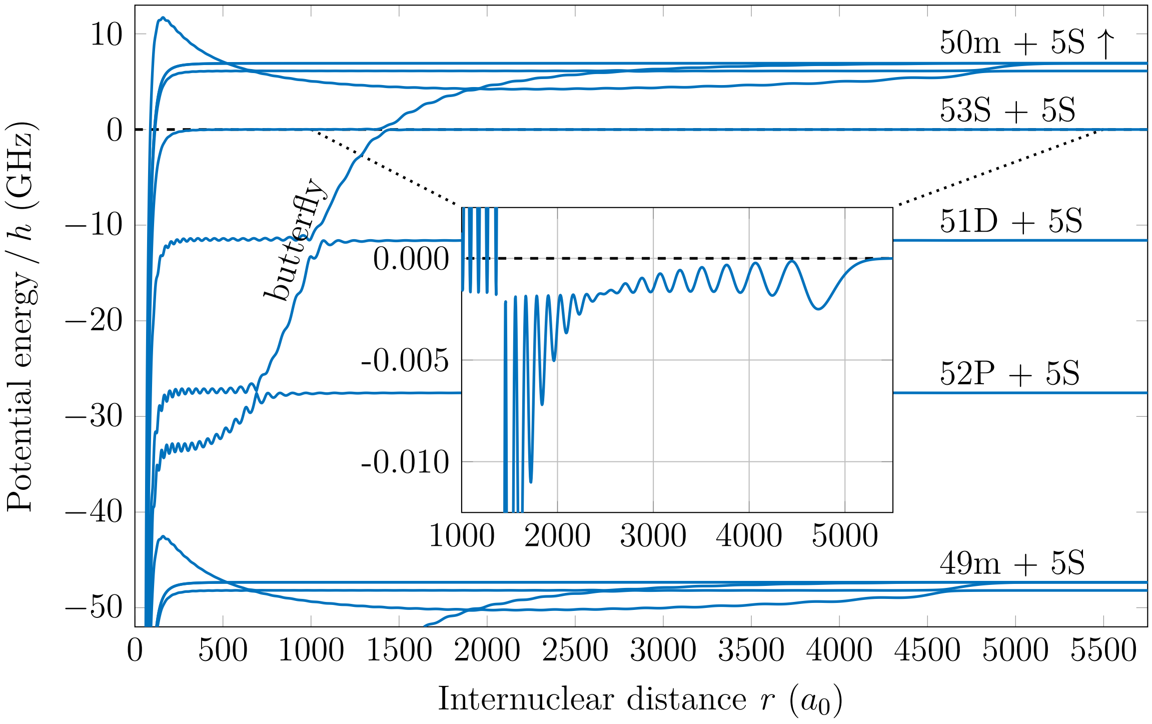

Fig. 6.8: Potential energy curve of a 53S + 5S state with its neighboring states. For short internuclear distances below $200\,a_0$, the polarization potential of the Rydberg ion core (see also figure 6.2) dominates the interaction potential. The butterfly state, as a consequence of the p-wave scattering in rubidium (see figure 6.6), originates from the hydrogenic manifold at large internuclear distances and then crosses all states down to the next lower manifold. The inset shows a zoom in of the 53S + 5S potential energy curve on the y-axis.

(figure 6.3) of the atoms in a Bose-Einstein condensate is of the order of the distance for which p-wave scattering dominates the interaction potential.

The scattering length in a partial wave expansion with angular momentum L is defined as

$$a_L = -\frac{\tan \delta_L}{k^{2L+1}}. \tag{6.17}$$

The scattering phase change, especially across $\delta_L = \pm\pi/2$, where the tangent of equation (6.17) diverges, has a strong influence on the potential energy curves. As plotted in figure 6.6, the phase shift for rubidium changes only slowly for s-wave scattering over the whole relevant electron kinetic energy range with respect to equation (6.12). The p-wave scattering phase instead rises fast until the electron reaches a kinetic energy of 50 meV. For a 53S state, for example, the p-wave scattering phase change plays a significant role for internuclear distances below 1500 a_0. The absolute scattering phase exceeds $\pi/2$, where the tangent diverges. As a consequence, the p-wave scattering interaction gives rise to the deep butterfly potential in rubidium, as shown in figure 6.8.

The position R of the resonance, as shown in figure 6.9, can be calculated by comparing the kinetic energy of the electron, given in equation (6.12), with the energy of the p-wave shape resonance $E_{\mathrm{res}} = 23\,\mathrm{meV}$ [82]

$$E_{\mathrm{kin}} = -\frac{1}{2n^2} + \frac{1}{R} = E_{\mathrm{res}}. \tag{6.18}$$

Towards high principal quantum numbers, n, the spatial position has an asymptotic behavior with a limit of

$$R_{\mathrm{max}} = \frac{1}{E_{\mathrm{res}}} = 1184\,a_0. \tag{6.19}$$

Compared to the resonance position, the butterfly state crosses the S state at a larger internuclear distance, with the numerically extracted values plotted in figure 6.9. The position of the crossing is defined by the internuclear distance at which the potential energy curve of the S state has 50 % S-character and 50 % butterfly character, which means $s(r) = 0.5$ from equation (6.16). With BEC densities of up to 5×10^{14} atoms/cm^3, the mean number of particles within the region of the butterfly crossing the S state, here defined as where the S-character is below $s(r) \leq 0.9$, does not exceed 0.4 atoms as shown in figure 6.10. Also, the energy of the first local maximum behind the anti-crossing of the S state can be analyzed and scales as $n^{-3.6}$ for the investigated quantum numbers as illustrated in figure 6.11. As a last interesting figure of merit, the slope of the butterfly potential crossing the nS state is evaluated to be approximately proportional to n^{-4} as shown in figure 6.12. The total depth and shape of the butterfly potential with respect to the absolute energy scaling of the Rydberg energies is the same for the investigated principal quantum numbers except for the radial position of the butterfly state as shown in figure 6.13.

The internuclear distance of the atoms within a Bose-Einstein condensate is on the order of the distance at which the excited nS Rydberg state crosses the butterfly state caused by the p-wave shape resonance. The consequences of this state crossing for Rydberg spectra are described in the following section. In addition, the electron-neutral interaction limits the lifetime of a Rydberg atom, which will be analyzed later in chapter 7.

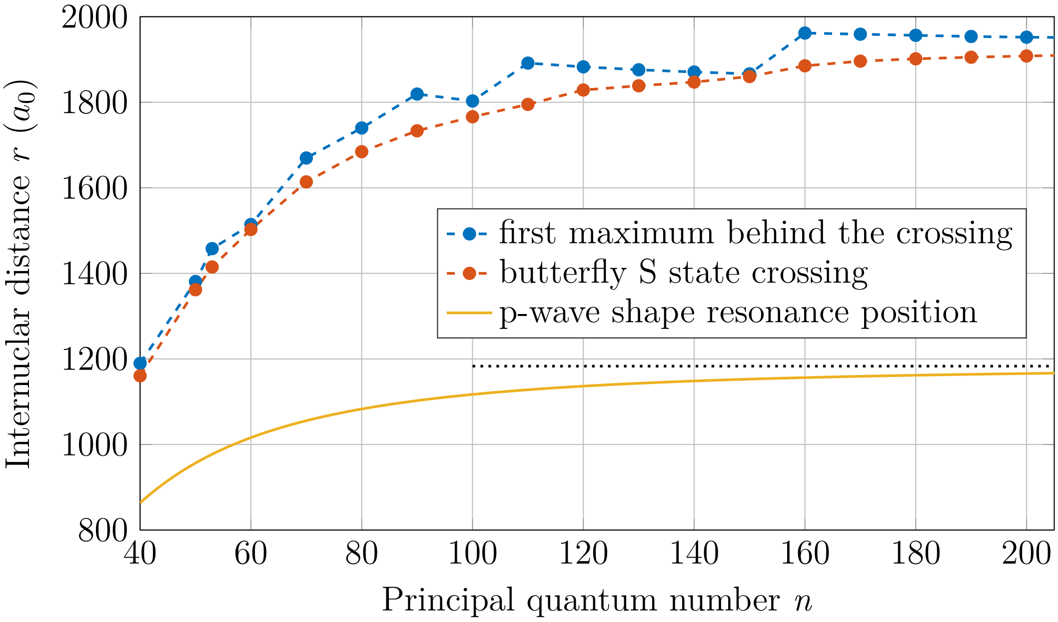

Fig. 6.9: Internuclear distances for p-wave shape resonance related properties. The red dots show the position, r_{cross}, of the anti-crossing of the butterfly state with the nS state. The position of the first local maximum of the $n\text{S} + 5\text{S}$ potential energy curve behind the anti-crossing, $r > r_{\text{cross}}$, is displayed in blue, whereas the p-wave shape resonance position at a kinetic energy of the Rydberg electron of 23 meV is plotted in yellow with the asymptote (dotted black) for high n calculated from equation (6.18).

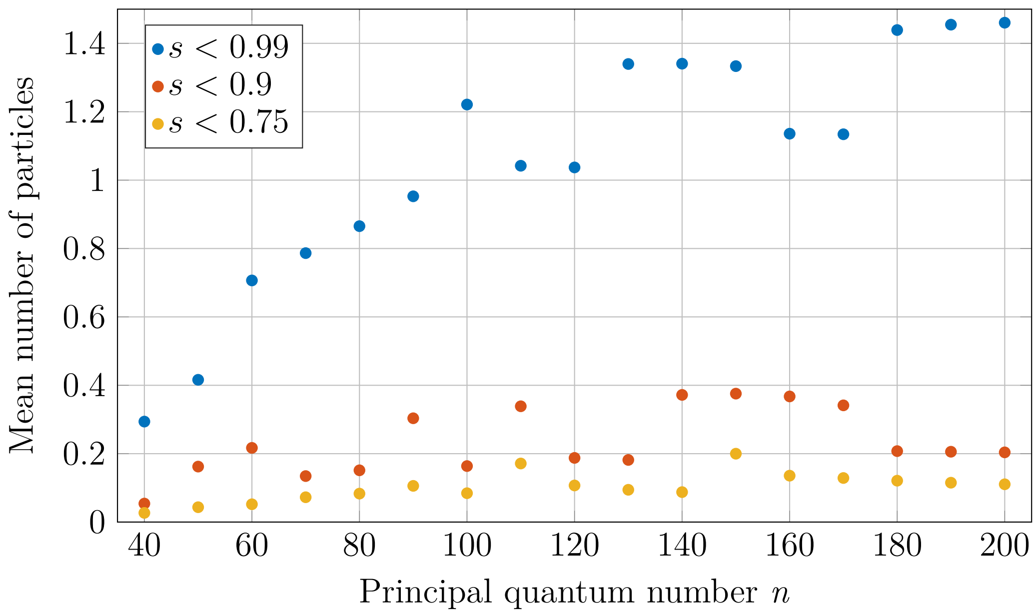

Fig. 6.10: Number of particles N inside the butterfly potential during the excitation of a target nS state for a density of $\rho = 5.2\times10^{14}\,\mathrm{cm}^{-3}$ (BEC peak density). The number of particles can be calculated from the volume $\mathcal{V}$ of the Rydberg orbit with the S-character $s(r)$ from equation (6.16) given in the legend, as $N = \mathcal{V}_{\mathrm{butterfly}}\rho$. The data points are not monotonously rising because of the oscillatory behavior close to the state crossing which highly depends on the principal quantum number.

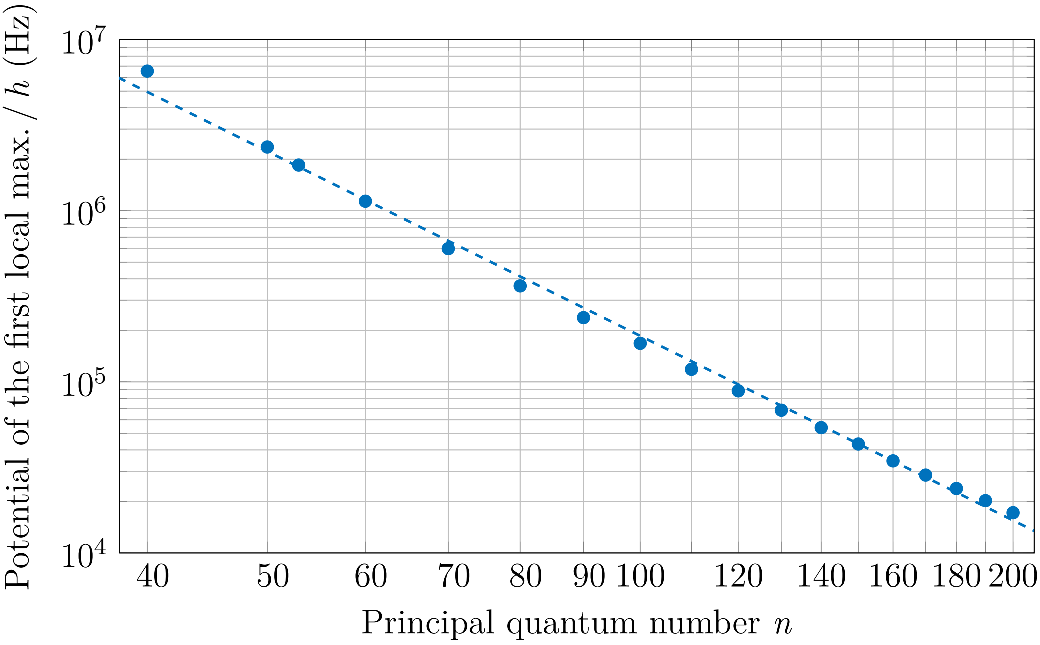

Fig. 6.11: Potential depth $\hat{V}$ of the first local maximum behind the anti-crossing of the butterfly and nS state with an internuclear distance $r > r_{\mathrm{cross}}$. The local maximum is approximately $\hat{V}/h = 1.9\times10^{11}\,n^{-3.6}\mathrm{Hz}$ according to the fit curve (dashed line), where h is the Planck constant.

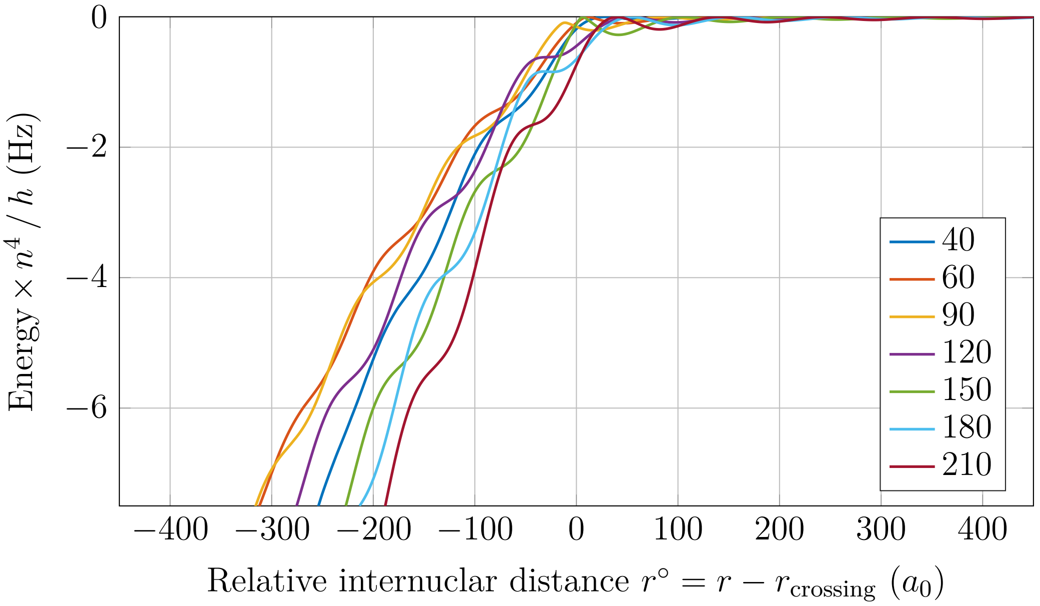

Fig. 6.12: Scaling behavior of the butterfly slope at the crossing, $r^\circ = 0$, for the nS states given in the legend. The potential energy curves are first raised to the power of 4 and afterwards the radial position is adjusted such that the anti-crossing of the butterfly and S state is at $r^\circ = 0$.

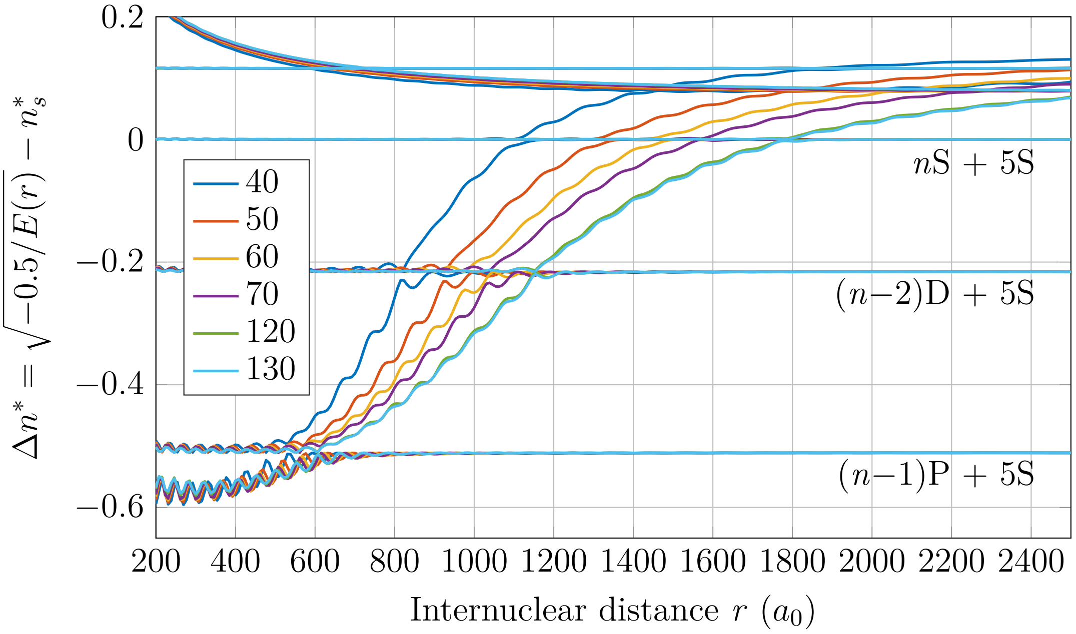

Fig. 6.13: Comparison of the potential energy curves for different $n\mathrm{S} + 5\mathrm{S}$ states without the polarization potential. The y-axis is scaled according to the energy difference of the manifolds $E_n(r) - E_{n\mathrm{S}}$ expressed in principal quantum numbers. The value 0 corresponds to the asymptote of the nS state shown in the legend, whereas ±1 corresponds to the $(n \pm 1)$S state.

6.4 Rydberg spectroscopy in a BEC

One of the pioneers in the field of optical spectroscopy was Anders Ångström, who investigated the light matter interaction. One of his major contributions was that he could demonstrate the presence of hydrogen and other elements in the sun in 1868 [84]. It was due to his effort that high resolution spectroscopy data was available for hydrogen. Therefore, Johann Balmer could identify in 1885 the system behind the absorption lines for hydrogen [85], which was soon after generalized for different species by Johannes Rydberg in 1888.

Rydberg atoms have been an interesting field of study from that time on. More recently, in the ultracold temperature regime, ultralong-range Rydberg molecules were predicted in 2000 [36] and first seen in 2009 [19]. These molecules were realized with increasing experimental control in different potential energy landscapes and with different atomic species [37, 79, 80, 86–90], where a single or few neutral atoms were bound typically at a distance of the classical orbital radius of the Rydberg electron. More deeply bound, so-called trilobite molecules [36], were realized in cesium [91] and by applying electric fields during the excitation in rubidium [38].

In the case of many atoms in the Rydberg orbit at higher densities, the bound states become unresolvable [S1, 39, 40, 92]. Still, each ground-state atom inside the Rydberg orbit interacts mainly due to elastic scattering of the Rydberg electron with the ground-state atoms as described in the beginning of chapter 6, which can be probed by performing Rydberg spectroscopy. In the following experimental work presented, the potential energy landscape of a Rydberg atom with the surrounding ground-state atoms was experimentally tested [S1]. With a peak density of 5.2×10^{14} atoms/cm^3 in the BEC, the potential energy curves can be probed down to a distance of $1000\,a_0$, according to the spatial distribution of the next neighboring particle at this density, as shown in figure 6.3.

6.4.1 Experimental parameters

The experiments carried out to probe the potential energy curves utilize a single Rydberg atom in a spin polarized Bose-Einstein condensate. Each Bose-Einstein condensate is probed 50 times and has a mean atom number of 1.4×10^6 ^{87}Rb atoms in the BEC and 0.3×10^6 in the thermal cloud, with a temperature of 300 nK. The atoms are magnetically trapped in the $\left|5\mathrm{S}_{1/2}, F=2, m_F=2\right\rangle$ state. The trapping frequencies of the QUIC trap [51] are $\omega_\mathrm{r}=2\pi\times200\,\mathrm{Hz}$ in the radial

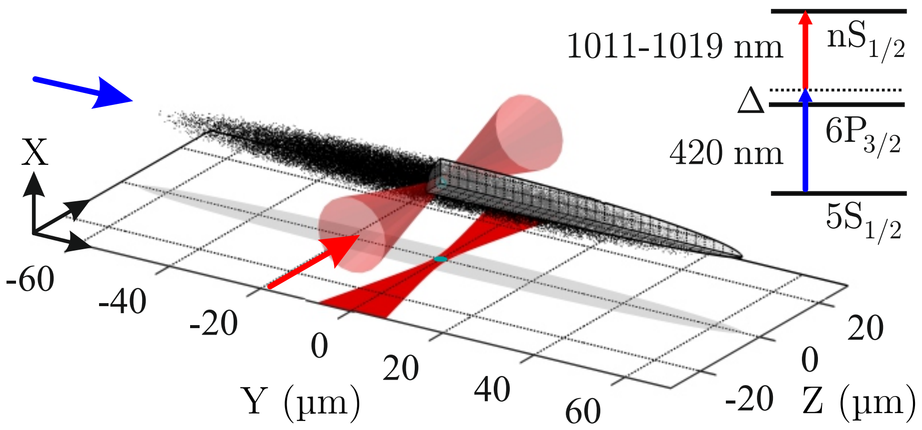

Fig. 6.14: Schematic of a localized Rydberg excitation in a BEC drawn to scale. The Rydberg atom is excited with a collimated 420 nm laser beam along the y-axis and a focused infrared laser along the z-axis with a waist of 2.1(3) µm, which defines the excitation volume inside the BEC. The quantization axis is defined by an offset magnetic field in the y direction. The extent of the classical Rydberg electron orbit for the highest Rydberg state under investigation (111S) is shown as a tiny solid sphere (cyan) at the very center of the BEC, and projected onto the bottom plane. A simplified level scheme of the two-photon excitation is illustrated in the upper right corner.

and $\omega_{\text{ax}} = 2\pi\times 15\,\text{Hz}$ in the axial direction, corresponding to Thomas-Fermi radii of 4.9 µm by 66 µm as shown in Fig. 6.14. The atom number and trap frequencies give rise to a peak density of the BEC of 5.2×10^{14} atoms/cm^3. For the Rydberg excitation a two-photon excitation scheme is applied (see also section 2.5), where the ground-state is coupled to the $\left|n\text{S}_{1/2}, m_S = 1/2\right\rangle$ state for principal quantum numbers n from 40 to 111, via the intermediate state $6\text{P}_{3/2}$. For the lower transition, the cloud is illuminated along the axial direction with pulsed 420 nm light, 2 mm in waist, to ensure a uniform Rabi frequency across the entire cloud. An intermediate state detuning of $\Delta = 80\,\text{MHz} \approx 56\,\Gamma$ is used in order to keep absorption and heating of the BEC, due to scattering of the 420 nm light, low. The upper transition to the Rydberg state is driven by an infrared laser with an n-dependent wavelength between 1011 nm and 1019 nm, focused down to a 2.1(3) µm waist. The 420 nm excitation light is circularly polarized (σ^+), and the infrared light is set to have linear polarization along the x-axis perpendicular to the magnetic field in the y-direction. Both excitation lasers are pulsed simultaneously for 2 µs, with a repetition rate of 2 kHz to create nS Rydberg atoms, which are subsequently electric field ionized 400 ns after the light fields are turned off. The field strength is set to be three times the ionization threshold field for the respective nS states in order to also detect the Rydberg atoms that undergo inelastic state-changing collisions [93, 94], which will be described in more detail in chapter 7. The ions are detected by a microchannel plate detector with a detection efficiency of 0.7. The spectral resolution is limited by the almost rectangular, 2 µs long, excitation pulse with a Fourier bandwidth of 450 kHz.

All Rydberg-BEC spectra were taken with a two-photon, single-atom Rabi frequency of 250 kHz, adjusted by the power of the infrared laser for the different principal quantum numbers, except for 40S, for which the power was set twice as high. The single-atom Rabi frequency was kept low to minimize the probability of creating multiple Rydberg excitations within the BEC. Each data point in the spectra presented below represents 500 measurements taken in 10 different clouds to improve the signal-to-noise ratio.

6.4.2 53S spectrum in a BEC

The features of a Rydberg spectrum in a BEC will be explained by means of the 53S Rydberg state. On average, there are 39 ground-state atoms at the typical peak density $\rho = 5.2 \times 10^{14}$ atoms/cm^3 of the BEC. The mean number of ground-state atoms $N = \mathcal{V}_{\mathrm{Ryd}}(n)\rho$ inside the volume of the Rydberg orbit $\mathcal{V}_{\mathrm{Ryd}}$ (see equation 6.8) for different principal quantum numbers n is shown in figure 6.15. Even for low principal quantum numbers, such as $n = 40$, the

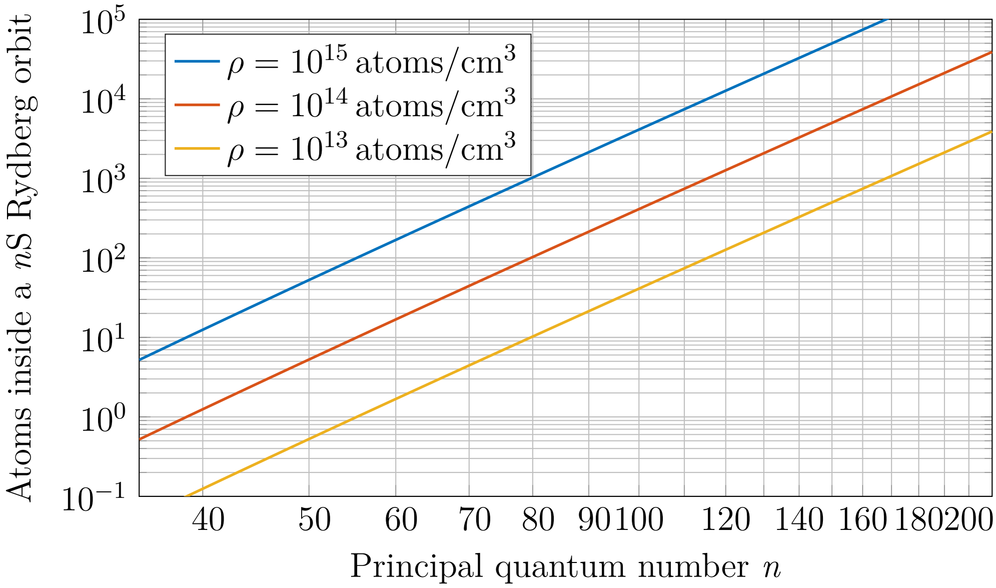

Fig. 6.15: Mean number of atoms N inside a nS Rydberg orbit.

spectrum cannot be described by single or few body interactions any more, which would lead to discrete lines in the spectrum. The high number of atoms inside the orbit lead to new features in the spectra observed. The 53S spectrum, shown in figure 6.16, can be split into different regions for which different mechanisms contribute to the observed signal:

The simple Fermi pseudopotential, as described in section 6.2, leads to a density shift of approximately $-10\,\mathrm{MHz}\,/\,(10^{14}\,\mathrm{atoms\,cm^{-3}})$ according to equation (6.9) in the case of a spin polarized rubidium sample. For the given BEC average peak density of $5.2\times10^{14}\,\mathrm{atoms/cm^3}$, the highest possible red shift from this model would result in $-52\,\mathrm{MHz}$. The signal beyond $\delta < -52\,\mathrm{MHz}$

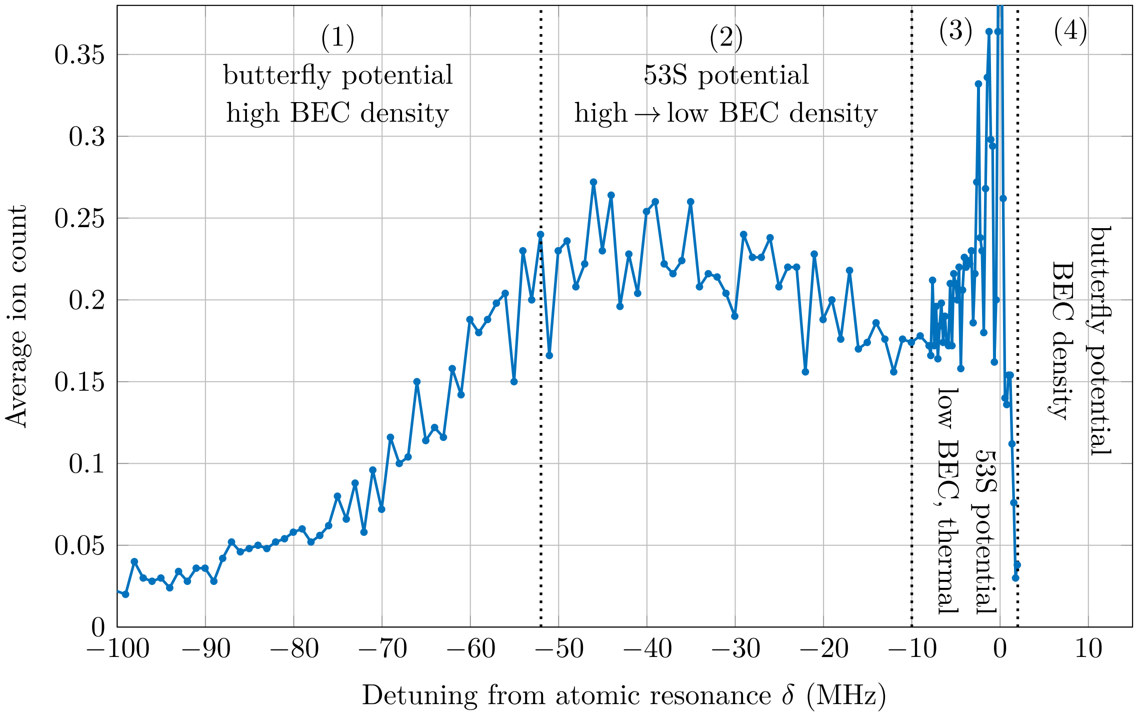

Fig. 6.16: BEC Spectrum of the 53S state. The potential can be divided into four parts from left to right: (1) The signal at high red detuning is a result of the butterfly state crossing the 53S state at a distance, which is on the order of the mean internuclear distance of the atoms in the BEC. (2) The signal from −52 MHz to −10 MHz could be described mainly by the s-wave scattering interaction at intermediate densities. (3) The signal at low red detuning is mainly coming from the lower BEC densities and the thermal portion of the atom cloud. Discrete bound states can be resolved there. (4) The measurement was stopped for blue detuning, but a finite signal is expected due to the repulsive part of the potential energy curve (figure 6.17).

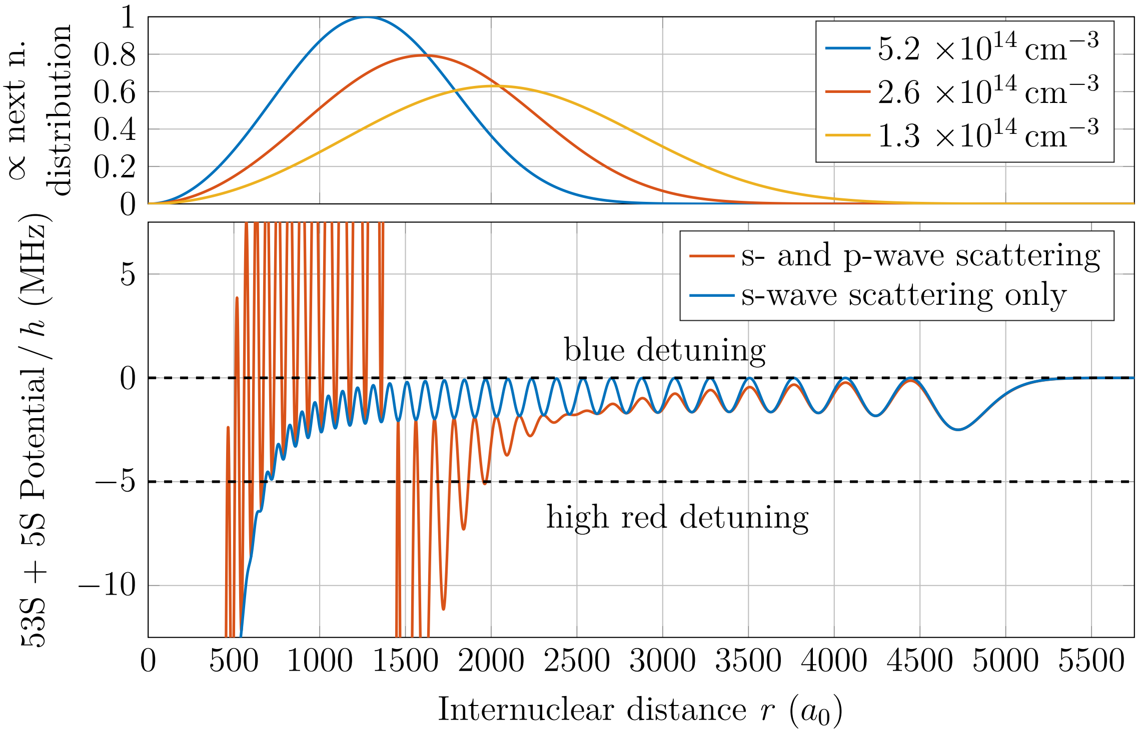

Fig. 6.17: The next neighbor distribution for different densities [69] is shown in the top graph. Especially at high densities, it is very likely to excite a particle in the region of the butterfly state crossing the S state. The bottom graph shows the comparison of s- and p-wave scattering potentials for the 53S + 5S state, both including the ion-neutral polarization potential. The butterfly state crossing the S state leads to large positive and negative deviations from the s-wave scattering potential and can therefore explain the long tails observed in the BEC spectra shown in figure 6.16.

cannot be described by the simple s-wave scattering model from Fermi any more. For example, at high red detuning $\delta = -100\,\text{MHz}$, the signal is a result of the butterfly state crossing the 53S state. In addition, the repulsive part of the butterfly potential contributes at a blue detuning $\delta > 0\,\text{MHz}$, for which s-wave scattering would predict no signal. The comparison of the spectra for s and s+p wave scattering potentials is shown in figure 6.17.

The internuclear distance of the crossing is around $1400\,a_0$ for 53S as shown in figure 6.9. With a mean interparticle distance of $1300\,a_0$ at the peak density calculated from equation (6.4) and shown in figure 6.3, the potential energy curve of this system is probed up to this distance and therefore the crossing is relevant. Due to the profound potential energy change with the p-wave contribution changing the potential energy surface by tens of MHz in this region, even a single particle within this region has a significant impact on the spectrum, which is visible as the long tail towards far red detuning.

For the signal between $-52\,\mathrm{MHz} \geq \delta \geq -10\,\mathrm{MHz}$, the s-wave scattering description mostly holds. Due to the different densities probed within the BEC and the focused laser beam, a broad signal according to the addressed density profile as plotted in figure 6.18 is observed.

The detuning range between $-10\,\mathrm{MHz} \geq \delta \geq 0\,\mathrm{MHz}$ shows signal from the atoms of the BEC and thermal cloud at lower densities. Discrete lines of the ground-state ultralong-range molecules [19] can be resolved for a 53S state, which have a binding energy of $N \times 1.4\,\mathrm{MHz}$ with N atoms in the outermost potential well of the Rydberg orbit.

For blue detuning $\delta > 0$, a non-zero signal is expected, because of the repulsive butterfly potential, which is again probed with the highest BEC density regions, for which the mean internuclear distances are smaller than the state crossing.

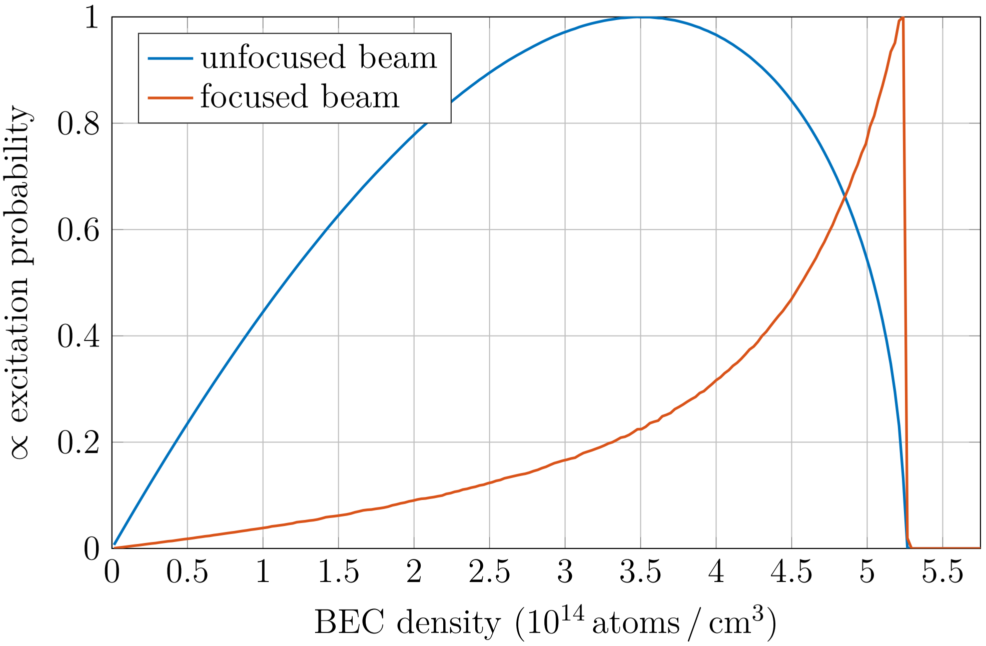

Fig. 6.18: Excitation probability of a Rydberg atom in the Bose-Einstein condensate according to equation (6.22) for an unfocused beam (blue) and a focused laser beam (red) of 2.1 µm waist, both normalized to 1. The excitation probability for the focused beam is peaked at the peak density of the center BEC region.

6.4.3 Infinite mass perturber model

As long as only a few neutral atoms are within a Rydberg orbit, the spectral lines can be obtained by calculating the bound states with the potential energy curve. But the line strength and the spectral shape for a high number of atoms within the Rydberg orbit cannot be estimated with this approach. Recently a new method, simulating the time dependent Schrödinger equation for a Rydberg impurity in Fock-space, has been developed by Richard Schmidt et al. [92] to address this question. A simpler, but still sufficient, approach is presented here, treating the atoms as point-like probes of the potential energy curve. In that sense they can be called infinite mass particles, neglecting the wave packet character of the ground-state atoms. Within this model all atoms are point particles with a random position $\mathbf{r}_j$, according to the measured bimodal distribution in the experiment. The BEC is assumed to have a perfect parabolic shape as shown in Fig. 6.14, as a consequence of applying the Thomas-Fermi approximation, whereas the thermal cloud has a Gaussian profile according to the measured temperature and trap frequencies. All atoms are treated as spatially uncorrelated assuming $\mathrm{T} = 0$.

To calculate a spectrum from this model the resonance shift, δ_i, assuming the atom labeled with i would be the Rydberg atom, is calculated via

$$\delta_i = \sum_{j \neq i} V(|\mathbf{r}_j - \mathbf{R}_i|), \tag{6.20}$$

evaluating the potential energy curve $V(r)$, surrounding the Rydberg atom $\mathbf{R}_i$ as shown in figure 6.19. This approach is valid as long as the neutral particles do not have a backaction on the electron wave function of the Rydberg atom. The spectrum $S(\delta)$,

$$S(\delta) = a \sum_i \frac{1}{\pi} \frac{\left(\frac{1}{2}\Gamma\right)^2}{(\delta - \delta_i)^2 + \left(\frac{1}{2}\Gamma\right)^2} \times I_i, \tag{6.21}$$

is finally calculated by summing over all Lorentzian contributions of each atom, taking into account its shift δ_i, the excitation bandwidth Γ, and the spatially varying excitation laser intensity $I_i = I(\mathbf{R}_i)$, relating to the incoherent excitation rate in the system. Each simulated spectrum is averaged over several atom configurations and normalized with a factor a according to $\int S(\delta) d\delta$ with respect to the experimental data. All parameters for the simulation come from measured or calculated properties and, as such, the simulation has no free parameters.

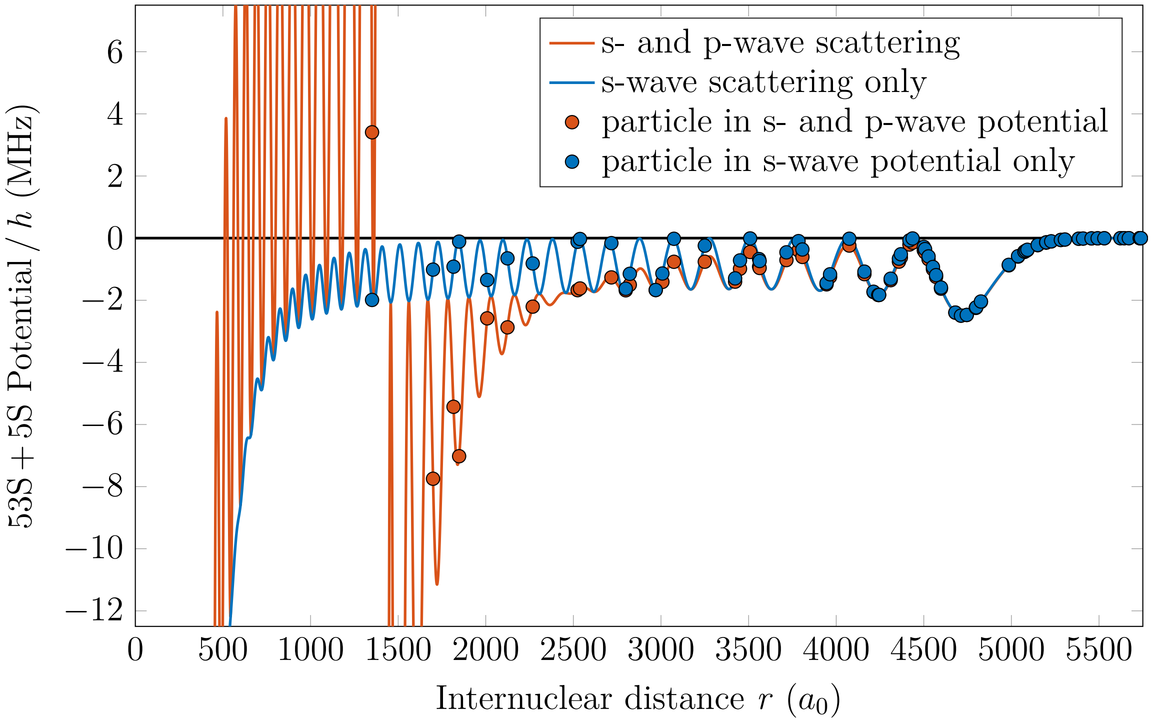

Fig. 6.19: Potential energy curves for a $53\mathrm{S}+5\mathrm{S}$ state, plotted for s- and p-wave scattering and s-wave scattering only with both including the polarization potential. Discrete particles are randomly placed in the potential according to the peak density ($\rho = 5.2 \times 10^{14}\,\mathrm{cm}^{-3}$) of the BEC, which has a mean interparticle distance of $1300\,a_0$. The available energy range is increased for s- and p-wave scattering due to the butterfly state crossing. For this particular configuration with 48 particles within the classical Rydberg orbit, the total density shift would result in $-78.7\,\mathrm{MHz}$ for s- and p-wave scattering (red) and $-51.2\,\mathrm{MHz}$ for s-wave scattering only (blue).

The experimentally observed spectrum of a 53S state is shown in figure 6.20, along with spectra from the model described above, with p-wave scattering included and excluded to show the significance. The model including s- and p-wave scattering and therefore the crossing of the butterfly potential, can reproduce the long tail towards red detuning as observed in the experiment. The overall line shape is described very well by this simple model. Discrete bound states, visible as sharp peaks in the detuning range $-8\,\mathrm{MHz} < \delta < 0\,\mathrm{MHz}$, cannot be expected from the semi-classical treatment. The discrepancy of the overall signal at low red detuning $-20\,\mathrm{MHz} < \delta < 0\,\mathrm{MHz}$ will be described later in section 6.4.4, where spectra for different quantum numbers are discussed. By removing the p-wave scattering interaction, the simulated spectrum almost follows the density distribution addressed by the excitation lasers (figure 6.18)

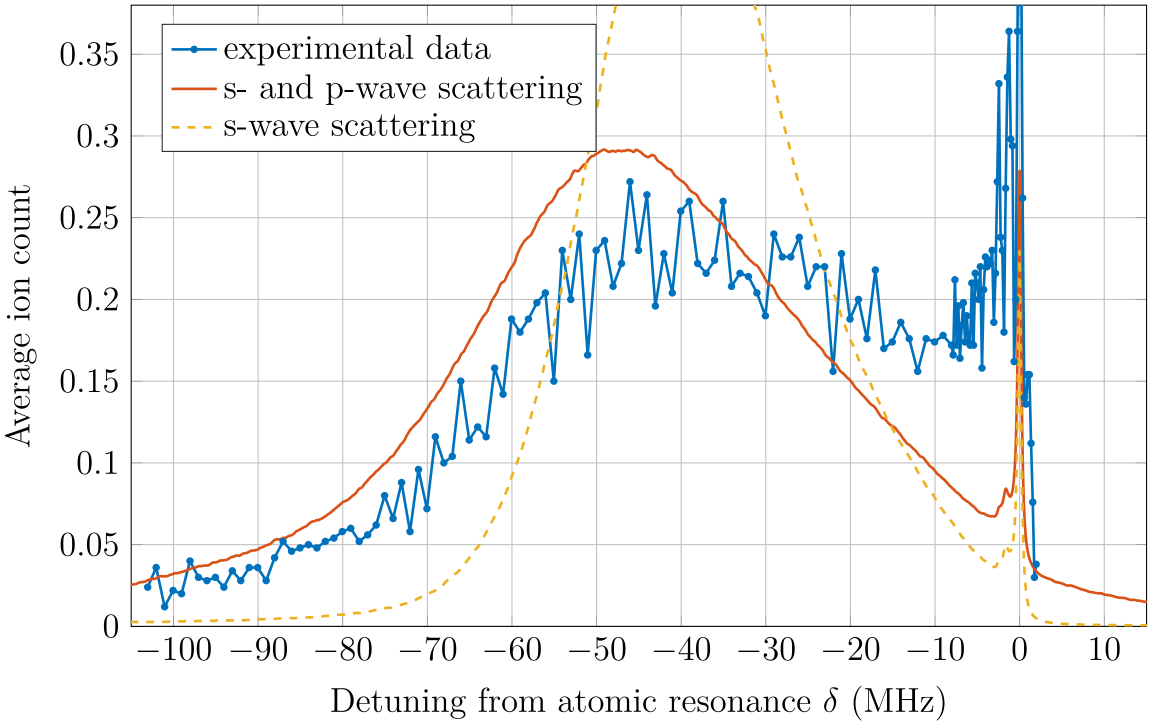

Fig. 6.20: Comparison of a measured 53S spectrum with a simulated spectrum from the infinite mass perturber model. The slope to high red detuning can only be described by taking into account p-wave scattering, and therefore including the butterfly potential. The crossing of the butterfly state causes deep positive and negative scattering potentials, especially for the closest ground-state, which broadens the spectrum. The simulated s-wave scattering potential (dashed yellow) almost exactly follows the excitation probability of the density distribution addressed, as shown in figure 6.18. The molecular lines in the experimental data at low red detuning cannot be reproduced by the semi-classical model.

according to equation (6.9). In the system, the focused laser beam highly favors excitations inside the high density region of the BEC. The probability $p(\rho_0)$ to excite an atom at a certain density ρ_0 depends on the laser intensity $I(\mathbf{r})$ and the density at this position itself $\rho(\mathbf{r})$, spatially integrated and the densities matched with the Kronecker delta δ:

$$p(\rho_0) = \int I(\mathbf{r})\rho(\mathbf{r})\delta(\rho(\mathbf{r}) - \rho_0)d\mathbf{r}. \tag{6.22}$$

Due to the focal spot of the excitation laser in the center of the BEC, the peak density region with 5.2×10^{14} atoms/cm^3 is most likely excited, as shown in figure 6.18. This is especially visible for the case of s-wave scattering only, because the p-wave broadening mechanism is not included.

To conclude, the simulation without p-wave scattering cannot describe the overall shape of the spectrum experimentally observed but is improved significantly by including p-wave scattering. The comparison of the spectra simulated with the spectrum measured gives evidence for the butterfly state crossing the target excited Rydberg state. The overall shape of the spectrum can be described by the infinite mass perturber model presented. Former approaches [70, 77, 81, 95, 96] could only predict an overall line shift and broadening as a function of the principal quantum number. With the model introduced here, the full spectral line shape is accessible and was compared to the high resolution spectroscopy performed.

6.4.4 BEC spectra at different principal quantum numbers

Over the measured range of the effective principal quantum number from $n=40$ to $n=111$, the radial size of the Rydberg atom, $r \propto n^2$, changes profoundly. As a result, the volume of a nS Rydberg orbit scales $\mathcal{V}_{n\mathrm{S}} \propto n^6$ as shown in equation (6.8). The mean number of atoms inside the Rydberg orbit, plotted in figure 6.15, can be calculated from the volume of the Rydberg orbit and the density of the background gas. For example, for a 53S state there are 39 ground-state atoms, on average, inside the Rydberg orbit at the peak density. For a 111S state, there are 4300 atoms, on average, inside the Rydberg orbit. Despite the large change of atoms inside the orbit, the measured spectra shown in figure 6.21 have a similar overall line shift, which is a result of the s-wave scattering potential scaling as n^{-6}, compensating the higher number of atoms inside the orbit proportional to n^6. The position of the butterfly state crossing the nS state is also changing with the principal quantum number, but on a minor scale, as explained in section 6.3.1 and shown in figure 6.9. The experimentally observed n-dependence of the spectra is a result of the size of the Rydberg orbit and the p-wave scattering interaction as explained in the following.

The broadening of the spectra is very different for the different principal quantum numbers investigated. For lower n, the number of atoms N inside the Rydberg orbit drops according to $N \propto n^6$. This leads to a higher relative standard deviation $\sqrt{N}/N$ of the number of atom within the orbit, which broadens the signal for lower n. In addition, the potential depth of the butterfly state scales with n^{-3} and hence, the energy range available per particle is extended. The spectrum at low n shows a very broad signal compared to high n, where the overall signal is almost proportional to the addressed density

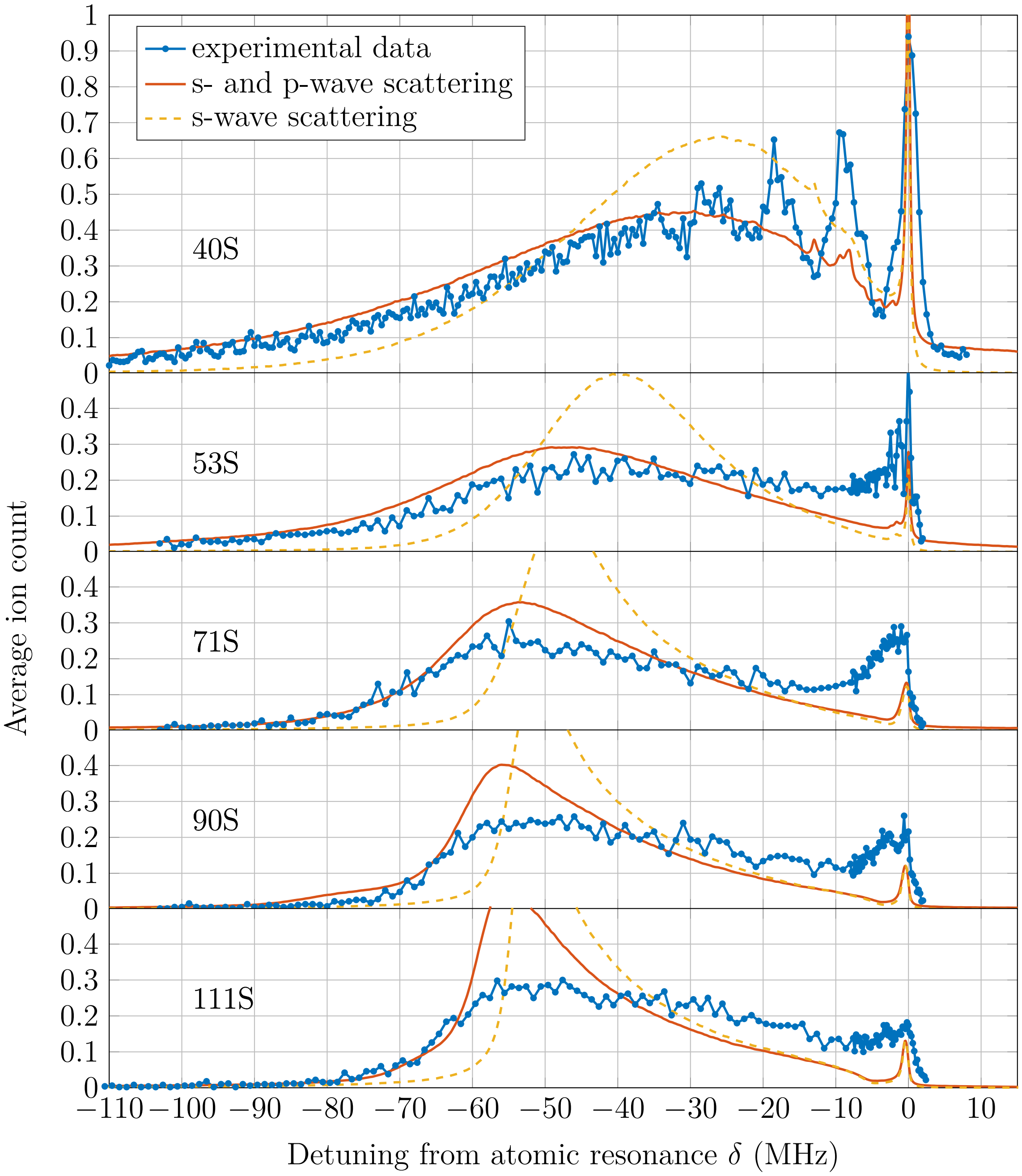

Fig. 6.21: BEC spectra taken at different principal quantum numbers, n, with the associated simulated spectra. Only by including the p-wave scattering, the broadening to far red detuning agrees with the experimental data. The signal at blue detuning measured only for 40S can be reproduced by the theory when p-wave scattering is taken into account. The extent to which the red detuned tail extends is lower for higher n because the number of atoms within the Rydberg orbit increases whereas the energy per particle decreases.

distribution shown in figure 6.18. If p-wave scattering is not taken into account and therefore the butterfly state does not exist, all simulated spectra are too narrow and especially the wings to the far red detuning vanish. In addition, the observed signal at blue detuning for 40S can only be described by the simulation which includes p-wave scattering. Hence, the measured spectra can only be explained by including p-wave scattering, which means that the butterfly state crossing is probed with the particles surrounding the Rydberg atom.

For 40S and 53S at low red detuning, discrete bound states are resolved, which is mainly signal out of the thermal cloud and the lower densities of the Bose-Einstein condensate. These discrete bound states cannot be described with the presented semi-classical model and therefore are not visible in the simulated spectra. Towards higher n, the broadening due to the butterfly state crossing becomes less important, so that the simulated signal more and more follows the excited density distribution. The measured spectra show instead a flatter signal distribution. The reason for this is still an open question. It could be that at higher n the model description breaks down, due to the enormous amount of atoms inside the Rydberg orbit, of which most of them only contribute weakly to the overall density shift. Also the treatment of the particles as point-like is a simplification of the system. In addition, the model does not take into account any spatial correlations, which are present in the cloud at finite temperature [97]. Furthermore, the backaction of a ground-state atom on the Rydberg electron wave function is not taken into account, which could be important, especially if one of the ground-state atoms is close to the state crossing.

Nevertheless, the overall agreement from the spectroscopic data, in particular the comparison of the experimental data and the modeled spectra with the p-wave scattering interaction turned on and off, shows the importance of p-wave scattering and therefore the butterfly state crossing the target nS state.

6.4.5 Laser detuning as a density probe

With s-wave scattering only, the particles inside the Rydberg atom contribute almost equally to the total density shift, as shown in section 6.2. Therefore, the detuning of the excitation laser could be used to bring a target density into resonance. Together with the inhomogeneous density profile of a cold atom cloud trapped in a harmonic trap potential, the spatial region in which a single Rydberg atom can be excited is selected by the excitation laser detuning and bandwidth [S2]. But due to the more realistic description of the scattering events, including p-wave scattering, this density selection becomes n-dependent, which is analyzed here within the presented infinite mass perturber model of section 6.4.3, assuming an excitation bandwidth of 100 kHz.

The theoretical sensitivity of laser detuning as a density probe is analyzed from simulated spectra of Rydberg atoms at different constant densities which are plotted in figure 6.22. For each density and principal quantum number, at least 10^5 spatial configurations are examined, probing the potential energy curve according to equation (6.20). For low quantum numbers (e.g. $n = 53$), the spectrum of a Rydberg atom within the semi-classical model is broadened due to the low number of particles inside the Rydberg volume and therefore the butterfly potential has an increased relevance. The shape resonance potential becomes less important for higher n and therefore the spectra are more narrow. Since the different spectra for different densities are well separated for high n (e.g. $n = 111$), it is possible to select a certain density region with the laser detuning. The full width at half maximum of these lines simulated, drops from 19 MHz at $n = 40$ to only 1.2 MHz at $n = 120$.

The density sensitivity was experimentally confirmed by scanning the focused excitation laser trough the short axis of the BEC, as shown in figure 6.23. For the highest laser detuning, $\delta = -55\,\mathrm{MHz}$, the maximum of the measured signal is in the very center of the BEC at $r = 0$. This changes when the excitation lasers are set to an intermediate detuning of $-24\,\mathrm{MHz}$ or $-12\,\mathrm{MHz}$. As a consequence, a small dip is visible in the signal at the very center of the BEC, because the atoms there are not resonant any more, even though the total atom number inside the excitation beam is higher compared to the beam moved to the side with $|r| > 0$, which agrees with the simulated signal.

Even though there is experimental evidence for the density sensitivity from the scan presented, there is one uncertainty which has to be treated carefully. From the comparison of the modeled and measured spectra as shown in section 6.4.4, the deviation between both increases for higher principal quantum numbers. This leads to the question whether the simulated sensitivity (figure 6.22) is accurate, especially for high principal quantum numbers. How strong this discrepancy affects the sensitivity is a topic for further investigations.

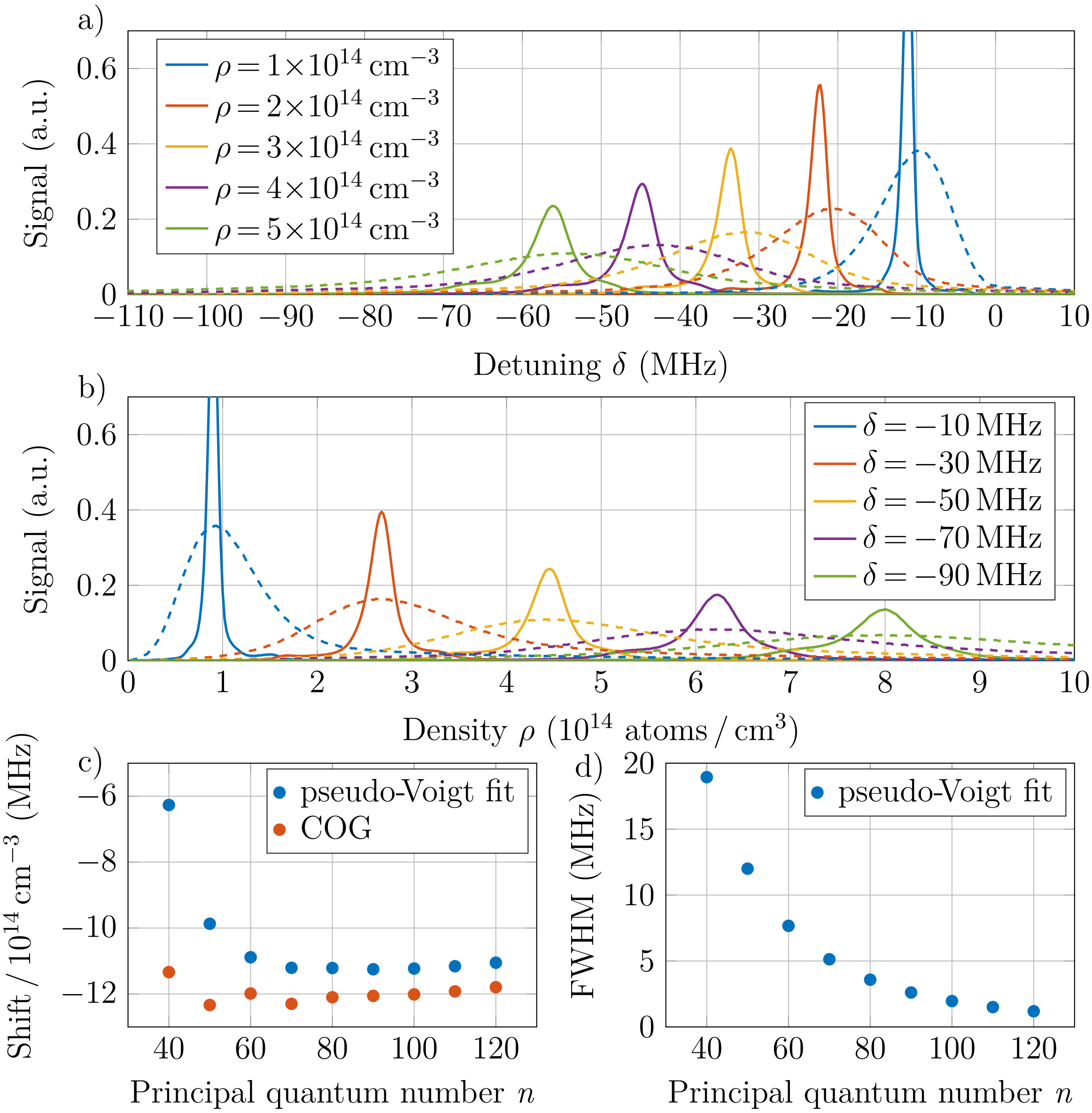

Fig. 6.22: (a) Simulated Rydberg spectra for constant BEC densities of a 53S (dashed line) and a 111S state (solid line) with the 53S signal enhanced by a factor of 2.5 for better visibility. The higher principal quantum number shows a narrow line compared to the broad signal for lower n. (b) The addressed density distribution for a specific laser detuning as the inverse of the parameters of (a) shows especially for high n that a target density can be addressed by the laser detuning. (c) Simulated mean shift for a density of 10^{14} atoms/cm^3, taking into account a detuning range of $-300\,\mathrm{MHz} \geq \delta \geq 100\,\mathrm{MHz}$. The blue dots show the center frequency of a pseudo-Voigt [98] fit of the simulated spectra, whereas the red dots show the center of gravity (COG) defined as $\int S(\delta) \times \delta \, d\delta / \int \delta \, d\delta$. (d) Full width at half maximum extracted out of the fitted pseudo-Voigt profile from (c).

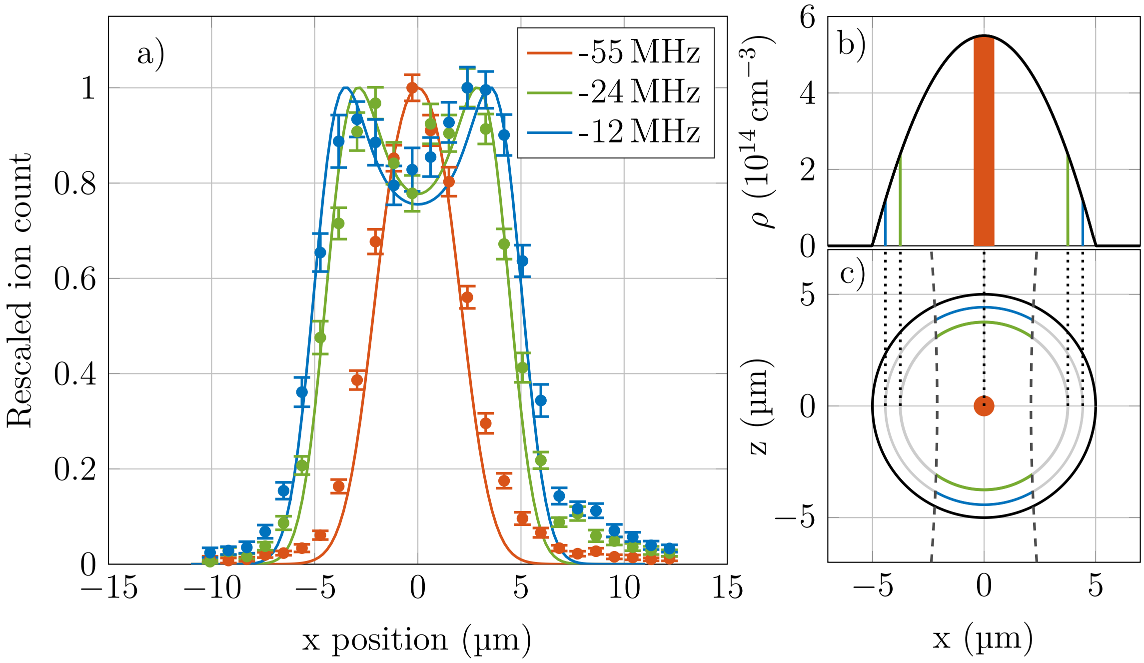

Fig. 6.23: (a) Ion signal (points with error bars) from scanning a focused excitation beam through the BEC with the expected signal from the simulation (solid lines). The highest detuning (red), with which the peak density is addressed, shows a maximum in the center, whereas the signal from lower detuning has its maximum outside the center region. (b) Schematic of the Thomas-Fermi profile with the lines indicating the probed density shells for the respective detuning. (c) Depiction of a cut through the BEC in the xz-plane. The colored solid part of the circle shows the overlap between the Gaussian beam (dashed) and the probed area of the density shell.

7

Inelastic collisions of a Rydberg atom

In the previous chapter, the influence of the elastic collisions of the Rydberg electron with the surrounding ground-state atoms was examined. In the time evolution of the Rydberg atom in the ultracold gas inelastic collisions become important. These collisions limit the lifetime of a Rydberg atom at high densities.

The reduced collisional lifetime of a Rydberg atom is of high interest, because Rydberg atoms are being utilized in increasingly denser environments for quantum optics [99, 100], quantum information schemes [28], quantum simulation [27], for studying electron-phonon interactions in a BEC [S4, 39, 101], polaron formation in dense quantum gases [102, 103], and production of long-range Rydberg molecules [19, 36, 76, 79, 80, 86]. Limitations of the interaction time of a Rydberg atom within a dense, cold quantum gas, have been observed [39], but the origin of the reduced Rydberg lifetime could not be explained.

At the outset of this work, the two most likely candidates limiting the lifetime of a Rydberg atom in the dense gas are either state changing collisions of the Rydberg atom with ground-state atoms, or the creation of Rb_2^+ molecules [104–109]. The role of the Rydberg electron in these two decay mechanisms, which will be explained in this chapter, was not well understood before. With regards to the lifetime it was unclear whether inelastic ion-neutral collisions dominate as discussed for Rydberg systems [106, 110] and observed in cold ion-hybrid traps [111], or inelastic electron-neutral collisions dominate as proposed in [106,

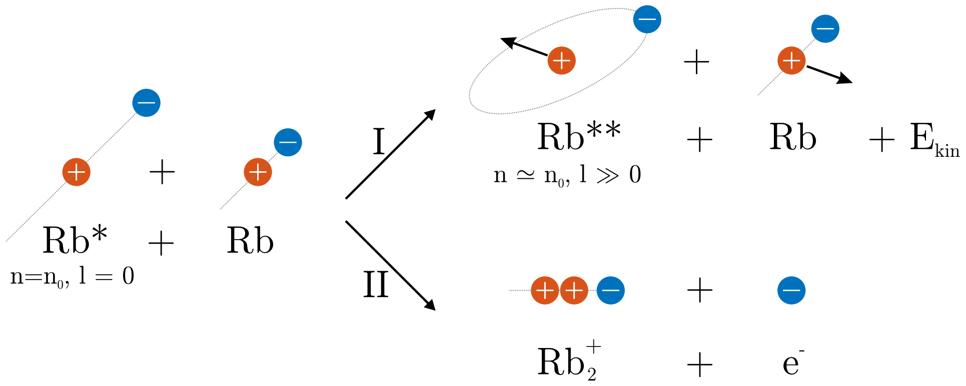

Fig. 7.1: Observed reaction products from an inelastic collision of a Rydberg atom Rb* with a ground-state atom Rb within a Bose-Einstein condensate. In the first, and predominant, reaction channel (I), the Rydberg atom changes its angular momentum without a significant change in principal quantum number. The second channel (II) forms deeply bound Rb_2^+ ions.

112] and shown experimentally in the late 1970's and early 1980's [113–115].

In the following sections, the two experimentally observed reaction channels (figure 7.1) are presented and discussed [S3]. Both experiments are performed in a Bose-Einstein condensate as described for the elastic collisions in section 6.4.1. The main difference between the experiments for elastic and inelastic collision is that the atoms are not ionized immediately after the excitation for studying the inelastic collisions. It is found that the observed ion signal depends on the evolution time of the system. The state change of the Rydberg atom is on a shorter timescale than the natural lifetime and, therefore, the interaction with the surrounding ground-state atoms must limit the lifetime of the Rydberg atom.

The collision takes place within a few microseconds. In the predominant reaction channel for the investigated parameter regime, the Rydberg atom changes its angular momentum without a significant change in principal quantum number (section 7.1). The released potential energy is shared between the two collision partners. In the second reaction channel, deeply bound Rb_2^+ ions are formed during the collision (section 7.2). The inelastic collision time for both reaction products is analyzed and compared in section 7.3. The surprising result from the measured inelastic collisional lifetimes of nS Rydberg atoms is that above a threshold principal quantum number they do not undergo a state-changing collision for tens of microseconds, which is significantly longer than below this threshold principal quantum number.

7.1 l-changing collisions

For the first time, the inelastic collision of the Rydberg electron was investigated with a single Rydberg excitation in a cold atom gas. The states of the reaction products were directly measured, including the energy released during the collision.

The predominant reaction channel for principal quantum numbers $n > 40$ is a collision of the Rydberg atom with a ground-state atom, changing the angular momentum of the Rydberg electron. The effective principal quantum number of the final state stays within $0 > \Delta n^* > -1$ below the initial state.

7.1.1 Kinetic energy release

During an inelastic collision of the Rydberg atom with a ground-state atom, energy is released from the Rydberg electron which both colliding atoms share. The energy released varies between 200 µeV and 26 µeV for the principal quantum numbers $n = 53$ and $n = 100$ and is equal to the energy difference $\Delta E \propto n^{-3}$ of the initial state to the closest hydrogenic manifold below. Therefore, the scattering partners leave the condensate with velocities of $15\,\mathrm{m\,s^{-1}}$ and $5.4\,\mathrm{m\,s^{-1}}$ respectively.

The released kinetic energy can be analyzed by evaluating the ion arrival time of the initially excited Rydberg atoms on the detector. For this measurement, Rydberg atoms are ionized after a long delay time ($\geq 50\,\mathrm{\mu s}$) compared to the collisional lifetime. The ionization electric field of $180\,\mathrm{V\,cm^{-1}}$ is chosen well above the ionization threshold of all investigated principal quantum numbers so that all Rydberg atoms are ionized, including the Rydberg atoms which underwent an inelastic collision. The observed time spread of the ions for a delay time of 50 µs (figure 7.2) is small for high principal quantum numbers (e.g. 133S: $\Delta t = \pm 20\,\mathrm{ns}$) in comparison to low quantum numbers, where a larger spread is observed (e.g. 53S: $\Delta t > \pm 100\,\mathrm{ns}$). A detailed explanation of how the released energy can be extracted out of the measured time spread of the ions is shown in the master thesis of Udo Hermann [47]. The method is summarized in the following:

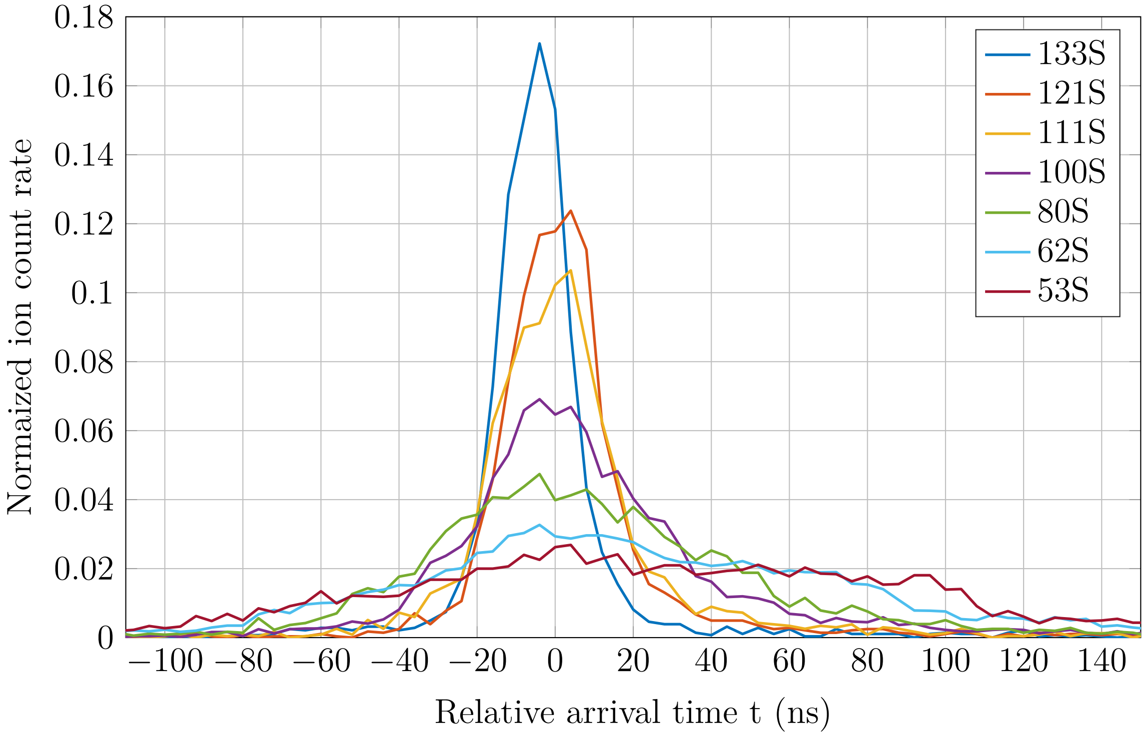

Fig. 7.2: Ion arrival time spread for Rydberg atoms ionized 50 µs after the excitations lasers are turned off. For the highest principal quantum numbers $n = 133$, the energy release due to the l-changing collision is low and therefore most of the ions arrive within $|t| < 20\,\mathrm{ns}$. For lower n, this spread exceeds ±100 ns, clearly showing a difference in the kinetic energy gained during the collision.

It is assumed that all Rydberg atoms are excited at the center of the Bose-Einstein condensate and do not move until they collide with a ground-state atom. This assumption is well justified due to the focused excitation beam creating the Rydberg atoms in the center of the Bose-Einstein condensate. The initial energy after the excitation coming from the photon recoil $k_\mathrm{B} \times 700\,\mathrm{nK}$ with the Boltzmann constant k_B is very low and can be neglected. This is also true for the kinetic energy of the background gas with a temperature of 300 nK only. After the collision, the collision partners travel in arbitrary, opposing directions and can be measured after a time of flight t. During that time, the particles fly a distance $r = \sqrt{\frac{2E}{m}}t$, with the kinetic energy E and a mass m. They leave the atom cloud fast, without any further collision. Since there is no preferred direction for the collision and the collision time itself is small compared to the time of flight, an atom, which underwent the l-changing collision, can be

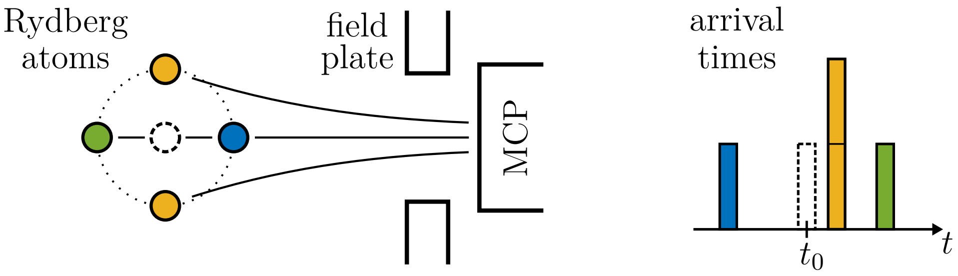

Fig. 7.3: 2D trajectories of the ionized Rydberg atoms which underwent an l-changing collision (left graph). The Rydberg atom gains kinetic energy during an l-changing collision and flies away from the center. At the moment of the ionization, the atom is positioned on a circle around the center and the distance depends only on the released energy and the time of flight. This leads to an asymmetric arrival time distribution as shown in the right graph.

found at the moment of the ionization on a sphere with radius r with respect to the excitation center as drawn in figure 7.3. The expected ion arrival time based on the position $\mathbf{r}$ is simulated[1], taking into account the full geometry of the science chamber and the electric fields. With this information, the relation can be inverted to fit and reconstruct the spatial distribution of the Rydberg atoms out of the arrival time spread, which is directly related to the kinetic energy of the particles. The total released energy

$$\Delta E = 2E_{\text{kin}} = m_{\text{Rb}} \left(\frac{r}{t_{\text{delay}} - t_{\text{coll}}} \right)^2 , \tag{7.1}$$

calculated from the delay time t_{delay} between the excitation and the ionization and the collision time t_{coll} later analyzed in section 7.3, is twice as high as the observed kinetic energy E_{kin} of the Rydberg atom because the energy is shared between both collision partners. The most likely energy release for the range of principal quantum number from $53 \geq n \geq 133$ of an initially excited S state is shown in figure 7.4. For principal quantum numbers smaller than 100, the energy release corresponds to the energy difference of the S state and the lower lying hydrogenic manifold $n-4, l \geq 3$. For higher principal quantum numbers, the time spread is not large enough to extract the most likely energy released, but the full width at half maximum of the energy distribution still suggests that the effective principal quantum number does not change more than one.

---

[1] All ion trajectories simulations were performed with SIMION from Scientific Instrument Services, Inc. (SIS)

The analysis of the released kinetic energy suggests that the state change does not exceed one effective principal quantum number towards the lower lying states. But the accurate final angular momentum of the Rydberg atom cannot be extracted out of the broad energy distribution measured. Therefore, the angular momentum change is probed with the state selective field ionization method as described in the following.

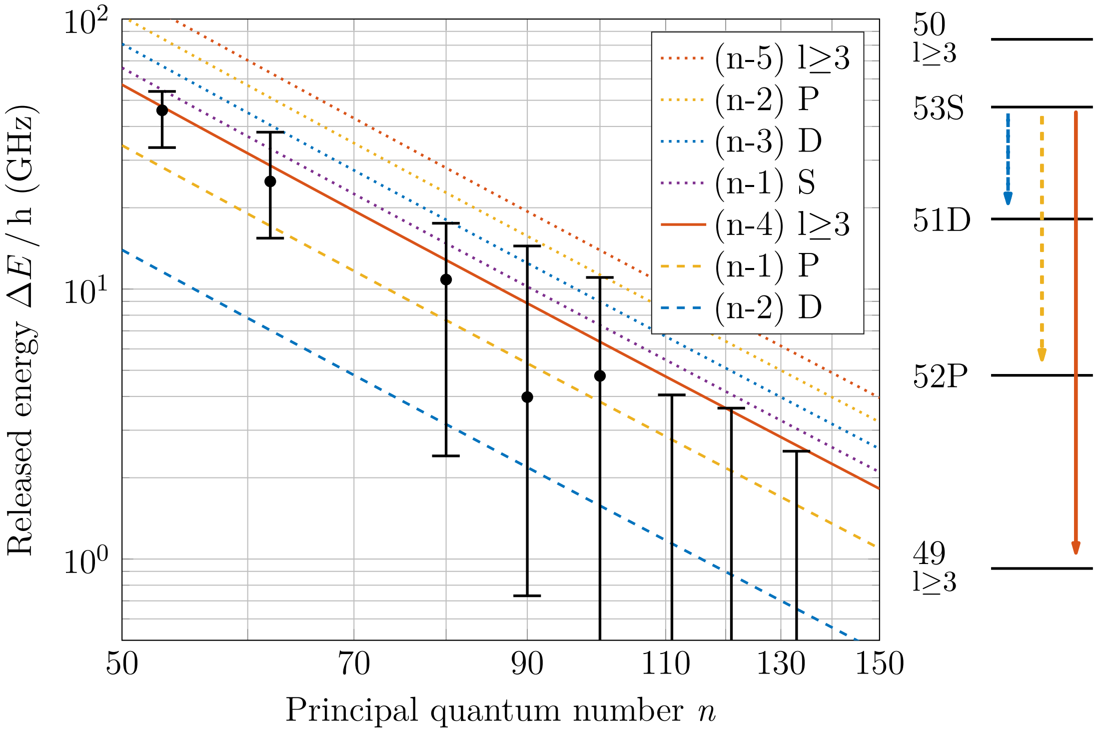

Fig. 7.4: Measured released kinetic energy due to an l-changing collision (left) together with the energy difference to the next neighboring states of a 53S Rydberg atom (right). The data points (dots) show the most likely energy release, whereas the error bars indicate the full width at half maximum of the distribution. For principal quantum numbers $n \geq 110$, the released energy and therefore the spread of the ions is low, so that no well-defined maximum inside the energy distribution can be extracted. The released energy plotted is twice the measured energy from the Rydberg atom because the total released energy is shared between the two collision partners equally.

7.1.2 Ionization threshold change

The ionization threshold of a Rydberg atom depends, among other things, upon its angular momentum [41]. Therefore, state selective field ionization is a commonly employed technique to study the state of a Rydberg atom [41, 93, 116–123]. For rubidium, the S state ionizes at a lower electric field compared to high angular momentum states. The required electric field is different because, for a given electric field slope, the state can ionize diabatically or adiabatically [41, 116]. It was experimentally tested that the applied ramp going to 6 V cm^{-1} within 3 µs shows the same signal for S and D states and therefore a change

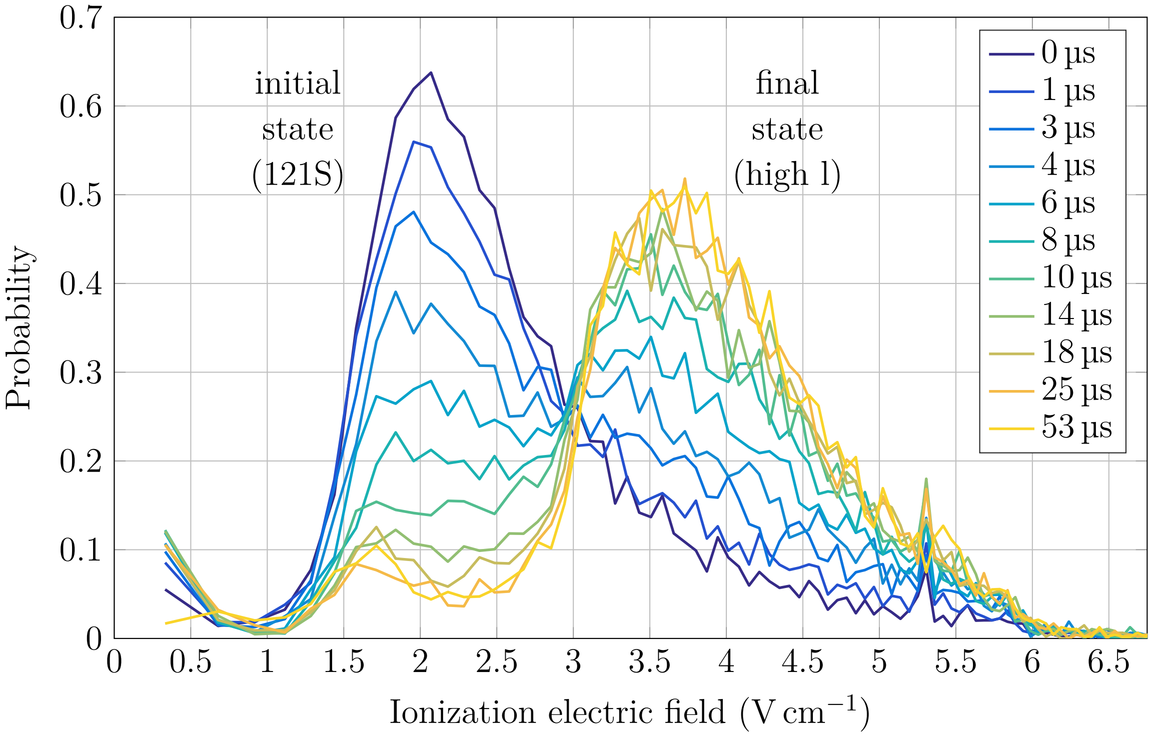

Fig. 7.5: State selective field ionization measurements of a 121S state for different delay times between the excitation and the ionization as given in the legend. If the ionization ramp, going from 0 to 6 V cm^{-1} within 3 µs, is immediately applied after a 500 ns excitation pulse, most of the signal is coming from an ionization field between 1.5 and 3 V cm^{-1}. After waiting long enough, the Rydberg atom undergoes an l-changing collision with a ground-state atom. As a consequence, the Rydberg atom in the new, high angular momentum, state requires a higher electric field to be ionized [41, 116]. The small spike at an electric field of 5.3 V cm^{-1} can be attributed to a very small fraction of deeply bound Rb$_2^+$ ions arriving at the detector.

in the ionization field means that the angular momentum must have changed to $l \geq 3$. With the ionization field ramp applied, the ion arrival time changes according to the time it takes to reach the ionization threshold. In addition, the ions accelerate faster if they are ionized later because of the higher electric field at the position of the atoms. The arrival time can be converted into the electric field at which the ion was ionized with an ion trajectory simulation. The spread in time from the kinetic energy gained, which was discussed in the previous section, is negligible compared to the spread due to the field ramp applied. Hence, the arrival time of the ions can be converted into the electric field at which the Rydberg atoms were ionized. The experimental data for a 121S Rydberg state with a field ramp going to $6\,\mathrm{V\,cm^{-1}}$ within $3\,\mathrm{\mu s}$ is shown in figure 7.5. The excitation detuning of $-12\,\mathrm{MHz}$ was chosen to address an intermediate density regime in the Bose-Einstein condensate for which many experiments can be performed in each Bose-Einstein condensate. For an ionization delay of $t = 0\,\mathrm{\mu s}$, most of the atoms ionize between 1.5 and $3\,\mathrm{V\,cm^{-1}}$. After the collision has happened, the required ionization is spread out between 3 and $6\,\mathrm{V\,cm^{-1}}$. This is in agreement with the theory of an l-changing collision, which predicts a 2x to 4x higher ionization threshold than the initial S state [41, 116]. The ionization field change was also measured with the state selective ionization method for $n = 133$ and 149 and the results agree very well with the theory of the discussed l-changing collision.

There are two other features to note in the state selective ionization threshold measurement shown in figure 7.5. The signal observed at ionization fields below $1\,\mathrm{V\,cm^{-1}}$ stems from Rb^+ ions already existing before the field ionization ramp is applied. The peak visible at $5.3\,\mathrm{V\,cm^{-1}}$ is a small number of Rb_2^+ molecules created.

The time resolved electric field resolution of the state selective ionization method is accurate as long as the rise time of the applied field ramp is slow compared to the flight time of the ions, which limits the ramp time to about $3\,\mathrm{\mu s}$ in the setup. But in addition, the rise time needs to be faster than the state changing collision time. Hence, this method is not suitable any more for low principal quantum numbers below $n = 100$ at which the collision time can be even below $1\,\mathrm{\mu s}$, as later shown in section 7.3. To investigate these states, the ionization electric field is applied with a single pulse which has a rise time of $200\,\mathrm{ns}$ only. Due to this fast turn on time, all states, except for the initial S state, ionize diabatically. Hence, we can only distinguish between S and higher angular momentum states with this method. An ionization threshold measurement for a 90S state is shown in figure 7.6. The ionization threshold changes by a factor of 2x to 4x according to the theory for an l-changing collision [41]. All measurements for principal quantum numbers between $50 \geq n \geq 150$ show a similar behavior when the electric field and the collision time is rescaled.

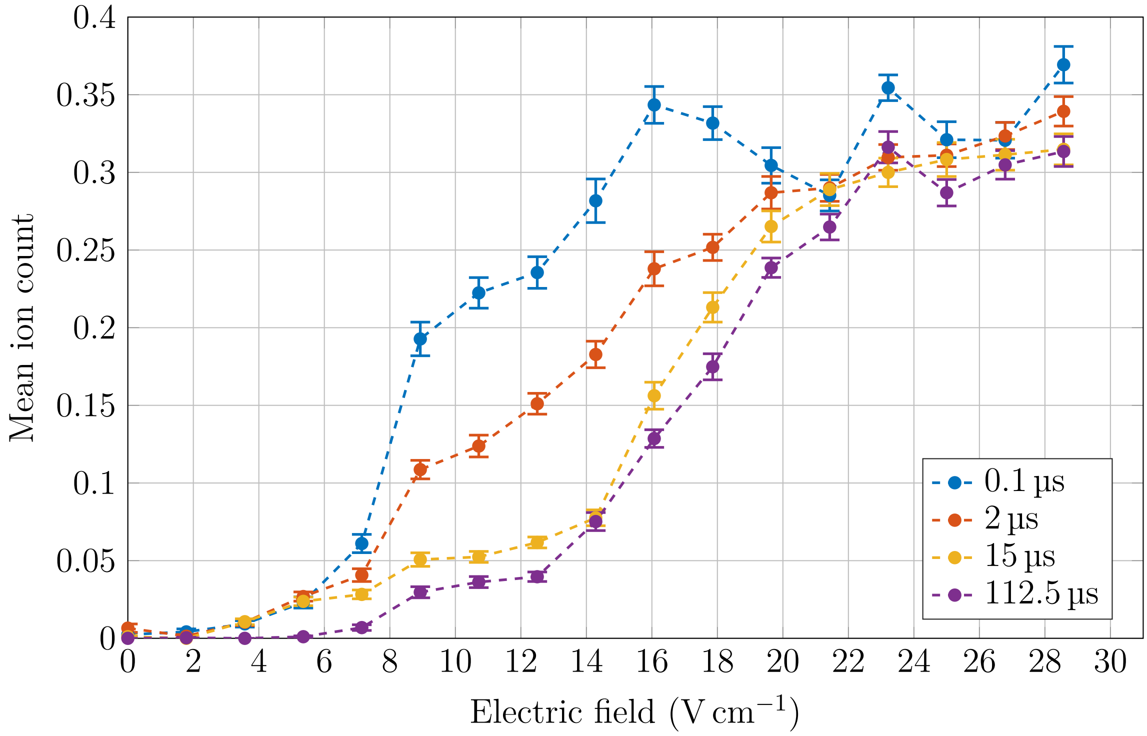

Fig. 7.6: Ionization threshold measurement of a 90S state for different delay times between the 1 µs excitation pulse and the ionization field applied. The final electric field is reached within 200 ns after the delay time given in the legend. The Rydberg atom can interact with the surrounding ground-state atoms during the delay time which finally leads to an inelastic collision. The electric field required to ionize the Rydberg atom changes by more than a factor of two due to the angular momentum change.

7.1.3 Reaction mechanism for l-changing collisions

Our experiments show that an inelastic collision of a Rydberg atom with a ground-state atom most likely leads to a high l-state within the next lower hydrogenic manifold, as compared to the initial state. This can be concluded from the ionization threshold change (see section 7.1.2) and the measured energy release of such a collision (see section 7.1.1). The former analysis shows that the Rydberg atom changes its angular momentum, and the latter limits the state change to one effective principal quantum number below the initially excited state.

A simple model explaining the observations can be constructed using semi-classical arguments, treating the neutral atoms within the model of section 6.4.3 as point-like particles inside the pair-potential energy curve as shown in figure 7.7. The ground-state atoms are attracted by the Rydberg core due to the ion-neutral polarization potential (section 6.1) and the Rydberg electron scattering by the ground-state atoms (section 6.2). Due to the negligible kinetic energy of the ground-state atoms, most atoms cannot escape the Rydberg orbit and travel through the potential landscape towards the Rydberg core. In particular, they move through the avoided crossings created by the p-wave contribution to the electron-neutral scattering. The Landau-Zener probability [118, 124], which describes the probability to adiabatically change the state, can be calculated by (SI units)

$$P_{LZ} = \exp\left(-2\pi\frac{|V_{12}|^2}{\hbar(dE/dt)}\right) = \exp\left(-2\pi\frac{|\Delta E|^2}{v\alpha}\right). \tag{7.2}$$

Here V_{12} is the matrix element connecting the two states and dE/dt is the slew rate, which can be calculated with the velocity v of the particle times the slope α of the potential energy curve at the crossing.

A ground-state atom which approaches the Rydberg core will always follow adiabatically the potential energy curve at the first crossing, as depicted in figure 7.7, because the available energy due to the photon recoil is too low ($k_B \times 700\,\mathrm{nK}$) to cross the state diabatically. This is different at the next state crossing, which is the butterfly state crossing the D state. The kinetic energy of a neutral atom at this point is much higher, and therefore the atoms stay with a high probability in the butterfly state according to equation (7.2). The subsequent P state crossing is fully diabatic, because it lies deeper in the potential energy curve. Finally, at internuclear distances $r < 100\,a_0$, the butterfly state mixes with the trilobite state [36]. Below $10\,a_0$ the repulsive inner potential repels the two particles (figure 6.2). As the two particles fly apart in an l-changing collision, the trilobite state turns into a high l Rydberg state within the next lower lying manifold compared to the initial state.

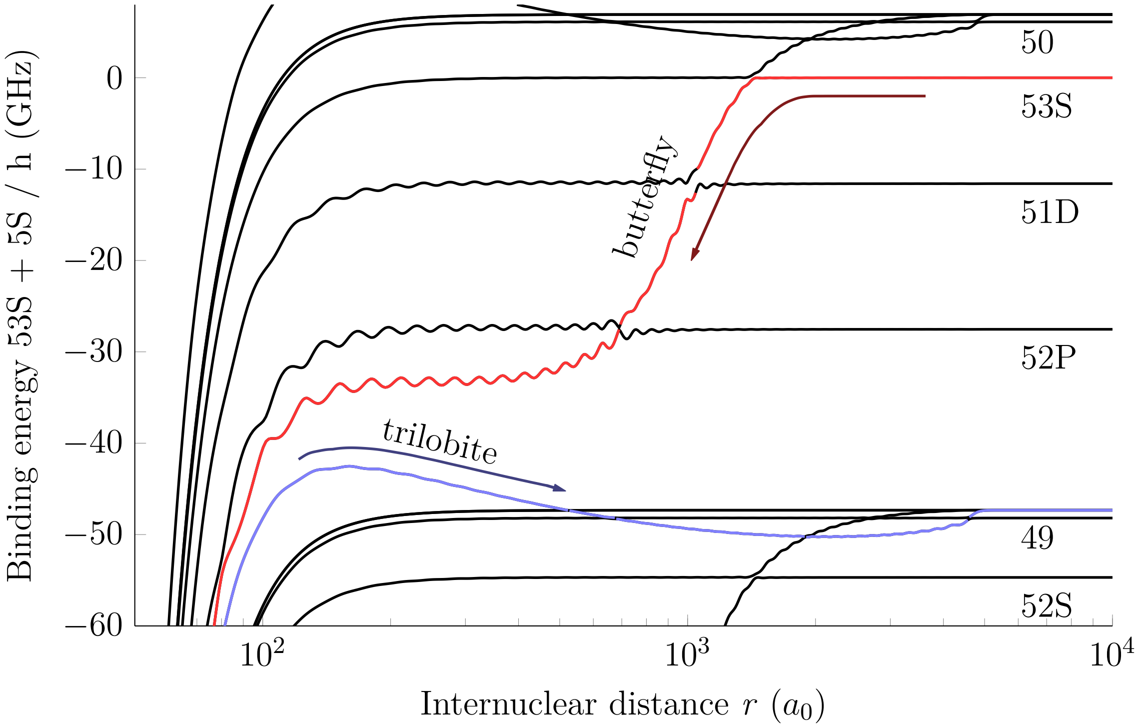

Fig. 7.7: Potential energy curve of the 53S + 5S state with the neighboring states. The arrows indicate a possible reaction mechanism for the l-changing collision: The Rydberg electron is initially excited in an nS state. A ground-state atom, in this example further out than the crossing of the butterfly and nS state, is attracted by the Rydberg core and adiabatically changes from the nS state into a butterfly state (red). At short range, $r \approx 50\,a_0$, and deep binding energies which are not shown in the graph, the butterfly state mixes with the trilobite state (blue) and when the ground-state atom leaves the Rydberg orbit again, the trilobite state turns into a mixture of high l-states in the lower lying hydrogenic manifold with respect to the initially excited nS state.

7.2 Rb_2^+ molecule formation

The second reaction channel for a Rydberg atom with a ground-state atom gives rise to deeply bound Rb_2^+ molecules [S3, 108]. This reaction product can be determined by the different flight time towards the detector due to the mass difference. The total amount of dimers arriving at the detector is independent of the applied ionization field. Hence, once the molecule is created, it must autoionize on a timescale much faster than the collision time.

The ratio between the two different reaction channels depends on the principal quantum number of the initial Rydberg state and was examined systematically, with the results shown in figure 7.8. For the lowest principal quantum number, $n = 40$, the number of l-changing collisions is comparable to the number of Rb_2^+ molecules created. For higher principal quantum numbers, the molecules vanish. In less than $10\,\%$ of the collisions for principal quantum numbers above $n = 90$, a molecule is formed. This ratio differs depending on the angular momentum of the initial state, showing more molecules for the D state compared to the S state at high principal quantum numbers. Experiments performed at lower densities ($\rho \approx 10^{13}\,\mathrm{cm}^{-3}$) by the group of Herwig Ott [109] also show a different branching ratio for $P_{3/2}$ Rydberg atoms, in this case with unpolarized ground-state atoms.

The reaction mechanism is not known in detail. One possible explanation for the ionic reaction product is that the ground-state 5S electron starts to oscillate between the Rydberg and the ground-state atom as they approach each other. This oscillating dipole can couple to the Rydberg electron, transferring binding energy of the molecule to the Rydberg electron until the molecule ionizes. This process is also called the dipole resonance mechanism which leads to the so called chemi-ionization processes in atom-Rydberg collisions. Both are described in detail in [108]. This mechanism could also explain why the fraction of Rb_2^+ molecules is low for high principal quantum numbers. The maximum energy a Rydberg electron can take away drops with n^{-2} according to the Rydberg formula [125]

$$\frac{1}{\lambda} = \frac{E}{hc} = Ryd\left(\frac{1}{n_1^2} - \frac{1}{n_2^2}\right) \tag{7.3}$$

with the vacuum wavelength λ, the energy difference E, the Planck constant h, the speed of light c, the Rydberg constant Ryd and the main quantum numbers n_1 and n_2. Due to the lower energy available to the continuum, $n_2 \to \infty$, it could be that the dimer cannot be stabilized any more.

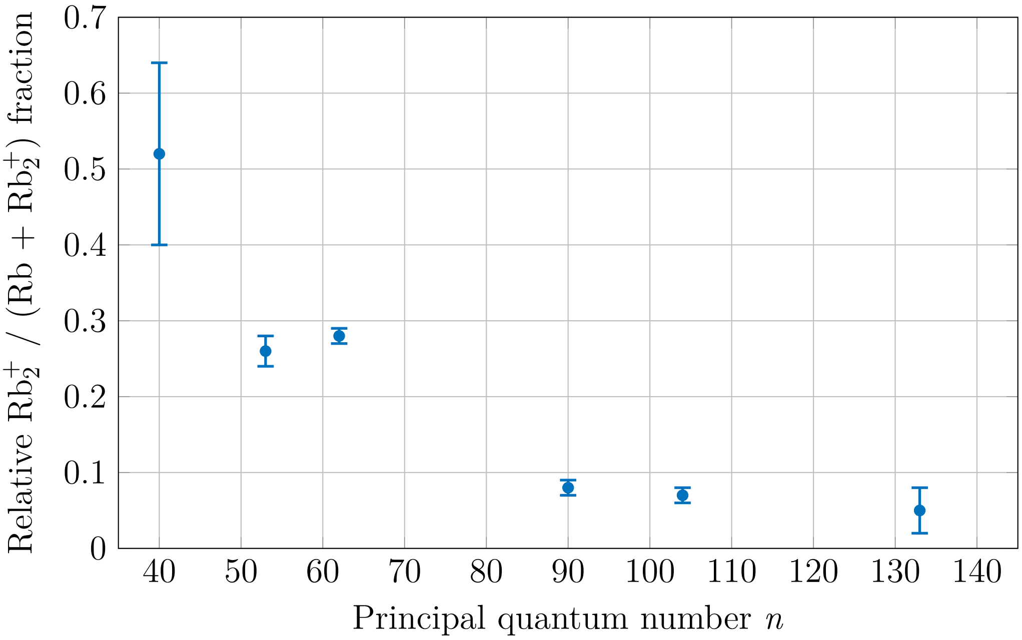

Fig. 7.8: Fraction of Rb_2^+ ions created compared to the total number of ions detected. The error bars indicate the confidence bounds of the fit from which the fraction is extracted. For the lowest investigated state, 40S, both reaction channels, the Rb_2^+ formation and the l-changing collision, are equally probable. For higher n, the dimer formation is suppressed and the probability drops below 10 % for $n \geq 90$.

The electron hopping can be explained with the potential energy curves of the two body system. The Rydberg atom is treated as an ion which is approached by a ground-state atom. Therefore, this is a one-electron system and the resulting potential can be calculated with the effective core potential [126]. The two adiabatic low-energy curves of the system were estimated by Andreas Köhn [127]:

Asymptotically for large internuclear distances, we have two degenerate states. If the ion (+) is the first atom, it is called in the following $|+,0\rangle$ and if the ion is the second atom, it is depicted by $|0,+\rangle$. Diagonalization of the Hamiltonian yields the bonding state

$$\left|{}^2\Sigma_g^+\right\rangle = |g\rangle = \frac{1}{\sqrt{2}}(|0,+\rangle + |+,0\rangle) \tag{7.4}$$

and the anti-bonding state.

$$\left|{}^2\Sigma_u^+\right\rangle = |u\rangle = \frac{1}{\sqrt{2}}(|0,+\rangle - |+,0\rangle). \tag{7.5}$$

The potential energy curves of the two states are shown in figure 7.9. The bonding state has a minimum at $9\,a_0$ with a depth of 770 meV ($h \times 187$ THz), which is in reasonable agreement with experimental findings [128]. The anti-bonding state seems to be purely repulsive, but has a shallow minimum at $\sim 23\,a_0$ with a well depth 10 meV ($h \times 2.4$ THz).

In the experiment, the atoms are not in an eigenstate $|g\rangle$ or $|u\rangle$ as they approach each other. Instead, the electron is located at one atom only,

$$|0,+\rangle = \frac{1}{\sqrt{2}}(|g\rangle + |u\rangle) \tag{7.6}$$

$$|+,0\rangle = \frac{1}{\sqrt{2}}(|g\rangle - |u\rangle). \tag{7.7}$$

These states are called quasi-diabatic states and the corresponding potential energy curves are obtained by transforming the matrix elements of the Hamiltonian accordingly, leading to identical potential energy curves for both states:

$$V_{0,+} = V_{+,0} = \frac{1}{2}(V_g + V_u). \tag{7.8}$$

In addition, the coupling potential results in

$$\left\langle 0,+ \middle| \hat{H} \middle| +,0 \right\rangle = \frac{1}{2}(V_g - V_u). \tag{7.9}$$

Both potentials are drawn in figure 7.9.

The interpretation is as follows: As the rubidium ion and ground-state atom approach each other they interact via the quasi-diabatic potential. But at the same time, the coupling potential drives the exchange of the electron of the ground-state atom. The electron will start to rapidly exchange between the two atoms with $\omega = 2V/\hbar$. The oscillating electron can couple to the Rydberg electron and transfers binding until the Rydberg electron is not bound anymore. This mechanism stabilizes the Rb_2^* Rydberg molecule which finally autoionizes and forms a Rb_2^+.

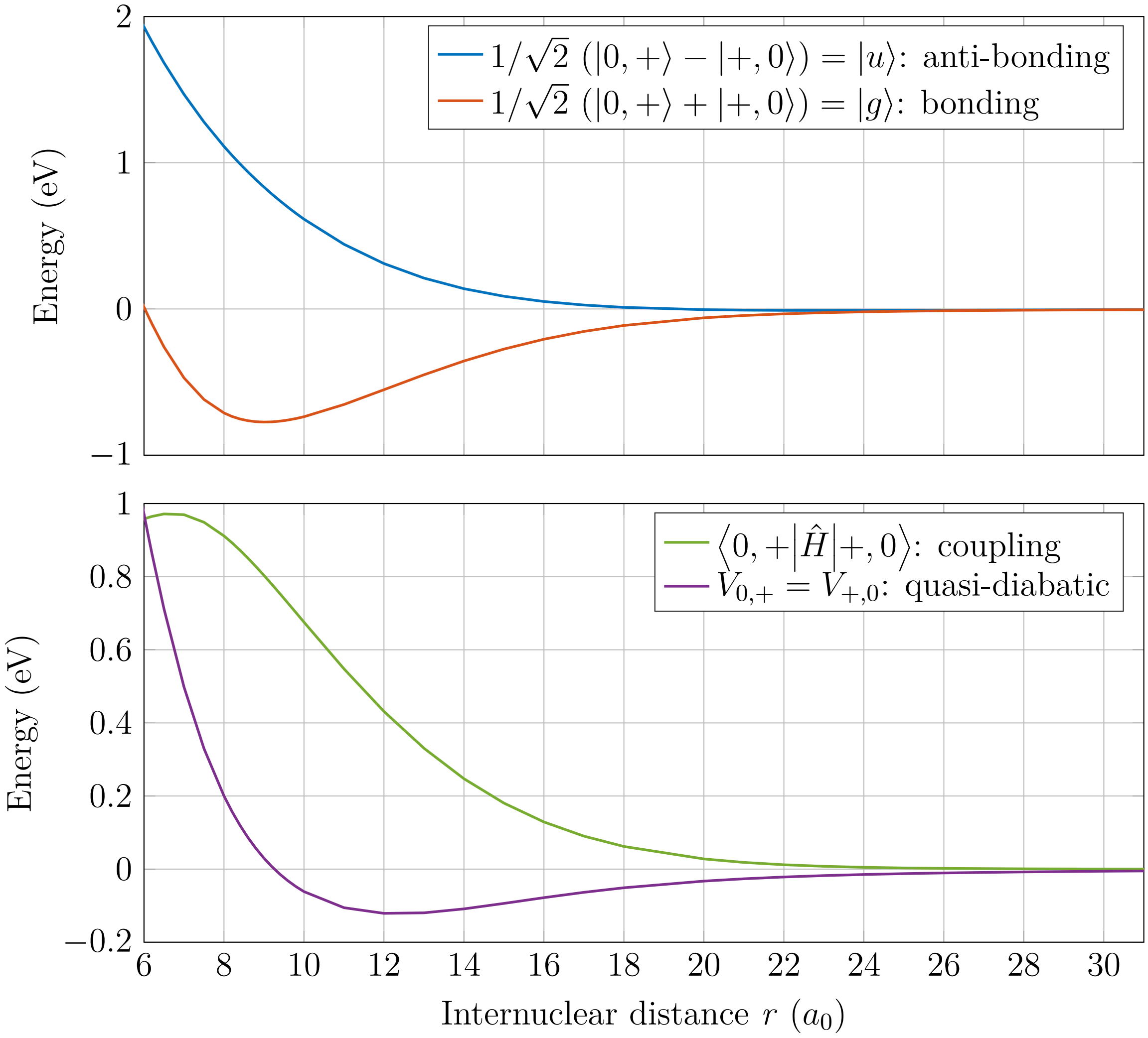

Fig. 7.9: The ground-state (bonding) of Rb + Rb^+ system is plotted together with the anti-bonding state in the upper graph. As the two atoms approach each other in the experiment, they start in the superposition state and observe the quasi-diabatic potential of the lower graph. The electron is hopping between the two atoms according to the coupling energy V with $\omega = 2V/\hbar$.

7.3 Collision dynamics

In addition to the static properties of the reactions described above, the time scale for the inelastic collisions are also analyzed. The collision time could in principle be examined from the state selective ionization measurement described in section 7.1.2, but to achieve a better time resolution, a two-step ionization scheme was applied instead of a continuous ramp. For example, for a 121S state (figure 7.5), a first ionization step with $3\,\mathrm{V\,cm^{-1}}$ was applied for a varying delay time t between the excitation pulse and the ionization. The electric field is chosen such that only atoms in the initially excited nS Rydberg state ionize and fly towards the detector, as well as the Rb_2^+ ions. The two different ions can be distinguished because they have different mass and therefore a different arrival time at the detector. A second ionization pulse with $7\,\mathrm{V\,cm^{-1}}$ ionizes all remaining Rydberg atoms which underwent an l-changing collision before the delay time t, which has prevented the ionization by the lower ionization pulse. By varying the delay time, the probability p to observe a reaction product can be fitted via $p(t) = 1 - \exp(-t/\tau)$. As an example, the analysis for the 100S state is plotted in figure 7.10. The resulting $1/e$ collision time τ varies between 1.9 and 4.5 µs depending on the laser detuning and therefore the addressed density. The l-changing collision time and the Rb_2^+ molecule formation time is shown for all investigated quantum numbers in figure 7.11. The time to create the molecules is about 1.5 to 2 times the l-changing collision time. All curves of the l-changing collision show a threshold behavior in the region of $90 \geq n \geq 110$, where the reaction time changes by a factor of up to 6 depending on the laser detuning. The collision time at a laser detuning of $-12\,\mathrm{MHz}$ ($\approx 1.2\times10^{14}\,\mathrm{atoms/cm^3}$) is between 1 and 2 µs for the investigated principal quantum numbers below the threshold $53 \geq n \geq 90$ and between 8 and 17 µs above the threshold for $111 \geq n \geq 149$. The latter collision time was also measured in an indirect way in the first experiments performed with single Rydberg excitations in a Bose-Einstein condensate [39] and shows a collisional lifetime on the same order of magnitude as the more precise measurements of the experiment described here.

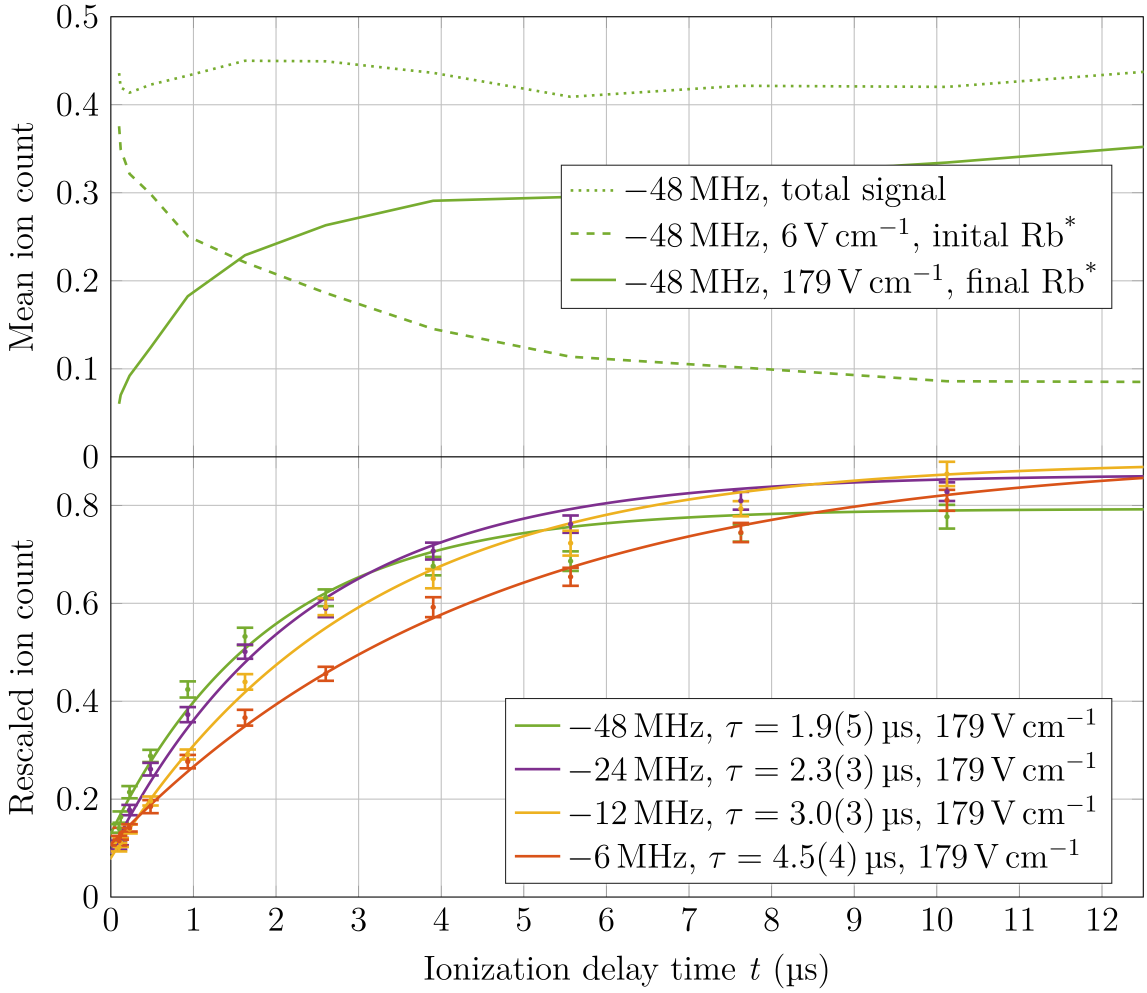

Fig. 7.10: Analysis of the inelastic collision time τ for l-changing collisions at 100S. The top graph shows the ion signal of the first ionization pulse of $6\,\mathrm{V\,cm^{-1}}$ (solid), which ionizes the excited 100S state but not higher angular momentum Rydberg states. With the subsequent higher ionization pulse of $179\,\mathrm{V\,cm^{-1}}$, also the atoms which underwent an l-changing collision (dashed) are ionized. The total sum of the Rydberg atoms (dotted) stays constant over the scan parameter, which is the delay time t between the excitation and the first ionization pulse. The bottom graph shows the ion signal of the second ionization pulse for different laser detuning, which is related to the density the Rydberg atom is excited in (see figure 6.22). All data points are measured 100 times within the same atom cloud and averaged over 18 different atom clouds. The solid line shows the $a - \exp((t - t_0)/\tau)$ fit out of which the collision time τ is extracted.

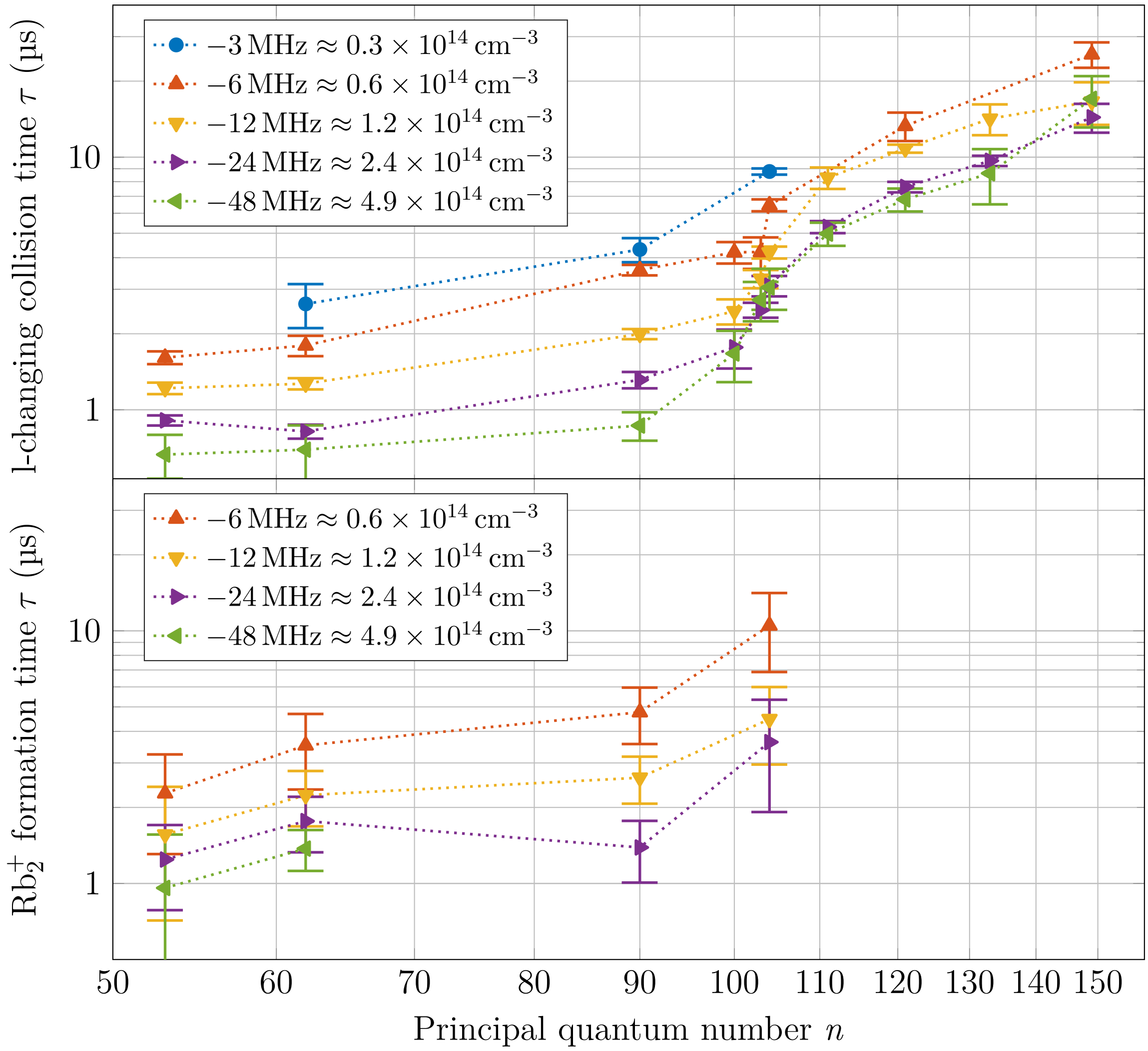

Fig. 7.11: Average formation time τ for an l-changing collision (top) and for Rb_2^+ molecules (bottom) measured for different excitation laser detuning. The addressed density due to the laser detuning is n-dependent as shown in figure 6.22, and therefore the value given in the legend depicts only the mean density addressed. The inelastic collision times were determined as shown in figure 7.10. The error bars of the data points indicate the confidence bounds of the fit taking into account multiple measurements at each data point. At a principal quantum number of approximately $n = 100$, a threshold is reached leading to significantly longer lifetimes of the Rydberg state for higher principal quantum numbers independent of the laser detuning and, therefore, the density. The measured formation time of Rb_2^+ is comparable to the l-changing collision time within the experimental uncertainty. For principal quantum numbers above 110, the relative fraction of Rb_2^+ dimers created is so low, that the reaction time could not be determined anymore.

7.3.1 Langevin capture model

The timescale of the observed collision time can be compared to the classical Langevin capture model [129], which only takes into account the attractive ion-neutral interaction potential discussed in section 6.1. The Rydberg core can be treated as an ion, because the electron orbit is larger than the mean interparticle distance and, therefore, the electron cannot shield the Rydberg core any more. Whether two atoms collide depends on the centrifugal barrier of the neutral and charged atom. The potential energy of this system can be written as

$$V(r) = \frac{l^2}{2\mu r^2} - \frac{\alpha}{2r^4}, \tag{7.10}$$

with the angular momentum l, the reduced mass μ, the polarizability α of the neutral atom, and the internuclear distance r. This finally leads to an energy independent rate constant [130]

$$k = 2\pi\sqrt{\frac{\alpha}{\mu}}. \tag{7.11}$$

The Langevin model gives an estimate of the collision time, in the case of the ion-neutral interaction dominating and no quantum effects playing a role for the collision. The corresponding Langevin collision rate for a sample of ^{87}Rb atoms with a density of 10^{14} atoms/cm^3 is 120 kHz, and thus the mean collision time is 8.2 µs. The collision rate is proportional to the density because it is a two body process. The Langevin model is not directly applicable to the setting in the experiment, in which only a single Rydberg atom is excited and only a single collision can happen with a particle which is initially already close to the Rydberg atom. In addition, the temperature is so low and the density so high that almost always the next neighboring particle to the Rydberg atom will collide first. A simulation of such a system, taking into account only the polarization potential, leads to a faster collision time $\tau_\alpha = 3.7\,\mu\text{s}$ in comparison to the Langevin model. The different collision times are shown in figure 7.12 together with the experimentally identified collision times.

7.3.2 Density dependence of the collision time

The local density of atoms inside the Rydberg orbit changes the resonance frequency and therefore the density depends on the excitation laser detuning. This correspondence has to be handled with care, as explained in section 6.4.5. But even with the density uncertainty taken into consideration, several conclusions can be drawn out of the analysis of the collision time versus the mean density addressed, this is shown in figure 7.12.

On the one hand, for low principal quantum numbers, $n \leq 62$, the measured l-changing collision time is always faster than the simulated collision time including the C_4 polarization potential of equation (6.1) only. That means that the interaction of a Rydberg electron with an incoming ground-state atom, which is not taken into account in this simulation, must accelerate the collision. This is in agreement with previous findings [109], in which the scattering cross section of such a collision was found to be largely increased by the Rydberg electron. On the other hand, for high principal quantum numbers, $n \geq 111$, the observed collision time is always longer than the simulated C_4 collision time, even without the effect from the electron accelerating the collision. Therefore, there must be a mechanism so far not accounted for, which reduces the probability for an l-changing collision at higher n. The transition between these two regimes is in the region of $90 \geq n \geq 110$, as shown in figure 7.11. The large size of the Rydberg electron wave function and the low kinetic energy of the particles makes it likely that a full quantum description is required here. One effect that only appears when the collision is treated fully quantum mechanically, is described in the next section.

7.3.3 Quantum reflections

Classically, solid particles are reflected in a potential energy surface as soon as all kinetic energy is converted into potential energy and a remaining gradient reverses the trajectory. In the quantum case, a wave packet is (partially) reflected when the size of the wave packet, the de Broglie wavelength [131]

$$\lambda(r) = \frac{h}{p} = \frac{h}{\sqrt{2m[E - V(r)]}}, \tag{7.12}$$

changes significantly over its own wavelength, which can be calculated with the Planck constant h, the momentum of the particle p, the mass m, the energy E

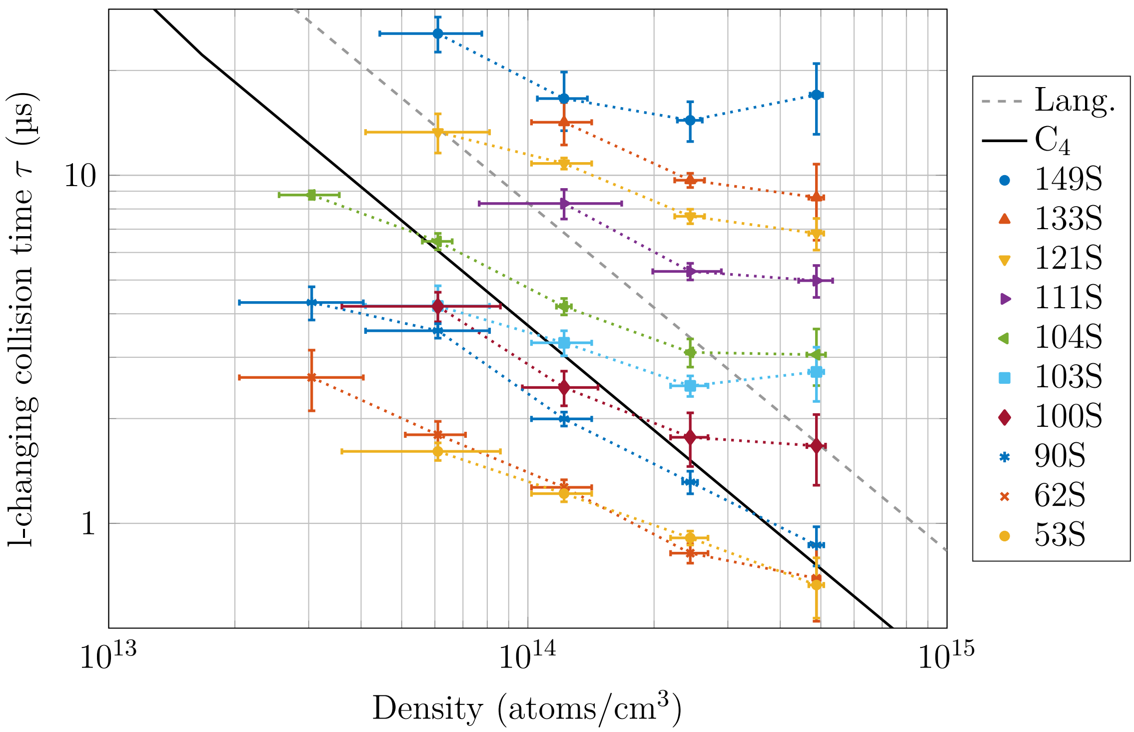

Fig. 7.12: Average formation time τ for an l-changing collision determined as shown in figure 6.22 for different excitation laser detuning, which is converted into an addressed mean density. There are several uncertainties in this conversion as explained in section 6.4.5. The error bars indicate the confidence bounds of the fit taking into account multiple measurements at each data point. As a comparison, the two body Langevin collision time is plotted as the dashed gray line together with the simulated collision time for the C_4 polarization potential, only as a black line.

and the potential energy $V(r)$. Whether quantum reflection plays a role in the system can be estimated by the derivative of the wavelength of the particle,

$$qr(r) = \left|\frac{d\lambda(r)}{dr}\right| \approx 1, \tag{7.13}$$

which is called quantum reflection value in the following. In the quantum case, a steep attractive potential will also lead to a reflection in contrast to the classical case, where the potential needs to be repulsive.

The initial de Broglie wavelength of a ^{87}Rb particle at a temperature of 1 µK, which represents an upper estimate of the initial energy of the particles, is therefore $\lambda \approx 6300\,a_0$, which is the radius of a 59S Rydberg orbit. Due to the very steep slope of the butterfly potential crossing the excited nS state, as shown in figure 6.8, there is the possibility that a ground-state atom is reflected at the crossing and does not enter the butterfly potential. This mechanism can delay the inelastic collision and therefore the time for an angular momentum change or the formation of a Rb_2^+ molecule. Unfortunately, a simple full wave packet simulation is not possible for such a system. On the one hand, the time integration steps need to be very small because of the large gradient at the crossing. On the other hand, the size of the wave packet is huge and therefore the number of time steps required to see the wave packet evolving in time cannot be covered with a direct simulation of the problem. Nevertheless, it can be motivated why it could be possible to have stronger quantum reflections for higher principal quantum numbers at the state crossing of the butterfly and the initially excited nS state, which seems to be counter intuitive due to the weaker potential for higher n. In the case of a r^{-a} potential, this behavior has been investigated [132] and it can be such that the reflections are stronger for weaker potentials.

From a semi-classical point of view, the n-dependence of the quantum reflection $qr_n(r)$ can be estimated from equation (7.13). The kinetic energy of the system is given by the photon recoil of the excitation lasers with $E = k_B \times 700\,\mathrm{nK}$. The incoming particle follows the potential $V_n(r)$ of the nS state crossing the butterfly state, as shown in figure 7.7. The different quantum reflection values $qr_n(r)$ are shown along with the corresponding potentials $V_n(r)$ in figure 7.13. The relative height of the quantum reflection value for different quantum numbers at the innermost maximum turning point of the potential before the state crossing is profoundly higher for higher principal quantum numbers due to the lower potential energy available. Therefore, it is reasonable that at higher principal quantum numbers a ground-state atom cannot enter the butterfly potential as fast as a ground-state atom in a lower Rydberg state due to quantum reflections. One has to note that the analyzed quantum reflection value is above the threshold value of one over a wide radial range, which is due to the very cold environment and the resulting large initial de Broglie wavelength of the particle. The treatment of the ground-state atoms as particles inside the potential energy curve reaches a limit there. Nevertheless, the relative comparison of the reflection strength gives an idea of how the mechanism could work, i.e. it could prevent the collisions of the ground-state atom with the Rydberg core. It has already been seen that quantum reflection from the butterfly state are the source for meta-stable bound states in Rydberg atoms [37]. The neutral atom is trapped outside the steep butterfly potential in this case. This supports the idea that in the full quantum treatment the bound and scattering states of the Rydberg atom cannot enter the butterfly state very fast.

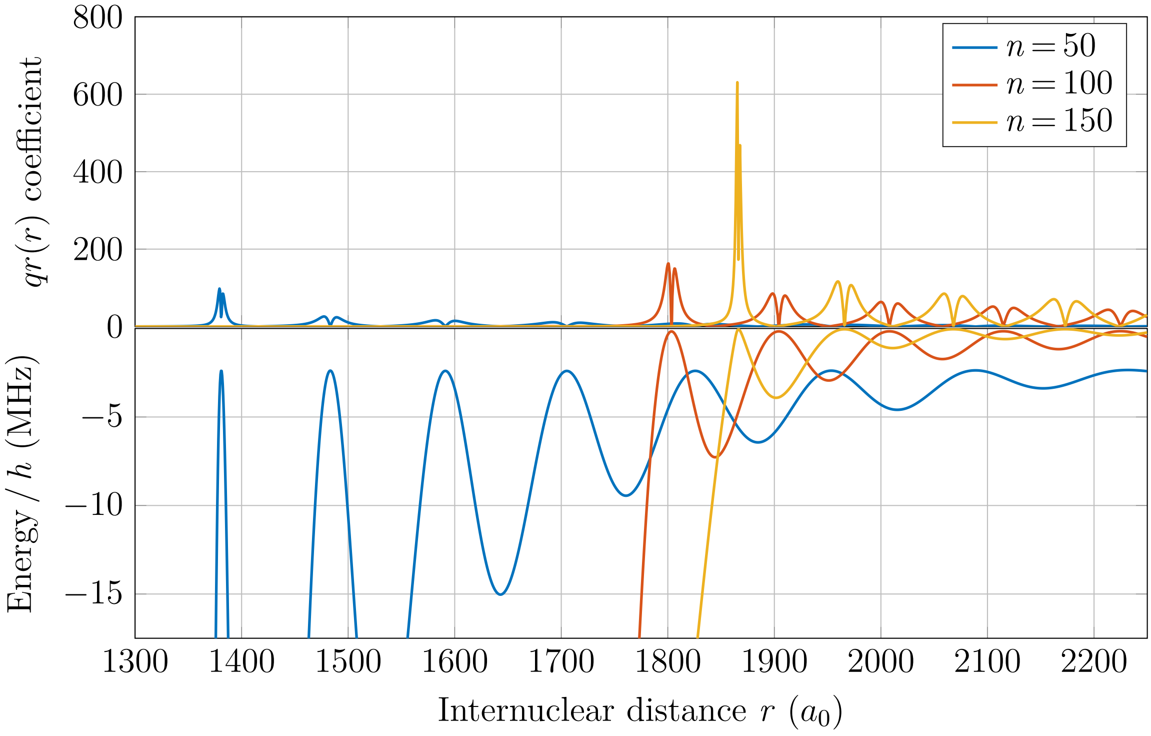

Fig. 7.13: The quantum reflection value $qr(r)$ from equation (7.13) is shown for different nS states versus the distance between the Rydberg core and the ground-state atom in the upper graph, with the corresponding potential energy curves in the lower. The position of the strongest reflection for each principal quantum number is at the closest maximum turning point before the butterfly state crossing. The reflection value for higher principal quantum numbers is higher, because the available energy of a particle at these states is lower due to the shallower potential compared to a low nS state.

Conclusion

The inelastic collision of a Rydberg atom with the surrounding ground-state atoms limits the lifetime of a Rydberg atom within the dense ultracold gas. Two reaction products were identified. Either the Rydberg atom changes its angular momentum or deeply bound Rb_2^+ molecules are created. The first mechanism dominates the reaction for Rydberg atoms in the S state above a principal quantum number $n=40$ at densities found in our Bose-Einstein condensate. The Rydberg electron accelerates the collision of a neutral and the Rydberg atom due to the attractive electron-neutral interaction. The butterfly state, as a consequence of the p-wave shape resonance, plays a key role for the collision dynamics. The molecule formation time is about 1.5 to 2 times the l-changing collision time.

The measured inelastic collisional lifetime shows an unexpected threshold behavior. The collision rate for Rydberg atoms above the threshold principal quantum number of approximately $n=100$ drops significantly and the lifetime exceeds tens of microseconds for higher principal quantum numbers. Interesting dynamical experiments can be performed with such a long lifetime. One example is a direct way to image the angular structure of the Rydberg electron, which is proposed in the following chapter.

8

Imaging a Rydberg electron orbital

The idea that an atom is the smallest constituent unit of ordinary matter has been present since antiquity. But due to their small size, with a diameter of 100 pm for hydrogen up to 520 pm for cesium as the biggest stable element [133], it is not possible to examine them with optical microscopes. Even in the beginning of the 20th century it was an open question whether this hypothesis was true or not. One key experiment to verify the atom hypothesis was performed by Ernest Rutherford in 1909 by shooting α-particles at a gold sheet [134]. In this experiment, most of the α particles passed the foil undisturbed, but a few were scattered into a big angle. This result showed that the mass of each particle is confined in a very small volume and the atom core must be charged to deflect the incoming particles. Later on, the charge number turned out to be the atomic number of the material investigated.

Soon after this discovery, in 1913, Niels Bohr could for the very first time, explain the emission spectra of pure elements with the idea of the Bohr model [135], supporting the new quantum treatment of nature as a fundamental concept introduced by Max Planck in 1900 [136]. Finally, Erwin Schrödinger developed the Schrödinger equation in 1926 [137], which describes how the quantum state of a quantum system changes with time with help of the so-called wave function.

Even though countless phenomena could be explained with this concept of the electron wave function, it was impossible for a long time to directly visualize the electron probability of an atom in an experiment. The first successful attempt was in 2013 by Stodolna et al. [138] for hydrogen, observing the nodal structure of a Stark state.

This chapter explains how the electron probability density of a Rydberg atom could be imaged in a rubidium BEC experiment. As a consequence of the previous chapter, showing Rydberg lifetimes above 10 µs at principal quantum numbers above 100 even at very high densities such as 5×10^{14} atoms/cm^3, the Rydberg atom stays long enough in the BEC and has a strong enough interaction potential to imprint the electron probability distribution as a density change onto the BEC. The strength of this effect makes it possible to detect the angular structure of a Rydberg orbit in a phase contrast image [S4, 101].

The density change within the BEC is caused by the attractive potential of the Rydberg electron scattering off ground-state atoms within its Rydberg orbit, which can be the dominant interaction in a rubidium BEC experiment. Due to this attractive interaction, which was discussed in section 6.2, the probability density of the atoms in the BEC flows like a liquid towards the areas of high Rydberg electron probability density, according to the scattering potential which mimics the absolute square of the Rydberg electron wave function.

8.1 Gross-Pitaevskii equation

The time evolution of a Bose-Einstein condensate including the interaction potential of a Rydberg atom can be calculated with the Gross-Pitaevskii equation [139]. The differential equation is a generalization of the Schrödinger equation for non-linear interactions and describes the time evolution of a quantum system of identical bosons:

$$i\hbar\frac{\partial}{\partial t}\psi(\mathbf{r},t) = \left(-\frac{\hbar^2}{2m}\nabla^2 + V_{\text{ext}}(\mathbf{r},t) + g|\psi(\mathbf{r},t)|^2\right)\psi(\mathbf{r},t). \tag{8.1}$$

The additional non-linear coupling term $g|\psi(\mathbf{r},t)|^2$, compared to the Schrödinger equation, with the coupling constant

$$g = \frac{2\pi\hbar^2 a_{\text{Rb}}}{\mu_{\text{Rb}}} = \frac{4\pi\hbar^2 a_{\text{Rb}}}{m_{\text{Rb}}} \tag{8.2}$$

includes the interaction between the bosons with the reduced mass μ. For ^{87}Rb atoms, the scattering length between the ground-state atoms is repulsive with approximately $a_{\text{Rb}} = 100\,a_0$ [140].

The external potential

$$V_{\text{ext}}(\mathbf{r},t) = V_{\text{mag}}(\mathbf{r}) + V_{\text{dip}}(\mathbf{r},t) + V_{\text{Ryd}}(\mathbf{r},t) \tag{8.3}$$

is given in our case by the interaction of the atoms with the magnetic trap

$$V_{\text{mag}}(\mathbf{r}) = \frac{1}{2} m \left((\omega_x r_x)^2 + (\omega_y r_y)^2 + (\omega_z r_z)^2 \right), \tag{8.4}$$

with the trap frequencies ω_x, ω_y and ω_z. The dipole trap potential [141],

$$V_{\text{dip}}(\mathbf{r}, t) = -\operatorname{Re}(\alpha) |E(\mathbf{r}, t)|^2, \tag{8.5}$$

caused by the excitation light, depends on the polarizability α and the electric field E of the laser beam. The final and most important interaction term for imaging the structure of a Rydberg electron is acting between the Rydberg electron and the ground-state atoms. The interaction is described with Fermi's pseudopotential [70] (section 6.2). The additional potential

$$V_{\text{Ryd}}(\mathbf{r}, t) = \frac{2\pi\hbar^2 a_{\text{e}}}{\mu_{\text{Rb-e}}} |\psi(\mathbf{r}, t)|^2 \approx \frac{2\pi\hbar^2 a_{\text{e}}}{m_{\text{e}}} |\psi(\mathbf{r}, t)|^2 \tag{8.6}$$

includes the Rydberg interaction and is described with the electron-atom s-wave scattering length a_{e}, which is in the case of triplet scattering for ^{87}Rb $a_{\text{e},\uparrow\uparrow} = -15.7\, a_0$ [S5].

8.1.1 Split operator method

The non-linear interaction of the bosons and the interaction of the Rydberg atom (equation 8.6) is included in the Gross-Pitaevskii equation (8.1) and must be integrated numerically to simulate the time evolution of the Bose-Einstein condensate with the impurity.

The split operator method [142] is a standard technique to integrate the time dependent Schrödinger equation

$$i\hbar \frac{\partial}{\partial t} \psi(\mathbf{r}, t) = \hat{H} \psi(\mathbf{r}, t), \tag{8.7}$$

which does not include the non-linear coupling term. The Hamilton operator of the Schrödinger equation is $\hat{H} = \hat{T} + \hat{V} = -\frac{\hbar^2}{2m}\nabla^2 + V(\mathbf{r}, t)$. To calculate a time step, the Hamilton operator $\hat{H}$ can be written in the exponential representation as

$$e^{-\frac{i}{\hbar}\hat{H}\Delta t} \approx e^{-\frac{i}{\hbar}\hat{T}\frac{\Delta t}{2}}\, e^{-\frac{i}{\hbar}\hat{V}\Delta t}\, e^{-\frac{i}{\hbar}\hat{T}\frac{\Delta t}{2}}. \tag{8.8}$$

The resulting error caused by $[\hat{T}, \hat{V}] \neq 0$ is proportional to the leading term $[[\hat{T}, \hat{V}], \hat{T} + 2\hat{V}]$ and is of the order of $(\Delta t)^3$. The idea of equation (8.8) is to perform, first, a half time step with the kinetic energy operator $\hat{T}$, then a full time step with the potential energy operator $\hat{V}$, and finally again a half step with the kinetic energy operator $\hat{T}$. The advantage of this method is that the potential energy operator $\hat{V}$ is diagonal in the exponential representation in space coordinates and $\hat{T}$ is diagonal in momentum space. To switch between momentum and real space representation of the wave function ψ, a simple (inverse) Fourier transformation has to be calculated, which can be computed very fast.

This method has to be modified to solve the non-linear Gross-Pitaevskii equation (8.1) because of the non-linear interaction term. It can be included by simply adding the non-linear term $g|\psi(\mathbf{r},t)|^2$ to the potential energy $\hat{V}\prime = \hat{V} + g|\psi(\mathbf{r},t)|^2$. The drawback of this change is that the integration error increases to $(\Delta t)^2$ instead of $(\Delta t)^3$ [142]. The time integration error can be reduced again by more sophisticated calculations to the order of $(\Delta t)^3$ or even $(\Delta t)^5$ as described in [142].

The split operator method was implemented in Matlab and the following simulations of the time evolution of a Bose-Einstein condensate, including the interaction of a single Rydberg atom, are based on this technique.

8.2 Interaction of a Rydberg atom with a BEC

As introduced in the Gross-Pitaevskii equation (8.1), different interactions have to be taken into account to propose an experiment which is able to visualize the shape of the Rydberg wave function. The principal quantum number of the excited state determines the size of the Rydberg atom, the lifetime, and therefore the interaction time, and the interaction potential depth. The number of atoms which the Rydberg electron interacts with is given by the BEC density and the Rydberg orbit size. To choose an appropriate quantum number, all of these effects are examined in the following. For the calculations below, the effective principal quantum number taking into account the quantum defect is depicted by n.

The imprint of the electron Rydberg orbital onto the density of the background gas is based on the interaction of the Rydberg electron and the ground-state atoms inside the Rydberg orbital (section 6.2). Ground-state atoms experiencing the attractive interaction potential start to flow towards the areas of high Rydberg electron probability.

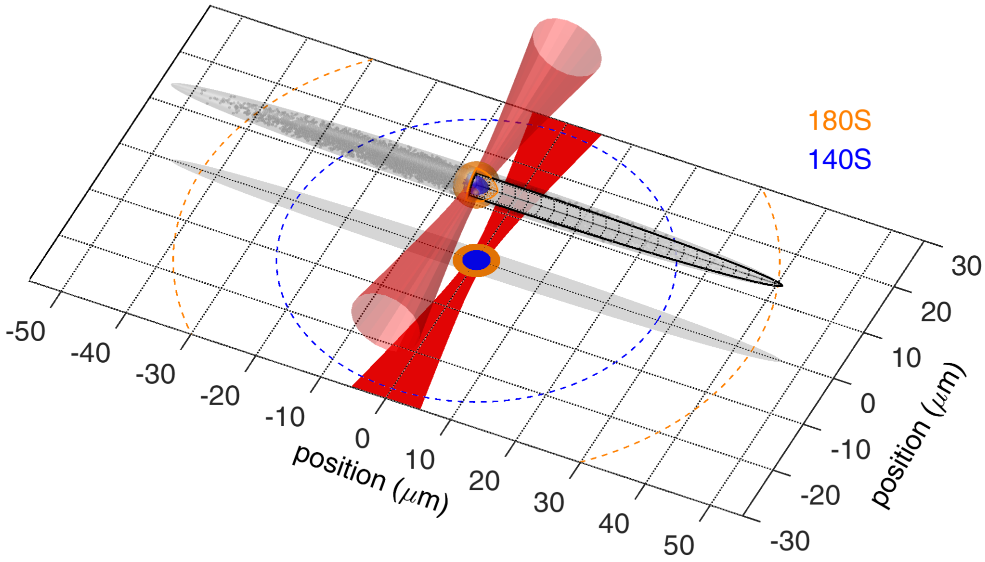

Fig. 8.1: Comparison of the length scales of the BEC (gray), the Rydberg excitation beam, the Rydberg orbitals of a 140S (blue) and 180S (orange) state, and the respective blockade radii (dashed). The low excitation probabilities used in the experiment together with the Rydberg blockade effect ensure that only one excitation is present in the BEC for both S and D Rydberg states.

The BEC many-particle wave function is well described by the Thomas-Fermi model [52] and is drawn in figure 8.1. It is assumed that the Rydberg atom is excited in the center of the BEC, which can be achieved by having focused crossed excitation beams and by taking advantage of the density shift (section 6.4.5, [S2]) by detuning the excitation lasers such that only the dense inner part of the BEC is resonant.

8.2.1 Size and shape of the Rydberg atom and the BEC

The radial size of a Rydberg atom $r_{\mathrm{orbit}} = 2n^2$ bohr, as shown in figure 8.2, should be chosen such that the structures which should be resolved are larger than the imaging resolution of the system, which is limited to $\lambda/2$ for light with the wavelength λ. For optical wavelengths, a resolution below 1 µm is hard to reach in an experimental setup. That means that only principal quantum numbers $n > 100$ with a radial size of $r > 1\,\mu\mathrm{m}$ are possible candidates to resolve a non-trivial structure of the Rydberg orbit. A Rydberg S orbit and two D orbits ($m_J = 1/2$ and $m_J = 5/2$) are shown in figure 8.3, first in 3D and integrated along the imaging direction in 2D to simulate the column density, which is the measurable quantity. To obtain a high contrast in the density profile the Rydberg size should match the BEC size. A too small Rydberg orbit will lead to a decreased contrast in the images because the imaging beam has to travel through a region where the light is simply absorbed or shifted in phase without gaining any information about the Rydberg structure. If the Rydberg orbit is bigger than the BEC, the trap repels the atoms attracted from the Rydberg electron and hence the imprint of the wave function is deformed. In

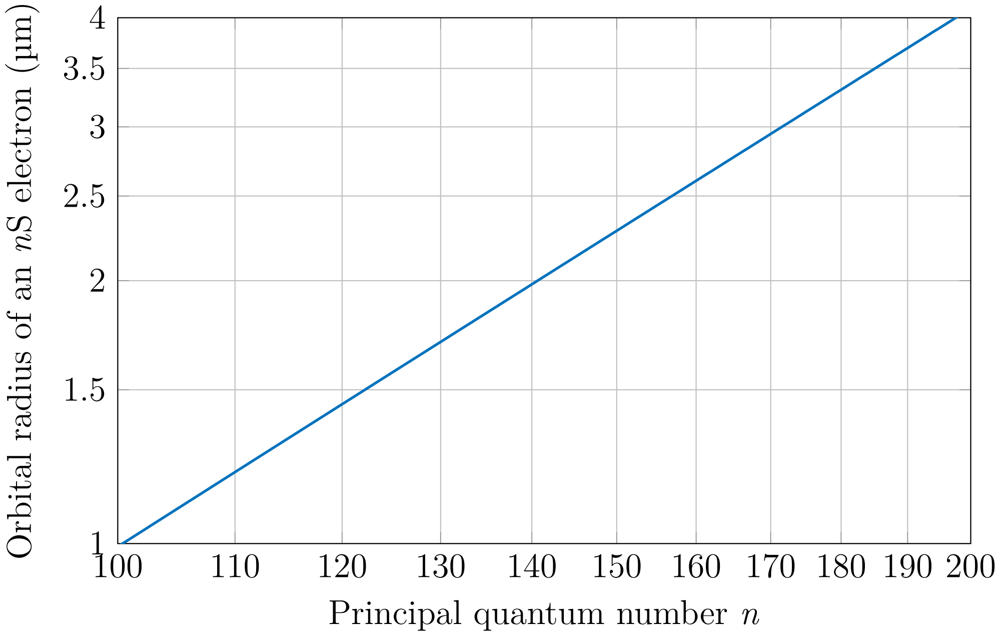

Fig. 8.2: Classical outer turning point of an nS electron. The radial size of a Rydberg atom is approximately equal to the classical outer tuning point $r = 2n^2 a_0$ and is between 1 and 4 µm for the reasonable quantum numbers $n = 100$ to 200 in rubidium.

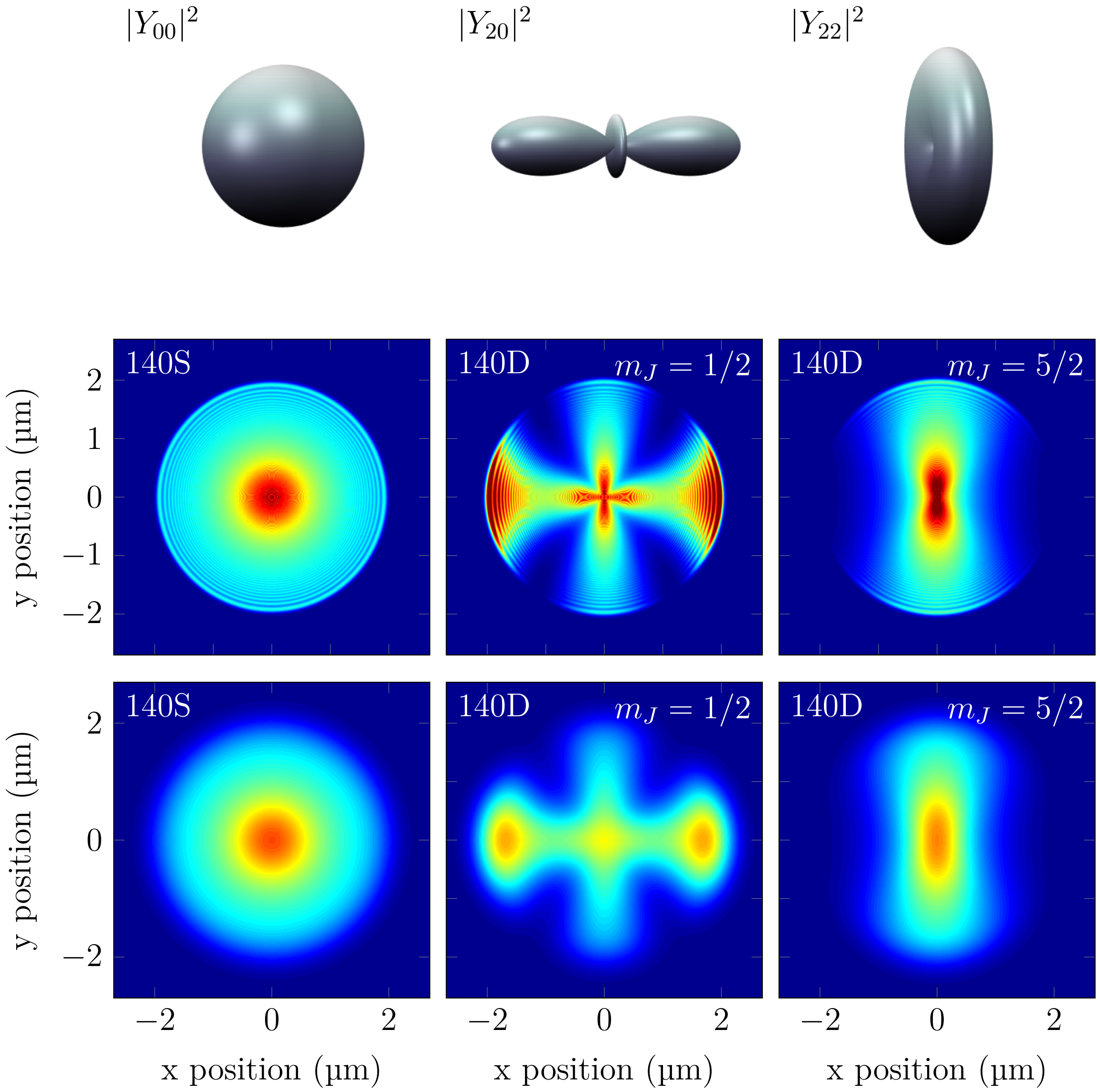

Fig. 8.3: Orbital structures in 3D and 2D. The first row shows from left to right the absolute square of the spherical harmonics Y_{lm} of a S, D $m_J = 1/2$, and D $m_J = 5/2$ orbit defining the angular density distribution of the Rydberg electron. The second row visualizes the integrated electron density along the imaging direction (z). By including a finite imaging resolution of 1 µm in the simulation, the radial structure washes out as shown in the last row, but the overall angular structure remains.

the end, a difference picture of a pure BEC and a BEC with the imprinted Rydberg orbit has to be evaluated. The contrast between these two pictures should be as high as possible, this can be reached by matching the radial BEC and the orbit size. In addition, it is preferable to have an elongated BEC, which has a flat density profile in the elongated direction, which means a flat density background towards this axis.

8.2.2 Phase contrast imaging

To image the change in column density, non-destructive[1] phase contrast imaging [45, 143] is a well suited imaging technique for this very dense gas. First, a reference image of the BEC is taken directly before the first excitation pulse is applied. Due to the non-destructiveness, several pictures of the same sample can be taken to visualize the time evolution of the imprint. Difference pictures between the reference image and the ones after the excitation can reveal the angular structure of the Rydberg orbit. This direct comparison also reduces the atom number shot noise, since the atoms are spatially projected in the first image and are the same for the following images. The effects of the imaging and excitation lasers on the BEC can be measured by blocking one of the excitation lasers to ensure no Rydberg excitation. The remaining noise sources are the imaging light and the camera itself. The dynamic range of the camera, and the finite imaging resolution will ultimately limit the achievable image quality.

8.2.3 Interaction time

The lifetime of a Rydberg atom, which is dominated by the collisional lifetime at the densities and quantum numbers suitable to perform wave function imaging, scales with the principal quantum number $\propto n^3$ in the range of $110 \geq n \geq 150$ as shown in figure 7.11 and with the density $\propto \rho^{-0.3}$ between $0.6 \times 10^{14} \geq \rho \geq 4.8 \times 10^{14}\,\mathrm{atoms/cm^3}$ as plotted in figure 7.12. Since the mean interaction time τ is only about 10 to 20 µs and the potential depth not more than tens of kHz, the attracted background atoms just begin to accelerate

---

[1] Phase contrast imaging is ‘non-destructive’ only in the sense that almost no atoms are lost during the measurement itself, because the absorption is kept very low due to the high imaging detuning. But the BEC wave function is projected into a number state of the measured column density as a consequence of the measurement itself and therefore the quantum state it was in before the measurement is destroyed.

towards the regions of higher Rydberg electron density during the time the Rydberg atom exists. A significant density change is only visible after a longer time evolution of the system, which will be discussed in detail in section 8.3.1 and 8.3.2. The main decay channel for the suitable Rydberg states is the l-changing collision, as described in chapter 7. After the inelastic collision the reaction product and, therefore, the Rydberg atom, leaves the condensate quickly without disturbing it. To improve the signal-to-noise in the experiment, post selection of the measured data can be done. Before taking the image, it is possible to probe, as described in section 7.1, whether the initially excited state is still present at the moment of the ionization. Therefore, only the images with a long imprint time of the Rydberg potential can be selected, leading to an improved signal-to-noise ratio. For example, in 10 % of the experiments, the lifetime of the Rydberg atom is 2.3 times the $1/e$ lifetime τ, as visualized in figure 8.4, which is, for an S state, between 23 and 46 µs, depending on the principal quantum number and density.

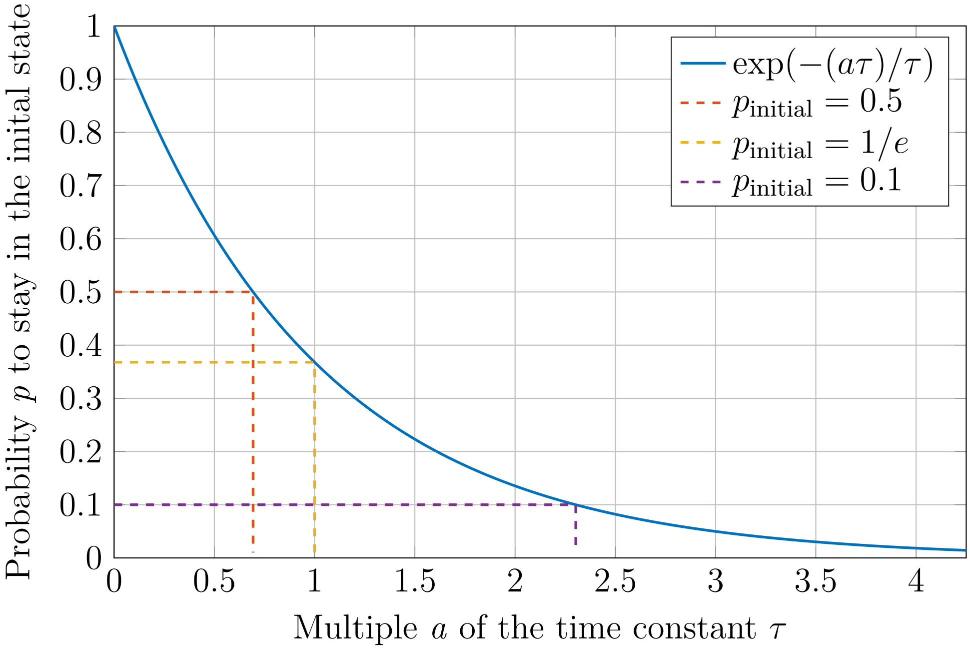

Fig. 8.4: Probability to stay in the initially excited state $p(t) = p(a\tau) = \exp(-(a\tau)/\tau)$ with respect to the collisional lifetime τ. For example, with a 10 % probability, the initially excited Rydberg atom is unaffected for 2.3 τ, which can be exploited by post selection of the experiments done.

8.2.4 Interaction strength

The interaction strength arises from the interaction potential $V_{\text{Ryd}} \propto n^{-6}$ of the Rydberg electron and the ground-state atoms (see figure 8.5) and the interaction time $\tau \propto n^3$, which is the lifetime of the Rydberg atom. Therefore, the interaction strength $V_{\text{Ryd}} \times \tau$ scales with $\propto n^{-3}$. This value should exceed the time integrated potential imprinted during the time of the excitation by the excitation lasers (V_{dip}, equation 8.5), so that the effect of the excitation lasers on the condensate is negligible. In addition, the imprint must be at least comparable to the chemical potential of the BEC, which is defined by the magnetic trap, the atom number, and the scattering length between the ground-state atoms.

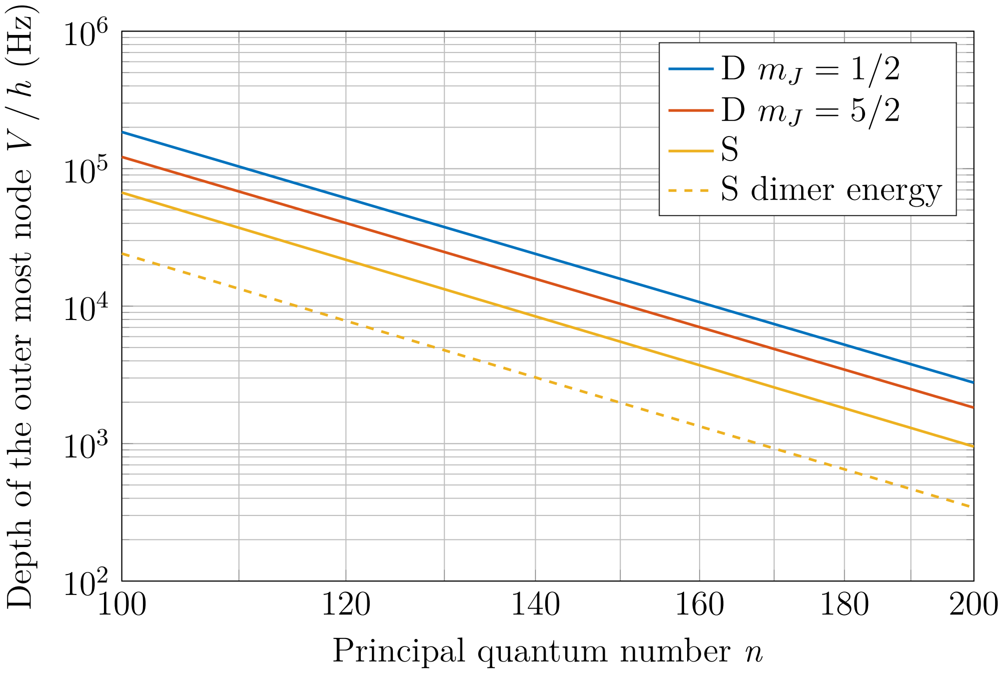

Fig. 8.5: Mean interaction potential of a single ground-state atom inside the Rydberg orbit, assuming a constant scattering length of $a = -15.7\,a_0$ [S5] of the electron and the neutral ground-state atoms, which scales with the effective principal quantum number as n^{-6}. For a comparison, the binding energy of the deepest ultra-long range S dimer [19] (dashed) is shown. The energy difference to the respective solid line of the S state is the zero-point energy of the molecule.

8.2.5 Finite number of atoms

A Bose-Einstein condensate is a degenerate gas consisting of indistinguishable bosons. Therefore, the whole many-body BEC must be treated with a single BEC wave function, and the absolute square of the wave function reflects the probability to find atoms at a certain position. Every spatial measurement technique will project the atom probability distribution at the moment of the measurement into a number state [144]. The imaging beam integrates, so to say, the atom number in the imaging direction, leading to a column density and therefore to an atom number N per area, which will show a shot to shot fluctuation of $\sqrt{N}$ since the position of the atoms are uncorrelated in a BEC [145] and follow a Poissonian distribution.

For a BEC with 5×10^4 atoms and a Thomas Fermi radius of 47 µm in the axial and 2.3 µm in the radial directions, the mean atom number in the central column with an area of 1 μm^2 is about 360 atoms, leading to a shot noise of about 6 %. Different atom numbers and the resulting noise levels are compared in figure 8.6. In the following, the atom number shot noise will be neglected because it will eventually average to zero by averaging over many images.

8.3 Suitable parameters for imaging an electron orbital

There are two different approaches available to create and detect the imprint of a Rydberg electron orbital within a BEC. In the first case, the imprint of only a single Rydberg atom is imaged. In the second case, new Rydberg atoms are excited consecutively and the imprint is imaged after several excitations.

The advantage of an experiment with a single Rydberg excitation only is that the initial conditions of the experiment are well defined and the experiments performed can be post-selected. Before the excitation, the BEC is in thermal equilibrium. By applying the excitation laser pulses, a Rydberg atom is excited and after a desired imprint time, the ionization and detection sequence is applied. If no ion arrives at the detector, either no Rydberg atom was excited or it has decayed early. So only if the Rydberg atom has stayed in the BEC for the entire desired interaction time is it detected as an ion. This post-selection method increases the signal-to-noise of the imprinted wave function, because only Rydberg atoms that have had a strong impact on the BEC are evaluated. The drawback of a single excitation is the limited impact time of this atom onto the BEC due to the finite lifetime of a Rydberg atom. Therefore, the imprint

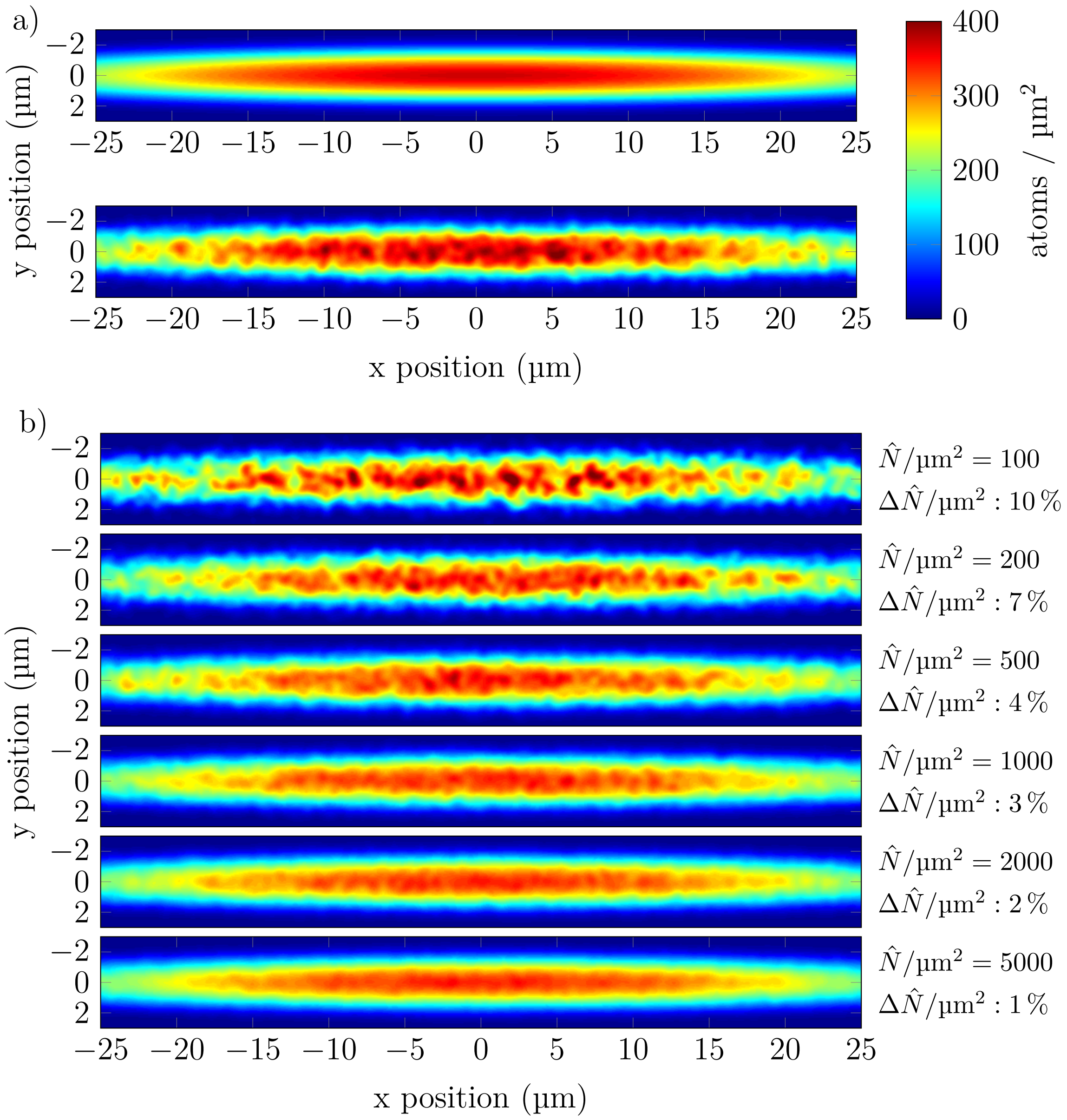

Fig. 8.6: (a) Comparison of the expected density profile without including atom number shot noise (top) and taking into account the projection into an atom number state [144] (bottom). The visualized BEC has 5×10^4 atoms and Thomas Fermi radii of 2.3 µm in radial and 47 µm in axial direction. The color indicates the number of atoms in a 1 µm^2 area according to the summed local density in this column. (b) Comparison of the atom number shot noise for different atom numbers. For simplicity only the atom number was rescaled such that the central column with an area of 1 µm^2 contains $\hat{N}$ atoms as shown on the right side of the figure. The relative atom number noise $\Delta\hat{N} = \sqrt{\hat{N}}/\hat{N}$ at the peak density is shown below.

potential needs to be deep so that the surrounding ground-state atoms can react to the imprinted potential. Hence, only the principal quantum numbers below 150 can lead to a measurable density change with the disadvantage that the Rydberg orbit structures are small and therefore a small BEC is required. The imaging resolution, in this case, will also limit the possible observable structures.

The second option is to excite Rydberg atoms consecutively within a BEC, allowing Rydberg atoms with much higher quantum numbers like $n = 180$ to be examined. These larger Rydberg orbits are easier to resolve. The Rydberg blockade effect [28] ensures that only one excitation is inside the excitation volume at a time. Since a new Rydberg atom is excited after one has decayed, the total interaction strength compared to the single excitation is much higher, with the disadvantage that the imprint washes out on the size of the spatial uncertainty where a Rydberg atom can be excited. From an experimental point of view, the electric field stability will limit the quantum number that can be reliably excited.

The advantages and disadvantages of the different methods are summarized in table 8.1. To perform the experiment, the target principal quantum number and the atom number of the BEC, which means the BEC size, have to be chosen carefully. The interplay between these parameters is sketched in figure 8.7.

Table 8.1: Comparison of the single and continuous excitation imprint methods.

	single excitation	**continuous excitation**
advantages	• defined imprint time • post selection possible	• larger density changes • larger structures possible
disadvantages	• time evolution required • limited interaction time	• keep exactly one excitation in the center
limits	• interaction strength	• electric field stability • spatial excitation uncertainty

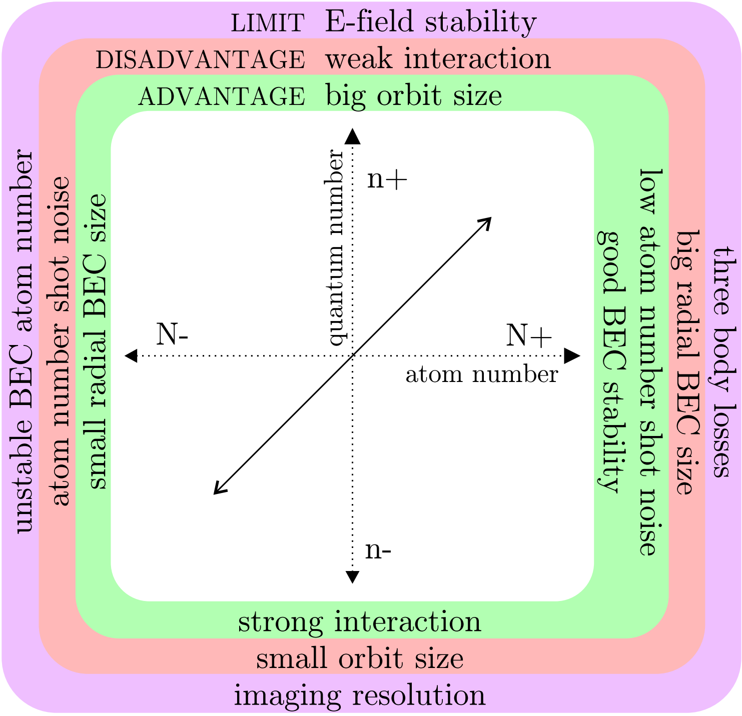

Fig. 8.7: Interplay of the atom number and principal quantum number. In the vertical axis, a big orbit size has as a consequence a weak interaction with the condensate, whereas a small orbit size is difficult to image. The horizontal axis shows that a big condensate is more stable and has lower atom number shot noise, but reduces the visibility if the imprint size is smaller than the radial BEC size. Therefore, both axes are not independent: the radial BEC size should approximately match the orbit size. That means that the parameters should only be changed along the solid arrow.

8.3.1 Single Rydberg excitation

A good parameter set for imaging a single Rydberg excitation consists of a condensate of 5×10^4 rubidium atoms, confined in a harmonic trap with radial and axial trap frequencies of $\omega_{\text{rad}} = 2\pi \times 200\,\text{Hz}$ and $\omega_{\text{ax}} = 2\pi \times 10\,\text{Hz}$. The chemical potential for these parameters is 940 Hz with a peak density of the atoms at the center of $1.2 \times 10^{14}\,\text{cm}^{-3}$. The corresponding Thomas Fermi radii are 2.3 µm in radial and 47 µm in axial direction. A suitable Rydberg orbit for this kind of experiment is a 140D $m_J = 1/2$ state as visualized in figure 8.8. The orbit size is about 2.0 µm and the potential depth of the outermost well is 24 kHz and causes a column density change of up to 30 % (figure 8.9) for a 20 µs interaction time of the Rydberg atom. The optimal imaging time to achieve the highest contrast depends mainly on the principle quantum number n, since this affects the structure size and depth of the imprinted potential.

A systematic study of the different parameters was performed by numerically simulating the time evolution of a single Rydberg excitation in a Bose-Einstein condensate. All simulations for this section were calculated on a $512 \times 32 \times 32$ grid with a cell edge length of 254 nm. The radial Rydberg potential is treated as a box potential by taking the mean radial interaction strength of the corresponding state as the potential depth. This simplification does not affect the resulting simulated images because even the largest radial structures are not resolvable by our imaging system which has a resolution of 1 µm. For example, the full width at half maximum of the outer most node of a $n = 150$ state is only 80 nm wide and therefore not resolvable. The angular Rydberg potential instead is modeled according to the real electron distribution taking into account the respective spherical harmonics. The time evolution was simulated with the split operator method of equation (8.8) with an integrations step of 0.2 µs solving the Gross-Pitaevskii equation (8.1). The Rydberg excitation is assumed to be at the very center of the BEC.

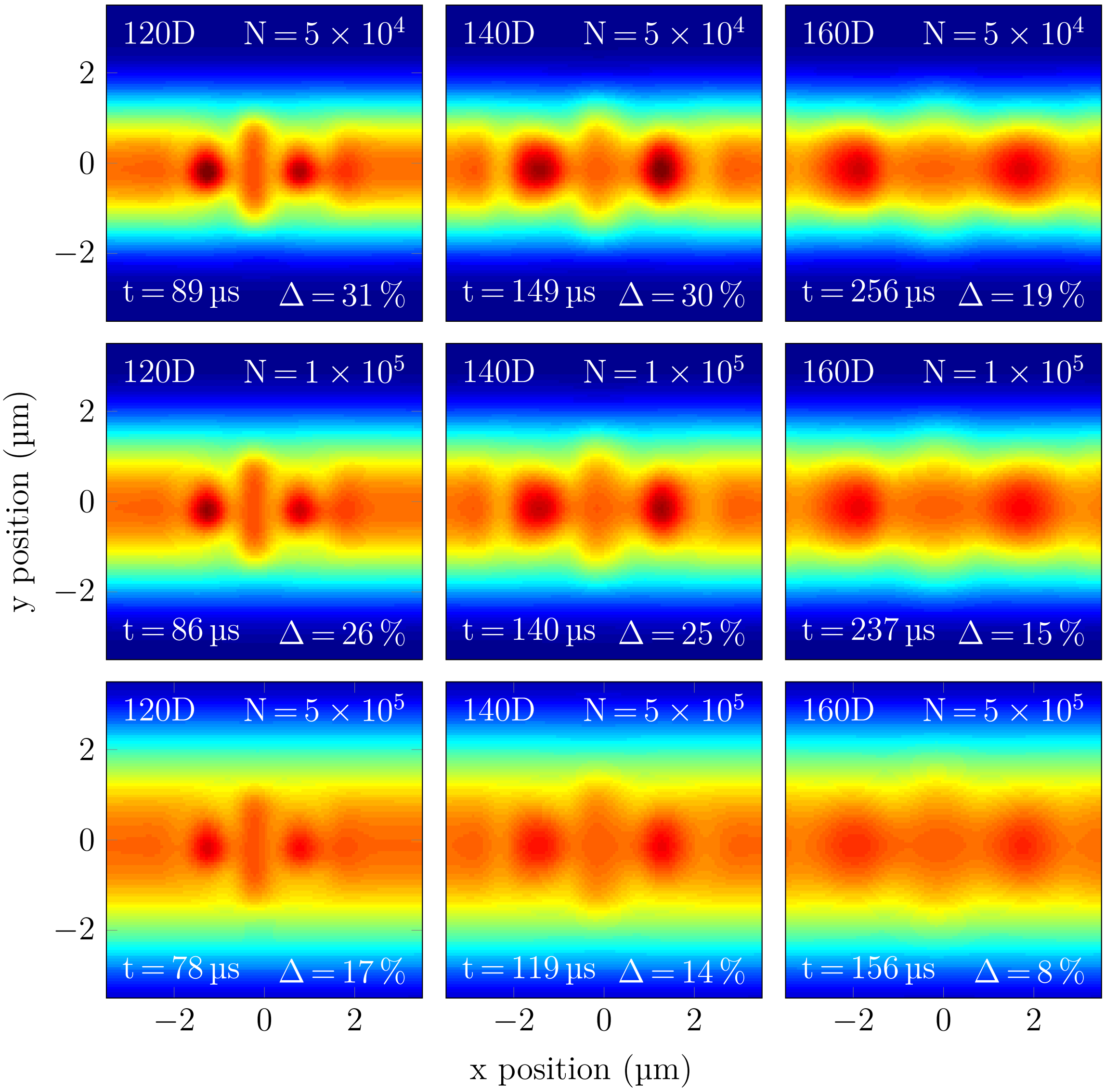

Fig. 8.8: Comparison of the simulated density change for different quantum numbers and BEC sizes for a single Rydberg excitation. By increasing the quantum number and, therefore, the radial size of the Rydberg orbit, the density change drops due to the weaker interaction. The imprint is also weaker if the radial size of the BEC exceeds the orbit size. The 140D $m_J = 1/2$ state with $N = 1 \times 10^5$ atoms is a good compromise between size and depth of the Rydberg electron potential. The orbit size of this Rydberg state is 2.0 µm and the interaction strength of the outermost potential well of the Rydberg atom is 24 kHz, which is enough to cause a density change of $\Delta = 25\,\%$ at the position of the outer most node assuming a Rydberg interaction time of 30 µs and an image taken at $t = 30 + 110\,\mu\text{s}$.

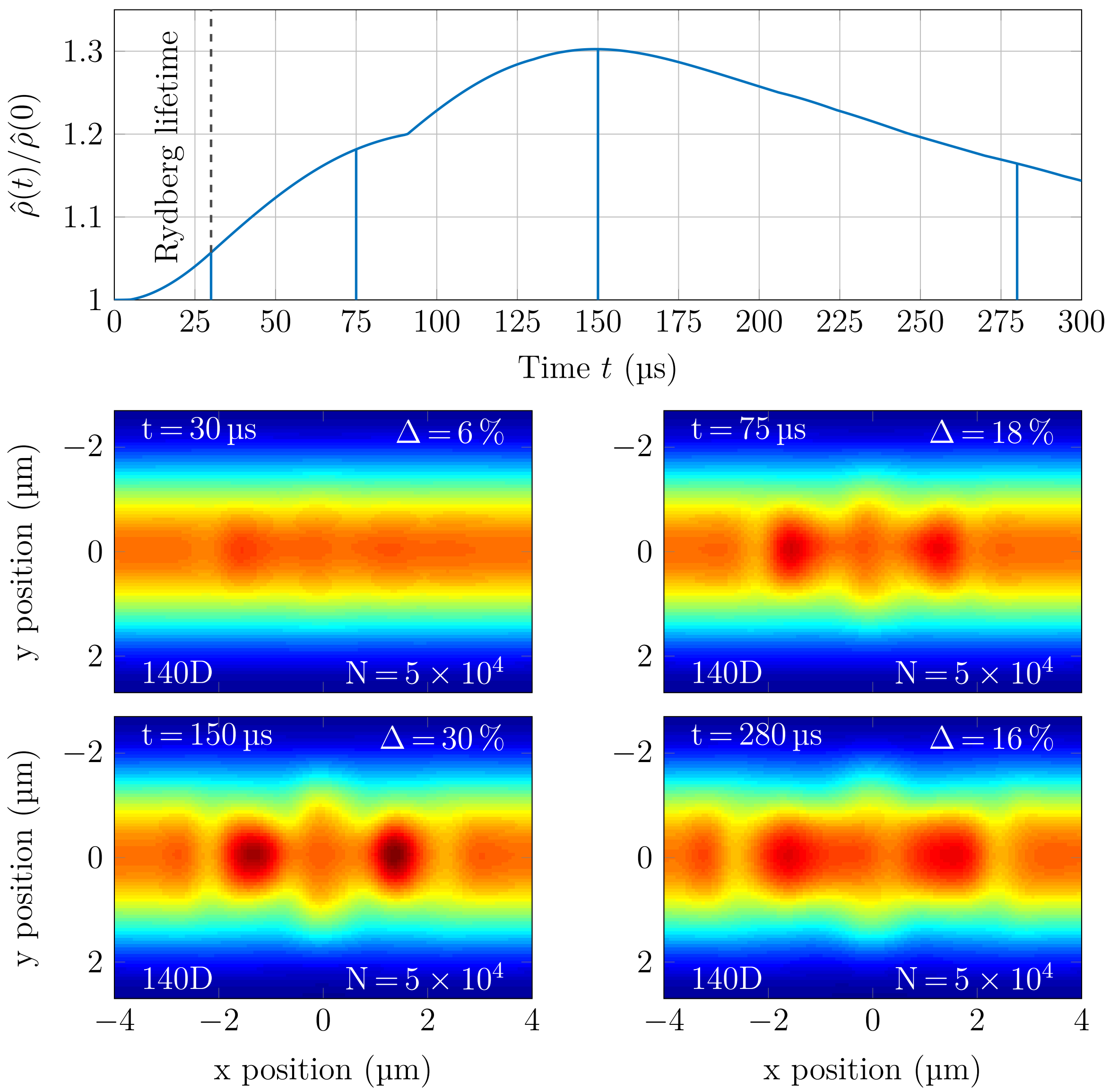

Fig. 8.9: Time evolution of the simulated column density with an imprint of a single 140D $m_J = 1/2$ Rydberg atom for 30 µs. The relative density change $\hat{\rho}(t)/\hat{\rho}(0)$ compares the peak density of time evolution of the BEC with the reference peak density at $t = 0$ µs. At the time when the Rydberg atom decays, $t = 30$ µs, only a density change of 5 % is visible. But since the atoms are in motion after the excitation and the background potential is almost flat in the interesting region, the atoms still move and the density change increases in the time evolution until a maximum is reached, which, for the chosen conditions, is at $t = 150$ µs. Afterwards, the radial structure of the Rydberg orbit washes out again.

8.3.2 Multiple Rydberg excitations

The second method to imprint the Rydberg potential onto the BEC density is to continuously re-excite a Rydberg atom in the center of the BEC. An excitation with narrow, crossed excitation lasers will lead, in the best case, to a spatial uncertainty of approximately 1 µm. This uncertainty in position will wash out the Rydberg electron structure within the image on this length scale. Due to the longer imprint made possible by re-exciting a Rydberg atom, also interaction potentials at much higher principal quantum numbers lead to a measurable density change within the BEC.

A BEC of 5×10^5 atoms in the same trap as the single shot experiment leads to a radial Thomas-Fermi radius of 3.7 µm, a chemical potential of 2.4 kHz, and a peak density of $3.0 \times 10^{14}\,\mathrm{cm}^{-3}$. The radial size of a 180D $m_J = 1/2$ atom is 3.3 µm, which matches the region of the background atoms where the column density is almost flat, and still has a peak potential depth in the outermost well of 5.2 kHz which is strong enough to imprint the wave function.

All simulations for the subsequent excitation method were performed as in the case of a single Rydberg excitation, but on a grid of $1024 \times 64 \times 64$ data points with a cell edge length of 195 nm. To take into account the time between decay and re-excitation of the Rydberg atoms, the imprint potential $V_{\mathrm{Ryd}}(\mathbf{r})$ is multiplied by a factor $0 \geq a \geq 1$. The fraction a causes an effective imprint potential according to the fraction of time different Rydberg atoms i were excited.

$$a = \frac{\sum_i T_{\mathrm{Ryd},i}}{T_{\mathrm{total}}} \tag{8.9}$$

The ideal case, in which the Rydberg atom would be re-excited immediately, would correspond to $a = 1$.

In figure 8.10, different states and sizes within the first 2.4 ms of the imprint in the BEC are compared with a relative imprint time fraction of $a = 0.5$. The simulation shows that a 180D $m_J = 1/2$ Rydberg state is suitable to reveal the angular structure of the Rydberg orbit in the density imprint of the BEC. The time dynamics of such an imprint is shown in figure 8.11. After an imprint time of 450 µs, the atoms within the orbit have rearranged according to the orbital structure. The relative density change in the outermost potential well reaches 21 % and therefore should be visible in a phase contrast image.

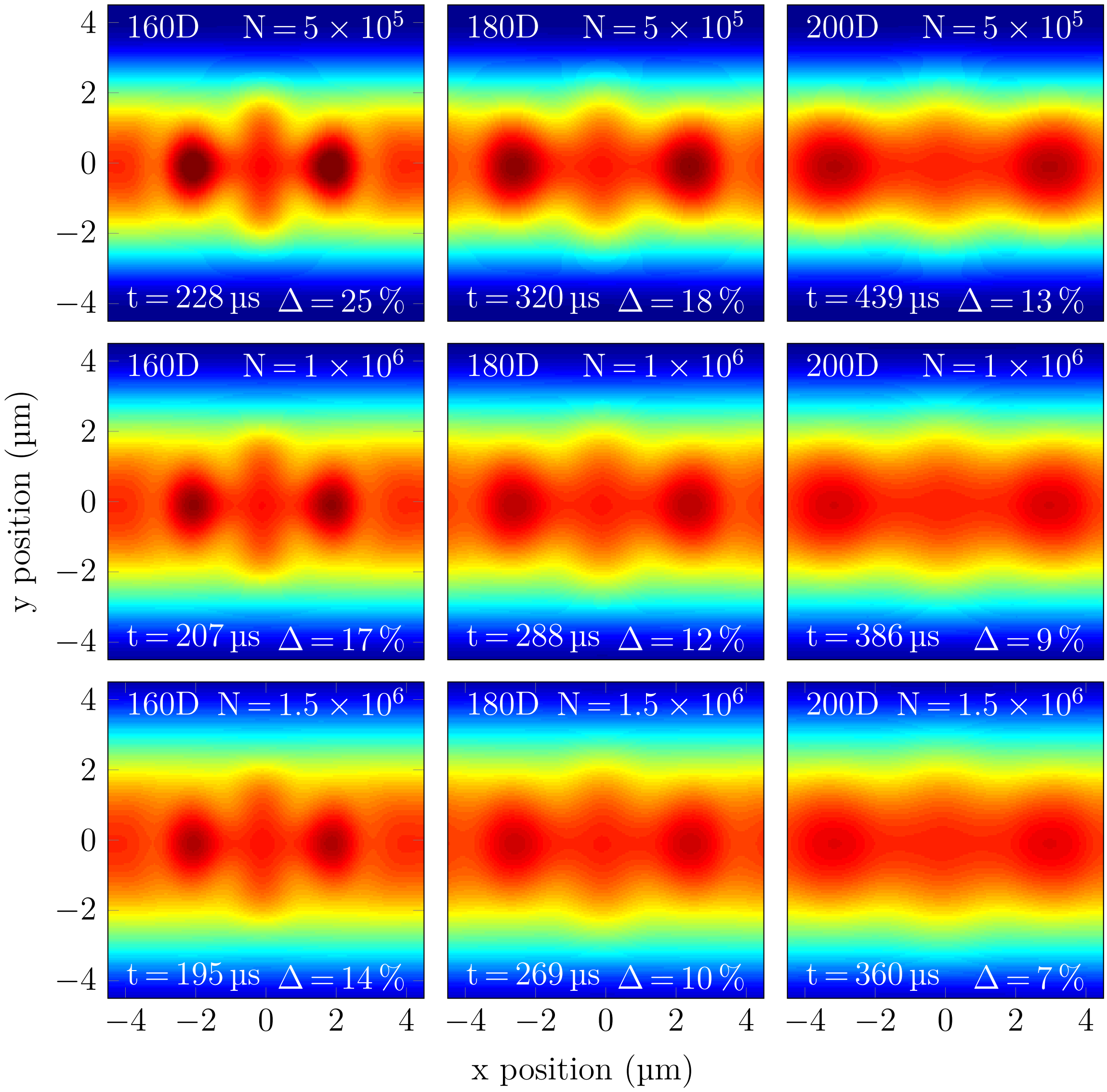

Fig. 8.10: Comparison of the simulated density change for different quantum numbers and BEC sizes for the case in which the Rydberg atom is re-excited. Compared to the imprint of the single Rydberg excitation shown in figure 8.8, higher principal quantum numbers are suited to imprint the wave function. The potential depth in the simulation is $V_{\mathrm{Ryd}}/2$, which means that for half of the total time the Rydberg atom is excited. All states were simulated for 2.4 ms and for each state the picture with the highest density change is drawn with the respective time t in the bottom left of each picture. The total atom number N is shown in the top right, whereas the relative density change Δ is given in the bottom right.

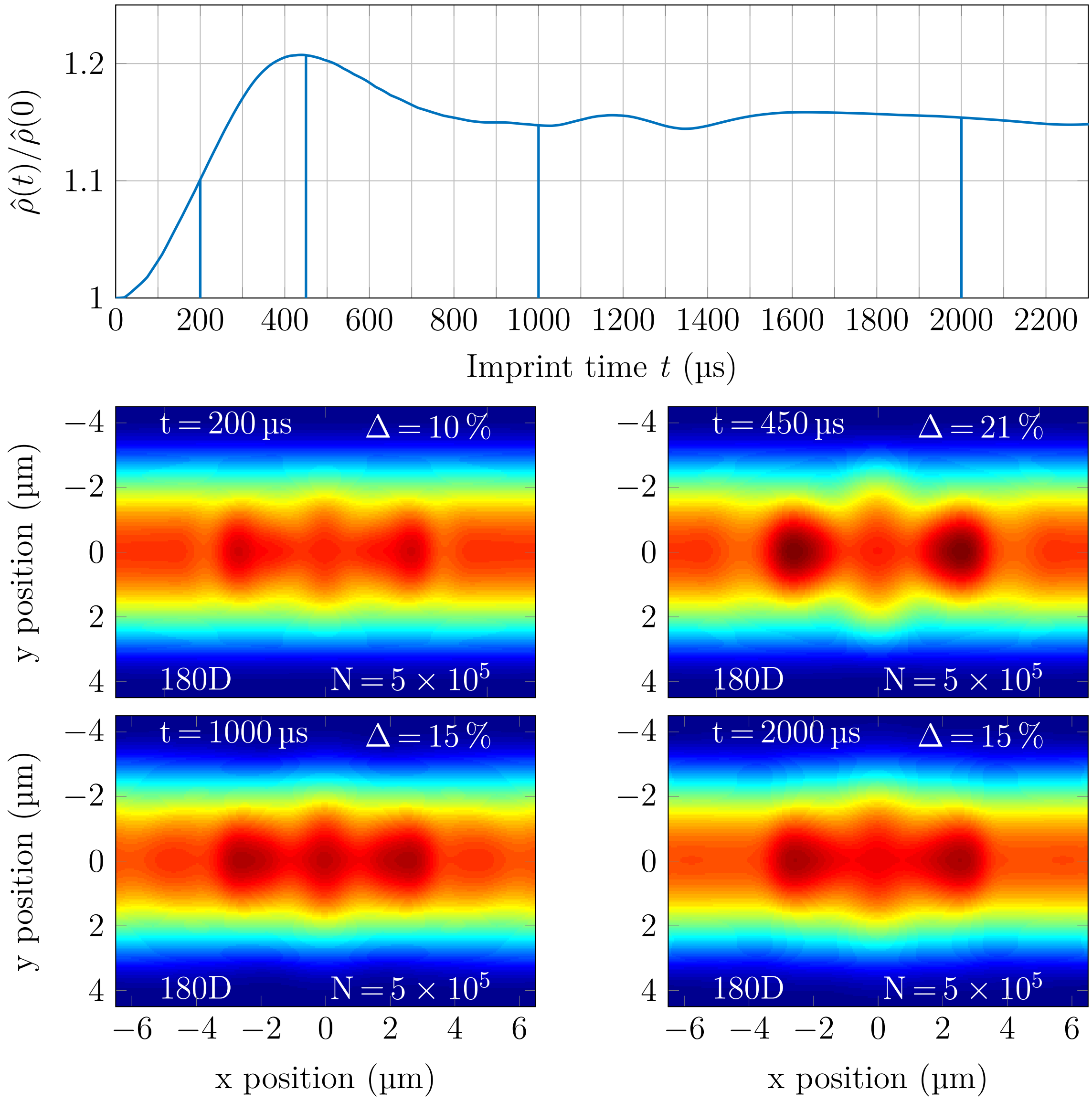

Fig. 8.11: Time evolution of the simulated column density with an imprint of a 180D $m_J = 1/2$ Rydberg atom. The potential depth in the simulation is $V_{\mathrm{Ryd}}/2$, which describes the case where a Rydberg exists in total for $t/2$. In the beginning of the time evolution the density change increases until a maximum is reached at $t = 450\,\mu\mathrm{s}$. Afterwards, the contrast drops again as the system is evolving into the new equilibrium state.

By simulating different relative imprint time fractions a, it turns out that the density change is, to first order, proportional to the time fraction a the Rydberg atom is in the condensate, as shown in figure 8.12. The challenge with this method is to keep this time fraction as high as possible without disturbing the imprint of the Rydberg electron by the re-excitation significantly.

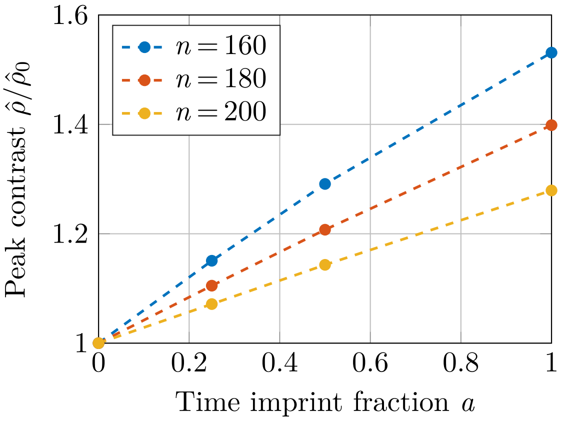

Fig. 8.12: Density constrast for different imprint time fractions a.

Conclusion

The attractive interaction of a Rydberg electron and the surrounding ground-state atoms creates a potential inside the Bose-Einstein condensate, which spatially mimics the absolute square of the electron wave function. The density distribution of the Bose-Einstein reacts to this potential imprint and, even if the Rydberg atom decays after tens of microseconds, the atom density increases at the positions where a high electron density has been over the next few hundred milliseconds. This density change can be directly optically imaged in real space with phase contrast imaging for example. The density change expected for a single Rydberg atom can be, for example, 30 % for a 140D $m_J = 1/2$ state with an orbital radius of 2 µm, so that the density change should be observable even in a single image of the Bose-Einstein condensate. Alternatively, Rydberg atoms can be excited consecutively to imprint higher principal quantum numbers and, for example, a density change of 21 % is expected for a 180D $m_J = 1/2$ state with an orbital radius of 3.3 µm. Hence, for the first time, the quantum electron wave function of a Rydberg S or D orbital could be made visible in a single shot experiment.

Conclusion and Outlook

The main contribution of this thesis to the research field of Rydberg atoms is twofold. First, a new apparatus to study Rydberg physics with ultracold rubidium atoms was designed and built up. With the new apparatus, second, the fundamental interactions of a single Rydberg atom and a Bose-Einstein condensate were studied.

New apparatus to investigate ultracold rubidium atoms

In the first phase of this doctoral research study, a versatile new experimental apparatus to investigate Rydberg atoms within an ultracold rubidium ensemble was built up. The design goals were set such that even a single Rydberg atom in a Bose-Einstein condensate could be investigated. As a result, the new apparatus can examine events which happen rarely with count rates well below one. This is possible due to the high signal-to-noise ratio from the excitation to the detection of the Rydberg atoms, and the long-term stability of the experiment. The safety mechanisms installed give the possibility of running the experiment over several days without supervision.

With the new setup we are able to excite Rydberg atoms with a 2.1 µm focused beam, and have an imaging system in place which has a resolution on the 1 µm scale. The pressure inside the science chamber is in the 10^{-11} mbar range and the magnetic trap is stable enough to hold the atoms for a few seconds without heating the sample significantly. A large, cigar shaped BEC of 1.7 million atoms is created every 25 s with a diameter of 10.2 µm in the radial and 136 µm in the axial direction. A single BEC can be probed several thousand times within an experiment cycle.

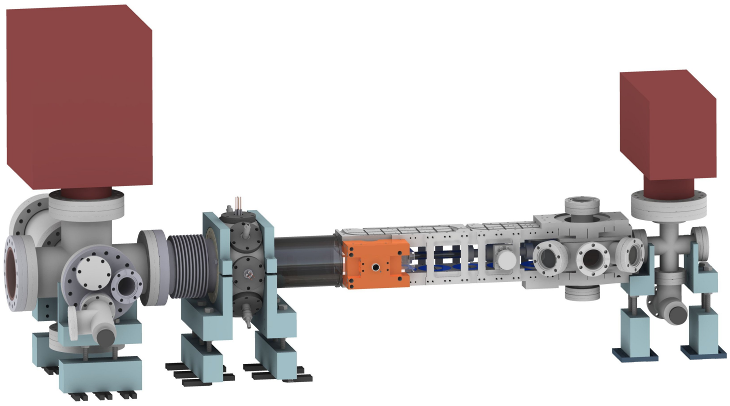

Engineering drawing of the experimental apparatus.

Several electronic components were developed during the building-up phase to meet the design goals. For example, the laser frequency can be changed several thousand times during a measurement of a single BEC reliably with the DDS frequency controller. The new devices developed are now used in several laboratories because of their good performance and reliability, as well as the universal experiment control software developed. The control software was written in C# as an up-to-date programming language. The control system should be maintainable over the life time of this experimental apparatus, which could be over a decade, as evidenced by the previous ultracold rubidium Rydberg experiment in Stuttgart. The imaging and evaluation software was implemented with modern design concepts and patterns in Matlab. Several extensive measurements can be evaluated with a single line of code and a caching system makes multiple analysis of the same measurement very efficient. Finally, all experiment cycles, which were ever performed, can be loaded again in the computer control or image evaluation software so that old measurements can be reviewed simply by typing in the unique count number of the experiment cycle.

The new apparatus is not specialized for a particular kind of experiment. With the possibilities at hand: the good and fast electric field control, the high detector efficiency, the very accurate optical resolution for the excitation and detection, the big and stable BEC, very different aspects of Rydberg atoms in an ultracold gas can be studied. These possibilities gave rise to investigations of the fundamental interactions of a single Rydberg atom and BEC. The elastic and inelastic collisions of a Rydberg atom with the surrounding ground-state atoms were examined in detail for quantum numbers from 40S to 149S. By exploring the very high density regime of ultracold atoms various aspects limiting the lifetime of a Rydberg atom are now understood, which is relevant, for example, for Rydberg experiments in increasingly denser environments in quantum optics [99, 100], quantum information schemes [28], quantum simulation [27], for studying electron-phonon interactions in a BEC [S4, 39, 101], polaron formation in dense quantum gases [102, 103], and production of ultralong-range molecules [19, 79, 80, 86]. The new insights and the conclusions of the work presented in this thesis is summarized in the following sections.

Rydberg Spectra in a BEC and elastic collisions

The spectra of a single Rydberg atom in a BEC [S1] can only be understood by the means of the involved potential energy curve of the Rydberg atom and a ground-state atom. Especially important is the p-wave shape resonance present in ^{87}Rb [82], which leads to a large energy shift in the spectra because the crossing of the butterfly state [76] with the excited nS state is in the range of the mean internuclear distance of particles in the BEC ($1300\,a_0$).

A new model which explains the measured spectra was developed, treating the atoms inside the Rydberg orbit as point-like particles, which is a very simple, but sufficient approach. Each single particle locally probes the potential energy curve and adds to the total energy shift of the Rydberg atom. This assumes no backaction of the particles onto the Rydberg electron wave function, which is valid as long as the ground-state atoms are outside the small region where the butterfly state crosses the excited nS state. The model agrees very well with low Rydberg states (40S) but deviates more and more for higher (111S). The main difference between these two Rydberg atoms is the mean number of ground-state atoms inside the orbit, which changes from 6.5 to 4100 for the peak density of $5.2{\times}10^{14}$ atoms/cm^3. While the number of particles is increased, the mean interaction strength drops from $h \times 7.8\,\text{MHz}$ to $h \times 12\,\text{kHz}$ where h is the Planck constant. With the large radial size, the large number of atoms inside the orbit, and the low interaction strength, the model loses its applicability which can be seen from the spectra measured, which is a topic for further investigations.

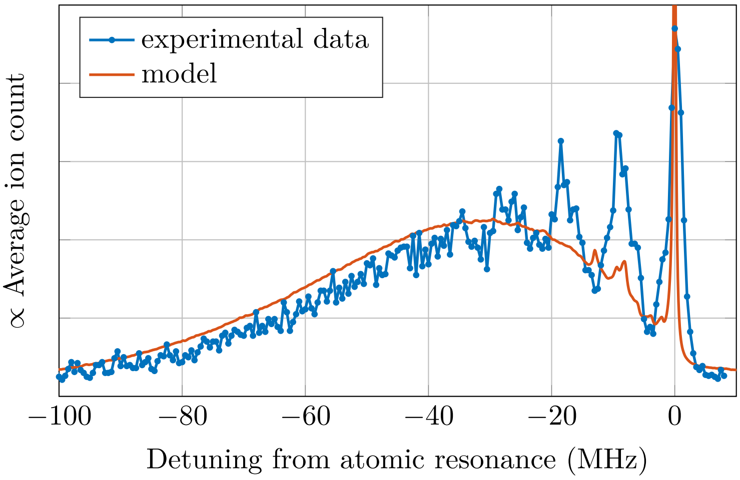

40S Rydberg spectrum with the simulated spectrum from the model developed.

Rydberg atoms as a density probe

The density shift of a Rydberg atom from Fermi's pseudopotential [70] is independent of the principal quantum number, and proportional to the density, with a shift of approximately 10 MHz for 10^{14} atoms/cm^3. The Rydberg electron probes the local density, or, by inverting the relation, the local density in resonance can be chosen by the laser detuning. The number of atoms N within a Rydberg orbit must be large enough to overcome the relative atom number fluctuation inside the orbit ($\sqrt{N}/N$), which otherwise leads to shot-to-shot deviations from the mean shift expected. The density probe technique was tested with 90S Rydberg atoms by moving the focused excitation through the narrow axis of a BEC. The measured signal agrees very well with the expected signal from the point-like particle model, which goes beyond the approach of Fermi and includes the full potential energy curve. The limits of this technique, especially for high principal quantum numbers for which the modeled spectra begin to deviate from the spectra measured, are still a topic to investigate. But with this tool at hand [S2], the position of the Rydberg excitation is not only determined by the spatial overlap of the excitation lasers, but in addition by the resonant density volume corresponding to the laser detuning. This can localize the excitation especially in a system with steep density gradients like a Bose-Einstein condensate.

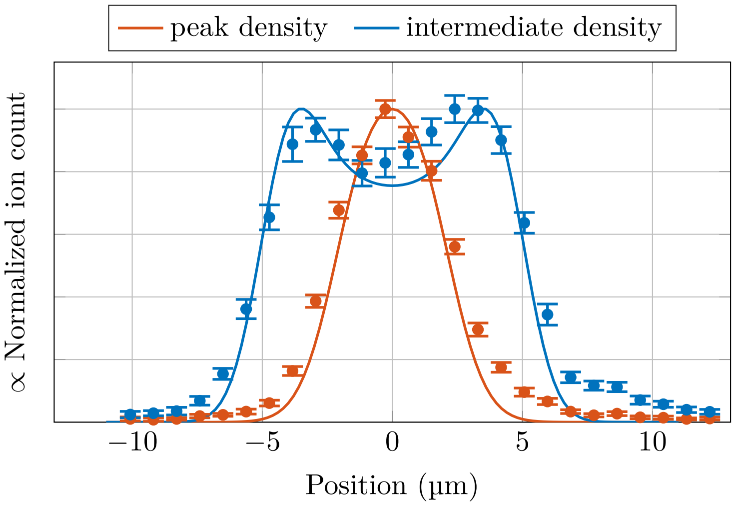

Experimental test of the Rydberg (90S) density probe by scanning the laser through the BEC with two different laser detuning. The simulation and the experiment agree.

Quantum chemistry and inelastic collisions

If a Rydberg atom has time to evolve after the Rydberg excitation, two reaction products are observed as a result of an inelastic collision of the Rydberg atom and a ground-state atom [S3]. Either a deeply bound Rb_2^+ ion is created, or the Rydberg atom changes its orbital angular momentum and gains kinetic energy together with the scattering partner. The branching ratio for both reactions products is equal for 40S Rydberg atoms in the BEC and drops for higher principal quantum numbers. Above $n = 90$, the fraction of Rb_2^+ molecules is below 10 %. The l-changing collision time ranges from below 1 µs at 53S to more than 10 µs at 149S. The molecule formation time is approximately 50 % to 100 % slower. The collisional lifetime increases unexpectedly in the range of 90S to 110S independent of the investigated background density.

It is very likely that the butterfly state plays a key role for the inelastic collision time. Within the introduced point-like particle model the butterfly state accelerates the collision. The measured fast collision time for low principal quantum numbers can only be explained by this additional attractive potential. At high principal quantum numbers, the collision is too slow compared to the simulations even without the butterfly potential. Hence, there must be a mechanism which prevents these inelastic collisions for higher n, which is open for investigation. Quantum reflections at the butterfly state potential energy curve could play a role as they are important in stabilizing ultralong-range Rydberg molecules [38]. The reaction mechanism for deeply bound Rb_2^+ molecules is also a topic for further investigations. It could be possible that the molecules can only be stabilized at lower n, because the energy of the Rydberg electron compared to the ionization threshold drops for higher n. Hence, the energy available to stabilize Rb_2^+ molecules is reduced.

In the following sections currently ongoing projects, ideas, and suggestions for the future, which are possible to realize with the new experimental apparatus are presented.

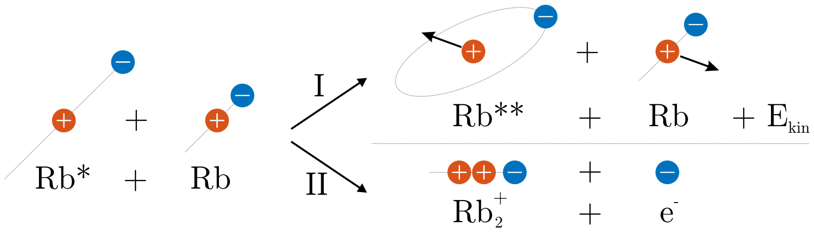

Investigated inelastic collisions.

Electron wave function imaging

The interaction of the Rydberg electron with ground-state atoms inside the Rydberg orbit creates an attractive potential, which modifies the BEC wave function in the time evolution of the perturbed system. The change in atom density reflects the electron probability density of the Rydberg electron. After studying the interplay of the different tunable parameters, two experiments are proposed [S4] to image the angular structure of a Rydberg electron orbit as an imprint on the density of a Bose-Einstein condensate. This should be possible even with a single shot experiment.

This new imaging technique gives the ability to visualize all kinds of electron wave functions, for states which are stable for tens of microseconds. For example, a butterfly state could be excited to see the interesting shape of the orbital and to compare it to theoretical calculations. Also, multiple Rydberg excitations could be written in the BEC at defined spatial positions with a spatial light modulator to study the interplay of the Rydberg atoms.

It will be interesting to see the limits of the different approaches applied in this thesis: The collisions of the Rydberg atoms in an ultracold gas were described semi-classically as point-like particles inside the potential energy curve. The electron wave function imaging is based on the time evolution of a Bose-Einstein condensate as a quantum object. The limits of the latter model will become visible as soon as the experiments of the electron wave function imaging will be performed.

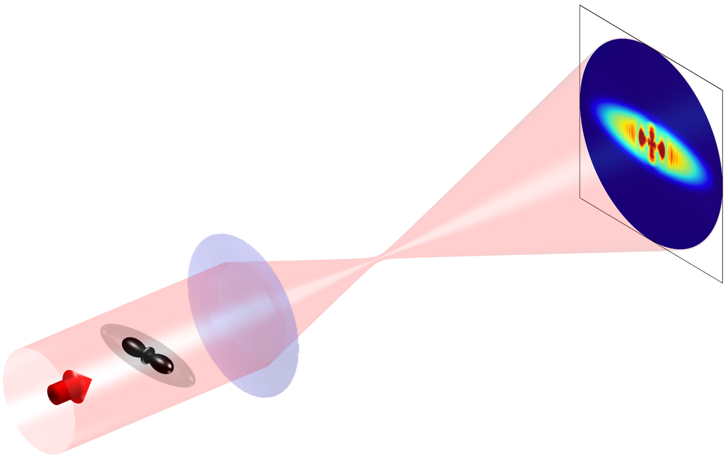

Imaging the imprint of a Rydberg electron orbit on the density of a BEC.

Reaction mechanism of Rb_2^+ creation

Some aspects of the quantum chemistry creating deeply bound Rb_2^+ molecules inside a Bose-Einstein condensate were investigated already within the work presented [S3]. It should be possible to understand the mechanism of ionic molecular formation in detail with a systematic study of the Rb_2^+ fraction created, the collision time for different initial states (S, D), and the density dependence of the process. The autoionization can be studied in addition with the second electron/ion detector installed, so that one detects the electron and the other the ion. There must be an interesting interdependence between the Rb_2^+ signal and the potential energy curve which can be seen already in a 40S spectra measured. It was observed that deeply bound Rb_2^+ molecules are not created from the atomic line or ultralong-range molecules, at least not on the same time scale.

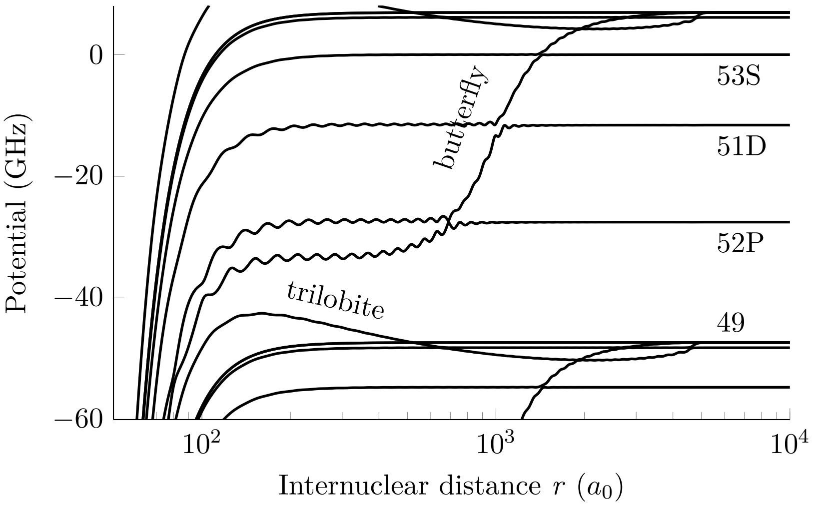

Potential energy curves of possibly involved states for the molecule formation for the 53S Rydberg state.

A single ion in a Bose-Einstein condensate

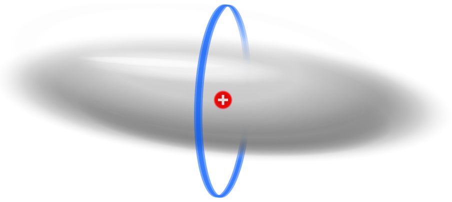

Fig. 8.13: Circular Rydberg atom with the electron orbit outside the BEC.

One future prospect for the experiment is to create a single ion inside the BEC. This can be achieved by exciting the Rydberg atom to a D state at a very high principal quantum number ($n \geq 200$, $r \geq 4\,\mu\text{m}$) and then transferring the Rydberg electron to a circular state along the narrow direction of the BEC. Hence, the electron would be outside the condensate and only the Rydberg atom core, which is effectively an ion, would interact with the BEC.

The interaction of the ion is dominated by the long range ion-neutral interaction ($r^* \sim 5000\,a_0$) in comparison to the short range interaction of the electron with the neutral particles ($r^* \sim 18\,a_0$), due to the mass difference and the different scattering length. With a mean interparticle spacing of only $1300\,a_0$ for the peak BEC density, the interaction is no longer binary but many-particle which can be described by the means of a polaron.

The quasi-particle originates from solid-states physics describing the motion of the electrons deforming a crystal. Polaron physics is involved in very famous phenomena like the colossal magnetoresistance [146] or high-temperature superconductivity [147]. An ion inside the Bose-Einstein condensate can capture hundreds of atoms into loosely bound states leading to mesoscopic molecular ions [103]. The impurity should lead to a self-trapping potential within the condensate [148], but the condensate can also collapse in a bosenova-like explosion [149] if the impurity deforms the atom density in the neighborhood too strongly. Polarons in the Bose-Einstein condensate would, for example, allow one to test predictions from the strong coupling regime in many body physics, which is not experimentally reachable in solid-state systems [102].

The polaron is only strongly coupled if s-wave scattering dominates the interaction. This can be achieved by exciting the Rydberg atom into a high circular Rydberg state [47, 150, 151]. The applicable excitation techniques would mean that the Rydberg core stays ultracold ($< 1\,\mu\text{K}$) and is able to probe the strong coupling regime in contrast to ion traps, which suffer from residual micromotion of the ion in the trap [152].

The newly designed apparatus has the capability to realize and test the ideas suggested. The single ion at ultracold temperatures inside the Bose-Einstein condensate is a milestone which would open up the field for a variety of new experiments.

Excitonic energy transport

Another interesting field of study which can be addressed, is quantum biology. It is known from research on light harvesting bacteria [153] that quantum effects play a key role [154] for the fast and efficient energy transport in the photosynthesis process of these animals. Theoretical studies of this topic [155–158] gave the first insights into how this energy transport on a mesoscopic scale requires quantum mechanics. This process can be mapped onto Rydberg atoms [32, 159] and first experiments have been performed [30, 31, 160] which show the possibility to simulate different aspects of the quantum processes with Rydberg atoms as a quantum simulator in a very simplified environment. The key ingredients, such as the coherent dynamics, disorder, and dephasing, are the same in the living system and the Rydberg system.

The new experimental setup provides the tools to study this interplay systematically. The energy transport nodes (Rydberg atoms) can be written into the atom cloud precisely with a spatial light modulator. One of the Rydberg atoms is afterwards driven to a higher state and the created exciton travels through the transport network due to the Rydberg-Rydberg interaction, and can be probed at any time. In such a system, the positions of the nodes can be modified (spatial light modulator), the coupling strength be changed (Rydberg state), and additional dephasing can be introduced (e.g. with a laser manipulating certain nodes).

The emerging field of quantum biology [33] raises many questions of our knowledge of nature. Our tailored quantum system is capable of answering questions at the intersection of quantum mechanics and thermodynamics which will be interesting to explore.

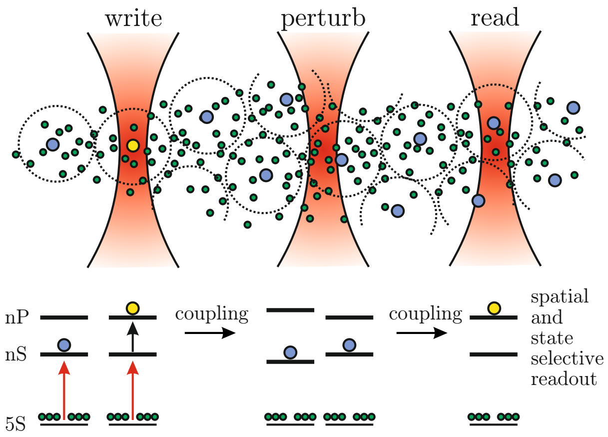

Schematic illustration of the excitonic energy transport in a Rydberg system.

A

Electronic Control

A.1 PID controller

An overview of the self-built PID controller is given in section 3.1. The design is based on a PID controller from the Massachusetts Institute of Technology, which is modified and upgraded. It is crucial that the operational amplifiers of this version are soldered directly onto the PCB, without using sockets. The additional stray capacitance of the socket would lead to a lower total bandwidth of the system. Here, the different stages of the controller are described with the schematic shown in figure A.1. The PID controller can be split up in three sections: the input, controller, and output stage.

Input stage The input stage can handle two different analog inputs: the inverting input (IC1A) and the non-inverting input (IC1D). An offset voltage can be added with the ERR_OFF potentiometer to the error signal and sets the lock voltage. The offset adjustment is non-linear and the range is limited to $\pm 1.36\,\mathrm{V}$ with resistor R27 and R47. All input and offset signals are summed up at IC1B. The error output is isolated over a buffer amplifier IC1C from the main signal.

PID stage The error signal within the controller section has three different pathways, each for one component. The P term is generated by IC6A with a variable gain setting from potentiometer R53. The total gain can be modified by exchanging the resistor R52 or potentiometer R53 of the inverting amplifier stage.

The integrator is realized with IC6C and the gain settings can be modified with potentiometer R48. Resistor R15, potentiometer R48, and capacitor CI determine the integration constant for the integrator and can be replaced, if the adjustable range does not meet the requirements.

The derivative part has to be activated with jumper D and is set by potentiometer R50. Resistor R58, capacitor CD, and potentiometer R50 determine the time constant and can be replaced, if necessary.

All three PID components can be activated with a switch on the front panel. It should be noted that each switch is connected to an integrated circuit switch (ADG221) which has a typical on resistance of 60 Ω. The switches act as a bypass for the feedback resistor/capacitor of the different operational amplifiers of the PID components. The finite on-resistance leads to a small leaking control signal, even if a component is deactivated by the external switches.

The rare but most common hardware defect of the PID controller is the analog switch IC4/IC8 and should be replaced first in case of an error.

Output stage The different signals from the PID components are summed up at IC11A in addition to an adjustable output offset and a scan input. The latter is deactivated as soon as the P controller is switched on with the analog switch IC4. The output offset can be set with the OUT_OFF potentiometer and is limited to ±1.36 V with Resistor R29 and R30. After the summation, the signal is routed to the FAST output, which can be inverted with jumper JP-FAST and JP-FAST2. In addition, this signal is routed to the SLOW output, which includes a low pass filter with resistors R37, R54, potentiometer R51, and capacitance CSL. The signal can be inverted with jumper JP-SLOW and JP-SLOW2. The SLOW output can control, for example, a piezo input stage of a laser, or can be directly applied to a piezo if the buffer amplifier LT1010 (IC-BUF) is soldered in, which can drive up to ±150 mA.

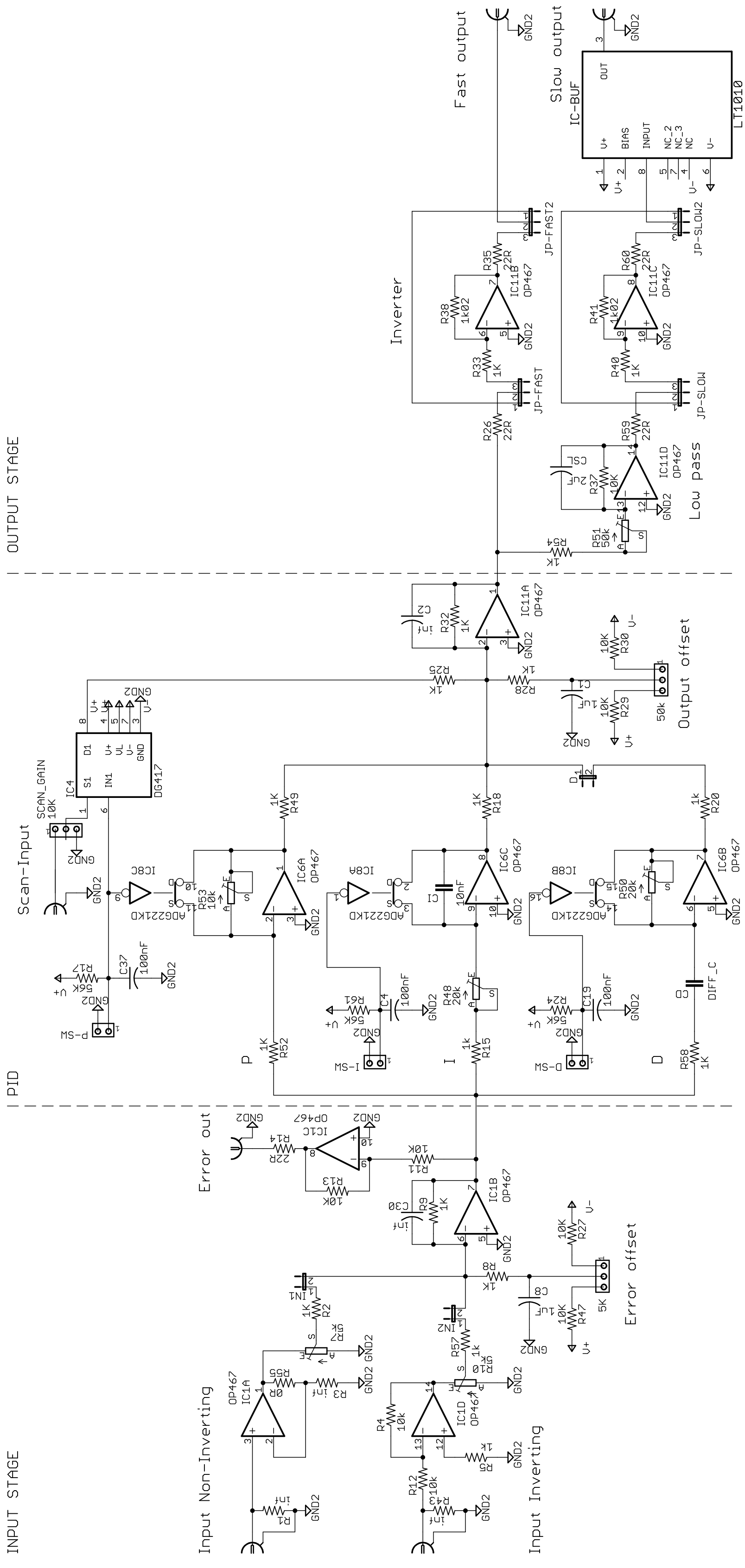

Fig. A.1: Schematic of the PID controller.

A.2 Isolated digital output

Every digital output signal from the National Instruments cards is isolated from the original ground plane with the isolation card shown in figure A.2. The isolation itself is realized with the ADuM6200C (ISO1) integrated circuit. The advantage of this integrated circuit is that not only the output signal is isolated but also a ground free supply voltage is provided for the output side. Hence, no additional DC/DC converter is required to power the isolated output side. The typical propagation delay for the digital isolator is 50 ns. The isolation integration circuit is followed by the 74ACT244 (IC1B) line driver which can drive 5 V into 50 Ω. Hence, it is possible to terminate output signals and to avoid signal reflections. Each card provides two output channels which share the same ground but are isolated from the input side. The output voltage can be changed between 3.3 V (default) and 5 V with switch S1. If 5 V are required, only one channel can be driven into 50 Ω, otherwise the power consumption exceeds the specifications of the power source (ISO1).

The digital input signals (IN_A and IN_B) can be overwritten with manual switches on the front panel for test purposes. Therefore, a circuit with two NAND Schmitt triggers [161] (MC74ACT132) is inserted into the signal line. Each Schmitt trigger has a propagation delay of typically 5 ns. A flip-flop circuit (e.g. IC3A and IC3B) is applied for debouncing the switches which avoids fast jumps back and forth of the output signal when the manual mode is chosen.

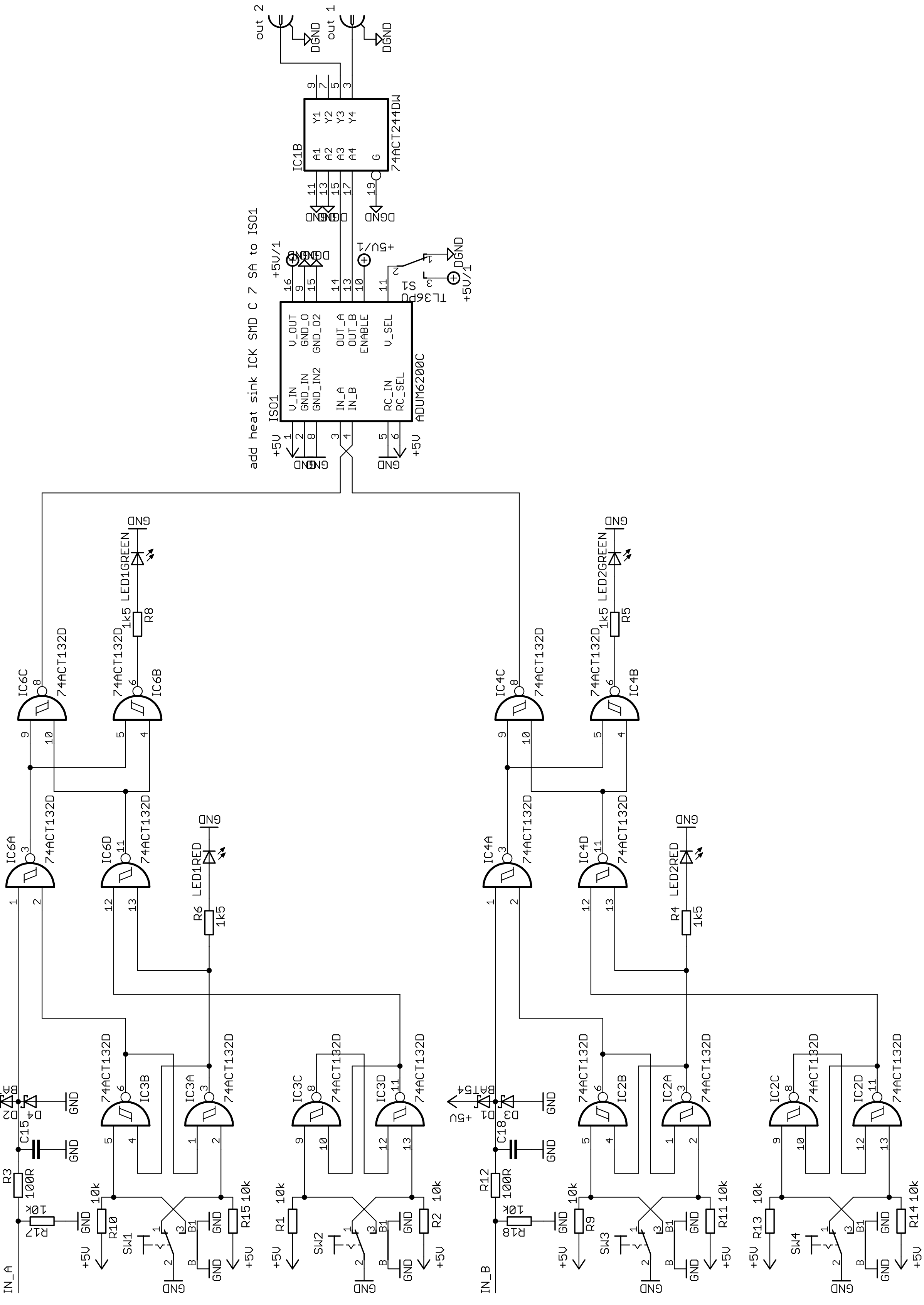

Fig. A.2: Schematic of the digital signal isolator.

A.3 Isolated analog output

The analog output isolation board is based on the isolation amplifier ISO124, which can be seen from the schematic shown in figure A.3. The high voltage offset of up to 50 mV demands an offset compensation circuit. The compensation voltage can be adjusted with the potentiometer OFFSET, which modifies the reference voltage of IC2A. A 2-pole low pass filter (IC2A and IC2B) at 100 kHz suppresses the output ripple of the amplifier, which is 20 $\mathrm{mV_{pp}}$ caused by the carrier frequency (500 kHz) of the signal transmission inside the isolator. A line driver (BUF634, IC7) is included in the feedback loop of the last amplifier stage so that an output voltage of ±10 V can be driven into 50 Ω. The gain of the amplifier can be fine adjusted with the GAIN potentiometer. The total gain can be set with resistor R5 with respect to the feedback resistor R4.

The isolated output supply voltage is generated by a Traco TEN3 DC/DC converter (PWS1). An optional DC/DC converter (PWS) can be soldered in for the input section so that the input is also isolated from the supply powering the whole board.

A bode diagram for the frequency response of the analog isolation card is shown in figure 3.6.

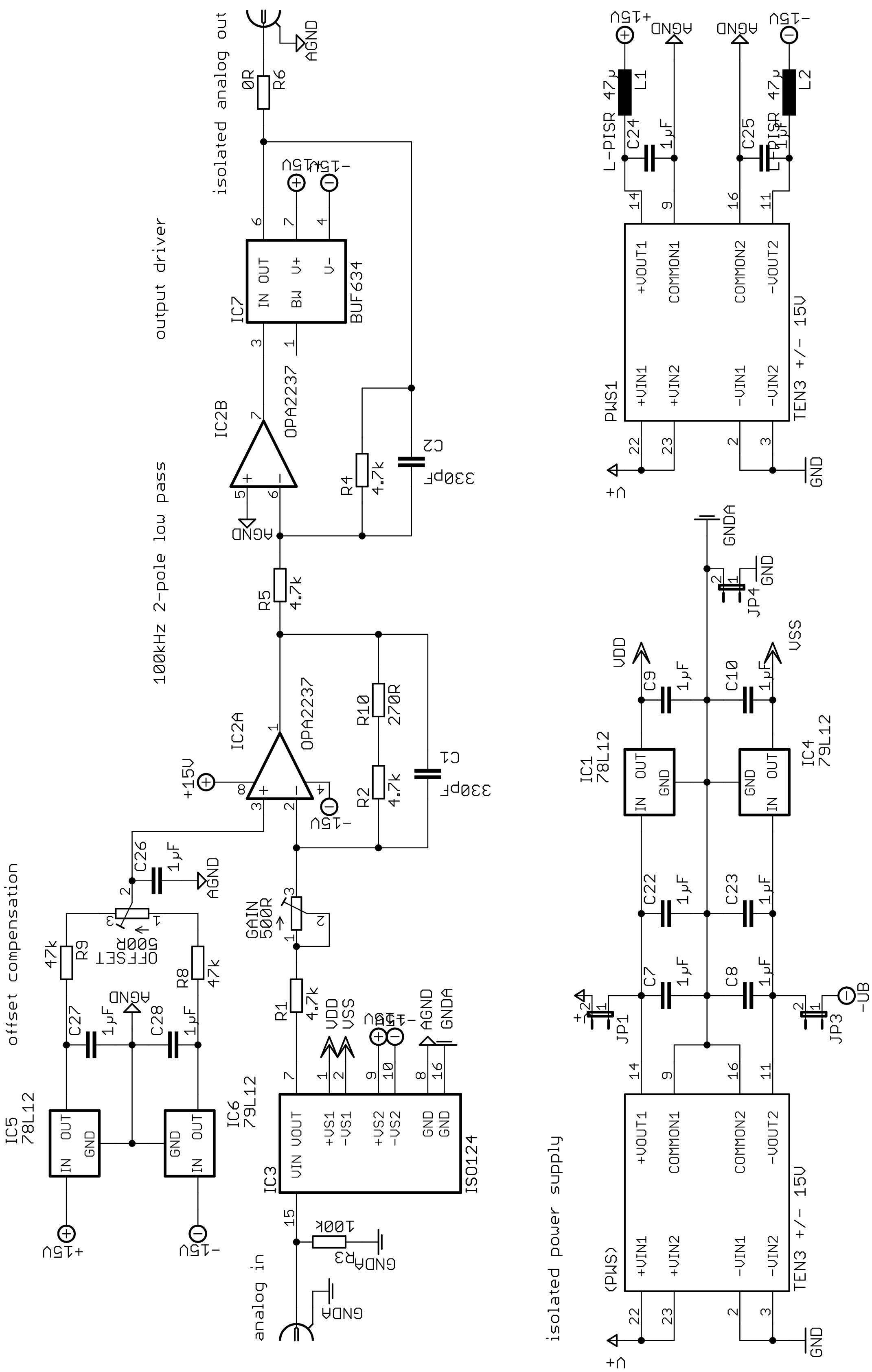

Fig. A.3: Schematic of the analog signal isolator.

A.4 IGBT driver

The electronics to power the coils for the magnetic transport and the traps has been described in section 3.4. Here, the schematic of the IGBT driver board is shown (figure A.5), and briefly discussed.

Every single power supply can only control the current of one coil (pair) at a time. It is possible to switch between the coils with the IGBTs installed. The address of the active coil can be selected with two digital channels and a two bit demultiplexer. The push-pull, rail-to-rail comparator LMC6762 (IC1-IC3) converts the digital signal into an output voltage of 0 (low) and 15V (high). This voltage level is required to reach the specifications (low drop, fast switching) of the IGBTs used. A resistor can be activated in parallel to the coils with the BYPASS channel. This can be used to smooth the turn on behavior of the coils. The resistor is not activated in the current experiment cycles because the current in the coils shows only a small overshooting in the very beginning, as shown in figure A.4.

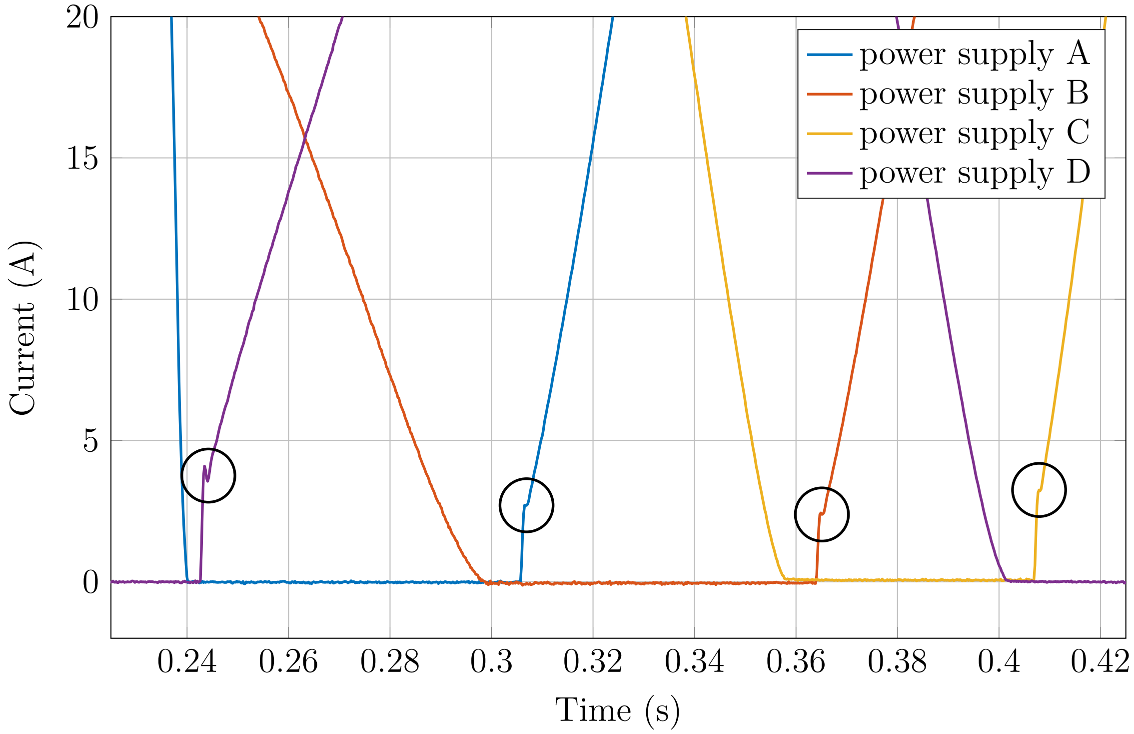

Fig. A.4: Overshooting of the turn on current of the coils (highlighted with the black circles). The diagram is a zoom in of the graph shown in figure 3.7.

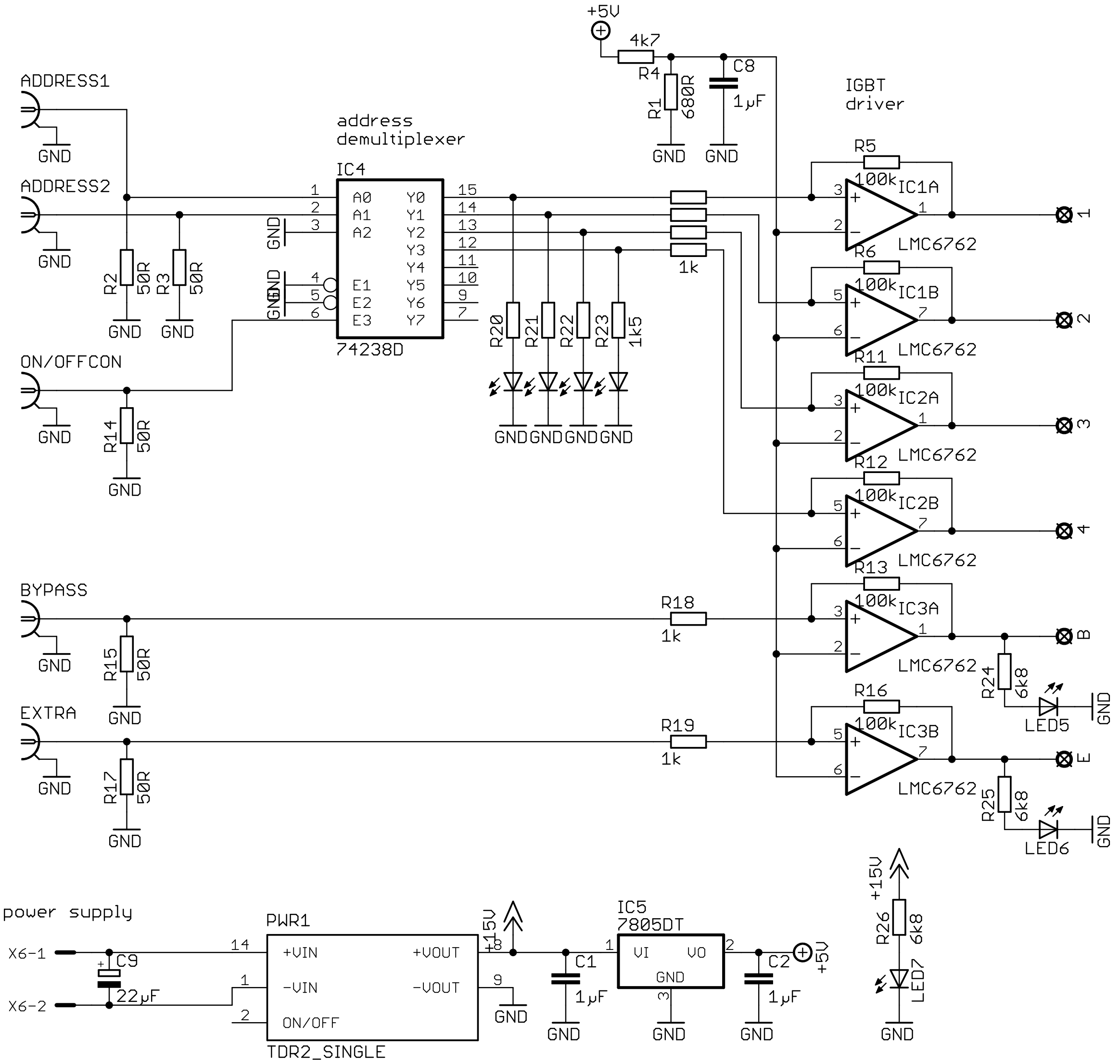

Fig. A.5: Schematic of the address demultiplexer and the IGBT driver.

A.5 Frequency generation via direct digital synthesis

The evaluation boards for the AD9858 (1 × 500 MHz) and AD9959 DDS (4 × 250 MHz) provide the required peripherals to generate the sine wave output without additional components. Only the chip itself has to be programmed, which is done by the self-built DDS controller board. An Arduino Due microcontroller with a core clock of 84 MHz and the built-in hardware serial peripheral interface (SPI) provides the functionality required to communicate with the DDS chip.

The schematic of the controller board is shown in figure A.6. Since the Arduino Due has no EEPROM on chip, an external EEPROM (24LC256, IC6) is attached to be able to load the last parameters used when the device is turned on again. The X-ENC inputs can be used to attach a rotary encoder and switch. The X-DISP communicates with the I2C display (LCD2004). The X-TRIG inputs are the main trigger inputs to change the frequency synchronously with respect to the experiment sequence. The ANALOG/AUX IN inputs can be used either as additional trigger inputs or to control the output frequency with an analog input. The second serial port of the Arduino is used to communicate with the computer control, with the signal is isolated with an isolated RS-232 line driver/receiver (ADM3251E, U1), to avoid ground loops. The unused internal USB serial port of the Arduino has the disadvantage that the Arduino resets every time the port is opened. The DDS evaluation board is connected over the flat band cable connector SV1 to the controller board.

Both DDS chips (AD9858 and AD9959) are programmed over the serial peripheral interface, which limits the minimum time to change the output frequency (4.5 µs). The faster DDS chip (AD9958) can also be programmed with a parallel interface. It would be an option to attach the parallel interface to the Arduino to speed up the communication, if required.

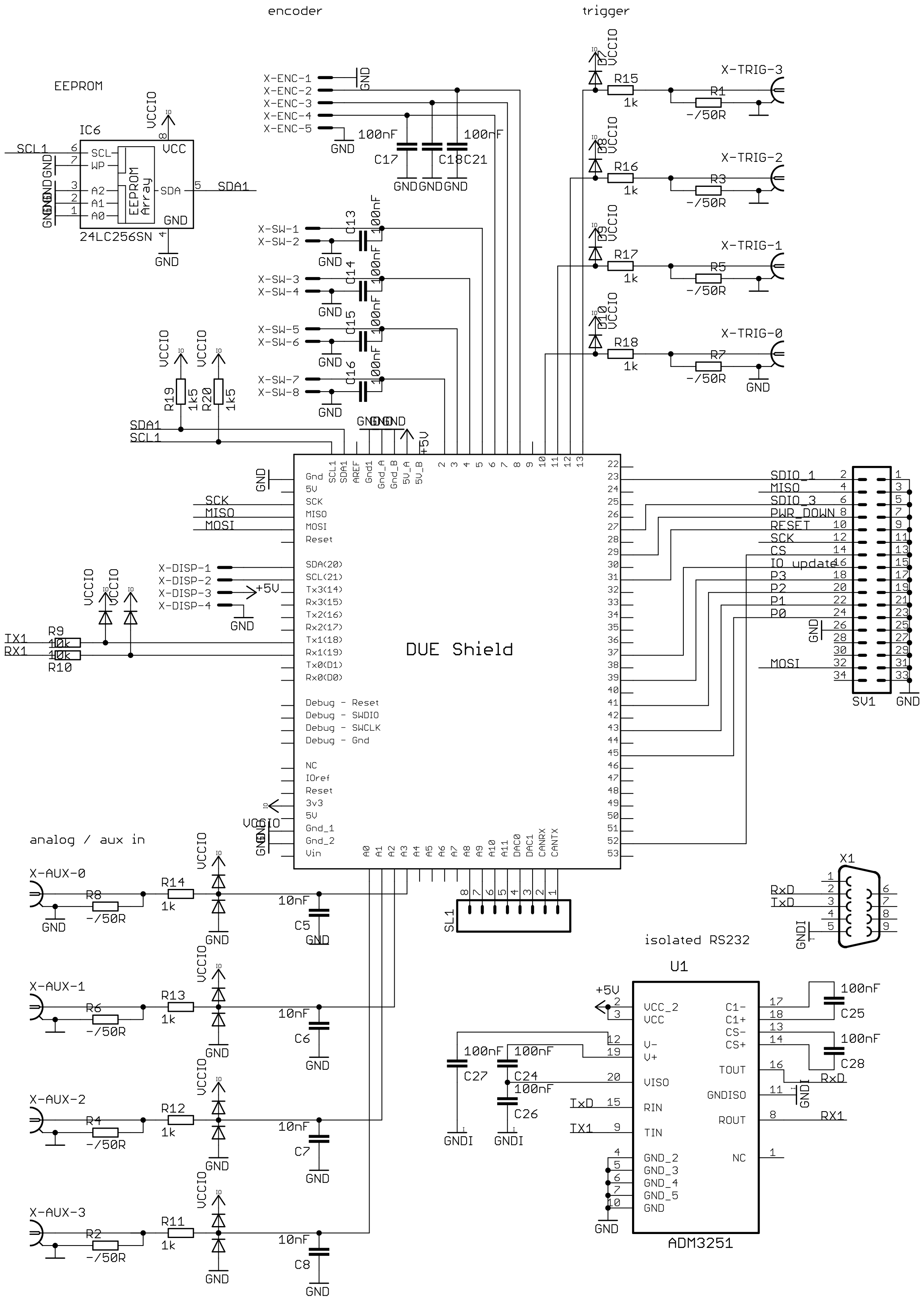

Fig. A.6: Schematic of the controller of a AD9959 DDS evaluation board.

A.6 Monitoring system of the experiment

The critical components which can cause physical damage to the experiment are the coils in the case of overheating, which can happen when the coils are not cooled properly or the current is on for too long at a too high current. The coils cannot withstand a continuous high current even if they are water cooled. Due to the space constraints, and the small geometry they have to have, no hollow conductors could be used for winding the coils. Instead, $2 \times 1\,\mathrm{mm}$ copper wires were used and the whole coil is cooled from the outside.

A surveillance system of the experiment was developed which protects from many possible error cases, which also incorporates redundant sensors (see section 3.5). The schematics of the surveillance controller are shown in figure A.7. An Arduino Mega was chosen as the microcontroller because it has many digital and analog input and output pins. Compared to the Arduino Due, it is powered with 5 V, which is advantageous for the devices and sensors connected.

For each power supply, one transducer is connected to monitor the output current (X21-X24). Together with the known resistance of the coils and the information about the currently active coil (X1-X12), the consumed power of each coil can be calculated and monitored. In addition, temperature sensors are connected to X13-X20 to measure the temperature of the coils and other components which can heat up (e.g. the IGBTs).

A limit for all sensor values is programmed into the microcontroller and if all are in the valid range, a relay in the interlock system of the power supplies unblocks the current output. As soon as a failure is detected, the output is locked until the sensor is in the valid range again. The operator has to press a hardware button to cancel the error.

The Arduino itself is monitored by a watchdog, which is used to detect and recover from malfunctions. It should be noted that not all shipped firmware versions of the Arduino have a working watchdog. The firmware/bootloader can be flashed with modified binaries so that the watchdog timer works properly.

All measured data from the controller can be accessed with the built-in serial USB interface. It should be considered to switch from the built-in serial USB to another serial interface of the Arduino with an additional external serial to USB adapter for the reason that the controller resets every time a connection is made to the built-in interface.

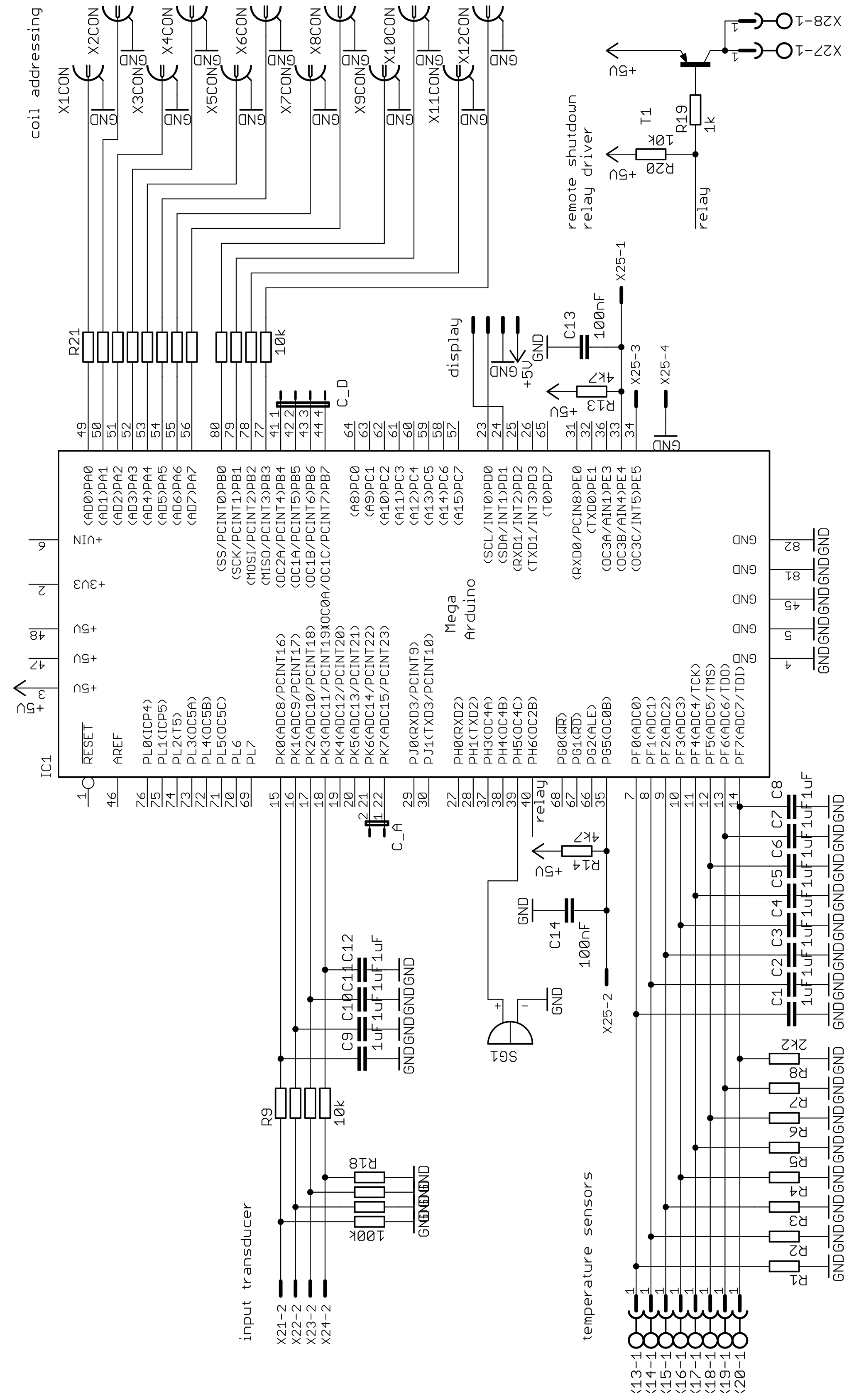

Fig. A.7: Schematic of the surveillance controller of the experiment.

B

Collective Rydberg excitation and dephasing

Rydberg excitations are often treated in the vicinity of many atoms as macroscopic objects, known as superatoms [162]. Due to the high polarizability of Rydberg atoms, Rydberg excitations can blockade each other [163] on a spatial distance of more than 100 µm for high principal quantum numbers. The uncertainty of which of the atoms is excited within the blockade volume leads to the so-called collective Rabi frequency, which is enhanced in comparison to the single atom Rabi frequency by a factor of $\sqrt{N}$ for N atoms inside the Rydberg blockade volume.

But this collective object can also be treated with respect to all included particles, this treatment is presented in the following:

A single atom in the system can be either a ground-state atom $|g\rangle$, or in the Rydberg atom $|r\rangle$. By adding a second atom the system has four states, $|gg\rangle$, $|gr\rangle$, $|rg\rangle$, and $|rr\rangle$, and the Hamiltonian in the rotating wave approximation [164] can be written as

$$H_{\mathrm{RWA}} = \begin{array}{c} \\ |gg\rangle \\ |gr\rangle \\ |rg\rangle \\ |rr\rangle \end{array} \begin{array}{c} \begin{array}{cccc} |gg\rangle & |gr\rangle & |rg\rangle & |rr\rangle \end{array} \\ \begin{pmatrix} 0 & \Omega/2 & \Omega/2 & .. \\ \Omega/2 & 0 & 0 & .. \\ \Omega/2 & 0 & 0 & .. \\ .. & .. & .. & \Delta \end{pmatrix} \end{array} \tag{B.1}$$

when the transition is driven resonantly but with an interaction shift Δ between two Rydberg atoms. Due to the large polarizability of the Rydberg atoms and, as a result, a strong interaction between them $\Delta \gg \Omega$, only one Rydberg excitation can exist in the system at a time in a fully blockaded system. Hence, the $|rr\rangle$ state is never occupied and can be eliminated.

The probability to have a Rydberg atom in the system can be calculated by $P_{\mathrm{Ryd}} = 1 - \rho_{gg}$ where ρ_{gg} is the entry of the density matrix for all atoms in the ground-state. The time evolution can be analyzed in the density matrix formalism with the von Neumann equation [165]

$$\frac{\partial \rho}{\partial t} = -\frac{i}{\hbar}[H, \rho]. \tag{B.2}$$

A system with only a single atom oscillates between the ground-state and the Rydberg state with the Rabi frequency Ω. For a system with N atoms the Hamiltonian leads to the collective Rabi frequency $\sqrt{N}\Omega$, for which an example is shown figure B.1.

Now an individual energy shift δ_i is introduced for each atom. The Hamiltonian for a three atom system is therefore

$$H_{\mathrm{RWA}} = \begin{array}{c} \\ |ggg\rangle \\ |rgg\rangle \\ |grg\rangle \\ |ggr\rangle \end{array} \begin{array}{c} \begin{array}{cccc} |ggg\rangle & |rgg\rangle & |grg\rangle & |ggr\rangle \end{array} \\ \begin{pmatrix} 0 & \Omega/2 & \Omega/2 & \Omega/2 \\ \Omega/2 & \delta_{-1} & 0 & 0 \\ \Omega/2 & 0 & \delta_0 & 0 \\ \Omega/2 & 0 & 0 & \delta_{+1} \end{pmatrix} \end{array}. \tag{B.3}$$

The detuning difference from one atom to the other is set constant, $\delta_i = i \times a$, with a detuning range going from $-\hat{\delta}$ to $\hat{\delta}$ which defines the constant a as $a = \hat{\delta}(N-1)/2$. The consequence of the detuning is a dephasing of the Rydberg atoms and hence, the probability to find an atom in the ground-state system

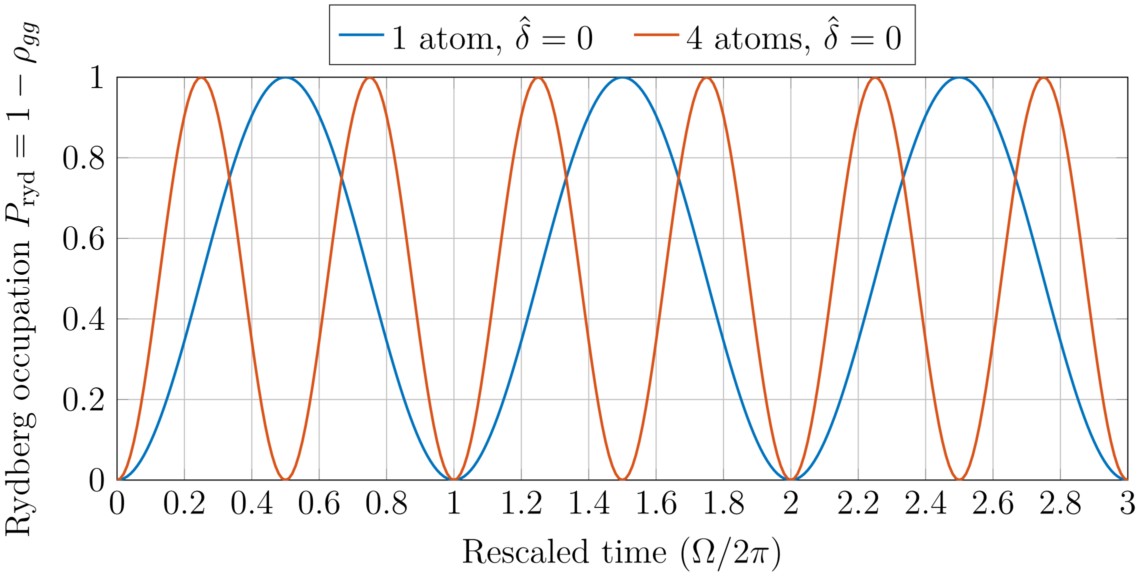

Fig. B.1: Rabi oscillation of a single atom (blue) and a collective Rabi oscillation for a fully blockaded system of $N = 4$ atoms (red). The Rabi frequency Ω of the blockaded system is enhanced by $\sqrt{N} = 2$.

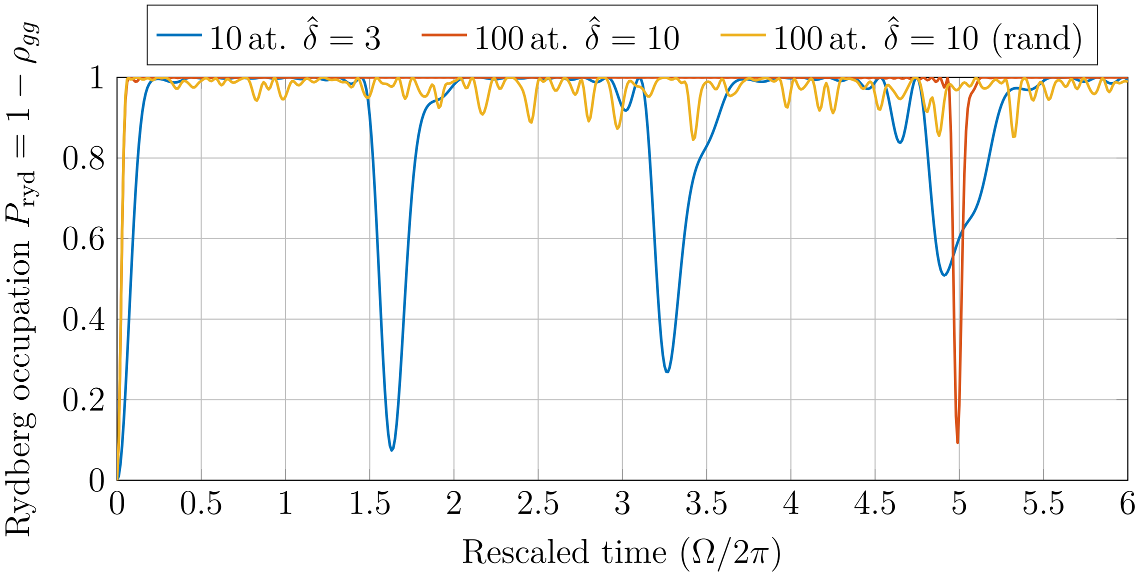

Fig. B.2: Rydberg level occupation for linearly spaced detuning δ from resonance (blue and red), and a random uniform detuning (red). The detuning is within the range $-\hat{\delta} < \delta < \hat{\delta}$ in both cases. The systems with linearly spaced detuning show strong revivals. The numerical errors from the simulation prevent the full reoccupation of the ground-state. The system with a random detuning shows only small revivals.

is reduced. In the special case of a linearly spaced detuning (constant a), the system has strong revivals in the time evolution. This changes if the δ_i is chosen randomly within a uniform distribution in an interval $-\hat{\delta} < \delta < \hat{\delta}$, as shown in figure B.2. The mean probability to find the atom in a Rydberg state exceeds 99 % in a system with $N = 300$ atoms inside the blockade sphere and a detuning of $\hat{\delta} = \sqrt{N}\Omega$ (figure B.3). A single photon, and not two, can be absorbed by such a medium, which leads to a deterministically subtraction of a photon from arbitrary light fields [166].

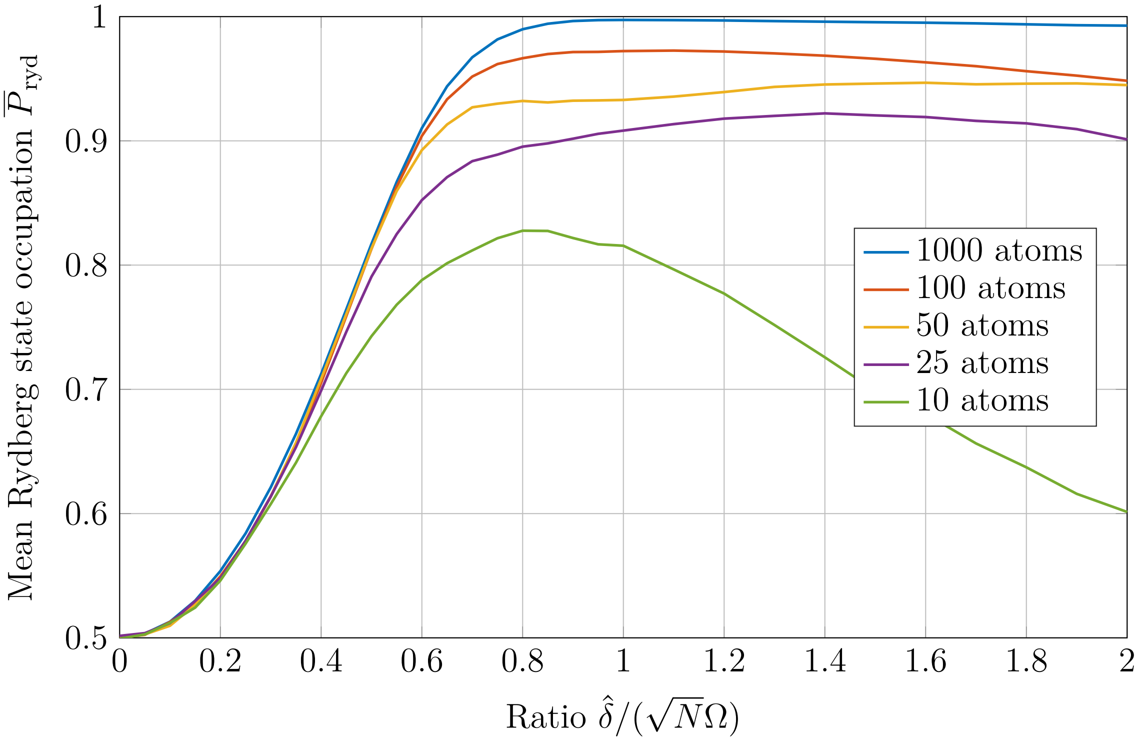

Fig. B.3: Mean Rydberg state occupation after the initial excitation from the ground-state for systems with uniform random detuning δ of each atom in the range of $-\hat{\delta} < \delta < \hat{\delta}$. The optimal frequency detuning is reached for $\hat{\delta} = \sqrt{N}\Omega$. More atoms store the excitation more efficiently and the mean revival of the ground-state is below 1 % for an atom numbers above 300.

Bibliography

[S1] M. Schlagmüller, T. C. Liebisch, H. Nguyen, G. Lochead, F. Engel, F. Böttcher, K. M. Westphal, K. S. Kleinbach, R. Löw, S. Hofferberth, T. Pfau, J. Pérez-Ríos, and C. H. Greene. "Probing an Electron Scattering Resonance using Rydberg Molecules within a Dense and Ultracold Gas". Phys. Rev. Lett. **116** (2016), 053001 (cit. on pp. 7, 19, 22, 78, 85, 151).

[S2] T. C. Liebisch et al. "Controlling Rydberg atom excitations in dense background gases". J. Phys. B At. Mol. Opt. Phys. **49** (2016), 182001 (cit. on pp. 7, 96, 129, 152).

[S3] M. Schlagmüller, T. C. Liebisch, F. Engel, K. S. Kleinbach, F. Böttcher, U. Hermann, K. M. Westphal, A. Gaj, R. Löw, S. Hofferberth, T. Pfau, J. Pérez-Ríos, and C. H. Greene. "Ultracold Chemical Reactions of a Single Rydberg Atom in a Dense Gas". Phys. Rev. X **6** (2016), 031020 (cit. on pp. 7, 19, 22, 102, 112, 153, 155).

[S4] T. Karpiuk, M. Brewczyk, K. Rzażewski, A. Gaj, J. B. Balewski, A. T. Krupp, M. Schlagmüller, R. Löw, S. Hofferberth, and T. Pfau. "Imaging single Rydberg electrons in a Bose–Einstein condensate". New J. Phys. **17** (2015), 53046 (cit. on pp. 8, 19, 30, 101, 126, 150, 154).

[S5] F. Böttcher, A. Gaj, K. M. Westphal, M. Schlagmüller, K. S. Kleinbach, R. Löw, T. C. Liebisch, T. Pfau, and S. Hofferberth. "Observation of mixed singlet-triplet Rb_2 Rydberg molecules". Phys. Rev. A **93** (2016), 032512 (cit. on pp. 22, 74–76, 127, 134).

[6] P. Higgs. "Broken symmetries, massless particles and gauge fields". Phys. Lett. **12** (1964), 132 (cit. on pp. 5, 13).

[7] P. W. Higgs. "Broken Symmetries and the Masses of Gauge Bosons". Phys. Rev. Lett. **13** (1964), 508 (cit. on pp. 5, 13).

[8] F. Englert and R. Brout. "Broken Symmetry and the Mass of Gauge Vector Mesons". Phys. Rev. Lett. **13** (1964), 321 (cit. on pp. 5, 13).

[9] G. S. Guralnik, C. R. Hagen, and T. W. B. Kibble. "Global Conservation Laws and Massless Particles". Phys. Rev. Lett. **13** (1964), 585 (cit. on pp. 5, 13).

[10] G. Aad et al. "Observation of a new particle in the search for the Standard Model Higgs boson with the ATLAS detector at the LHC". Phys. Lett. B **716** (2012), 1 (cit. on pp. 5, 13).

[11] B. P. Abbott et al. "Observation of Gravitational Waves from a Binary Black Hole Merger". Phys. Rev. Lett. **116** (2016), 061102 (cit. on pp. 5, 13).

[12] A. Einstein. *Näherungsweise Integration der Feldgleichungen der Gravitation*. Sitzungsberichte der Königlich Preussischen Akademie der Wissenschaften Berlin. part 1: 688–696., 1916 (cit. on pp. 5, 13).

[13] A. Einstein. *Über Gravitationswellen*. Sitzungsberichte der Königlich Preussischen Akademie der Wissenschaften Berlin. part 1: 154–167, 1918 (cit. on pp. 5, 13).

[14] S. Bose. "Plancks Gesetz und Lichtquantenhypothese". Zeitschrift für Phys. **26** (1924), 178 (cit. on pp. 5, 14, 23).

[15] A. Einstein. *Quantentheorie des einatomigen idealen Gases. Zweite Abhandlung*. Preussischen Akademie der Wissenschaften, 1925 (cit. on pp. 5, 14, 23).

[16] M. H. Anderson, J. R. Ensher, M. R. Matthews, C. E. Wieman, and E. A. Cornell. "Observation of bose-einstein condensation in a dilute atomic vapor." Science **269** (1995), 198 (cit. on pp. 5, 14, 23).

[17] K. Davis, M. Mewes, M. Andrews, N. van Druten, D. Durfee, D. Kurn, and W. Ketterle. "Bose-Einstein Condensation in a Gas of Sodium Atoms". Phys. Rev. Lett. **75** (1995), 3969 (cit. on pp. 5, 14, 23).

[18] R. Löw. "A versatile setup for experiments with Rubidium Bose Einstein condensates: From optical lattices to Rydberg matter". PhD Thesis. Stuttgart, 2006 (cit. on pp. 6, 19, 20).

[19] V. Bendkowsky, B. Butscher, J. Nipper, J. P. Shaffer, R. Löw, and T. Pfau. "Observation of ultralong-range Rydberg molecules". Nature **458** (2009), 1005 (cit. on pp. 6, 19, 62, 73, 85, 90, 101, 134, 150).

[20] D. Hooper and E. A. Baltz. "Strategies for Determining the Nature of Dark Matter". Annu. Rev. Nucl. Part. Sci. **58** (2008), 293 (cit. on p. 13).

[21] J. A. Frieman, M. S. Turner, and D. Huterer. "Dark Energy and the Accelerating Universe". Annu. Rev. Astron. Astrophys. **46** (2008), 385 (cit. on p. 13).

[22] E. F. Keane et al. "The host galaxy of a fast radio burst". Nature **530** (2016), 453 (cit. on p. 13).

[23] Y. Fukuda et al. "Evidence for Oscillation of Atmospheric Neutrinos". Phys. Rev. Lett. **81** (1998), 1562 (cit. on p. 13).

[24] Q. R. Ahmad et al. "Measurement of the rate of nu(e) + d -> p + p + e(-) interactions produced by (8)B solar neutrinos at the Sudbury Neutrino Observatory." Phys. Rev. Lett. **87** (2001), 071301 (cit. on p. 13).

[25] Q. R. Ahmad et al. "Direct evidence for neutrino flavor transformation from neutral-current interactions in the Sudbury Neutrino Observatory." Phys. Rev. Lett. **89** (2002), 011301 (cit. on p. 13).

[26] M. T. Hassan, T. T. Luu, A. Moulet, O. Raskazovskaya, P. Zhokhov, M. Garg, N. Karpowicz, A. M. Zheltikov, V. Pervak, F. Krausz, and E. Goulielmakis. "Optical attosecond pulses and tracking the nonlinear response of bound electrons". Nature **530** (2016), 66 (cit. on p. 14).

[27] H. Weimer, M. Müller, I. Lesanovsky, P. Zoller, and H. P. Büchler. "A Rydberg quantum simulator". Nat. Phys. **6** (2010), 382 (cit. on pp. 14, 101, 150).

[28] M. Saffman, T. G. Walker, and K. Mølmer. "Quantum information with Rydberg atoms". Rev. Mod. Phys. **82** (2010), 2313 (cit. on pp. 14, 30, 67, 101, 137, 150).

[29] J. A. Sedlacek, A. Schwettmann, H. Kübler, R. Löw, T. Pfau, and J. P. Shaffer. "Microwave electrometry with Rydberg atoms in a vapour cell using bright atomic resonances". Nat. Phys. **8** (2012), 819 (cit. on p. 14).

[30] G. Günter, H. Schempp, M. Robert-de-Saint-Vincent, V. Gavryusev, S. Helmrich, C. S. Hofmann, S. Whitlock, and M. Weidemüller. "Observing the dynamics of dipole-mediated energy transport by interaction-enhanced imaging." Science **342** (2013), 954 (cit. on pp. 14, 157).

[31] D. Barredo, H. Labuhn, S. Ravets, T. Lahaye, A. Browaeys, and C. S. Adams. "Coherent excitation transfer in a spin chain of three Rydberg atoms." Phys. Rev. Lett. **114** (2015), 113002 (cit. on pp. 14, 157).

[32] D. W. Schönleber, A. Eisfeld, M. Genkin, S. Whitlock, and S. Wüster. "Quantum simulation of energy transport with embedded Rydberg aggregates." Phys. Rev. Lett. **114** (2015), 123005 (cit. on pp. 14, 157).

[33] S. Huelga and M. Plenio. "Vibrations, quanta and biology". Contemp. Phys. **54** (2013), 181 (cit. on pp. 14, 157).

[34] R. Heidemann, U. Raitzsch, V. Bendkowsky, B. Butscher, R. Löw, L. Santos, and T. Pfau. "Evidence for coherent collective Rydberg excitation in the strong blockade regime." Phys. Rev. Lett. **99** (2007), 163601 (cit. on p. 19).

[35] R. Heidemann, U. Raitzsch, V. Bendkowsky, B. Butscher, R. Löw, and T. Pfau. "Rydberg excitation of Bose-Einstein condensates." Phys. Rev. Lett. **100** (2008), 033601 (cit. on p. 19).

[36] C. H. Greene, A. S. Dickinson, and H. R. Sadeghpour. "Creation of Polar and Nonpolar Ultra-Long-Range Rydberg Molecules". Phys. Rev. Lett. **85** (2000), 2458 (cit. on pp. 19, 73, 85, 101, 111).

[37] V. Bendkowsky, B. Butscher, J. Nipper, J. B. Balewski, J. P. Shaffer, R. Löw, T. Pfau, W. Li, J. Stanojevic, T. Pohl, and J. M. Rost. "Rydberg trimers and excited dimers bound by internal quantum reflection". Phys. Rev. Lett. **105** (2010), 163201 (cit. on pp. 19, 73, 85, 122).

[38] W. Li, T. Pohl, J. M. Rost, S. T. Rittenhouse, H. R. Sadeghpour, J. Nipper, B. Butscher, J. B. Balewski, V. Bendkowsky, R. Löw, and T. Pfau. "A homonuclear molecule with a permanent electric dipole moment". Science **334** (2011), 1110 (cit. on pp. 19, 73, 85, 153).

[39] J. B. Balewski, A. T. Krupp, A. Gaj, D. Peter, H. P. Büchler, R. Löw, S. Hofferberth, and T. Pfau. "Coupling a single electron to a Bose-Einstein condensate". Nature **502** (2013), 664 (cit. on pp. 19, 85, 101, 116, 150).

[40] A. Gaj, A. T. Krupp, J. B. Balewski, R. Löw, S. Hofferberth, and T. Pfau. "From molecular spectra to a density shift in dense Rydberg gases". Nat. Commun. **5** (2014), 4546 (cit. on pp. 19, 85).

[41] T. F. Gallagher. *Rydberg Atoms*. Cambridge: Cambridge University Press, 1994 (cit. on pp. 20, 27, 107–109).

[42] S. Jennewein. “Building an Apparatus for Cold Rubidium Rydberg Atoms”. Diploma thesis. Universität Stuttgart, 2012 (cit. on pp. 22, 47, 48, 51).

[43] C. Tresp. “A Setup for Highly Precise Excitation and Detection of Rydberg Atoms”. Master thesis. Universität Stuttgart, 2012 (cit. on pp. 22, 28, 29).

[44] F. Engel. “Entwicklung eines FPGA basierten Pulsgenerators mit Nanosekunden-Auflösung fur schnelle Rydberg-Experimente”. Bachelor thesis. Universität Stuttgart, 2013 (cit. on p. 22).

[45] T. Schmid. “High precision excitation, manipulation and detection of Rydberg atoms”. Master thesis. Universität Stuttgart, 2014 (cit. on pp. 22, 30, 36, 56, 132).

[46] U. Hermann. “A nanosecond-resolution computer control system for deterministic excitation of Rydberg superatoms”. Bachelor thesis. Universität Stuttgart, 2012 (cit. on p. 22).

[47] U. Hermann. “Analysing and improving high resolution Rydberg field ionization statistics”. Master thesis. Universität Stuttgart, 2014 (cit. on pp. 22, 26, 29, 103, 156).

[48] F. Böttcher. “Rydberg Molecules Bound By Mixed Singlet-Triplet Scattering”. Master thesis. Universität Stuttgart, 2015 (cit. on p. 22).

[49] F. Engel. “Ultracold chemistry of a Rydberg atom in a rubidium-87 BEC”. Master thesis. Universität Stuttgart, 2016 (cit. on p. 22).

[50] M. Greiner, I. Bloch, T. W. Hänsch, and T. Esslinger. “Magnetic transport of trapped cold atoms over a large distance”. Phys. Rev. A **63** (2001), 031401 (cit. on p. 23).

[51] T. Esslinger, I. Bloch, and T. W. Hänsch. “Bose-Einstein condensation in a quadrupole-Ioffe-configuration trap”. Phys. Rev. A **58** (1998), R2664 (cit. on pp. 24, 85).

[52] C. J. Pethick and H. Smith. *Bose-Einstein Condensation in Dilute Gases*. 2nd. Cambridge University Press, 2002 (cit. on pp. 24, 129).

[53] C. Moosbrugger. *ASM Ready Reference: Electrical and Magnetic Properties of Metals*. ASM International, 2000, 285 (cit. on p. 26).

[54] M. Mack, F. Karlewski, H. Hattermann, S. Höckh, F. Jessen, D. Cano, and J. Fortágh. "Measurement of absolute transition frequencies of ^{87}Rb to nS and nD Rydberg states by means of electromagnetically induced transparency". Phys. Rev. A **83** (2011), 052515 (cit. on pp. 27, 28, 76).

[55] D. A. Steck. *Rubidium 87 D line data (revision 2.1.5)*. 2015 (cit. on p. 27).

[56] J. E. Sansonetti. "Wavelengths, Transition Probabilities, and Energy Levels for the Spectra of Rubidium (Rb I through Rb XXXVII)". J. Phys. Chem. Ref. Data **35** (2006), 301 (cit. on p. 27).

[57] D. C. Harris and M. D. Bertolucci. *Symmetry and Spectroscopy: An Introduction to Vibrational and Electronic Spectroscopy*. 1978 (cit. on p. 27).

[58] Hamamatsu Photonics. *Photomultiplier Tubes - Basics and Applications*. 3rd. TOTH9001E03a, 2007 (cit. on p. 30).

[59] L. Mandel. "Sub-Poissonian photon statistics in resonance fluorescence". Opt. Lett. **4** (1979), 205 (cit. on p. 30).

[60] T. C. Liebisch, A. Reinhard, P. R. Berman, and G. Raithel. "Atom counting statistics in ensembles of interacting Rydberg atoms." Phys. Rev. Lett. **95** (2005), 253002 (cit. on p. 30).

[61] R. Loudon. *The Quantum Theory of Light*. 3rd. OUP Oxford, 2000, 448 (cit. on p. 30).

[62] T. Hagglund. *PID Controllers: Theory, Design and Tuning*. 2nd. ISA, 1995 (cit. on p. 34).

[63] J. Szczepkowski, R. Gartman, M. Witkowski, L. Tracewski, M. Zawada, and W. Gawlik. "Analysis and calibration of absorptive images of Bose-Einstein condensate at nonzero temperatures." Rev. Sci. Instrum. **80** (2009), 053103 (cit. on p. 57).

[64] W. F. Holmgren, M. C. Revelle, V. P. A. Lonij, and A. D. Cronin. "Absolute and ratio measurements of the polarizability of Na, K, and Rb with an atom interferometer". Phys. Rev. A **81** (2010), 053607 (cit. on p. 70).

[65] M. R. Flannery, D. Vrinceanu, and V. N. Ostrovsky. "Long-range interaction between polar Rydberg atoms". J. Phys. B At. Mol. Opt. Phys. **38** (2005), S279 (cit. on p. 70).

[66] P. R. Fontana. "Theory of Long-Range Interatomic Forces. I. Dispersion Energies between Unexcited Atoms". Phys. Rev. **123** (1961), 1865 (cit. on p. 70).

[67] A. Jraij, A. Allouche, M. Korek, and M. Aubert-Frécon. "Theoretical electronic structure of the alkali-dimer cation Rb_2^+". Chem. Phys. **290** (2003), 129 (cit. on pp. 70, 71).

[68] J. Pérez-Ríos and C. H. Greene. "Communication: Classical threshold law for ion-neutral-neutral three-body recombination." J. Chem. Phys. **143** (2015), 041105 (cit. on p. 70).

[69] P. Hertz. "Über den gegenseitigen durchschnittlichen Abstand von Punkten, die mit bekannter mittlerer Dichte im Raume angeordnet sind". Math. Ann. **67** (1909), 387 (cit. on pp. 72, 89).

[70] E. Fermi. "Sopra lo Spostamento per Pressione delle Righe Elevate delle Serie Spettrali". Nuovo Cim. **11** (1934), 157 (cit. on pp. 72, 94, 127, 152).

[71] E. Amaldi and E. Segrè. "Effetto della Pressione Sui Termini Elevati Degli Alcalini". Nuovo Cim. **11** (1934), 145 (cit. on pp. 72, 74).

[72] E. Amaldi and E. Segrè. "Effect of Pressure on High Terms of Alkaline Spectra". Nature **133** (1934), 141 (cit. on pp. 72, 74).

[73] M. Born and R. Oppenheimer. "Zur Quantentheorie der Molekeln". Ann. Phys. **389** (1927), 457 (cit. on pp. 72, 78).

[74] B. Numerov. "Note on the numerical integration of $d^2x/dt^2 = f(x,t)$". Astron. Nachrichten **230** (1927), 359 (cit. on p. 75).

[75] J. Pérez-Ríos. *private communication*. Department of Physics and Astronomy, Purdue University, 2016 (cit. on p. 75).

[76] E. L. Hamilton, C. H. Greene, and H. R. Sadeghpour. "Shape-resonance-induced long-range molecular Rydberg states". J. Phys. B At. Mol. Opt. Phys. **35** (2002), L199 (cit. on pp. 74, 75, 80, 101, 151).

[77] A. Omont. "On the theory of collisions of atoms in rydberg states with neutral particles". J. Phys. **38** (1977), 1343 (cit. on pp. 74, 94).

[78] A. A. Khuskivadze, M. I. Chibisov, and I. I. Fabrikant. "Adiabatic energy levels and electric dipole moments of Rydberg states of Rb2 and Cs2 dimers". Phys. Rev. A **66** (2002), 042709 (cit. on p. 74).

[79] D. A. Anderson, S. A. Miller, and G. Raithel. "Angular-momentum couplings in long-range Rb_2 Rydberg molecules". Phys. Rev. A **90** (2014), 062518 (cit. on pp. 74, 80, 85, 101, 150).

[80] H. Saßmannshausen, F. Merkt, and J. Deiglmayr. "Experimental characterization of singlet scattering channels in long-range Rydberg molecules". Phys. Rev. Lett. **114** (2015), 133201 (cit. on pp. 76, 85, 101, 150).

[81] I. I. Fabrikant. "Interaction of Rydberg atoms and thermal electrons with K, Rb and Cs atoms". J. Phys. B At. Mol. Phys. **19** (1986), 1527 (cit. on pp. 76, 77, 94).

[82] C. Bahrim and U. Thumm. "Low-lying $^3P^o$ and $^3S^e$ states of Rb^- , Cs^- , and Fr^-". Phys. Rev. A **61** (2000), 022722 (cit. on pp. 77, 81, 151).

[83] V. A. Davydkin, B. A. Zon, N. L. Manakov, and L. P. Rapoport. "Quadratic Stark Effect on Atoms". JETP **33** (1971), 70 (cit. on p. 78).

[84] A. J. Ångström. *Recherches sur le spectre solaire*. 1868 (cit. on p. 85).

[85] J. J. Balmer. "Notiz über die Spectrallinien des Wasserstoffs". Ann. Phys. **261** (1885), 80 (cit. on p. 85).

[86] J. Tallant, S. T. Rittenhouse, D. Booth, H. R. Sadeghpour, and J. P. Shaffer. "Observation of blueshifted ultralong-range Cs_2 Rydberg molecules". Phys. Rev. Lett. **109** (2012), 173202 (cit. on pp. 85, 101, 150).

[87] M. A. Bellos, R. Carollo, J. Banerjee, E. E. Eyler, P. L. Gould, and W. C. Stwalley. "Excitation of weakly bound molecules to trilobitelike Rydberg states". Phys. Rev. Lett. **111** (2013), 053001 (cit. on p. 85).

[88] A. T. Krupp, A. Gaj, J. B. Balewski, P. Ilzhöfer, S. Hofferberth, R. Löw, T. Pfau, M. Kurz, and P. Schmelcher. "Alignment of D-state Rydberg molecules". Phys. Rev. Lett. **112** (2014), 143008 (cit. on p. 85).

[89] B. J. DeSalvo, J. A. Aman, F. B. Dunning, T. C. Killian, H. R. Sadeghpour, S. Yoshida, and J. Burgdörfer. "Ultra-long-range Rydberg molecules in a divalent atomic system". Phys. Rev. A **92** (2015), 031403 (cit. on p. 85).

[90] A. Gaj, A. T. Krupp, P. Ilzhöfer, R. Löw, S. Hofferberth, and T. Pfau. "Hybridization of Rydberg Electron Orbitals by Molecule Formation". Phys. Rev. Lett. **115** (2015), 023001 (cit. on p. 85).

[91] D. Booth, S. T. Rittenhouse, J. Yang, H. R. Sadeghpour, and J. P. Shaffer. "Production of trilobite Rydberg molecule dimers with kilo-Debye permanent electric dipole moments". Science **348** (2015), 99 (cit. on p. 85).

[92] R. Schmidt, H. R. Sadeghpour, and E. Demler. "Mesoscopic Rydberg Impurity in an Atomic Quantum Gas". Phys. Rev. Lett. **116** (2016), 105302 (cit. on pp. 85, 91).

[93] G. W. Foltz, E. J. Beiting, T. H. Jeys, K. A. Smith, F. B. Dunning, and R. F. Stebbings. "State changing in Na(nd)-electron collisions". Phys. Rev. A **25** (1982), 187 (cit. on pp. 87, 107).

[94] R. G. Rolfes, D. B. Smith, and K. B. MacAdam. "l-changing depopulation of Na s and p Rydberg states by ion impact". Phys. Rev. A **37** (1988), 2378 (cit. on p. 87).

[95] V. M. Borodin and A. K. Kazansky. "The adiabatic mechanism of the collisional broadening of Rydberg states via a loosely bound resonance state of ambient gas atoms". J. Phys. B At. Mol. Opt. Phys. **25** (1992), 971 (cit. on p. 94).

[96] M. E. Henry and R. M. Herman. "Collisional broadening of Rydberg-atom transitions by ground-state alkali atoms". J. Phys. B At. Mol. Opt. Phys. **35** (2002), 357 (cit. on p. 94).

[97] V. Guarrera, P. Würtz, A. Ewerbeck, A. Vogler, G. Barontini, and H. Ott. "Observation of local temporal correlations in trapped quantum gases". Phys. Rev. Lett. **107** (2011), 160403 (cit. on p. 96).

[98] T. Ida, M. Ando, and H. Toraya. "Extended pseudo-Voigt function for approximating the Voigt profile". J. Appl. Crystallogr. **33** (2000), 1311 (cit. on p. 98).

[99] H. Gorniaczyk, C. Tresp, J. Schmidt, H. Fedder, and S. Hofferberth. "Single-photon transistor mediated by interstate Rydberg interactions". Phys. Rev. Lett. **113** (2014), 053601 (cit. on pp. 101, 150).

[100] D. Tiarks, S. Baur, K. Schneider, S. Dürr, and G. Rempe. "Single-photon transistor using a Förster resonance". Phys. Rev. Lett. **113** (2014), 053602 (cit. on pp. 101, 150).

[101] J. Wang, M. Gacesa, and R. Côté. "Rydberg Electrons in a Bose-Einstein Condensate". Phys. Rev. Lett. **114** (2015), 243003 (cit. on pp. 101, 126, 150).

[102] W. Casteels, J. Tempere, and J. T. Devreese. "Polaronic Properties of an Ion in a Bose-Einstein Condensate in the Strong-Coupling Limit". J. Low Temp. Phys. **162** (2010), 266 (cit. on pp. 101, 150, 156).

[103] R. Côté, V. Kharchenko, and M. D. Lukin. "Mesoscopic Molecular Ions in Bose-Einstein Condensates". Phys. Rev. Lett. **89** (2002), 093001 (cit. on pp. 101, 150, 156).

[104] L. Barbier and M. Cheret. "Experimental study of Penning and Hornbeck-Molnar ionisation of rubidium atoms excited in a high s or d level (5d≥nl≥11s)". J. Phys. B At. Mol. Phys. **20** (1987), 1229 (cit. on p. 101).

[105] V. S. Lebedev. "Ionization of Rydberg atoms by neutral particles. II. Mechanisms of the perturber-core scattering". J. Phys. B At. Mol. Opt. Phys. **24** (1991), 1993 (cit. on p. 101).

[106] I. Beigman and V. Lebedev. "Collision theory of Rydberg atoms with neutral and charged particles". Phys. Rep. **250** (1995), 95 (cit. on p. 101).

[107] A. Kumar, B. Saha, C. Weatherford, and S. Verma. "A systematic study of Hornbeck Molnar ionization involving Rydberg alkali atoms". J. Mol. Struct. Theochem **487** (1999), 1 (cit. on p. 101).

[108] A. A. Mihajlov, V. A. Srećković, L. M. Ignjatović, and A. N. Klyucharev. "The Chemi-Ionization Processes in Slow Collisions of Rydberg Atoms with Ground State Atoms: Mechanism and Applications". J. Clust. Sci. **23** (2012), 47 (cit. on pp. 101, 112).

[109] T. Niederprüm, O. Thomas, T. Manthey, T. M. Weber, and H. Ott. "Giant Cross Section for Molecular Ion Formation in Ultracold Rydberg Gases." Phys. Rev. Lett. **115** (2015), 013003 (cit. on pp. 101, 112, 120).

[110] A. P. Hickman. "The effect of core interactions in l-mixing collisions of Rydberg atoms with rare gases". J. Phys. B At. Mol. Phys. **14** (1981), L419 (cit. on p. 101).

[111] A. Härter, A. Krükow, A. Brunner, W. Schnitzler, S. Schmid, and J. H. Denschlag. "Single Ion as a Three-Body Reaction Center in an Ultracold Atomic Gas". Phys. Rev. Lett. **109** (2012), 123201 (cit. on p. 101).

[112] A. P. Hickman. "Relation between low-energy-electron scattering and l-changing collisions of Rydberg atoms". Phys. Rev. A **19** (1979), 994 (cit. on p. 101).

[113] T. F. Gallagher, S. A. Edelstein, and R. M. Hill. "Collisional angular-momentum mixing of Rydberg states of Na by He, Ne, and Ar". Phys. Rev. A **15** (1977), 1945 (cit. on p. 102).

[114] R. K. Janev and A. A. Mihajlov. "Excitation and deexcitation processes in slow collisions of Rydberg atoms with ground-state parent atoms". Phys. Rev. A **20** (1979), 1890 (cit. on p. 102).

[115] E. de Prunele and J. Pascale. "Theoretical model for the collision of high Rydberg atoms with neutral atoms or molecules". J. Phys. B At. Mol. Phys. **12** (1979), 2511 (cit. on p. 102).

[116] A. Walz-Flannigan, J. R. Guest, J.-H. Choi, and G. Raithel. "Cold-Rydberg-gas dynamics". Phys. Rev. A **69** (2004), 063405 (cit. on pp. 107, 108).

[117] T. H. Jeys, G. W. Foltz, K. A. Smith, E. J. Beiting, F. G. Kellert, F. B. Dunning, and R. F. Stebbings. "Diabatic Field Ionization of Highly Excited Sodium Atoms". Phys. Rev. Lett. **44** (1980), 390 (cit. on p. 107).

[118] J. R. Rubbmark, M. M. Kash, M. G. Littman, and D. Kleppner. "Dynamical effects at avoided level crossings: A study of the Landau-Zener effect using Rydberg atoms". Phys. Rev. A **23** (1981), 3107 (cit. on pp. 107, 110).

[119] G. B. McMillian, T. H. Jeys, K. A. Smith, F. B. Dunning, and R. F. Stebbings. "High-resolution field ionisation of Na(ns, nd) Rydberg atoms". J. Phys. B At. Mol. Phys. **15** (1982), 2131 (cit. on p. 107).

[120] Y. Kishimoto, M. Tada, K. Kominato, M. Shibata, S. Yamada, T. Haseyama, I. Ogawa, H. Funahashi, K. Yamamoto, and S. Matsuki. "Systematic observation of tunneling field-ionization in highly excited Rb Rydberg atoms". Phys. Lett. A **303** (2002), 279 (cit. on p. 107).

[121] M. Tada, Y. Kishimoto, M. Shibata, K. Kominato, S. Yamada, T. Haseyama, I. Ogawa, H. Funahashi, K. Yamamoto, and S. Matsuki. "Manipulating ionization path in a Stark map: Stringent schemes for the selective field ionization in highly excited Rb Rydberg". Phys. Lett. A **303** (2002), 285 (cit. on p. 107).

[122] A. Gürtler and W. van der Zande. "l-state selective field ionization of rubidium Rydberg states". Phys. Lett. A **324** (2004), 315 (cit. on p. 107).

[123] M. Jones, B. Sanguinetti, H. Majeed, and B. Varcoe. "Evolutionary optimization of state selective field ionization for quantum computing". Appl. Soft Comput. **11** (2011), 2079 (cit. on p. 107).

[124] C. Zener. "Non-Adiabatic Crossing of Energy Levels". Proc. R. Soc. A Math. Phys. Eng. Sci. **137** (1932), 696 (cit. on p. 110).

[125] W. Ritz. "Magnetische Atomfelder und Serienspektren". Ann. Phys. **330** (1908), 660 (cit. on p. 112).

[126] P. Fuentealba, H. Stoll, L. von Szentpaly, P. Schwerdtfeger, and H. Preuss. "On the reliability of semi-empirical pseudopotentials: simulation of Hartree-Fock and Dirac-Fock results". J. Phys. B At. Mol. Phys. **16** (1983), L323 (cit. on p. 113).

[127] A. Köhn. *private communication*. Institute for Theoretical Chemistry, Universität Stuttgart, 2014 (cit. on p. 113).

[128] M. Shafi, C. L. Beckel, and R. Engelke. "Diatomic molecule ground state dissociation energies". J. Mol. Spectrosc. **42** (1972), 578 (cit. on p. 114).

[129] P. Langevin. "Une formule fondamentale de théorie cenétique". Ann. Chem. Phys **5** (1905), 245 (cit. on p. 119).

[130] G. Gioumousis and D. P. Stevenson. "Reactions of Gaseous Molecule Ions with Gaseous Molecules. V. Theory". J. Chem. Phys. **29** (1958), 294 (cit. on p. 119).

[131] L. de Broglie. "The reinterpretation of wave mechanics". Found. Phys. **1** (1970), 5 (cit. on p. 120).

[132] A. Pasquini. "Quantum Reflection of Bose-Einstein Condensates". PhD Thesis. Massachusetts Institute of Technology, 2007, 69 (cit. on p. 122).

[133] J. C. Slater. "Atomic Radii in Crystals". J. Chem. Phys. **41** (1964), 3199 (cit. on p. 125).

[134] E. Rutherford. "The scattering of α and β particles by matter and the structure of the atom". Philos. Mag. Ser. 6 **21** (1911), 669 (cit. on p. 125).

[135] N. Bohr. "On the Constitution of Atoms and Molecules". Phil. Mag. Ser. 6 **26** (1913), 1 (cit. on p. 125).

[136] M. Planck. "Über das Gesetz der Energieverteilung im Normalspektrum". Ann. Phys. **309** (1901), 553 (cit. on p. 125).

[137] E. Schrödinger. "An Undulatory Theory of the Mechanics of Atoms and Molecules". Phys. Rev. **28** (1926), 1049 (cit. on p. 125).

[138] A. S. Stodolna, A. Rouzée, F. Lépine, S. Cohen, F. Robicheaux, A. Gijsbertsen, J. H. Jungmann, C. Bordas, and M. J. J. Vrakking. "Hydrogen Atoms under Magnification: Direct Observation of the Nodal Structure of Stark States". Phys. Rev. Lett. **110** (2013), 213001 (cit. on p. 125).

[139] F. Dalfovo, S. Giorgini, L. P. Pitaevskii, and S. Stringari. "Theory of Bose-Einstein condensation in trapped gases". Rev. Mod. Phys. **71** (1999), 463 (cit. on p. 126).

[140] M. Egorov, B. Opanchuk, P. Drummond, B. V. Hall, P. Hannaford, and A. I. Sidorov. "Measurement of s -wave scattering lengths in a two-component Bose-Einstein condensate". Phys. Rev. A **87** (2013), 053614 (cit. on p. 126).

[141] R. Grimm, M. Weidemüller, and Y. B. Ovchinnikov. "Optical Dipole Traps for Neutral Atoms". Adv. At. Mol. Opt. Phys. **42** (2000), 95 (cit. on p. 127).

[142] J. Javanainen and J. Ruostekoski. "Symbolic calculation in development of algorithms: split-step methods for the Gross–Pitaevskii equation". J. Phys. A. Math. Gen. **39** (2006), L179 (cit. on pp. 127, 128).

[143] M. R. Andrews, M.-O. Mewes, N. J. van Druten, D. S. Durfee, D. M. Kurn, and W. Ketterle. "Direct, Nondestructive Observation of a Bose Condensate". Science (80-.). **273** (1996), 84 (cit. on p. 132).

[144] D. A. R. Dalvit, J. Dziarmaga, and R. Onofrio. "Measurement-induced squeezing of a Bose-Einstein condensate". Phys. Rev. A **65** (2002), 033620 (cit. on pp. 135, 136).

[145] M. Schellekens. "Hanbury Brown Twiss Effect for Ultracold Quantum Gases". Science (80-.). **310** (2005), 648 (cit. on p. 135).

[146] A. P. Ramirez. "Colossal magnetoresistance". J. Phys. Condens. Matter **9** (1997), 8171 (cit. on p. 156).

[147] B. Keimer, S. A. Kivelson, M. R. Norman, S. Uchida, and J. Zaanen. "From quantum matter to high-temperature superconductivity in copper oxides". Nature **518** (2015), 179 (cit. on p. 156).

[148] F. M. Cucchietti and E. Timmermans. "Strong-coupling polarons in dilute gas Bose-Einstein condensates." Phys. Rev. Lett. **96** (2006), 210401 (cit. on p. 156).

[149] R. M. Kalas and D. Blume. "Interaction-induced localization of an impurity in a trapped Bose-Einstein condensate". Phys. Rev. A **73** (2006), 043608 (cit. on p. 156).

[150] R. G. Hulet and D. Kleppner. "Rydberg Atoms in "Circular" States". Phys. Rev. Lett. **51** (1983), 1430 (cit. on p. 156).

[151] D. A. Anderson, A. Schwarzkopf, R. E. Sapiro, and G. Raithel. "Production and trapping of cold circular Rydberg atoms". Phys. Rev. A **88** (2013), 031401 (cit. on p. 156).

[152] A. Härter, A. Krükow, A. Brunner, and J. Hecker Denschlag. "Minimization of ion micromotion using ultracold atomic probes". Appl. Phys. Lett. **102** (2013), 221115 (cit. on p. 156).

[153] G. S. Engel, T. R. Calhoun, E. L. Read, T.-K. Ahn, T. Mancal, Y.-C. Cheng, R. E. Blankenship, and G. R. Fleming. "Evidence for wavelike energy transfer through quantum coherence in photosynthetic systems." Nature **446** (2007), 782 (cit. on p. 157).

[154] G. R. Fleming, S. F. Huelga, and M. B. Plenio. "Focus on quantum effects and noise in biomolecules". New J. Phys. **13** (2011), 115002 (cit. on p. 157).

[155] M. B. Plenio and S. F. Huelga. "Dephasing-assisted transport: quantum networks and biomolecules". New J. Phys. **10** (2008), 113019 (cit. on p. 157).

[156] F. Caruso, A. W. Chin, A. Datta, S. F. Huelga, and M. B. Plenio. "Highly efficient energy excitation transfer in light-harvesting complexes: The fundamental role of noise-assisted transport". J. Chem. Phys. **131** (2009), 105106 (cit. on p. 157).

[157] A. W. Chin, S. F. Huelga, and M. B. Plenio. "Coherence and decoherence in biological systems: principles of noise-assisted transport and the origin of long-lived coherences." Philos. Trans. A. Math. Phys. Eng. Sci. **370** (2012), 3638 (cit. on p. 157).

[158] S. Hoyer, F. Caruso, S. Montangero, M. Sarovar, T. Calarco, M. B. Plenio, and K. B. Whaley. "Realistic and verifiable coherent control of excitonic states in a light-harvesting complex". New J. Phys. **16** (2014), 045007 (cit. on p. 157).

[159] R. Côté, A. Russell, E. E. Eyler, and P. L. Gould. "Quantum random walk with Rydberg atoms in an optical lattice". New J. Phys. **8** (2006), 156 (cit. on p. 157).

[160] D. P. Fahey, T. J. Carroll, and M. W. Noel. "Imaging the dipole-dipole energy exchange between ultracold rubidium Rydberg atoms". Phys. Rev. A **91** (2015), 062702 (cit. on p. 157).

[161] O. H. Schmitt. "A thermionic trigger". J. Sci. Instrum. **15** (1938), 24 (cit. on p. 162).

[162] T. M. Weber, M. Höning, T. Niederprüm, T. Manthey, O. Thomas, V. Guarrera, M. Fleischhauer, G. Barontini, and H. Ott. "Mesoscopic Rydberg-blockaded ensembles in the superatom regime and beyond". Nat. Phys. **11** (2015), 157 (cit. on p. 173).

[163] M. D. Lukin, M. Fleischhauer, R. Cote, L. M. Duan, D. Jaksch, J. I. Cirac, and P. Zoller. "Dipole Blockade and Quantum Information Processing in Mesoscopic Atomic Ensembles". Phys. Rev. Lett. **87** (2001), 037901 (cit. on p. 173).

[164] C. Cohen-Tannoudji, J. Dupont-Roc, and G. Grynberg. *Atom-photon interactions: basic processes and applications*. 1992 (cit. on p. 173).

[165] F. Schwabl. *Statistical Mechanics*. **5**. Springer Science & Business Media, 2002, 574 (cit. on p. 174).

[166] J. Honer, R. Löw, H. Weimer, T. Pfau, and H. P. Büchler. "Artificial atoms can do more than atoms: deterministic single photon subtraction from arbitrary light fields." Phys. Rev. Lett. **107** (2011), 093601 (cit. on p. 176).

Danksagung

Um ein Kind zu erziehen, braucht es ein ganzes Dorf.
Afrikanisches Sprichwort

Übertragen gilt diese Weisheit auch für die Grundlagenforschung. Nur durch die universitäre Ausbildung und anschließend durch die Einbindung im Team konnte ich das erreichen, was ich jetzt erreicht habe – dafür möchte ich Danke sagen.

An erster Stelle geht mein Dank an Tilman Pfau, der unser Institut so stark in der Rydberg-Physik positioniert hat und die nötigen finanziellen Mittel heranzieht sowie und ein Klima schafft, in dem sich Ideen entfalten können und gut genährt werden.

Großer Dank geht an das Superatoms-Kernteam. Huan war mein Wegbegleiter von der ersten Stunde an, du hast mir viele Aufgaben abgenommen, so dass ich meine Stärken voll einbringen konnte. Danke auch an Sebastian und Robert, für eure Vision für unser Projekt und die vielen wichtigen Entscheidungen, die ihr inspiriert und mitentschieden habt. Insbesondere möchte ich Sebastian für die Möglichkeit danken, dass ich immer und jederzeit mit meinen Fragen zu dir kommen konnte. Wenn du sie nicht sofort kompetent beantworten konntest, hat es meist nur wenige Stunden gedauert, bis du eine tiefere Einsicht in die Thematik liefern konntest.

Danke auch an Stephan und Christoph, die im ersten Jahr mit das Fundament für unser Experiment gelegt haben, an die Thomas dann anknüpfen konnte, Danke auch hierfür. Mit dem Hinzugewinn von Graham hat sich meine Lernkurve im Bereich der ultrakalten Atomphysik deutlich nach oben geneigt. Danke für die vielen guten Fragen, mit denen du mich ins Nachdenken gebracht hast, sowie dem täglichen Englisch-Sprachkurs mit dir. Als Tara mit ins Team gekommen bist, hat sich die Gruppendynamik sehr positiv verändert. Danke dafür, dass du uns und mich so tatkräftig unterstützt und gefördert hast. Mit deinem Einsatz englische Texte zu schreiben und zu korrigieren hast du viel bewegt.

Danke an Karl, Kathrin, Fabian und Felix, mit denen ich in den letzten Jahren am Experiment arbeiten durfte. Ich hoffe, dass ihr einige der Ideen, die noch offen sind umsetzen könnt und dass euch die Maschine noch viele Jahre gute Dienste leisten wird. Ich wünsche euch darüber hinaus, dass euch neue bahnbrechende Dinge einfallen, mit denen ihr die Rydberg-Physik weiter prägen könnt.

Harald, vielen Dank für die Pflege und Wartung der EDV. Nur dadurch haben wir die nötigen Tools an der Hand, effizient arbeiten zu können. Auch der Einsatz unserer Mitarbeiter in der Administration, Astrid, Bea, beide Karins, Nadine und Oli, hat mir viel Freiraum gegeben, mich vorwiegend auf die Physik konzentrieren zu können.

Danke auch an den 4. Stock, insbesondere Jonathan und Anita, von denen ich viel lernen konnte und die mir immer tatkräftig zur Seite standen, wenn ich Rat gesucht habe.

Balu und Bernhard möchte ich dafür danken, dass sie mir als Doktoranden Vorbilder waren in der Zeit meiner Diplomarbeit. Bei euch habe ich gelernt, wie viel Spaß es machen kann, im Team nach guten Fragen und Antworten zu suchen, um neue Physik zu entdecken.

Vielen Dank auch an Chris und Jesus für die vielen endlosen Stunden, in denen jeder von uns die Geduld und Motivation aufgebracht hat, unsere komplexen Ergebnisse zu diskutieren und schlussendlich erfolgreiche Publikationen daraus generieren zu können. Jeder von uns konnte viel lernen in dieser Zeit.

Meinen Eltern und Geschwistern möchte ich dafür danken, dass sie mich mein Leben lang unterstützt und das naturwissenschaftliche Interesse geweckt haben.

Meiner Frau Monika danke ich, dass sie mir den Rücken freigehalten hat in den Zeiten in denen viel los war und dass sie mir immer zur Seite steht.

Helmut und Markus möchte ich danken dafür, dass ich jetzt durch sie und mit ihnen die Möglichkeit habe mit Swabian Instruments eine neue Firma zu gründen, mit der wir High-Tech Geräte-Entwicklung vor Ort betreiben können und der Forschung und darüber hinaus der Wirtschaft Geräte an die Hand geben, mit denen bisher schwierig oder nicht lösbare Probleme und Fragestellungen beantwortet werden können.

Wohl dem Menschen, der Weisheit erlangt, und dem Menschen, der Einsicht gewinnt! Denn es ist besser, sie zu erwerben, als Silber, und ihr Ertrag ist besser als Gold. Sie ist edler als Perlen, und alles, was du wünschen magst, ist ihr nicht zu vergleichen.

Sprüche 3, 13-15